TOWARDS A NEW MEASUREMENT OF THE NEUTRON ELECTRIC DIPOLE MOMENT

Dissertation

zur

Erlangung der naturwissenschaftlichen Doktorwürde
(Dr. sc. nat.)

vorgelegt der

Mathematisch-naturwissenschaftlichen Fakultät

der

Universität Zürich

von

ANDREAS KNECHT

von

WALD ZH

Promotionskomitee

Prof. Dr. Ulrich Straumann (Vorsitz, Leitung der Dissertation)

Prof. Dr. Klaus Kirch

Zürich, 2009

Abstract

Searches for the neutron electric dipole moment (nEDM) are of fundamental importance in understanding the nature of the baryon asymmetry of the universe and the underlying connection to CP violation. The work for this thesis was conducted in connection to the nEDM project at the Paul Scherrer Institut and in the course of the dissertation several substantial contributions to the project were achieved:
The first short EDM measurements have been conducted showing that the EDM apparatus is in principle fully functional and that all the subsystems can be operated reliably over several days. Additionally, an analysis of the taken data has been performed.
For the upcoming EDM measurements beginning in 2010, the expected systematic errors have been assessed and necessary countermeasures suggested. Together with the increase in statistics at the new PSI source for ultracold neutrons (UCN), this should result in a measurement setting a limit of 5×10^{-27} $e$cm at 95% C.L. limit or detecting a neutron EDM of 1.3×10^{-26} $e$cm with $5\,\sigma$ significance after two years of data taking.
Several false effects exist which depend on the velocity of the UCN. In order to being able to measure the neutron electric dipole moment as a function of UCN velocity, an efficient velocity dependent UCN detection system has been developed and successfully tested.
The concept of mirror matter is a proposed extension of the Standard Model of particle physics, which globally reconciles parity violation and provides a viable Dark Matter candidate. The theory also allows for neutron to mirror-neutron oscillations. Such oscillations have been searched for in dedicated measurements using the EDM spectrometer. No indication has been found and a limit on the oscillation time $\tau_{nn'}$ has been set at $\tau_{nn'} > 141\,\mathrm{s}$ (95% C.L.) for negligible mirror magnetic fields B' and $\tau_{nn'} > 12.0\,\mathrm{s}$ (95% C.L.) for any B' between 0 and 12.5 μT.

Zusammenfassung

Die Suche nach dem elektrischen Dipolmoment des Neutrons (nEDM) ist von fundamentaler Bedeutung im Verständnis der Baryonenasymmetrie des Universums und dem Zusammenhang mit CP-Verletzung. Die Arbeit für diese Doktorarbeit wurde im Rahmen des nEDM-Projektes getätigt und im Verlaufe der Dissertation wurden mehrere wesentliche Beiträge zu diesem Projekt erreicht:
Die ersten, kurzen EDM-Messungen wurden durchgeführt, die zeigten, dass das EDM-Spektrometer prinzipiell funktioniert und über mehrere Tage verlässlich betrieben werden kann. Zusätzlich wurde eine Analyse der gewonnenen Daten durchgeführt.
Für die kommenden EDM Messungen ab 2010 wurden die systematischen Falscheffekte abgeschätzt und nötige Gegenmassnahmen vorgeschlagen. Zusammen mit der erhöhten Statistik an der neuen PSI Quelle für ultrakalte Neutronen (UCN) ist eine Messung, die zu einem Limit von $5 \times 10^{-27}\,e$cm bei 95% C.L. oder zu einer Entdeckung eines EDM von $1.3 \times 10^{-26}\,e$cm mit einer Signifikanz von $5\,\sigma$ führt, möglich.
Es existieren mehrere Falscheffekte, die von der Geschwindigkeit der UCN abhängen. Um das EDM als Funktion der UCN-Geschwindigkeit messen zu können wurde ein effizientes, geschwindigkeitabhängiges Detektionssystem entwickelt und erfolgreich getestet.
Das Konzept von Spiegelmaterie ist eine vorgeschlagene Erweiterung des Standardmodells der Teilchenphysik, die global die Paritätsverletzung behebt und gleichzeitig mögliche Kandidaten für Dunkle Materie bietet. Die Theorie führt auch zu Neutron - Spiegelneutron Oszillationen. Solche Oszillationen wurden in dedizierten Messungen mit dem EDM-Spektrometer gesucht. Es konnten keine Hinweise gefunden werden und daher wurde ein Limit auf die Oszillationszeit $\tau_{nn'}$ von $\tau_{nn'} > 141\,$s (95% C.L.) für vernachlässigbare Spiegelmagnetfelder B' und $\tau_{nn'} > 12.0\,$s (95% C.L.) für B' zwischen 0 und 12.5 μT gesetzt.

CONTENTS

LIST OF FIGURES

LIST OF TABLES

1 INTRODUCTION

1.1. ULTRACOLD NEUTRONS

Ultra Cold Neutrons (UCN) are neutrons with kinetic energies below ~300 neV. These energies correspond to velocities below ~8 $\frac{\mathrm{m}}{\mathrm{s}}$, wavelengths bigger than ~50 nm or temperatures below ~3 mK - hence the name. Due to these low energies, UCN can undergo total reflection from many materials under arbitrary angles of incidence. The possibility to store neutrons for times up to the free neutron lifetime τ_n opened another door for precise measurements of fundamental properties of the neutron.

It was Fermi who first realised that the coherent scattering of slow neutrons results in an effective interaction potential for neutrons, which is positive for many materials [1]. This effect was experimentally demonstrated by Fermi and Zinn [2] and Fermi and Marshall [3]. Ya. B. Zel'dovich [4] in 1959 was the first to predict the possibility of storing neutrons in sealed containers if their velocities were low enough. The first to experiment [5] with UCN was the group of F. L. Shapiro at Dubna aiming for an improved measurement of the neutron electric dipole moment (nEDM). At about the same time, Steyerl in Munich performed experiments with very slow neutrons [6].

1.1.1. GRAVITATIONAL INTERACTION

The interaction of UCN with the gravitational potential of the Earth is given by

$$V_g = m_n g h \approx 103 \frac{\mathrm{neV}}{\mathrm{m}} h. \tag{1.1}$$

The accessible energy scale of the gravitational interaction is therefore very comparable to UCN kinetic energies. A UCN with a kinetic energy of 300 neV will therefore not rise higher than ~3 m.

1.1.2. WEAK INTERACTION

The main effect of the weak interaction on the UCN is the decay of the free neutron according to the reaction

$$n \rightarrow p + e^- + \overline{\nu}_e. \tag{1.2}$$

There exists a discrepancy between the two most precise measurements of the neutron lifetime τ_n. While Arzumanov et al. quote a value of $\tau_n = (885.4 \pm 0.9_{stat} \pm 0.4_{syst})$ s [7], Serebrov et al. measured with a similar accuracy $\tau_n = (878.5 \pm 0.7_{stat} \pm 0.3_{syst})$ s [8]. The difference amounts to 6.9 ± 1.2 s or almost six standard deviations. An issue that still remains to be solved in neutron physics.

1.1.3. MAGNETIC INTERACTION

Due to its magnetic moment μ_n, the UCN interacts with external magnetic fields. The strength of the potential is given by

$$V_m = -\boldsymbol{\mu}_n \cdot \boldsymbol{B} \approx \pm 60 \frac{\text{neV}}{\text{T}} B\,. \tag{1.3}$$

An inhomogeneous magnetic field therefore exerts a force on a UCN:

$$\boldsymbol{F}_m = -\boldsymbol{\nabla} V_m = \pm \mu_n \boldsymbol{\nabla} \boldsymbol{B}(\boldsymbol{r}) \tag{1.4}$$

Due to the fact that the magnetic potential is of opposite sign for the two spin components, it is clear that the spin antiparallel to the magnetic field will be accelerated towards higher fields (so called high field seeker) and vice versa (low field seeker). Using magnetic fields therefore allows only for the storage of polarized UCN. A suitably configured magnetic field of 1 T will allow to store UCN with kinetic energies up to 60 neV.

Applying the $\boldsymbol{\nabla}$-operator only onto the magnetic field $\boldsymbol{B}$ in Eq. (1.4) is valid under the condition that the spin of the neutron follows the changing magnetic field at all times adiabatically. This condition is fulfilled when the temporal change of the magnetic field along the UCN trajectory is much less than the precession frequency (Larmor frequency) of the neutron magnetic moment in the field [9]:

$$\frac{1}{B}\frac{\mathrm{d}B}{\mathrm{d}t} \ll \frac{2\mu_n B}{\hbar} = \omega_L \tag{1.5}$$

Generally, one expresses the spin precession of particles as

$$\boldsymbol{\omega}_L = -\gamma \boldsymbol{B}\,. \tag{1.6}$$

γ is the gyromagnetic ratio given as $\gamma = \frac{2\mu}{\hbar}$ and the minus sign results in the correct direction of the spin precession with respect to the orientation of $\boldsymbol{B}$ and the sign of γ. The above equation will be used again in several of the following sections. For the neutrons, γ_n amounts to $-2\pi \times 29.164702 \frac{\text{Hz}}{\mu\text{T}}$ [10]. UCN in a field of 1 μT will thus precess at a frequency $\frac{\omega}{2\pi}$ of ~29 Hz.

1.1.4. STRONG INTERACTION

The strong interaction is responsible for the binding of neutrons and protons in the nucleus of an atom. Over this short length scale (~1 fermi = 10^{-15} m) it is strong enough to overcome the electromagnetic repulsion of the protons.

The strong interaction governs also the interaction of UCN with material walls resulting in either reflection or absorption. These two processes can be described by a complex potential $V_F = V - iW$ (called Fermi potential) that takes into account the averaging over many nuclei (see subsequent paragraphs) - which is valid for the long wavelength UCN. Typical values for $\Re(V_F)$ lie in the range of UCN kinetic energies. A small overview is given in Table 1.1.

Material	$\Re(V_F)$ [neV]	n [10^{22} cm^{-3}]	a_{coh} [10^{-12} cm]
Ni^{58}	335	9.0	1.44
C (diamond)	306	17.6	0.67
Ni	252	9.0	1.03
Fe	210	8.5	0.95
C (graphite)	195	11.5	0.67
Al	54	6.0	0.35
Ti	-45	5.6	-0.33

Table 1.1.: Values for the real part of the Fermi potential V_F for a set of materials together with the number densities n and the bound coherent scattering length a_{coh} needed for the evaluation of $\Re(V_F)$ using Eq. (1.13). Data are taken from [9, 11].

SCATTERING

The derivation of the scattering properties of UCN is taken from [9]. In general, the total wave function of a scattered particle outside the interaction potential - where $V(r) = 0$ - has the form

$$\Psi = \Psi_i + \Psi_{scat} = e^{i\mathbf{kr}} + f(\theta)\frac{e^{ikr}}{r}. \tag{1.7}$$

The total wave function is therefore given as a superposition of the incident wave $\Psi_i = e^{i\mathbf{kr}}$ and the scattered wave $\Psi_{scat} = \frac{e^{ikr}}{r}$ modified by a scattering potential dependent scattering amplitude $f(\theta)$. Due to the fact that the UCN wavelength is much larger than the range of the strong interaction, $f(\theta)$ is constant:

$$f(\theta) = \text{const} = -a \tag{1.8}$$

The constant a is the experimentally determinable scattering length appearing in the differential cross section as

$$\frac{\mathrm{d}\sigma}{\mathrm{d}\Omega} = |f(\theta)|^2 = a^2. \tag{1.9}$$

Since the strength of the strong interaction potential $V(\mathbf{r} - \mathbf{r}_{nucl})$, where $\mathbf{r}_{nucl}$ is the position of the scattering nucleus, is much larger than the neutron energy, the application of perturbation theory is in principle not valid. Fermi realised however [1], that due to the fact that the changes in the wave function occur only over small distances, it is possible to introduce an effective potential describing the scattering process to good approximation. This effective potential can be written as

$$U_F(\mathbf{r} - \mathbf{r}_{nucl}) = \frac{2\pi\hbar^2 a_B}{m_n}\delta^{(3)}(\mathbf{r} - \mathbf{r}_{nucl}), \tag{1.10}$$

where $a_B = \frac{m_n}{\mu}a$ is the bound nucleus scattering length and $\mu = \frac{m_n m_{nucl}}{m_n + m_{nucl}}$ is the reduced mass.

As the UCN wavelength is large compared to the size of nuclei, a multitude of nuclei take part in the scattering process. The corresponding total potential is therefore given as a sum of individual scattering potentials:

$$V(\mathbf{r}) = \sum_i U_F(\mathbf{r} - \mathbf{r}^i_{nucl}) = \frac{2\pi\hbar^2}{m_n}\sum_i a^i_B \delta^{(3)}(\mathbf{r} - \mathbf{r}^i_{nucl}) \tag{1.11}$$

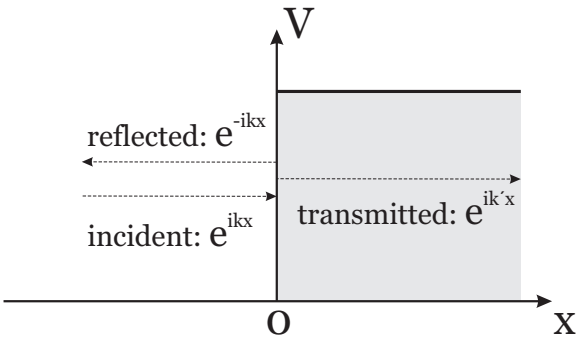

Figure 1.1.: Ansatz for the solution of a potential step with the three wave functions: (i) incident, (ii) reflected and (iii) transmitted.

The total wave function is then given (in analogy to Eq. (1.7)) as

$$\Psi(\mathbf{r}) = e^{i\mathbf{k}_0\mathbf{r}} - \sum_i a_B^i \Psi_i(\mathbf{r}^i_{nucl}) \frac{e^{ik_0|\mathbf{r}-\mathbf{r}^i_{nucl}|}}{|\mathbf{r}-\mathbf{r}^i_{nucl}|}, \tag{1.12}$$

where $\Psi_i(\mathbf{r}^i_{nucl})$ is the value of the incident wave function at the location of the ith nucleus. Transforming the above equation into an integral equation and applying the operator $\nabla^2 + k_0^2$, one finds the Schrödinger equation for a particle moving in an effective potential

$$V(\mathbf{r}) = \frac{2\pi\hbar^2}{m_n} n(\mathbf{r}) a_{coh} \tag{1.13}$$

with a_{coh} being the bound atom coherent scattering length and $n(\mathbf{r})$ the nuclear number density. This potential is the volume average of the single potentials Eq. (1.11) and the real part of the potential V_F defined in Section 1.1.4 relevant for the reflection of UCN on material walls.

REFLECTION

Eq. (1.13) can be used to describe the material as a step in potential with the height given as $V = \frac{2\pi\hbar^2}{m_n} na$. The ansatz to the solution of this problem is then simple and given as (see also Fig. 1.1)

$$\Psi = \begin{cases} e^{ik_x x} + Re^{-ik_x x} & x < 0 \\ Te^{ik'x} & x > 0 \end{cases} \tag{1.14}$$

with the potential step located at $x = 0$, the incident wave coming from the left and $k' = \sqrt{\frac{2m_n}{\hbar^2}(E_\perp - V)}$ defined by the available energy inside the material. $E_\perp$ is the amount of energy of the incident neutron perpendicular to the potential step. Continuity conditions at the potential step yield the solutions for the two amplitudes

$$R = \frac{\sqrt{E_\perp} - \sqrt{E_\perp - V}}{\sqrt{E_\perp} + \sqrt{E_\perp - V}} \tag{1.15}$$

$$T = 1 - R \tag{1.16}$$

For the case $E_\perp > V$, k' is real and the reflection probability $|R|^2 < 1$. For the case $E_\perp < V$, the reflection probability is $|R|^2 = 1$ and k' imaginary, i.e., the transmitted wave is exponentially decaying. It is clear that if the total neutron energy is smaller than the potential $E < V$, the particle will be reflected under any angle of incidence and can be stored.

Due either to absorption (neutron capture) or inelastic up-scattering, the UCN can get lost upon reflection. This loss process is controlled by the imaginary part of the Fermi potential as introduced in Sec. 1.1.4. This can be deduced from the time dependent Schrödinger equation. Based on that equation, one arrives at an equation of continuity for the probability density $\rho = |\Psi|^2$. Having an imaginary part in the potential $\Im(V_F) = W$ results in an additional part in the continuity equation given by

$$\left(\frac{\partial \rho}{\partial t}\right)_{add} = -\frac{2W}{\hbar}\rho\,. \tag{1.17}$$

The solution to this differential equation is simply given by

$$\rho(t) = \rho_0 e^{-\frac{2W}{\hbar}t} \equiv \rho_0 e^{-\frac{t}{\tau_l}}\,. \tag{1.18}$$

On the other hand, the loss decay constant τ_l is simply given by

$$\frac{1}{\tau_l} = \sum_i n_i \sigma_l^i v\,, \tag{1.19}$$

summing over the different nuclear species with densities n_i and loss cross sections σ_l^i for UCN of velocity v. The Fermi potential is therefore for a pure material given as

$$V_F = V - iW = n\left(\frac{2\pi\hbar^2}{m_n}a - i\frac{\hbar}{2}\sigma_l v\right). \tag{1.20}$$

Repeating the above calculations for R with this complex potential results in (under the assumption $W \ll V$)

$$|R|^2 = 1 - 2\frac{W}{V}\sqrt{\frac{E_\perp}{V - E_\perp}} \equiv 1 - \mu(E,\theta) \tag{1.21}$$

where one defines the wall loss probability per bounce $\mu(E,\theta)$ as a function of UCN energy E and incident angle θ given by[1]

$$\mu(E,\theta) = 2\frac{W}{V}\sqrt{\frac{E\cos^2\theta}{V - E\cos^2\theta}}\,. \tag{1.22}$$

1.1.5. PRODUCTION

The basic principle in the production of UCN consists of the sufficient deceleration of neutrons stemming either from fission (nuclear reactors) or spallation (accelerator driven). Firstly, the neutrons are moderated with suitable materials down to energies in the cold neutron regime (∼ meV). For the next step in deceleration, there exist at the moment two different approaches:

[1] Often, one defines also $\eta = \frac{W}{V}$ as the loss probability per bounce.

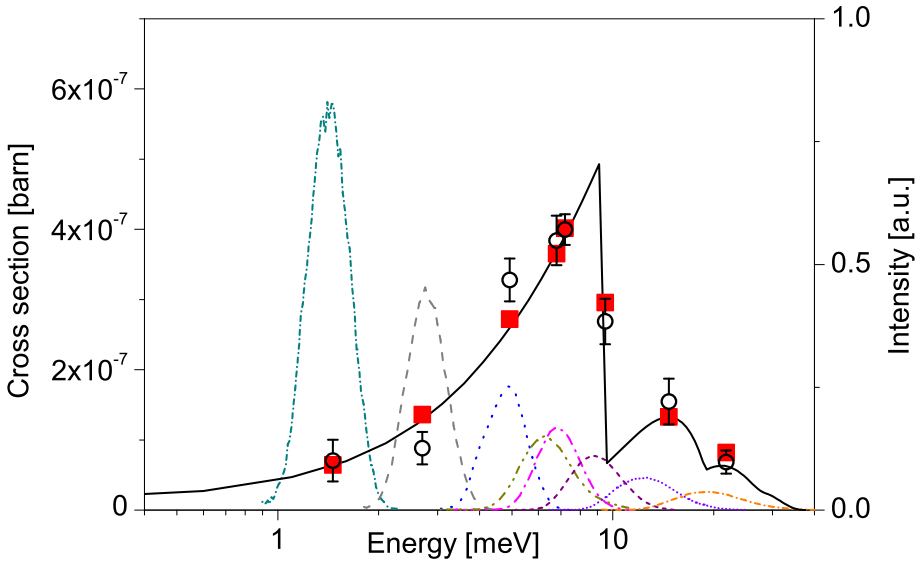

Figure 1.2.: UCN production cross section as a function of incident cold neutron beam energy for solid deuterium [12]. The two peaks to the right correspond to multi-phonon excitations.

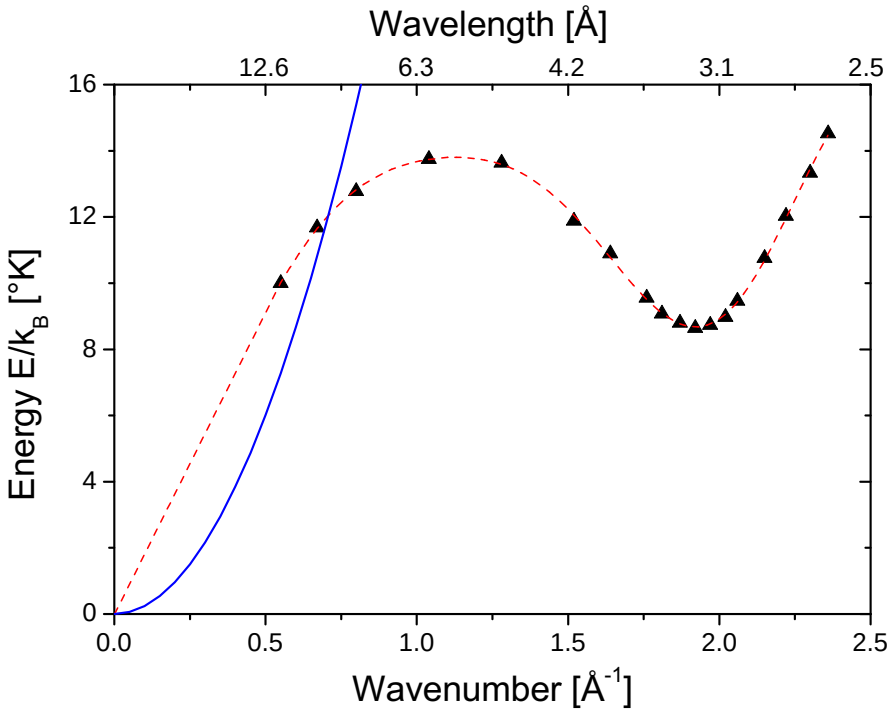

Figure 1.3.: Energy dispersion curve for free neutrons (solid line) and for superfluid ^{4}He (dashed line and triangles) [13]. At an incident wavelength of 8.9 Å, all of the neutron energy can be transformed into phonon excitations of the superfluid helium leaving the neutron energy in the UCN region.

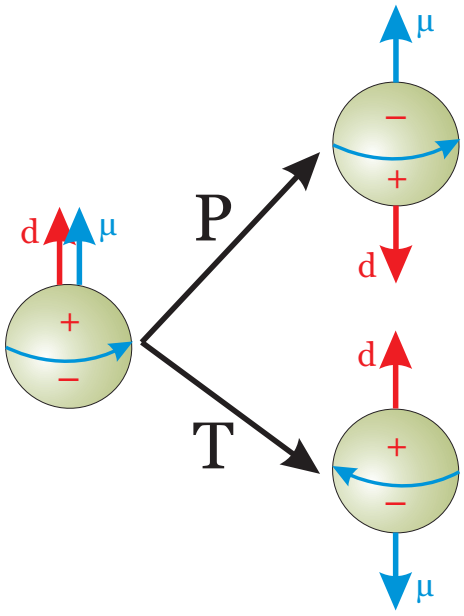

Figure 1.4.: Figure depicting the P and T violating nature of an electric dipole moment. The two transformed states are intrinsically distinguishable from the original state and thus violate P and T symmetry.

1) Vertical extraction (further deceleration in the gravitational field) and scattering at receding blades [14, 15]. This method is exploited at the Institut Laue-Langevin (ILL, Grenoble, France) resulting in a UCN density of up to 50/cm^3. The gravitational and mechanical transformation of the energy spectrum into the UCN regime is governed and limited by Liouville's theorem stating that the phase space density of the neutrons remains constant in time.

2) Conversion by means of down-scattering inside a suitable material [16]. In this process energy is transferred from the incident cold neutron into phonon excitations of the material. The inverse process is highly suppressed due to the low temperature of the material. Such conversion processes are thus called superthermal. Suitable materials are, e.g., solid Deuterium ($^2H_2$) and superfluid Helium (see Fig. 1.2 and 1.3). For both, it has been shown that UCN production is possible, see e.g. [17, 18].

1.2. NEUTRON ELECTRIC DIPOLE MOMENT

A permanent electric dipole moment is the exact analogon to a magnetic dipole moment with the difference of coupling to an electric instead of a magnetic field. The Hamiltonian of such a particle in a an electric and magnetic field can thus be written as:

$$\mathcal{H} = -\frac{\mu}{s}\boldsymbol{s}\cdot\mathbf{B} - \frac{d}{s}\boldsymbol{s}\cdot\mathbf{E} \tag{1.23}$$

Additionally, the presence of an EDM violates both parity (P) and time reversal (T) symmetry (see Fig. 1.4). Due to the fact that the combined symmetry CPT (where C denotes charge conjugation) has to be unbroken (see, e.g., [19]), an EDM violates also CP. So far, no EDM has been measured.

1.2.1. MOTIVATION

The universe, as we observe it, is made of matter. All the antimatter that has been produced at the beginning of our universe (Big Bang) has since annihilated with matter producing photons. With the apparently still available matter, this presents a highly asymmetric situation. The latest measurements on the baryon to photon ratio resulted in [20]

$$\eta_B \equiv \frac{n_B}{n_\gamma} = 6.12^{+0.20}_{-0.25} \times 10^{-10} \tag{1.24}$$

According to Sakharov [21], three criteria have to be fulfilled in order for such an asymmetry to appear:

- Violation of baryon number (B) symmetry.
- Violation of charge conjugation (C) and the combined symmetry of charge conjugation and parity (CP).
- Departure from thermal equilibrium.

As the amount of CP violation in the Standard Model of particle physics is not sufficient to fulfill the above Sakharov conditions - a corresponding calculation within the Standard Model results in $n_B/n_\gamma \approx 10^{-18}$ [22] -, finding an EDM (corresponding to a new source of CP violation) and understanding the universe are therefore tightly entwined.

1.2.2. THEORY

In the Standard Model, the only source of CP violation stems from the imaginary phase of the quark mixing matrix (named CKM after its discoverers Cabibbo, Kobayashi and Maskawa [23, 24]). For a qualitative explanation why this is the case see Appendix A.1. As the amount of CP violation in the CKM-Matrix is very small and the contributions to the neutron EDM stem from loop effects, the predictions are tiny $d_n \approx 10^{-32} \ldots 10^{-30} e\text{cm}$ [25] compared to the current upper limit of $2.9 \times 10^{-26} e\text{cm}$ [26].

THE STRONG CP PROBLEM

Gauge invariance allows the incorporation of an additional term in the QCD Lagrangian in analogy to the field strength term of the electromagnetic fields [27]:

$$\mathscr{L}_\theta = -\theta \frac{\alpha_s}{8\pi} \tilde{G}^a_{\mu\nu} G^a_{\mu\nu}, \tag{1.25}$$

called "θ term". $G^a_{\mu\nu}$ is the gluon field strength tensor. This term leads to a a neutron EDM of

$$|d_n| \approx \theta \times 10^{-16}\, e\text{cm}. \tag{1.26}$$

The current limit on d_n implies that

$$\theta < 10^{-10}. \tag{1.27}$$

As the parameter θ has the significance of an angle and can thus adopt values between 0 and π, it is regarded as very unnatural as to why the angle should be fine-tuned to zero

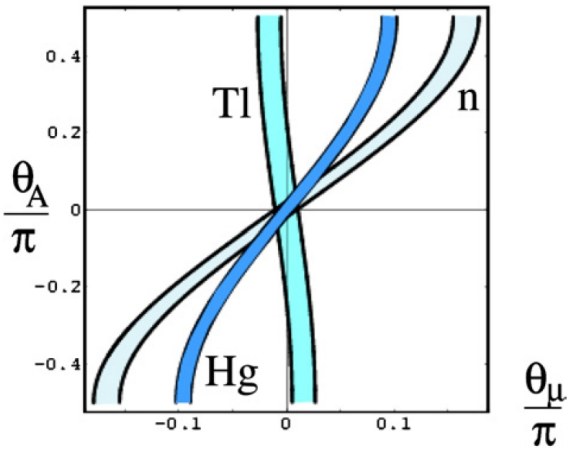

Figure 1.5.: Constraints on two CP violating phases for a given supersymmetric model from the experimental limits of the neutron, mercury and thallium EDM (from [30]).

to such a high degree. This is regarded as the strong CP problem and people have been trying to find the underlying mechanism responsible for the fine-tuning ever since.

In 1977, Peccei and Quinn put forward a mechanism to explain the smallness of the "θ term" by introducing pseudoparticles [28] - the so called axions. So far, no evidence for such particles has been found.

THE SUSY CP PROBLEM

In supersymmetric models, the EDM of the neutron can be generated at lower order than in the Standard Model. Moreover, in the minimal versions there are two CP violating phases present. This results in predictions for the neutron EDM of the order $d_n \approx 10^{-28} \ldots 10^{-25} e\text{cm}$. Predictions usually have the simplified form [29]

$$d_n \sim \left(\frac{300\,\text{GeV}}{M}\right)^2 \sin\phi \times 10^{-24}\, e\text{cm}, \tag{1.28}$$

where M is the typical SUSY mass scale and ϕ a combined CP violating phase. As in the strong CP problem the current limits require either the SUSY mass scale to be large or the CP violating phases to be small - the SUSY CP problem.

Figure 1.5 illustrates the constraints that the experimental limits from the neutron, mercury and thallium EDM pose on two SUSY CP violating phases. Both phases are constrained to be $< 10^{-2}$.

1.2.3. EXPERIMENTAL TECHNIQUE

From Eq. (1.23), the precession frequency ν of the neutron due an electric and magnetic field can be derived:

$$h\nu^{\uparrow\uparrow} = |2\boldsymbol{\mu}_n \cdot \boldsymbol{B} + 2\boldsymbol{d}_n \cdot \boldsymbol{E}| \tag{1.29}$$

$$h\nu^{\uparrow\downarrow} = |2\boldsymbol{\mu}_n \cdot \boldsymbol{B} - 2\boldsymbol{d}_n \cdot \boldsymbol{E}| \tag{1.30}$$

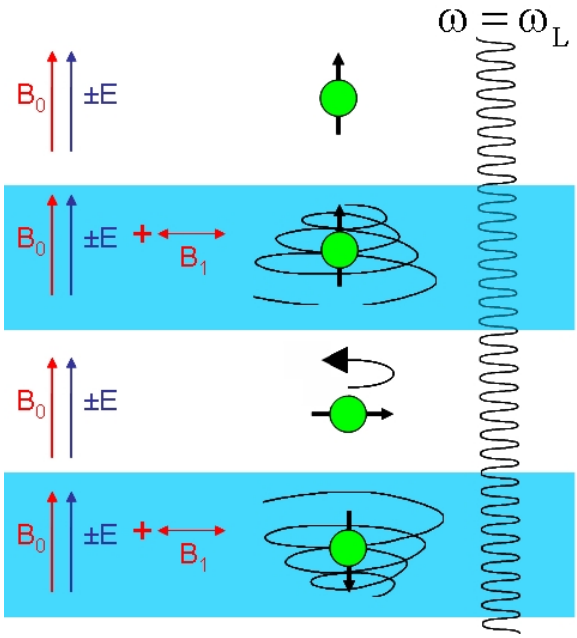

Figure 1.6.: Illustration of Ramsey's method of separated oscillatory fields. For details see text. Illustration adapted from [31].

where the arrows indicate parallel or anti-parallel field configurations. The neutron EDM is then directly given as the difference of these two frequencies:

$$d_n = -\frac{h}{4E}\left(\nu^{\uparrow\uparrow} - \nu^{\uparrow\downarrow}\right) \tag{1.31}$$

The two major experimental difficulties now lie (i) in the precise determination of the precession frequency and (ii) in the requirement $B^{\uparrow\uparrow} \approx B^{\uparrow\downarrow}$ for the two measurements.

RAMSEY'S METHOD OF SEPARATED OSCILLATORY FIELDS

In 1950, Ramsey invented the method of using separate oscillatory fields [32] to measure the spin precession of a quantum mechanical system. The basic principle is illustrated in Fig. 1.6. The ensemble is initially polarised along the main field axis. A linear oscillatory field perpendicular to the main field and of a given duration turns the spin into the plane perpendicular to the main field after which it is gated off (however not switched off and therefore keeping its phase relation). After a certain time of free precession, the oscillatory field is gated back in and induces the second $\pi/2$ flip of the spin.

The actual effect of these two oscillatory pulses depends on the frequency ω used for these pulses compared to the Larmor precession frequency ω_0 around the main field. If ω is exactly equal to ω_0, the spin does a complete π flip. Otherwise, the spin acquires a phase shift during the free precession causing a characteristic resonance pattern (see Fig. 1.7). The width of the central valley in the Ramsey resonance pattern (and therefore the sensitivity of the measurement) depends on $\frac{1}{T}$ with T being the free precession time. If ω is too far away from the resonance frequency, the spin cannot be flipped at all. In practice, one measures the polarisation at four different working points in the resonance curve (where the change is steepest) and does a fit to the central fringe in order to obtain the resonance frequency.

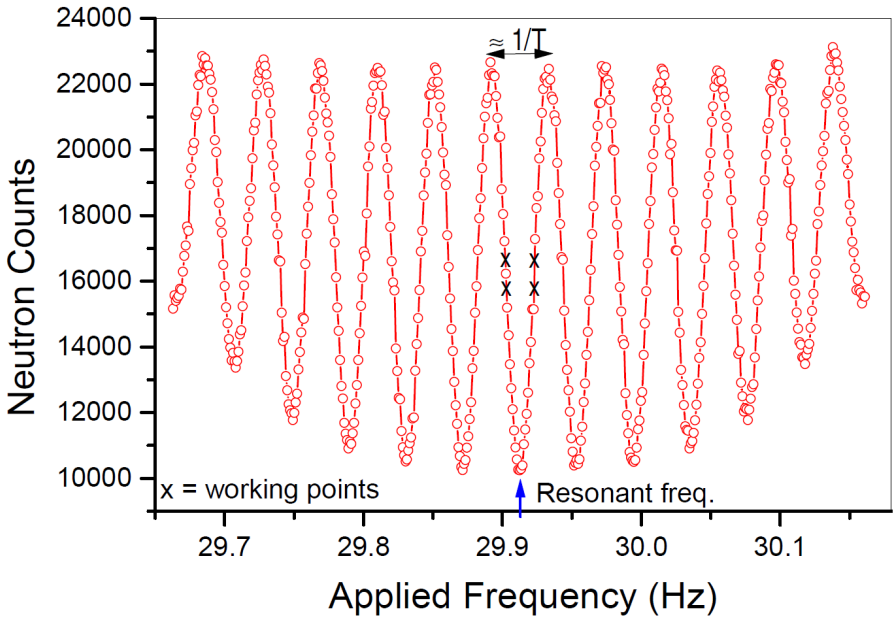

Figure 1.7.: Ramsey resonance curve showing the spin up UCN counts as a function of applied frequency of the oscillatory magnetic field acting on an initially spin up ensemble. The crosses x show the working points used to extract the resonance frequency by fitting the central fringe. Plot from [31].

MAGNETIC FIELD CONTROL

The efforts concerning the magnetic field are threefold:

(i) The use of a magnetic shield to suppress the effects of exterior magnetic fields and magnetic field changes on the measurement. A magnetic shield typically consists of multiple layers of so called Mu-metal - a material with very high magnetic permeability μ (typically around 20 000). Its effectiveness is expressed in the so called shielding factor given as the ratio of the external field to the internal field. For a typical size cylindrical shield, the transverse shielding factor is of the order of a few 10 000, whereas the axial shielding factor is roughly a factor 10 smaller. Therefore the internal main magnetic field used for the EDM measurement is oriented in the transverse direction.

(ii) The generation of a homogeneous magnetic field inside the magnetic shield. The requirements for a homogeneous magnetic field come from two sides. Firstly, any magnetic gradient will lead to different precession frequencies at different positions and therefore produce loss of phase correlation (i.e., polarisation). Secondly, a magnetic field gradient together with the motional magnetic field $\boldsymbol{v} \times \boldsymbol{E}$ will mimic an EDM signal during the measurements (see Sec. 3.2).

(iii) The measurement of the magnetic field inside the magnetic shield. Magnetometers can either be placed surrounding the precession chamber or - given a suitable method - as a so called co-magnetometer inside the precession chamber. Such a co-magnetometer directly allows the knowledge of the volume averaged magnetic field inside the precession chamber. Fast magnetometers can also be used to actively control the current going through the main field coil and additional trim coils to further reduce the effects of external fields penetrating the magnetic shield.

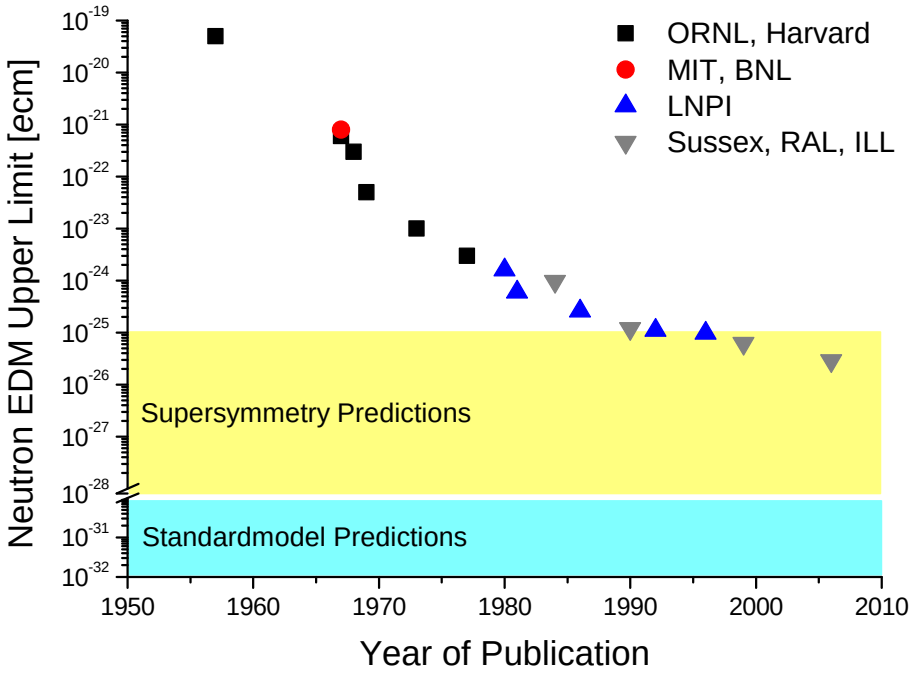

Figure 1.8.: Evolution of the measured upper limit on the neutron EDM as a function of year. The two bands show the prediction from Supersymmetry and the Standard Model.

1.2.4. HISTORY OF NEUTRON EDM EXPERIMENTS

Figure 1.8 shows the evolution of the measured upper limit on the neutron EDM as a function of year. So far, six orders of magnitude have been covered since the beginning of measurements in the 50s and thereby put more stringent constraints on theoretical models than probably any other experimental value [33]. Up to 1977, experiments with neutron beams were conducted, whereas afterwards the experiments with stored UCN took over.

BEAM EXPERIMENTS

The first experiments used beams of neutrons (first thermal and later cold neutrons) in order to search for the neutron EDM. The first experiment was completed in 1951 at Oak Ridge National Laboratory (and published in 1957 [34]) and resulted in an upper limit of $5 \times 10^{-20}\,e$cm. A schematic is shown in Fig. 1.9. The system is a direct implementation of Ramsey's method of separated oscillatory fields (see Sec. 1.2.3). The polarised neutrons pass a first radio-frequency coil to induce the first $\pi/2$ flip, traverse the region of superimposed electric and magnetic field (parallel or anti-parallel), pass the second RF-coil and are counted after the spin analyser consisting of magnetised iron.

In 1967, the so called crystal EDM was performed at MIT [35]. It relied on the strong Coulomb fields found in matter of up to 10^{11} V/m. Neutrons were scattered on the planes of a Cadmium-Sulphur crystal (CdS) with a superimposed magnetic field. The final result was the upper limit of $8 \times 10^{-22}\,e$cm. The difficulty to align the crystal planes to the superimposed magnetic field stopped further progress with this technique. Recently, the idea of exploiting the high electric fields in crystals has been taken up again [36].

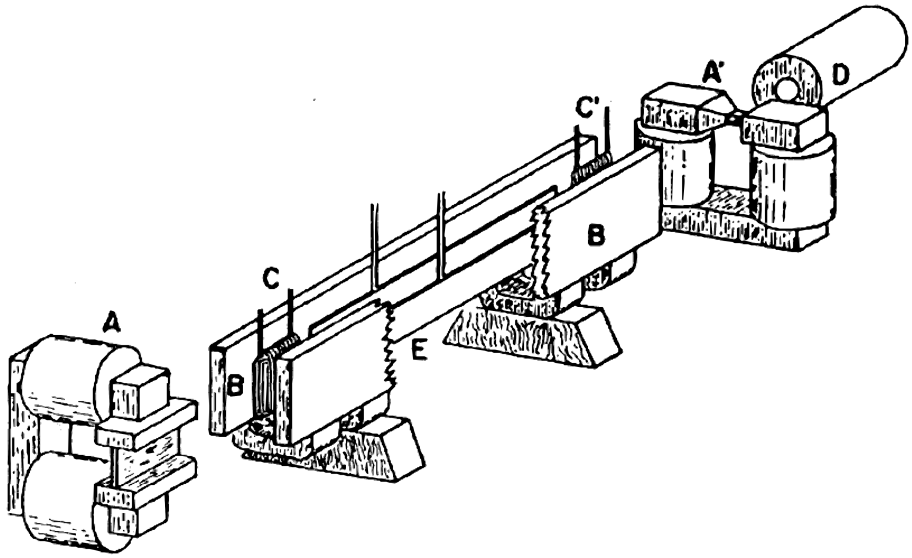

Figure 1.9.: Schematic of the first neutron EDM experiment. A and A' are the magnetised iron polariser and analyser, B the poles for the homogeneous magnetic field, C and C' the RF coils for the $\pi/2$ flips, D the BF_3 neutron counter and E the electrodes for the generation of the homogeneous electric field. Picture from [34].

The experiments at Oak Ridge National Laboratory continued (two other beam experiments have been conducted at Brookhaven National Laboratory [37] and Institute of Atomic Physics Bucharest [38]) to steadily improve on the upper limit. In the late 70s the apparatus was moved to the Institut Laue-Langevin in Grenoble, France, in order to profit from the much higher neutron flux available. The limit obtained in 1977 was $3 \times 10^{-24}\, e$cm and marked the end of beam experiments to search for the neutron EDM. This last experiment was already heavily plagued by systematic effects (e.g., the $\boldsymbol{v} \times \boldsymbol{E}$ motional field due to the directed beam of neutrons) for which no solutions could be found.

STORAGE EXPERIMENTS

The possibility to store neutrons allowed for Ramsey cycles of much longer duration (of $\mathcal{O}(100\text{ s})$) and with neutrons of much lower velocity. In contrast to the beam experiments, the $\pi/2$ pulses are in this case not separated in space but in time with the UCN staying in the precession chamber for the whole Ramsey sequence.

The first experiment to use UCN was conducted at the Leningrad Nuclear Physics Institute (LNPI, now Petersburg Nuclear Physics Institute (PNPI)) in 1980 [39] (see Fig. 1.10 for a schematic drawing). It featured a double chamber to measure the magnetic and electric field parallel and antiparallel case simultaneously. Cs magnetometers were used to control the magnetic field environment. After continued improvement over the course of more than 10 years, the final limit of $9.7 \times 10^{-26}\, e$cm [40] was achieved.

The second experiment had started only slightly later, in 1984 [41] (see Fig. 1.11 for a schematic drawing). It featured a single chamber and Rb magnetometers for magnetic field control. The experimental setup was changed in the early 90s to incorporate a

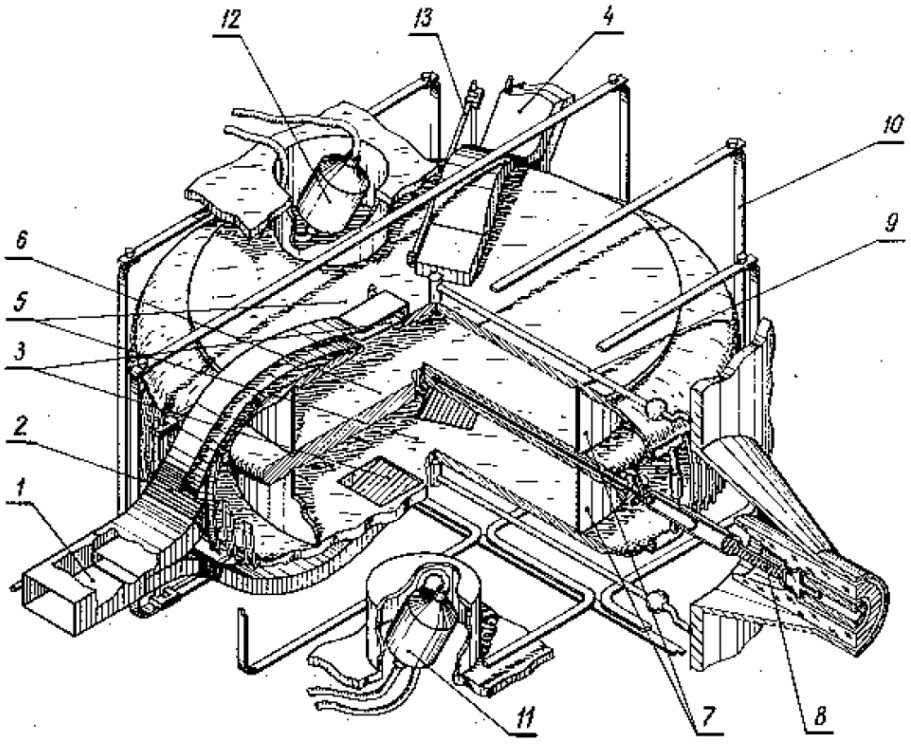

Figure 1.10.: Schematic of the first nEDM experiment with UCN. Picture from [39].

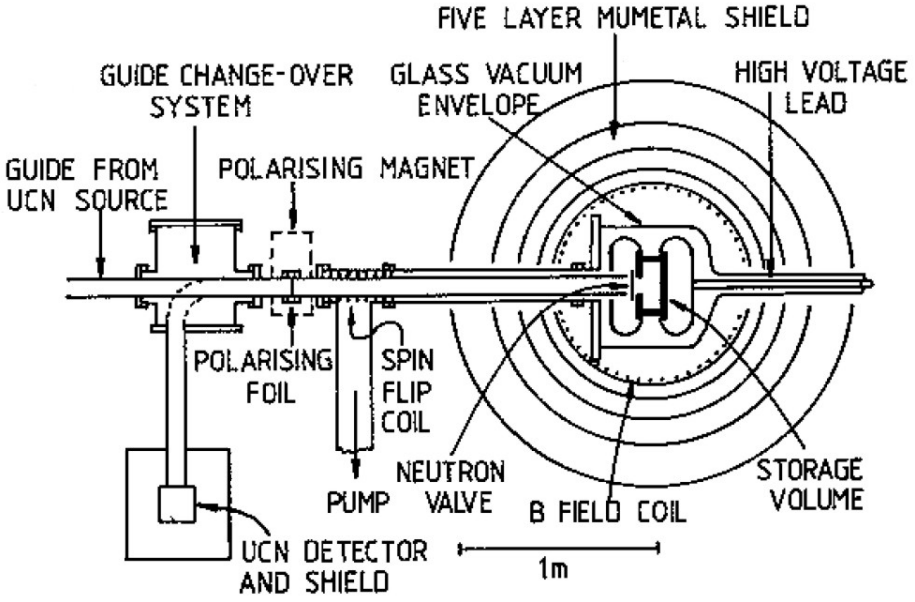

Figure 1.11.: Schematic of the nEDM apparatus which later, after some adaptations, lead to the current best limit on the neutron EDM. Picture from [41].

so called co-magnetometer - ^{199}Hg in this case - adopting its present form (see Sec. 2.1). With this configuration the main systematics (magnetic field fluctuations) could be substantially reduced and the present best limit on the neutron EDM was reported in 2006 of $2.9 \times 10^{-26}\, e$cm [26].

1.3. nEDM PROJECT AT PSI

Together with an European based collaboration consisting of currently 15 institutions [42], a project has been started at the Paul Scherrer Institut (PSI) to pursue a search for the neutron EDM. For this purpose, we obtained on loan from the Sussex-Rutherford-ILL collaboration their EDM spectrometer with which they previously obtained the current best limit on the neutron EDM [26]. The Sussex-Rutherford-ILL collaboration moved on to a new technique of measuring the neutron EDM: the CryoEDM experiment [43].

With the apparatus at our disposal, we adopted a three phase strategy towards a new measurement of the neutron EDM.

1.3.1. PHASE I: nEDM AT ILL

The main goal of this first phase was to understand the subtleties of EDM experiments and to improve and partly refurbish the old apparatus. For this purpose, measurements were conducted in Grenoble at the Institut Laue-Langevin. As the inherited apparatus had suffered from a sharp drop in the magnetic field homogeneity after a vacuum accident, in which the iron coated Silicon wafer used for polarising the UCN had broken, the biggest attention was devoted to recovering the magnetic properties of the apparatus. For this purpose, much of the interior equipment such as electrodes, storage chamber, UCN shutter and HV feedthrough had been replaced.

Good magnetic field conditions could only be recovered at the end of this phase during the last measurements at ILL. Key to this success was the careful screening of all components inside the vacuum tank for any sources of magnetic fields. Several magnetic pieces such as stainless steel helicoils and an electric vacuum feedthrough had been found and were removed. While we had built in the electric vacuum feedthrough ourselves, the stainless steel helicoils had been mounted in the aluminium vacuum tank many years ago and seem to have become more and more magnetised in the course of time.

Additionally, we had developed a replacement for the quartz storage chamber: a polystyrene chamber coated with deuterated polystyrene on the inside in order to be suitable for UCN storage [44]. The chamber has the required volume resistivity of $> 10^{16}\,\Omega$cm, an increased Fermi potential of (161 ± 10) neV (compared to ~95 neV for Quartz) and, as an additional extra, deuterated polystyrene performs better in keeping the polarisation of the stored mercury atoms.

Also, we had operated up to 8 Cs magnetometers [45] placed around the storage chamber. Some of them could be used to actively stabilise the main field and certain trim coils in feedback mode.

Last but not least, the damaged HV power supply had been repaired and could be operated again.

(i) (ii)

Figure 1.12.: (i) Lifting down of the nEDM apparatus from its stand at ILL. (ii) Insertion of the magnetic shield into the thermal house at PSI.

At the same time, R&D started towards a new apparatus: n2EDM.
Phase I ended in March 2009 with the move of the apparatus to PSI - see Fig. 1.12.

1.3.2. PHASE II: NEDM AT PSI

The final result of the measurements by the Sussex-Rutherford-ILL collaboration amounted to $d_n = (0.2 \pm 1.5(\text{stat}) \pm 0.7(\text{syst})) \times 10^{-26}\, e\text{cm}$ [26]. Thus, with the experiment currently being limited by statistics, the goal is to improve on that result by measuring with the apparatus at the new UCN source at PSI [46]. For typical experiments, the new PSI source is expected to provide 100 times more UCN than currently available at ILL. With an accompanying improvement in the control of the systematic effects (see Sec. 3.4), an overall improvement of a factor 5 is feasible. Since March 2009, work on setting up the experiment and initital tests are ongoing. EDM measurements are expected to start in Spring 2010 after the UCN source has gone online.

The setup of the experiment at PSI can schematically be seen in Fig. 1.13. The main items are: (i) A 5 T superconducting magnet, which is used to polarise the incoming UCN beam[2] and which, together with a spin flipper in its fringe field, allows to select the incoming spin orientation, (ii) an outer 3-axis compensation coil system, which allows to actively compensate magnetic fields up to first order, and (iii) a two floor thermal house, which will protect the magnetic shield from thermal fluctuations affecting its shielding properties. The aimed at stability is ±0.1 °C on the second floor, where the experiment is located, and ±0.5 °C in the first floor - the counting room.

[2]Thereby improving the available statistics and polarisation as with this setup the UCN will have to pass only once through the magnetised polarisation foil, which achieves only polarisations of about 90% and has a transmission of about 90%. In the passage through the superconducting magnet both of these values are expected to be 100%.

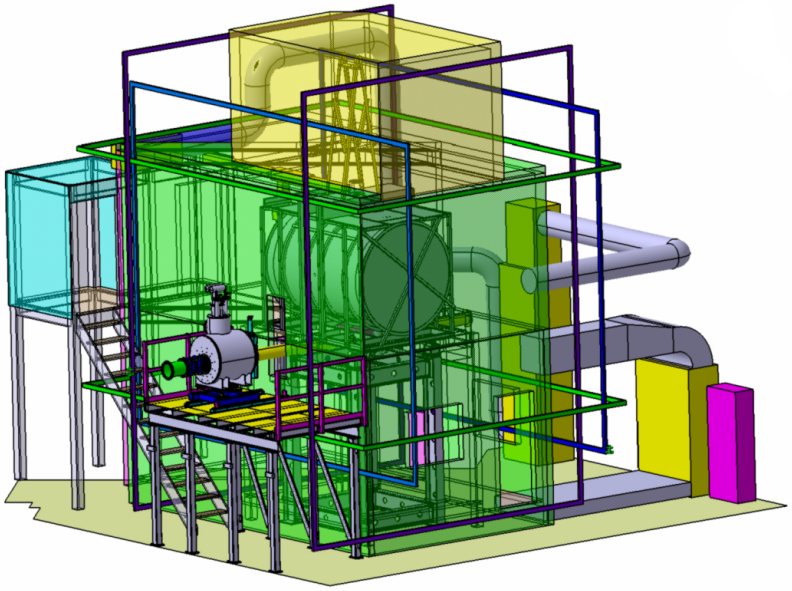

Figure 1.13.: Setup of the nEDM apparatus in the area south of the new PSI UCN source. Shown are the superconducting magnet used to polarise the incoming UCN beam, the outer 3-axis compensation coil system, and the thermal house keeping the temperature at the magnetic shield stable to ±0.1 °C.

During this phase, there will be continued R&D towards n2EDM and towards the end of phase II its construction and setting up.

1.3.3. Phase III: n2EDM

The basic layout for the new apparatus n2EDM has been agreed on and is shown in Fig. 1.14. It consists of:

- A vertical double stack of UCN storage chambers with the HV electrode in the middle allowing for a simultaneous measurement with parallel and anti-parallel electric and magnetic fields.
- The use of co-magneotometers. Among those, there will be an improved mercury co-magnetometer. The use of an additional ^{129}Xe oder ^{3}He co-magnetometer is currently being evaluated.
- An array of ~100 Cs magnetometers.
- 2 large cylindrical ^{3}He magnetometers on top and on the bottom of the stack of UCN chambers read out by Cs magnetometers. Covering the full flux in the main field direction, they will allow to directly measure the volume averaged magnetic field gradient over the two UCN storage chambers.
- 5 layer magnetic shielding.

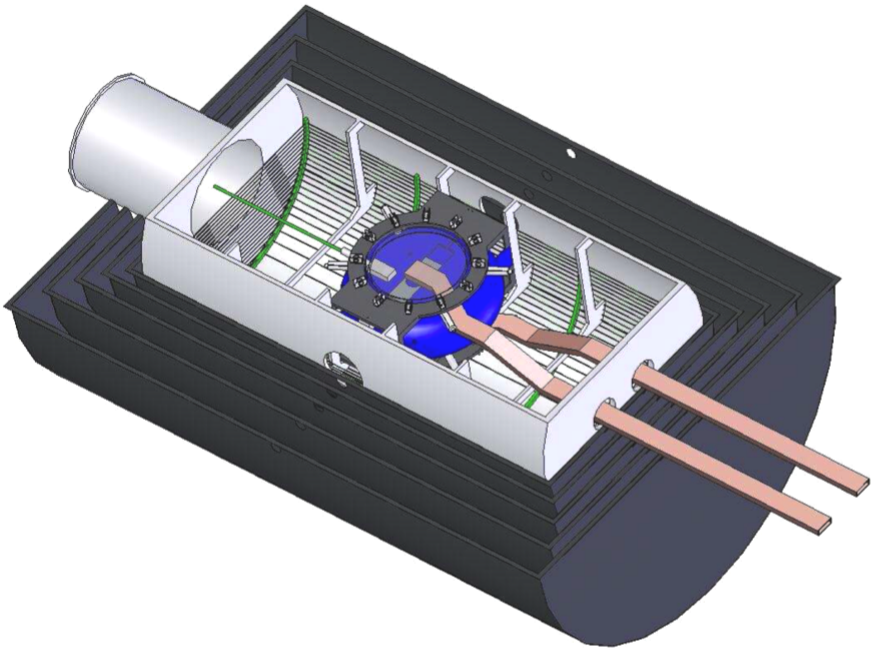

Figure 1.14.: Conceptual layout of the new EDM apparatus n2EDM. For details see text.

With the available statistics at the PSI UCN source and an increased control on systematics due to the above concept, a search for the neutron EDM with a sensitivity of 5×10^{-28} $e$cm is envisaged.

2 nEDM Apparatus at ILL

2.1. Description

Fig. 2.1 shows a schematic of the nEDM apparatus of the Sussex-Rutherford-ILL collaboration and which is currently on loan to our collaboration (see Sec. 1.3). The apparatus is the successor of the experiment shown in Fig. 1.11. The magnetic shield had been reused after removing the innermost layer - and thus reducing the number of layers to four - and turning the orientation to a vertical position. I will briefly describe the essential components:

2.1.1. UCN

The experiment was located at the PF2/NEDM beamline of the Institut Laue-Langevin in Grenoble. The available UCN densities close to the turbine amount to approximately 50 UCN/cm^3. In the EDM apparatus, one typically achieved to fill 1-2 polarised UCN/cm^3. As the storage chamber of the experiment is about 2 m above the beamline level, the energies of the storable UCN start at 200 neV on the beamline level. In order to transport as many of those UCN as possible, the incoming beamline consists of stainless steel guides coated with ^{58}NiMo having a Fermi potential of 318 neV [47] and being nonmagnetic. Below the experiment, a switch is located which can pneumatically change between a curved guide (^{58}NiMo coated glass tube) connecting the incoming beamline with the storage chamber and a straight guide (^{58}NiMo coated) connecting the storage chamber to the UCN detector.

After the polarising foil (see next section), the UCN are guided in a Be coated glass tube to the storage chamber (Fermi potential of about 250 neV and both the guide and the coating are nonmagnetic). After filling for usually 40 s, a UCN shutter closes the storage volume. The shutter consists of a horizontally sliding piece made out of Teflon and an insert made of Be coated copper which is in contact with the UCN. As the shutter mechanism is located below the storage chamber, a small cylindrical volume of radius 3.4 cm and height 4 cm forms at the bottom of the storage chamber after closing of the shutter. In order to achieve a good storage performance for the UCN and mercury atoms (see below), great care has to be taken in order to attain an excellent closing of the shutter mechanism and the storage volume in the closed position.

The storage chamber consists of two electrodes made of aluminium and coated with diamond-like carbon (Fermi potential of about 230 neV) and a resistor ring made of Quartz (Fermi potential of 95 neV) and later improved to a deuterated polystyrene coated polystyrene ring (Fermi potential of 160 neV). The resistor ring resides in 15 mm deep grooves in order to hide its edges for an improved HV compatibility.

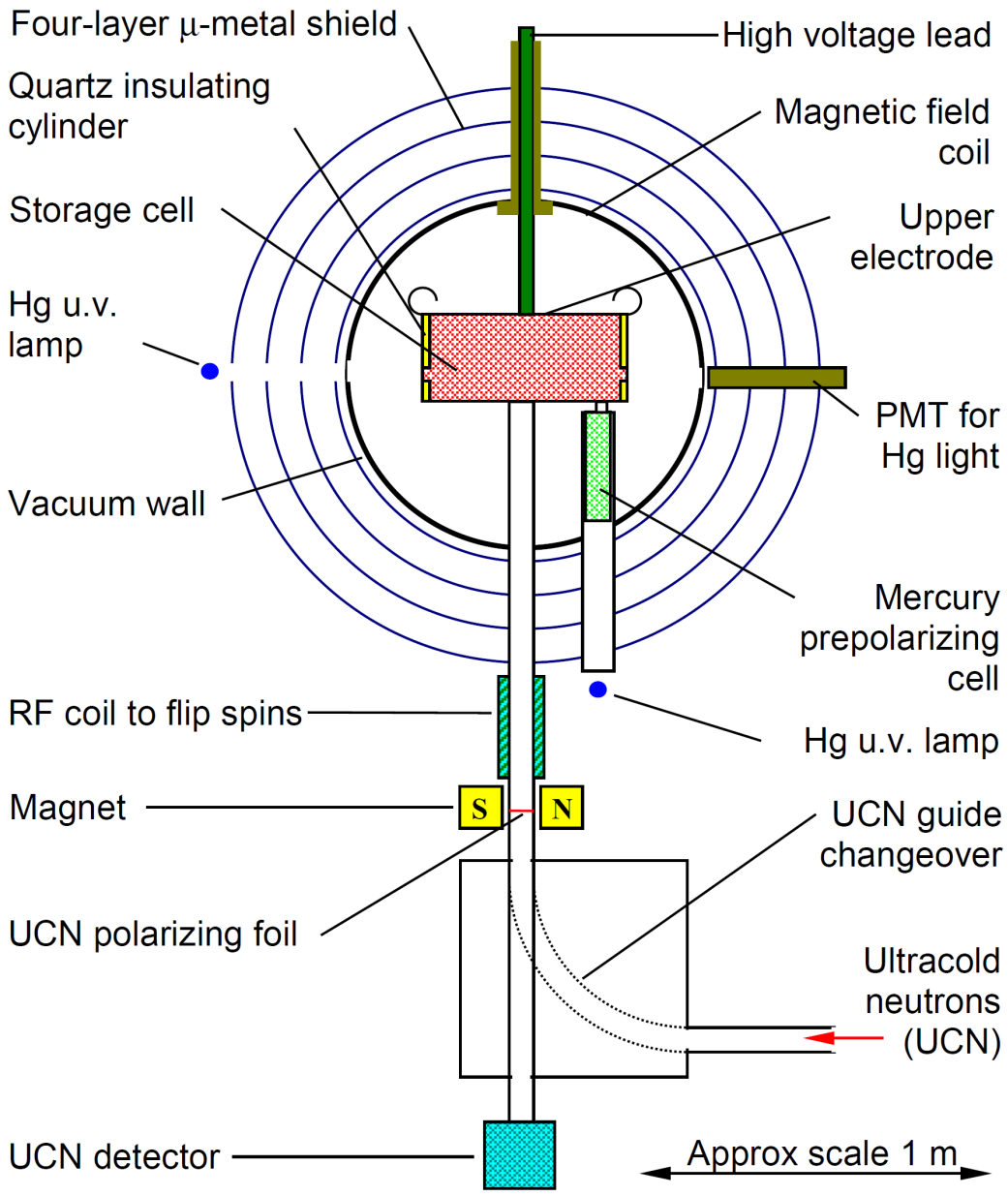

Figure 2.1.: Schematic of the Sussex-Rutherford-ILL apparatus for the search of the neutron EDM. For details see text. Picture taken from [31].

2.1.2. POLARISER AND SPIN FLIPPER

The polariser consists of a thin aluminium foil of thickness 20 μm which is coated by a 200 nm layer of iron. Typical loss of UCN through the foil amounts to approximately 10% per passage and the polarisation or analysing power achieved is approximately 90%. This can be improved by using an iron coated silicon wafer as previously installed. Although both the aluminium foil and the silicon wafer are very sensitive to differential pressures above and below, the consequences of destroying the iron coated silicon wafer are much more severe as the shattered, magnetic pieces will become distributed all over the vacuum tank. As this happened once to the Sussex-Rutherford-ILL collaboration (see Sec. 1.3) and once more during our measurements, we decided to replace the wafer with the aluminium foil. The foil is clamped in between two of the UCN guides in a special holder. Around the foil but on the outside of the vacuum enclosure, permanent magnets are placed producing a field of approximately 50 mT at the centre of the foil. This is enough to produce a fully magnetised iron layer corresponding to an effective magnetic field of ~2 T. The Fermi potential of the iron of 210 neV is thus effectively altered to 330 neV and 90 neV for the two spin states (see Eq. (1.3)). The spin state being able to pass through the polariser was defined as being spin up. The polarising foil is placed about 1.5 m below the storage volume. The storable spin up UCN thus need a minimal energy of 150 neV at the place of the polariser. With a Fermi potential of 90 neV for the spin up UCN, one does thus not loose any spin up UCN during the passage through the polariser. On the other hand, spin down UCN with energies above 330 neV are able to pass the polariser. Their energy will thus be above 180 neV in the storage chamber and they can neither in the Quartz nor in the deuterated polystyrene chamber be stored. As one can see from these numbers, care has to be taken in the exact placement of the polariser when going to higher Fermi potentials in the storage chamber.

The spin flipper above the polarising foil serves to count the number of spin down UCN after storage (or also to fill the chamber with spin down UCN). As only spin up UCN are able to pass the polariser, the spin down UCN have to be flipped before their passage through the polariser. The spin flipper is placed in the gradient field of the permanent magnets used for the magnetisation of the polarising foil. It works according to the method of fast adiabatic spin flip pioneered in [48] where, given a static gradient field and a perpendicular oscillating field, the spin will follow the effective field adiabatically thereby reversing its direction. The frequency used for the oscillating field is 18 kHz corresponding to a gradient field of approximately $2\pi f/\gamma_n \approx 0.6$ mT. The spin flip efficiency will be 100% if the adiabicity paramater k fulfills (see, e.g., [49])

$$k = \left| \frac{\gamma_n B_{\mathrm{rf}}^2}{v \partial B_z/\partial z} \right| \gg 1 \,. \tag{2.1}$$

Here, B_{rf} is the field strength of the oscillating field, v the UCN velocity and $\partial B_z/\partial z$ the gradient of the static field.

In normal EDM operations, the UCN detection process takes place in three phases: (i) 8 s of counting with spin flipper off and thus counting spin up UCN, (ii) 20 s of counting with spin flipper on thus counting spin down UCN, and (iii) again counting spin up UCN for 12 s with spin flipper off. The sequence has been chosen in that way as to equalise the amount of leakage of one spin component into the counting of the other and thus to obtain equal polarisation values α (see Sec. 2.1.5).

	Measurement at ILL	Measurement at PSI	Calculation
x	21 500	>13 300	24 000
y	1935	>1600	3600
z	6500	>8600	24 000

Table 2.1.: Measured shielding factors together with a calculation assuming a permeability of 20 000. x is in the direction of the mercury light, y along the cylindrical axis, and z in vertical direction. The measurements at PSI show a presently not explained dependence of the shielding factor on the applied field strength. The values given here for the PSI measurements are the extrapolations to zero applied field using a parabolic fit to the data, while the ILL values were taken at a fixed magnetic field value of ~10 μT at 1 m distance without varying its strength.

2.1.3. Magnetic Shield and Internal Magnetic Field Coil

The magnetic shield around the experiment is used to reduce the influence of external magnetic fields. It consists of 4 layer of 1.5 mm thick Mu-metal (a nickel-iron alloy of approximately 75% nickel, 15% iron, copper and molybdenum) with an effective permeability of 20 000[1]. The shield has a cylindrical shape, where the innermost layer has a diameter of 1.14 m and a length of 1.61 m increasing to a diameter of 1.93 m and a length of 2.76 m for the outermost layer. The end caps on both sides are removable giving access to the vacuum tank and the interior set-up. The shield has several holes providing access for different equipment. The largest holes are at the bottom (vacuum pump, UCN guide, and mercury prepolariser) and at the top (HV feedthrough).

The shielding factor (the reduction factor of an external magnetic field at the center of the chamber) has been measured at ILL using a 1.4 m diameter coil producing a field of 10 μT at a distance of 1 m [50] and recently after its move to PSI using the large compensating magnetic field coils (see Fig. 1.13). The shielding factors can be found in Table 2.1. The fact that the z-direction is much worse than what is given by the calculation most probably is due to the influence of the large holes in that direction of the shield.

The internal magnetic field coil provides the holding field of about 1 μT for the precession of the spins during measurements. It is wound directly onto the cylindrical vacuum tank producing a field B_{0z} in the vertical direction. In order to produce a homogeneous field in the inside, the spacing between the different windings are equidistant in z-direction (so called $\cos\theta$-geometry). The homogeneity of the internal field is one of the key items to reach a high sensitivity for EDM measurements, because inhomogeneous fields will lead to loss of UCN polarisation and introduce false effects mimicking a true EDM (see Sec. 3.4). At the points where the large inserts from the HV feedthrough, UCN guide, mercury polariser, and vacuum access pass into the vacuum tank, the geometry of the field coil is disturbed and has to be corrected for by adding solenoids around these inserts. In addition, several more trim coils are wound onto the vacuum tank. However, we usually found their influence to be small compared to the large effect of the coils correcting for the holes in the main field coil. Those measu-

[1] Single pieces of Mu-metal have a few times larger permeability. However, in large objects consisting of several joint pieces of Mu-metal the effective permeability gets reduced due to slits, holes, etc.

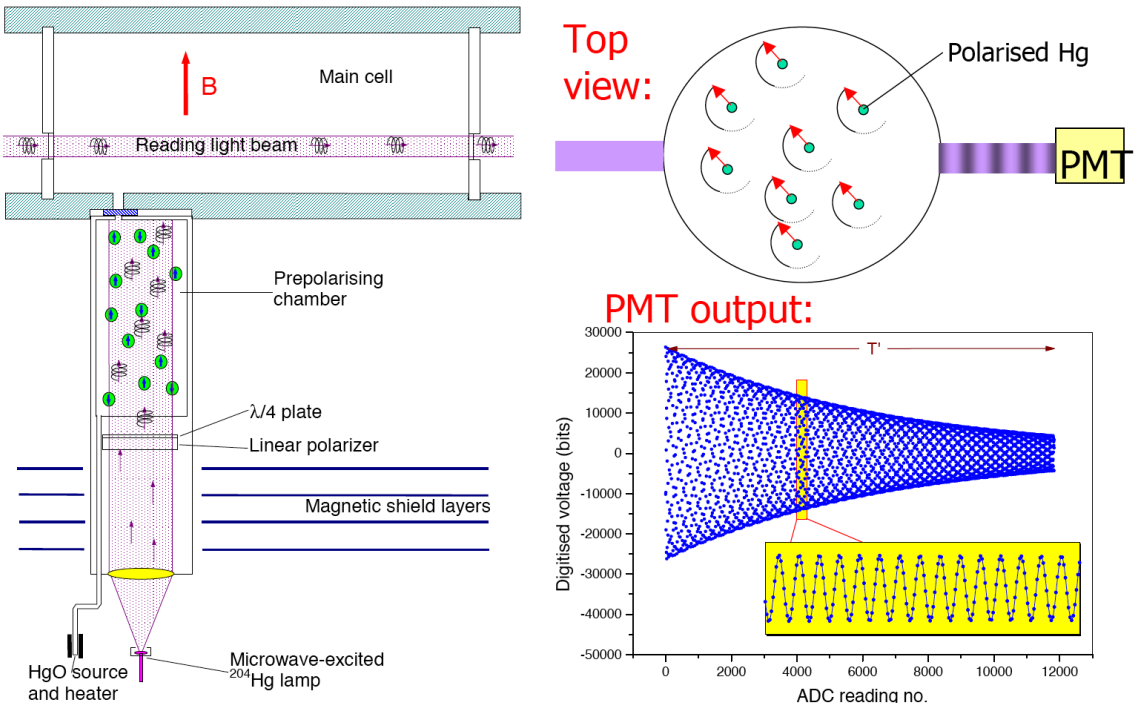

Figure 2.2.: Schematic of the mercury co-magnetometer used in the EDM measurements. For details see text. Picture taken from [31].

rements were usually done during the time when the magnetic field homogeneity was not at its best though (see Sec. 1.3.1), their influence becomes certainly larger close to optimal magnetic field homogeneity.

2.1.4. MERCURY CO-MAGNETOMETER

One of the key items of this apparatus is the mercury co-magnetometer shown in detail in Fig. 2.2 [26, 51]. It allows to measure the average magnetic field in the UCN storage chamber during the same time as the actual neutron EDM measurement. With these measurements, the effects of external field fluctuations can be heavily reduced by normalising the measured neutron frequency by the measured mercury frequency (see Fig. 2.3). The fact that the centres of gravity of the UCN and mercury are not exactly the same and thus the measured average field is not exactly the same makes the normalisation procedure not 100% perfect and leads to additional effects but allows to estimate the average gradient $\partial B_{0z}/\partial z$ (see Sec. 2.2 and 3.4).

For the co-magnetometer the stable mercury isotope ^{199}Hg is used, which has a nuclear spin $\frac{1}{2}$. The atoms are produced by dissociation of mercury oxide ^{199}HgO at a temperature of about 200 °C. The mercury atoms enter into the mercury prepolariser, which is located inside the shield and magnetic field coil. There, the atoms are polarised by optical pumping using circularly polarised light at 253.7 nm from a ^{204}Hg discharge lamp located below the polariser. The dissociation and pumping process takes place continuously. At the beginning of each measurement cycle, polarised atoms are released into the UCN storage chamber from the polariser. The polarised mercury atoms are

then flipped by $\pi/2$ using a rotating field at ~8 Hz perpendicular to the main field and precess freely around the holding field. The UCN are affected only marginally by this oscillating field as their resonance frequency lies at ~30 Hz.

An additional ^{204}Hg discharge lamp is located on the outside of the magnetic shield with its light traversing the storage chamber and being detected on the other side by an ultraviolet sensitive photomultiplier tube (see Fig. 2.1). The light is circularly polarised with the plane of polarisation perpendicular to the precessing mercury spins. The absorption cross section of the light then depends on the position of the precessing spin an will lead to a sinusoidal modulation between $\sigma_0(1+P)$ and $\sigma_0(1-P)$, where P is the polarisation of the mercury atoms. As the cross section is modulated, thus also the transmitted light intensity measured by the photomultiplier tube will be modulated and the precession frequency of the mercury atoms becomes directly measurable. The measured light intensity provides two pieces of information: (i) The measured dc intensity for the two cases with (I) an without (I_0) mercury atoms in the chamber yields the amount of absorption $A = \frac{I_0 - I}{I_0}$ and thus essentially the density of mercury atoms. (ii) The measured frequency f_{Hg} of the modulated signal is directly correlated to the magnetic field B via $B = \left|\frac{2\pi f_{Hg}}{\gamma_{Hg}}\right|$ using the gyromagnetic ratio $\gamma_{Hg} = 2\pi \times 7.590313\,\frac{\mathrm{Hz}}{\mu\mathrm{T}}$ [10, 52].

2.1.5. Performance Parameters

The performance of the apparatus was usually assessed with a few parameters:

- **UCN storage time τ**: The storage time characterises the ability to store UCN. The amount of UCN N remaining after the confining time[2] t_s is then given by $N = N_0 e^{-t_s/\tau}$, where N_0 is the amount of initially filled UCN. UCN are lost due to beta decay, absorption or upscattering on rest gas or walls, and leakage through slits. While the loss due to beta decay is independent of UCN energy, the two later loss mechanisms do depend on UCN energy and thus the storage time depends on energy. In order to account for that, the storage curve - the amount of remaining UCN as a function of t_s - was thus usually fitted with two exponentials:

  $$N = A_1 e^{-t_s/\tau_1} + A_2 e^{-t_s/\tau_2} \tag{2.2}$$

  The interpretation then being the storage time for fast and slow UCN. Typical good values were $\tau_1 \approx 40$ s and $\tau_2 \approx 190$ s. For a single exponential fit, this amounted to $\tau \approx 90$ s.

- **UCN polarisation holding times T_1 and T_2**: The ability to hold the polarisation of the UCN is measured with two time constants: T_1 is the time constant for holding the polarisation of the spins aligned to the magnetic field and T_2 for holding the polarisation of the spins perpendicular to the magnetic field. For T_1, the value $\alpha = \frac{N_{up} - N_{down}}{N_{up} + N_{down}}$ is measured as a function of t_s without any manipulation of the spin, while for T_2 two $\pi/2$-flips are performed as in the normal EDM measurements. The frequency of the RF-field is chosen to correspond to the resonance frequency (estimated from a previous mercury frequency). The calculated value α then corresponds to the visibility of the central fringe of the Ramsey resonance pattern.

[2] Often, t_s is also called storage time.

The obtained values for α were fitted with

$$\alpha = \alpha_0 e^{-t_s/T_{1,2}} \tag{2.3}$$

yielding the polarisation holding times T_1 and T_2 together with the initial value α_0. Having to pass twice through the polarisation foil, the achieved degree of polarisation with the polarising foil amounts to $\sqrt{\alpha_0}$. Typical good values were $T_1 \approx 1500$ s, $T_2 \approx 200$ s, and $\alpha_0 \approx 0.85$ (after the change from the silicon wafer to the aluminium foil: $\alpha_0 \approx 0.8$). After removing large magnetic inhomogeneities (see Sec. 1.3.1), T_2 times of approximately 400 s were measured.

- **Mercury leakage time**: The mercury atoms, having a velocity of approximately 150 m/s, are much more heavily affected by slits. It is for that reason that there are additional O-rings placed into the grooves of the electrodes to provide a tight sealing. The mercury leakage time is estimated from the dc offset of the measured light intensity at the beginning and the end of the storage period. Typical values amount to a few hundred seconds.

- **Mercury polarisation lifetime T_2**: The measured modulation at the photomultiplier tube shows an exponentially damped amplitude (see Fig. 2.2). This is due to the loss of polarisation of the precessing mercury spins. While the depolarisation for UCN is determined mainly by inhomogeneous magnetic fields, the mercury is due to its much higher velocity less sensitive to magnetic inhomogeneities but much more susceptible to random spin flips during wall collisions due to sticking at the wall for about $10^{-7\pm1}$ s upon contact [47]. In order to improve on the polarisation lifetime, regular oxygen discharge cleanings are performed, during which impurities on the walls are cleaned. For that purpose, about 1 mbar of oxygen is filled into the chamber and the HV turned up to 150 kV. Typical T_2 lifetimes achieved right after oxygen discharge cleanings are $T_2 \approx 100$ s.

2.2. A SAMPLE NEDM ANALYSIS

2.2.1. INTRODUCTION

In the beginning of December 2007, the nEDM apparatus was not yet optimally performing but for the first time in a configuration that data could be taken with all the subsystems running. In total 3 days of data have been taken.

- **UCN**: An initial α_0 of 0.74 was achieved. The characteristic spin depolarisation constants were: $T_1 \approx 650$ s and $T_2 \approx 170$ s. The storage time used was 150 s with a total number of counted UCN of ~5100.

- **Hg magnetometer**: The Hg magnetometer was running smoothly throughout the measurements. The leakage time amounted to ~ 500 s and the depolarisation lifetime to ~ 90 s with a drop to ~ 80 s over the course of the measurement period. The signal to noise ratio was ~ 450 corresponding to a frequency error of ~ 0.6 μHz or measurements of the magnetic field with a sensitivity of ~80 fT.

- **Cs magnetometer**: 3 running Cs magnetometers were installed below the bottom electrode (in order to be protected against the HV). No synchronisation between the Cs data acquisition and the nEDM data acquisition was in place yet. The data had to be synchronised by hand offline (see Section 2.3). In the nEDM analysis, the data from the Cs magnetometers was not used but was included in the analysis of the stability of the magnetometric signals (see Section 2.3).
- **HV**: As the old, bipolar Cockcroft-Walton HV generator was broken, an emergency solution was put in place. Two 130 kV HV power supplies from Spellman (Model SL130 [53]) were installed. The polarity had to be switched manually by changing the HV cable from one power supply to the other. The EDM data was taken at ±100 kV with a change in polarity every 2 hours.
- **Magnetic Field**: The field direction of the B_0 field was "down". Only the "top hole" and the "bottom 2" trimcoils were powered at values 41 and 25, respectively.[3]

2.2.2. Measurement of the Neutron Resonance Frequency f_n

The central valley of the Ramsey resonance pattern (see Fig. 1.7) follows to excellent agreement the functional form [27, 51, 54]

$$N_i = N_{\text{avg}}\left[1 \mp \alpha \cos\left(\pi \frac{f_{n,i} - f_{\text{RF},i}}{\Delta\nu}\right)\right].^{4} \tag{2.4}$$

$N_{\text{avg}} = \frac{N_{\text{min}}+N_{\text{max}}}{2}$ denotes the average UCN counts given the maximal and minimal counts along the Ramsey resonance, $\alpha = (N_{\text{max}} - N_{\text{min}})/(N_{\text{max}} + N_{\text{min}})$ the fringe visibility of the interference pattern, $f_{\text{RF},i}$ the frequency of the applied $\frac{\pi}{2}$-pulse in cycle i, $f_{n,i}$ the neutron precession frequency in cycle i, and $\Delta\nu = \frac{1}{2(T+2t_{\text{RF}}/\pi)}$ the width of the resonance (T being the free precession time and t_{RF} the duration of the $\frac{\pi}{2}$-pulse). It is interesting to note that fluctuations in UCN flux during filling will shift the resonance frequency in opposite directions for spin up and down. Therefore, averaging the obtained resonance frequencies for the two spin states reduces this systematic error substantially.

Online Analysis

In the online analysis of the nEDM DAQ, every cycle a fit to the latest 4 measurement using Eq. (2.4) with free parameters N_{avg}, α and $f_{n,i}$ is performed. In the following analysis, these values for f_n have been used.

Offline Analysis

Offline, the Rutherford-Sussex-ILL collaboration used a different approach [51, 54]. The full data from a run (a few hundred cycles) was fitted using Eq. (2.4) to obtain the average values for N_{avg}, α and f_n. For each cycle, Eq. (2.4) can then be inverted to extract $f_{n,i}$. Such a procedure has been implemented in our collaboration in the thesis of S. Roccia [55] for the analysis of the data in [56].

[3] These are the values that are set in the data acquisition. The values correspond approximately to mA.

[4] This is equivalent to the functional dependence of $N_i = N_{\text{min}} + (N_{\text{max}} - N_{\text{min}})\sin^2\left(\frac{\pi}{2}\frac{f_{n,i}-f_{\text{RF},i}}{\Delta\nu}\right)$ for spin up (replacing $\sin^2(\ldots)$ by $\cos^2(\ldots)$ for spin down) found in [47].

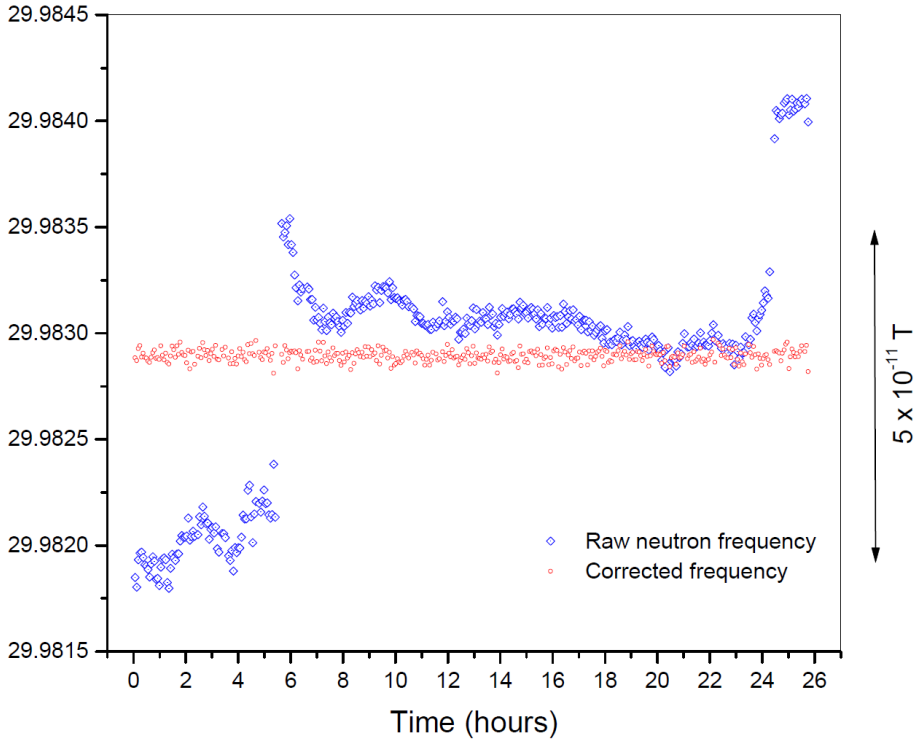

Figure 2.3.: Comparison of the measured raw neutron frequency and the neutron frequency normalised by the Hg frequency. Plot taken from [31].

2.2.3. MEASUREMENT OF THE MERCURY RESONANCE FREQUENCY f_{Hg}

The precession of the polarised ^{199}Hg atoms inside the storage chamber leads to a modulation in intensity of the circularly polarised (perpendicular to the polarisation of the ^{199}Hg atoms) light from a ^{204}Hg discharge lamp traversing the chamber. The light is read out by a photomultiplier and digitised at 100 Hz (the precession frequency being ~8 Hz) in a 16-bit ADC. The oscillating signal can then directly be fitted to extract f_{Hg} [51].

2.2.4. EXTRACTION OF THE NEUTRON EDM

The basic principle to extract the neutron EDM is simple and has already been given in Section 1.2.3. Equation (1.31) can be slightly changed to stress the major experimental problem somewhat more explicitly:

$$d_n = \frac{1}{4E}\left[-h(f_{\uparrow\uparrow} - f_{\uparrow\downarrow}) + 2\mu_n(B_{\uparrow\uparrow} - B_{\uparrow\downarrow})\right] \tag{2.5}$$

and thus changes in the B field for the two separate measurements in parallel $\uparrow\uparrow$ and antiparallel $\uparrow\downarrow$ configuration can mimic or mask a true EDM.

In order to reduce such systematic effects substantially, the Hg co-magnetometer is used to normalise the measured neutron frequencies (see Fig. 2.3). As the fast Hg atoms sample the B field in the storage chamber uniformly, whereas the centre of gravity of the UCN is $\Delta h \equiv \langle z\rangle_{Hg} - \langle z\rangle_n \approx 2.8\,\text{mm}$ lower [57] and thus the chamber is sampled slightly differently, the normalisation procedure is not completely perfect. In the presence of

a vertical gradient $\partial_z B_{0z}$ the ratio $\frac{f_n}{f_{Hg}}$ is shifted away from the ratio expected from the gyromagnetic factors. The shift is given as [26, 57]

$$\begin{aligned} R_a &= \left| \frac{f_n}{f_{Hg}} \frac{\gamma_{Hg}}{\gamma_n} \right| \\ &= \left| \frac{B_{0z} + \partial_z B_{0z} \langle z \rangle_n}{B_{0z} + \partial_z B_{0z} \langle z \rangle_{Hg}} \right| \\ &\approx \begin{cases} 1 - \frac{\partial_z B_{0z}}{|B_{0z}|} \Delta h, & B_{0z}\,\text{up} \\ 1 + \frac{\partial_z B_{0z}}{|B_{0z}|} \Delta h, & B_{0z}\,\text{down} \end{cases} \end{aligned} \tag{2.6}$$

After all, the normalisation of the neutron data with the mercury co-magnetometer reduces the effect of changes in B on the nEDM extraction to the point of changes in B which are proportional to E and which affect the neutron and mercury frequency differently.

For the ratios $\frac{f_n}{f_{Hg}}$, the dependence on the neutron EDM is then given as

$$\frac{f_n^{\downarrow\downarrow/\downarrow\uparrow}}{f_{Hg}} = \left| \frac{\gamma_n}{\gamma_{Hg}} \right| \mp \frac{2 d_{meas}}{h f_{Hg}} |E| + \Delta h \frac{\partial_z B_{0z}}{B_{0z}} \left| \frac{\gamma_n}{\gamma_{Hg}} \right| \tag{2.7}$$

where the "+" in the third term has to be changed to "-" for B-field up. There are now two possibilities to extract d_{meas}: Either by fitting the ratios $\frac{f_n}{f_{Hg}}$ as a function of E, where the slope m provides an estimate of d_{meas}[5]

$$d_{meas} = -\frac{m}{2} \langle h f_{Hg} \rangle , \tag{2.8}$$

or in the case of equal $|E|$ values by subtracting the ratios for the parallel and anti-parallel case:

$$d_{meas} = -\frac{\langle h f_{Hg} \rangle}{4|E|} \left(\left\langle \frac{f_n^{\downarrow\downarrow}}{f_{Hg}} \right\rangle - \left\langle \frac{f_n^{\downarrow\uparrow}}{f_{Hg}} \right\rangle \right) \tag{2.9}$$

Figure 2.4 shows the histogram of the frequency ratios used to extract the neutron EDM. Positive (negative) HV corresponds to an electric field pointing down (up). The few values at a value $R_a - 1$ of approximately 34 ppm stem from one run with slightly different magnetic field conditions. The following cuts were applied to the data:

- χ^2 of the mercury frequency fit $\chi^2_{Hg} < 4$.
- χ^2 of the neutron frequency fit $\chi^2_n < 9$.
- In order to have similar magnetic field conditions, the R_a values were constrained to $2 \times 10^{-5} < R_a - 1 < 4 \times 10^{-5}$.

[5] It is often a bit tricky to track the signs through the terms involving absolute values. A way to check the sign of d_n: If the frequency is larger for parallel fields, then d_n has the same sign as μ_n, i.e., a negative sign.

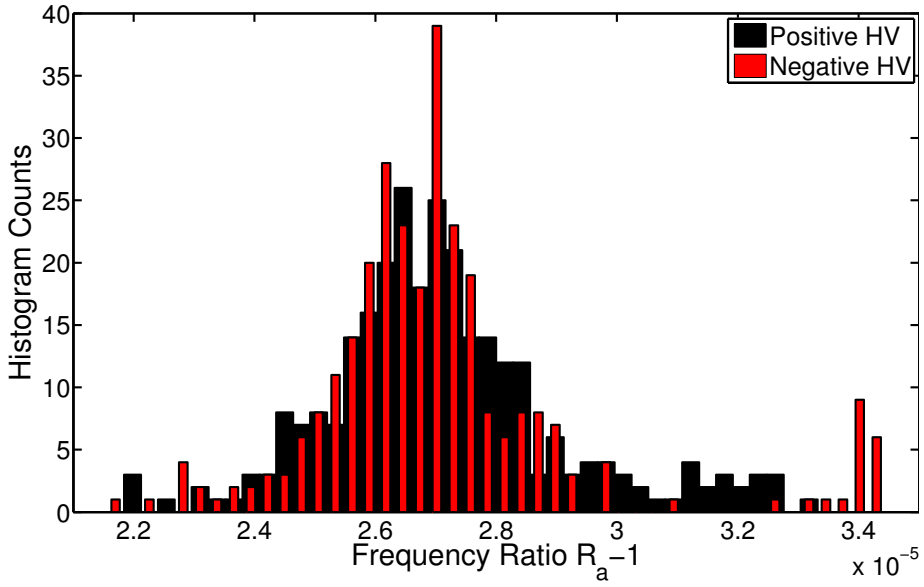

Figure 2.4.: Histogram of the measured frequency ratios after cuts used to extract the neutron EDM.

The errors on the averages were assessed by calculating the standard deviation of the two distributions in Fig. 2.4 and dividing by the square root of the number of measurements. The average values amount to:

$$\begin{aligned} \left\langle \frac{f_n^{\downarrow\downarrow}}{f_{Hg}} \right\rangle &= 3.84246213(45) \\ \left\langle \frac{f_n^{\downarrow\uparrow}}{f_{Hg}} \right\rangle &= 3.84246215(51) \end{aligned} \tag{2.10}$$

This translates into a value for d_{meas} of

$$d_{meas} = (0.17 \pm 6.57) \times 10^{-25}\, e\text{cm} \tag{2.11}$$

for both ways of extracting d_{meas} - a value consistent with 0.

STATISTICAL SENSITIVITY

The statistical sensitivity for measuring d_n is given by [27, 58]

$$\sigma_{d_n} = \frac{\hbar}{2\alpha E T \sqrt{N}}. \tag{2.12}$$

For the operational parameters of $\alpha \approx 0.3$, $E \approx (100\,\text{kV})/(12\,\text{cm})$, $T = 150\,\text{s}$, and $N \approx 5100$ UCN per cycle, this translates into a sensitivity of $1.2 \times 10^{-23}\, e$cm per cycle. In total, 573 cycles of data (after cuts) were taken during these 3 days yielding an expected statistical sensitivity of $\sim 5.1 \times 10^{-25}\, e$cm. The error in Eq. (2.11) is fairly consistent with that expectation as magnetic field fluctuations will always lead to a broadening of the distributions found in Fig. 2.4.

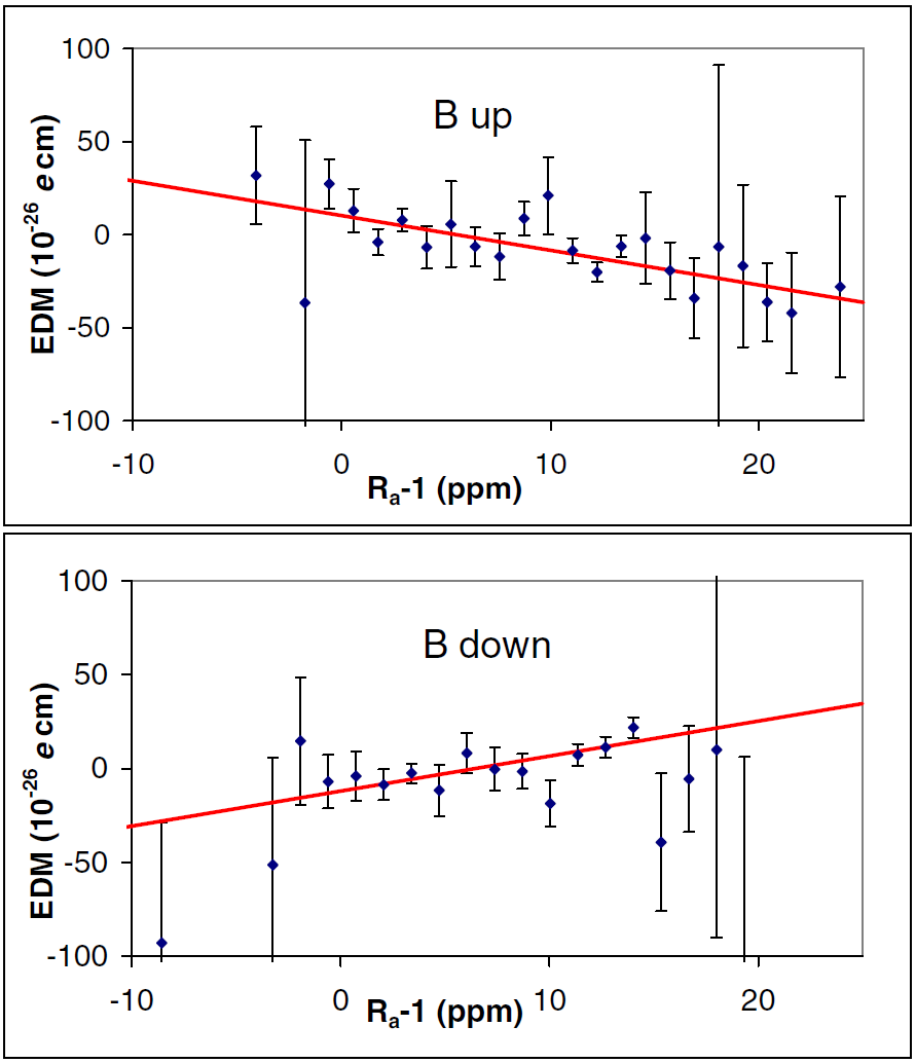

Figure 2.5.: The measured EDM as a function of the value $R_a - 1$, i.e., as a function of the gradient $\partial_z B_{0z}$, for the two cases of magnetic field up and down. Figure taken from [26].

2.2.5. SUSSEX ANALYSIS

The measured value d_{meas} will not be the true EDM of the neutron d_n but will have contributions from other sources:

$$d_{meas} = d_n + d_{f,n} + \left|\frac{\gamma_n}{\gamma_{Hg}}\right| (d_{Hg} + d_{f,Hg}) \tag{2.13}$$

d_{Hg} is the EDM of the ^{199}Hg, which has been shown to be less than $d_{^{199}Hg} < 3.1 \times 10^{-29}\, e$cm (95% C.L.) [59], and $d_{f,n}$ and $d_{f,Hg}$ are the false effects picked up by the neutron and mercury, respectively. The most severe false effect has proven to be due to geometric phases (as described in Sec. 3.2). In that case and for this specific apparatus, one has $\left|\frac{\gamma_n}{\gamma_{Hg}}\right| d_{f,Hg} \approx -15 d_{f,n}$ and therefore the geometric phase of the mercury is the largest systematic effect. In order to overcome this effect, the Sussex-Rutherford-ILL collaboration analysed their data as a function of $R_a - 1$, i.e., as a function of the

gradient. Although, it is unfortunate that the mercury atoms and the UCN do not measure exactly the same magnetic field, it can be turned into an advantage in this analysis as this allows to measure the EDM as a function of the gradient. Figure 2.5 shows the measured EDM as function of $R_a - 1$ for the two cases of magnetic field up and down. The measured EDM depends on R_a as (see Eq. (2.6), (3.10) and [26, 57])

$$\begin{aligned} d^{\uparrow}_{meas} &= d_n - k(R_a - R^{\uparrow}_{a0}) \\ d^{\downarrow}_{meas} &= d_n + k(R_a - R^{\downarrow}_{a0}) \end{aligned} \tag{2.14}$$

where the slope k is the linear dependence of the geometric phase of the mercury on the gradient and $R^{\uparrow}_{a0}$ and $R^{\downarrow}_{a0}$ the values of R_a at which the gradient is zero. As seen in Section 3.4, there are also other effects than the gradient $\partial_z B_{0z}$, which can shift R_a leading to non-zero values of R_{a0} [55, 60]. Fitting Eq. (2.14) to the data in Fig. 2.5, one obtains the values for k, $R^{\uparrow}_{a0}$, and $R^{\downarrow}_{a0}$. Evaluating the data at the crossing point of the two equations ($d^{\uparrow}_{meas} = d^{\downarrow}_{meas}$ leading to $R_a = \frac{R^{\uparrow}_{a0}+R^{\downarrow}_{a0}}{2}$), one obtains

$$d_{meas} = d_n + k\frac{R^{\uparrow}_{a0} - R^{\downarrow}_{a0}}{2}. \tag{2.15}$$

This extracted value is now free of the geometric phase of the mercury, the main systematic effect. However, it is now susceptible to differential shifts $R^{\uparrow}_{a0} - R^{\downarrow}_{a0}$ of the values R_a for the two cases of magnetic field up and down, which have to be assessed carefully. See Section 3.4 for the assessment of such kind of effects.

2.2.6. BLIND ANALYSIS

In order to devise a strategy for a blind analysis for a future EDM analysis, one has to look at the following equation, showing the dependence of the ratio of frequencies on the EDM of the neutron and mercury:

$$\frac{f_n}{f_{Hg}} = \left|\frac{\gamma_n}{\gamma_{Hg}}\right| + \frac{2(d_n + |\gamma_n/\gamma_{Hg}|d_{Hg})}{h f_{Hg}} E \tag{2.16}$$

The best way to blind the outcome is, in my opinion, to introduce (i) an artificial neutron EDM and (ii) an artificial mercury EDM[6]. Introducing an artificial EDM in both channels is necessary as one will certainly also analyse the two channels individually. The introduced, artificial EDM should be picked at random up to the current limits on the corresponding EDM. This translates into $\pm 3 \times 10^{-26}\, e$cm for the neutron channel and $\pm 3 \times 10^{-29}\, e$cm for the mercury channel. In the neutron channel, the shift can best be introduced by shifting the RF frequencies f_{RF} used in the extraction of the resonance frequency in proportion to E. The resonance frequencies can then be recomputed upon the unblinding of the data. In the mercury channel, the shift is best introduced after fitting the precession signal of the mercury atoms. For a differential shift $\Delta f = f^{\uparrow\uparrow} - f^{\uparrow\downarrow}$, the corresponding EDM amounts to

$$d = -\frac{h}{4E}\Delta f = -1.24 \times 10^{-18}\, e\text{cm s}\, \frac{100\,\text{kV/12 cm}}{E}\Delta f. \tag{2.17}$$

[6] Care has to be taken in presentations of the analysis group to people knowing the introduced EDM that they not give away the blinding by their reactions. This can be avoided if the analysis group introduces their own artificial EDM in such presentations.

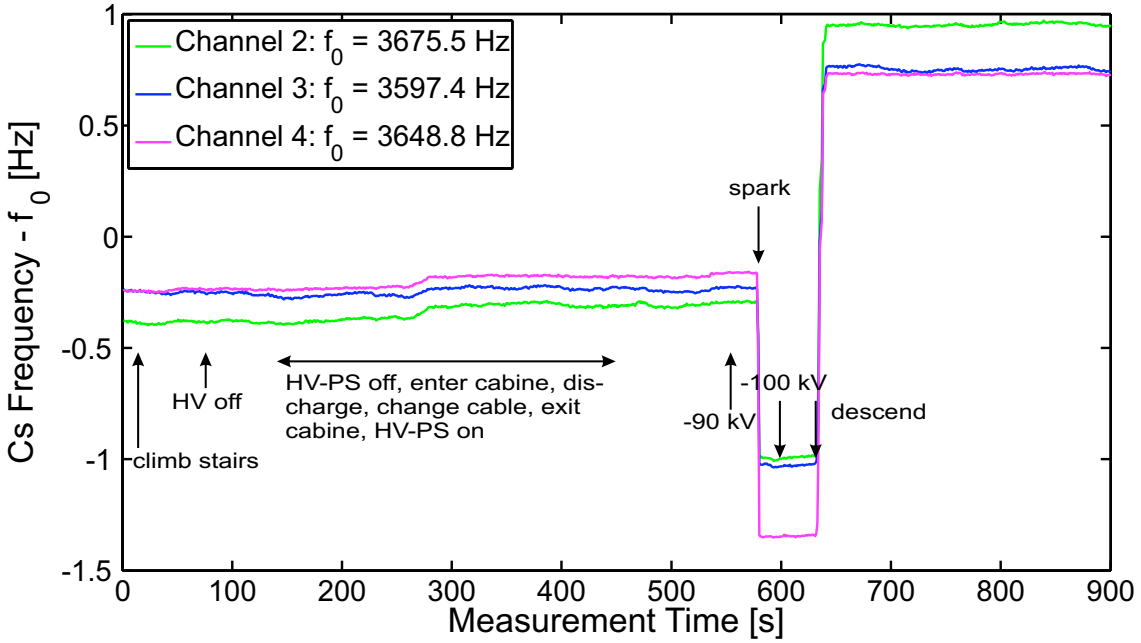

Figure 2.6.: Magnetic field seen by the Cs magnetometers during reversal of the HV. There is a clear correlation between the change in magnetic field and an occuring spark.

2.3. Stabilities of the Magnetometric Signals

During the first few days of the measurement period aimed at performing EDM measurements (see Sec. 2.2), the goal was to measure false EDM effects due to large gradients with the mercury as the reactor had been shutdown due to a failure. However, it was soon discovered that due to the manual operation of the HV power supplies the ramping up of the high voltage was not smooth enough leading to frequent sparks. During dedicated reversals in which all procedures were exactly timed and the Cs magnetometers were running at the same time, it was then discovered that each of the sparks lead to a different magnetic field environment inside the shielding. The reason for this is most probably a small magnetisation of the Mu-metal shielding due to the flowing current during the spark. One of these measurements is shown in Fig. 2.6.

Instead of searching for a false EDM, the data were then used to evaluate the stability of the different magnetometric signals and thus the amount of magnetic field noise present under normal running conditions. In addition to these mercury data, also the data from the above neutron EDM measurements were analysed with that goal. The main magnetic field coil was operated in two different configurations: (i) In the “free field” mode, the current was supplied by the standard stable current source. (ii) In the “locked field” mode, the current was supplied by a PID controlled power supply that locked to the magnetic field measured by the Cs magnetometer 4. See Fig. 2.7 for a sketch of the magnetometer positions.

With no synchronisation available between the Cs magnetometer and the neutron and mercury frequency data, the synchronisation had to be accomplished by hand offline. There were two offsets that had to be taken into account: (i) The offset between

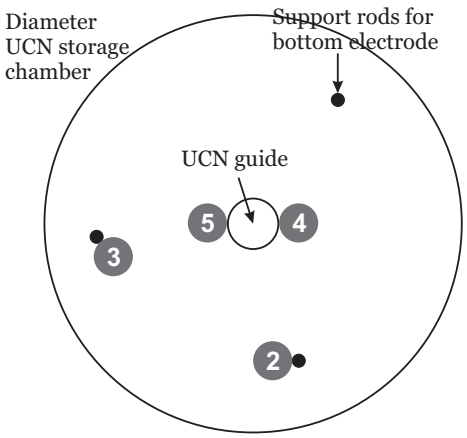

Figure 2.7.: Placement of the Cs magnetometers approximately 25 cm below the storage chamber. Cs magnetometer 5 was not operational. The diameter of the storage chamber amounts to 47 cm and the diameter of the incoming beamline to 7 cm.

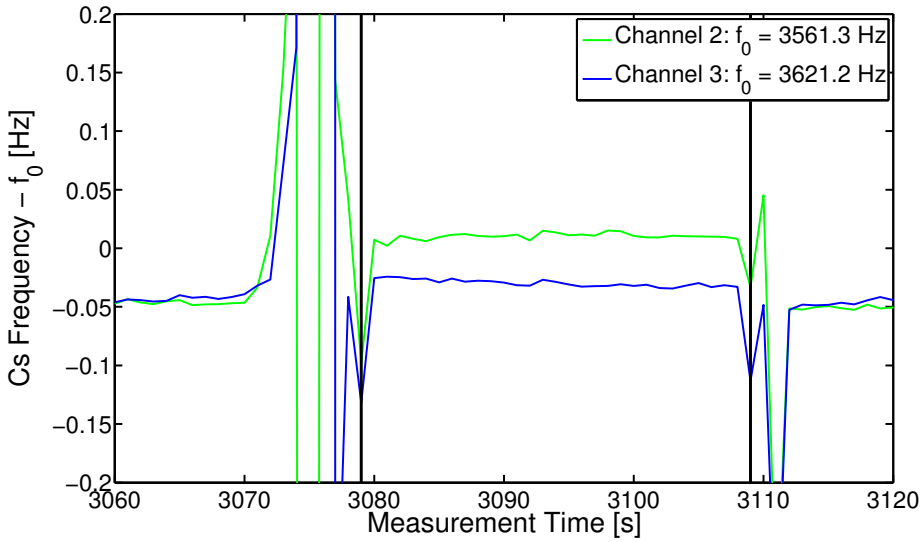

Figure 2.8.: Offline synchronisation of the Cs magnetometer signals to the beginning and the end of the neutron and mercury precession. The spikes in the Cs data are due to the RF fields used to flip the mercury and neutron spin. The vertical bars show the beginning and end of the precession frequency as recorded by the EDM data acquisition.

Magnetometer	Time	$\frac{\sigma_f}{\langle f \rangle}$	Magnetometer	Time	$\frac{\sigma_f}{\langle f \rangle}$
Locked Field			Free Field		
Hg	day	6×10^{-6}	Hg	day	1×10^{-5}
	night	3×10^{-6}		night	1×10^{-6}
Cs 2/3	day	6×10^{-6}	Cs 2/3	day	2×10^{-5}
	night	4×10^{-6}		night	5×10^{-6}
			Cs 4	day	2×10^{-5}
				night	2×10^{-6}

Table 2.2.: Stabilities of the magnetometric signals given as the standard deviation σ_f divided by the mean frequency $\langle f \rangle$ for the cases of locked and free field and during day and night.

the starting of the Cs data acquisition and the EDM data acquisition and (ii) an additional offset for the first cycle in the neutron and mercury data, where the waiting time for the availability of UCN from the source is measured differently than in the following cycles. For this reason, the one second averages of the extracted Cs frequencies were overlaid with the timing of the beginning and end of the neutron and mercury precession. The two offsets were then changed by hand until they matched the beginning and end of the neutron and mercury precession as shown in Fig. 2.8. It is fortunate that the Cs magnetometers actually see the RF fields used for the flipping of the mercury and the neutron spins, which allowed to perform this synchronisation. The one second averages of the Cs data during the precession time were then averaged to yield the average frequency of the Cs magnetometers as used later in the analysis. What can also be seen in Fig. 2.8 is that the UCN shutter is slightly magnetic leading to a change in magnetic field in its closed position compared to the open position.

Figure 2.9 shows a part of the measured data during the mercury runs for the free and locked field case. It is immediately clear by looking at these two plots, that neither in the locked nor in the free field case do the Cs magnetometers see the same magnetic field fluctuations as the mercury. Several of the fluctuations seen by the mercury show up with different amplitudes (size and direction) or are not seen at all by the Cs magnetometers. This is also the reason why the Cs data could not be used to normalise the mercury data in the above mentioned attempt to measure the false EDM of the mercury. In order to evaluate the stability of the signals, the standard deviation was calculated for the data in between HV reversals and divided by its mean. In Table 2.2, the averages over those values are given for measurements during the day (usually noisy magnetic field environment due to crane operations, etc.) and night and for the free and locked field case. It is interesting to note that the highest stability is achieved in the free field mode during the night. During the day however, the locking of the field improves on the stability. From this, one can conclude that the field locking improves the stability in a magnetic noisy environment but has detrimental effects during magnetically quiet periods of time. However, a more sophisticated locking of the field using several Cs magnetometers and controlling not only the main field but also trim coils might result in a better performance.

Figure 2.10 shows data taken during the neutron EDM runs in the free field mode

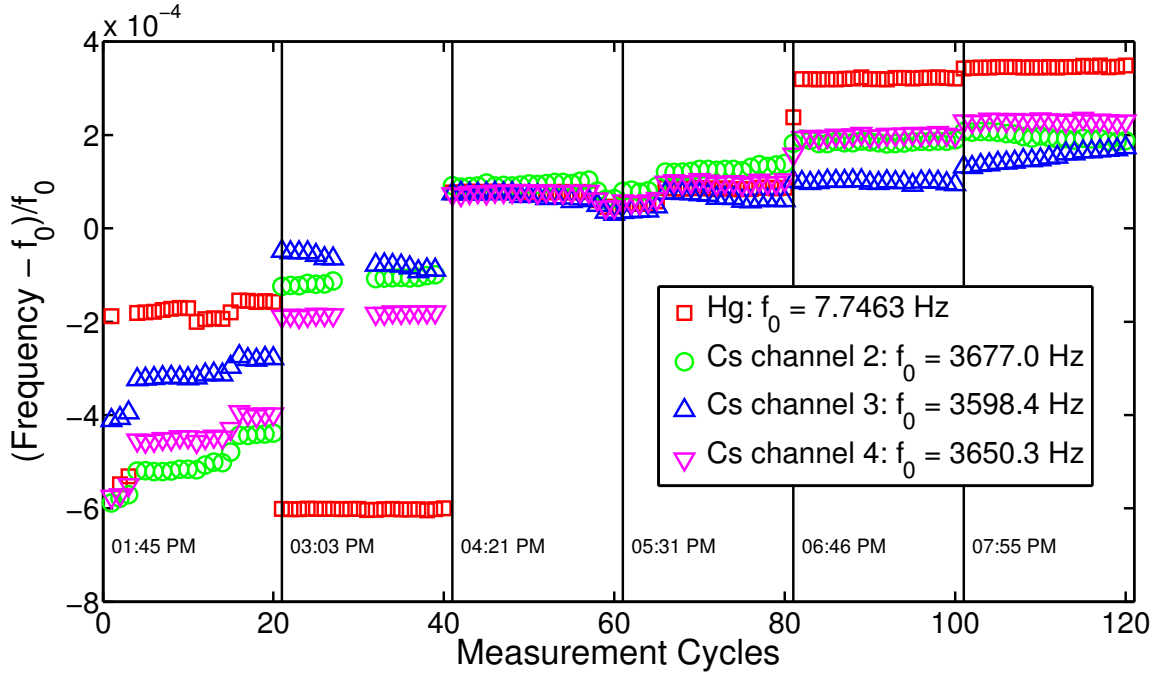

(i)

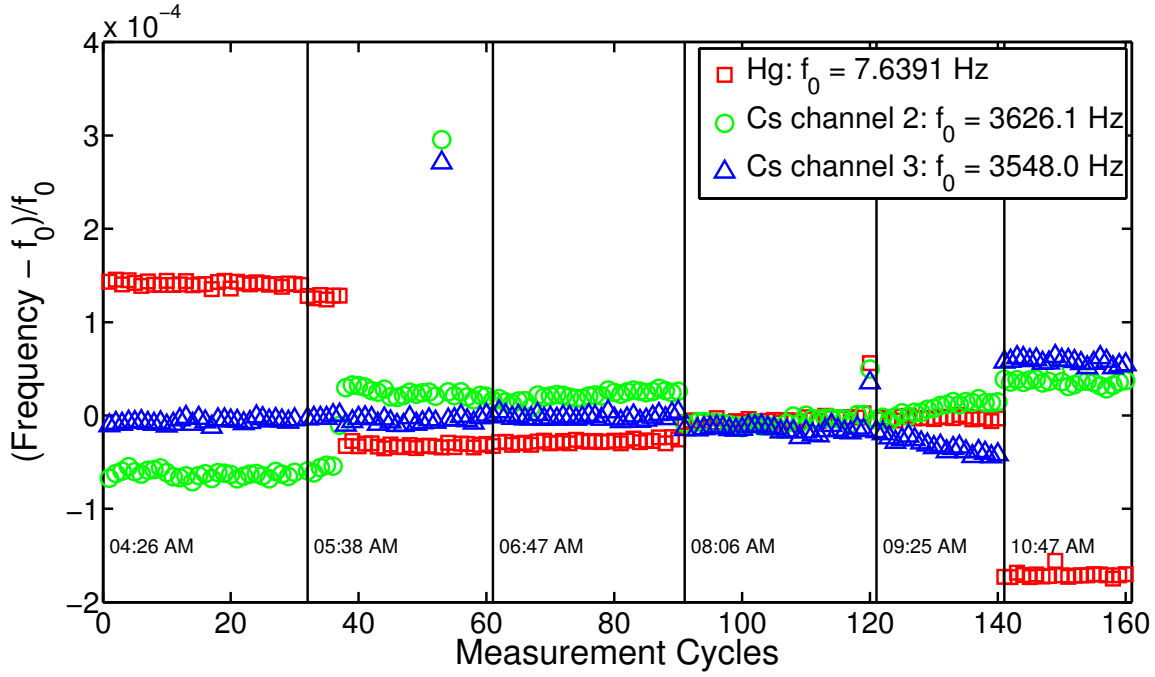

(ii)

Figure 2.9.: Part of the mercury runs data. (i) shows the measured frequencies with "free field" and (ii) the frequencies for the "locked field" case. Each vertical line corresponds to a reversal of the HV.

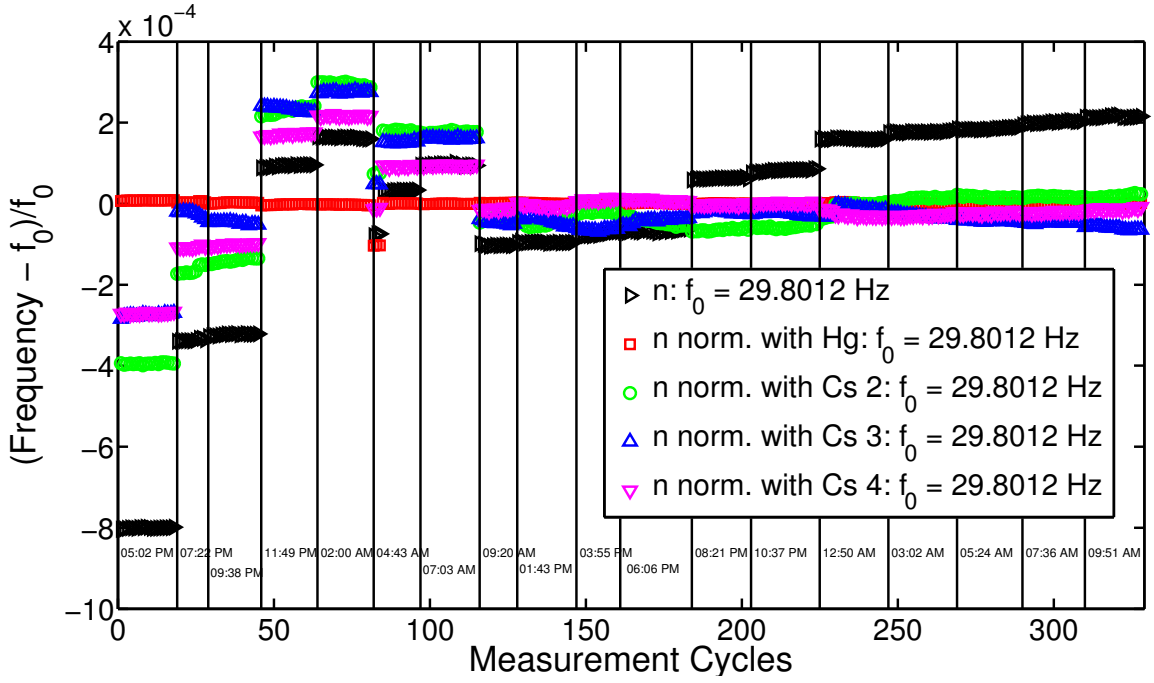

Figure 2.10.: Part of the data from the neutron runs. Shown is the neutron frequency and the normalised neutron frequency by either one of the Cs magnetometers or the Hg magnetometer. Only, the mercury signal is able to adequately normalise the neutron frequency. Data have been taken in the free field mode.

Magnetometer	$\frac{\sigma_f}{\langle f \rangle}$	Magnetometer	$\frac{\sigma_f}{\langle f \rangle}$
Locked Field		Free Field	
n	3×10^{-6}	n	2×10^{-6}
n/Hg	9×10^{-7}	n/Hg	9×10^{-7}
Hg	3×10^{-6}	Hg	2×10^{-6}
Cs 2/3	5×10^{-6}	Cs 2/3	5×10^{-6}
		Cs 4	3×10^{-6}

Table 2.3.: Stabilities of the magnetometric signals given as the standard deviation σ_f divided by the mean frequency $\langle f \rangle$ for the cases of locked and free field. No difference between day and night was observed. “n/Hg” denotes the neutron frequency normalised by the mercury.

of operation. In the figure, the extracted neutron frequency is presented together with the neutron frequency normalised to the mercury or either one of the Cs magnetometers. It is clear that only the mercury magnetometer is apt to adequately normalise the neutron data. Table 2.3 shows the corresponding stability numbers as already extracted for the mercury runs. These measurements were conducted during the weekend where there were no heavy operations such as moving the large reactor crane, etc., pursued. Consequently, there were no differences observed between the stability of the magnetic field during day and nights. Let me conclude with some remarks drawn from the data presented in Tables 2.2 and 2.3:

- The locking of the field improves the stability during magnetically noisy periods, but has a detrimental effect during magnetically quite periods.
- The Cs magnetometers see at their position larger fluctuations in the magnetic field than the mercury or neutron. Additionally, Cs magnetometers 2 and 3 experience even larger magnetic field fluctuations than Cs magnetometer 4 located closer to the centre of the magnetic shield.
- The statistical sensitivity of the magnetic field measurement is for the neutrons given by [51]

$$\sigma_B = \frac{1}{2\pi\gamma_n \alpha T\sqrt{N}} \tag{2.18}$$

with the visibility α, the precession time T and the amount of detected UCN N. During the measurement period, this amounted to $\sim$ 1 pT or a factor 10^{-6}. At the same time, the sensitivity of the mercury magnetometer amounted to 70 fT or 7×10^{-8} [51]. The normalisation procedure of the neutron frequency thus reduced the amount of fluctuations down to the statistical level. With the sensitivity of the Cs magnetometers still exceeding the sensitivity of the mercury magnetometer, it is clear that all of the observed fluctuations are due to actual changes in the magnetic field environment.

2.4. ANALYSIS OF THE SPIN COUNTING SCHEME IN THE NEDM APPARATUS

In March 2007, measurements were performed to analyse the spin counting scheme of the nEDM apparatus. The basic idea was to measure the losses that occur in the sequential spin analysis for the spin component that has to remain stored while the other spin component is being counted. Two main series of measurements were conducted called “storage with spin flipper on” and “storage with spin flipper off”.

The measurement sequence for the “storage with spin flipper on” was: (i) filling of UCN for 40 s, (ii) filling of Hg and corresponding $\pi/2$-flip (4 s), (iii) waiting/cleaning time of 5 s, (iv) opening of shutter, spin flipper (SF) on and counting of spin down UCN for time t, and (v) SF off and counting of spin up UCN for 40 s. The measured data is shown in Fig. 2.11 together with an exponential fit to the spin up counts resulting in a characteristic time of $\tau = 25.0 \pm 0.1$ s. This and all of the following exponential fits are a rough simplification of the actual shape of the curves. As the characteristic constants depend on energy of the UCN, one would need to fit the data with a sum of exponentials.

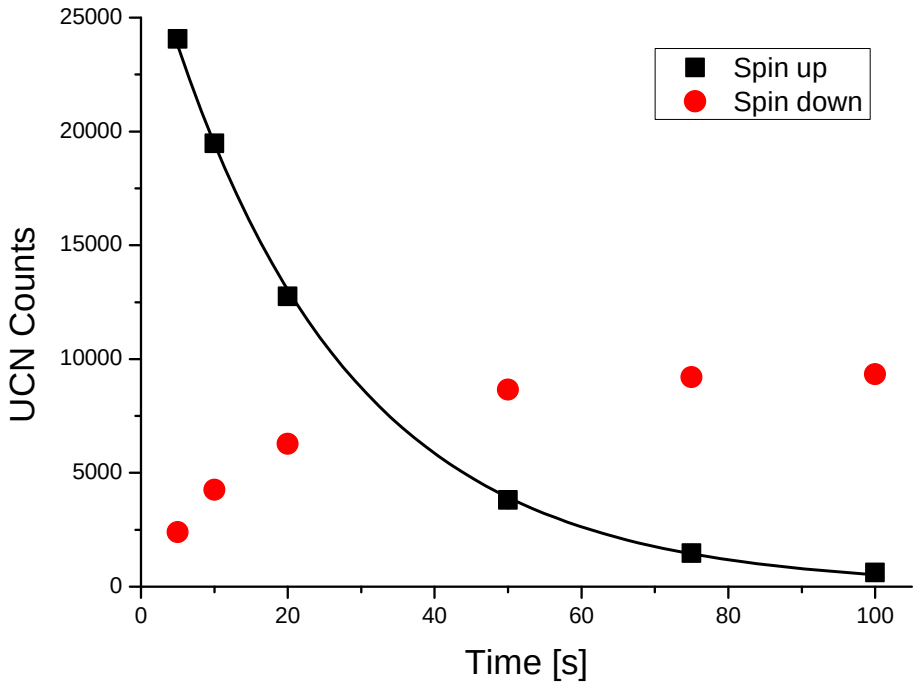

(i)

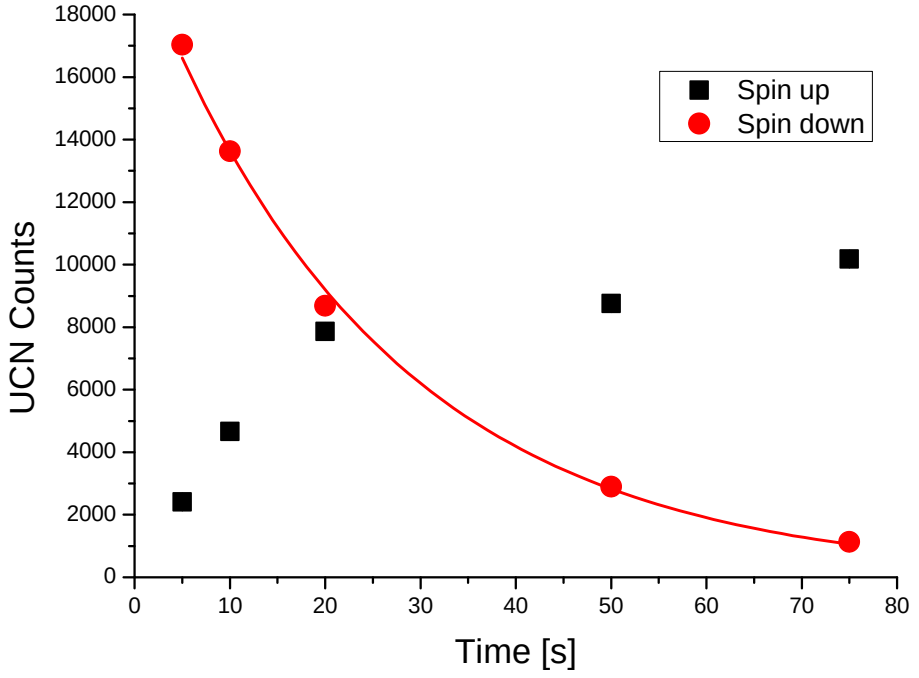

(ii)

Figure 2.11.: (i) Measured UCN counts for spin down for a time t followed by counting spin up for 40 s during the measurement sequence with the spin flipper on. Error bars are smaller than the symbols. (ii) Measured UCN counts for spin up for a time t followed by counting spin down for 40 s during the measurement sequence with the spin flipper off. For more details see text.

The measurement sequence for "storage with spin flipper off'" is slightly different: (i) filling of UCN for 40 s, (ii) filling of Hg and corresponding $\pi/2$-flip (4 s), (iii) first on resonance neutron $\pi/2$-flip (2 s), (iv) waiting/cleaning time of 15 s and measuring the mercury spin precession to estimate the neutron resonance frequency, (v) second on resonance neutron $\pi/2$-flip (2 s), (vi) opening of shutter, SF off and counting of spin up UCN for time t, and (vii) SF on and counting of spin down UCN for 40 s. The measured counts for this case are shown in Fig. 2.11 also with an exponential fit to the spin down counts resulting in $\tau = 25.4 \pm 0.2$ s. The two extracted values match very nicely. The fact that the amount of spin up counts is so much larger in the second measurement than the amount of spin down counts in the first measurement is due to the loss of polarisation during the $\pi/2$-flips and storage.[7]

In order to roughly model these results, some additional time constants are needed. The storage time constant of the storage chamber itself was measured to be $\tau_{chamber} = 83.2 \pm 0.6$ s (using a single exponential). The above measured time constants τ are a combination of losses in the chamber with time constant $\tau_{chamber}$ and losses in the system shutter, input guide and polarising foil with time constant $\tau_{s/g/f}$. The three time constants obey the relation:

$$\frac{1}{\tau} = \frac{1}{\tau_{chamber}} + \frac{1}{\tau_{s/g/f}} \tag{2.19}$$

and thus $\tau_{s/g/f} = 35.7 \pm 0.3$ s for SF on and $\tau_{s/g/f} = 36.6 \pm 0.3$ s for SF off, in reasonable agreement.

Additionally, the counting time constant was measured to be $\tau_{count} = 11.4 \pm 0.6$ s. It is the characteristic time constant connected to the time needed for the UCN to leave the storage volume and being detected. It is obtained by fitting the detected amount of UCN as a function of time with the function $f(t) = N\left(1 - \exp(-t/\tau_{count})\right)$. As one is still losing UCN in the storage chamber during the detection process, the true time constant for the process of the UCN falling into the exit of the storage chamber τ_{det} has to be extracted from τ_{count} and $\tau_{chamber}$. The amount of detected UCN N_{det} after time t is given as:

$$\begin{aligned} N_{det}(t) &= \int_0^t \frac{1}{\tau_{det}} N(t')\mathrm{d}t' \\ &= \int_0^t \frac{1}{\tau_{det}} N_0 e^{-t'\left(\frac{1}{\tau_{det}} + \frac{1}{\tau_{chamber}}\right)} \mathrm{d}t' \\ &= N_0 \frac{1}{\tau_{det}} \left(\frac{1}{\tau_{det}} + \frac{1}{\tau_{chamber}}\right)^{-1} \left(1 - e^{-t\left(\frac{1}{\tau_{det}} + \frac{1}{\tau_{ch}}\right)}\right) \end{aligned} \tag{2.20}$$

where N_0 is the number of stored UCN. Comparing Eq. (2.20) with the function fitted to the detected amount of UCN, we have

$$\frac{1}{\tau_{count}} = \frac{1}{\tau_{det}} + \frac{1}{\tau_{chamber}} \tag{2.21}$$

and thus $\tau_{det} = 13.2 \pm 0.8$ s.

[7] I only realised later that the measurements could have been done in a more elegant way by switching on the SF during filling instead of performing the two $\pi/2$-flips.

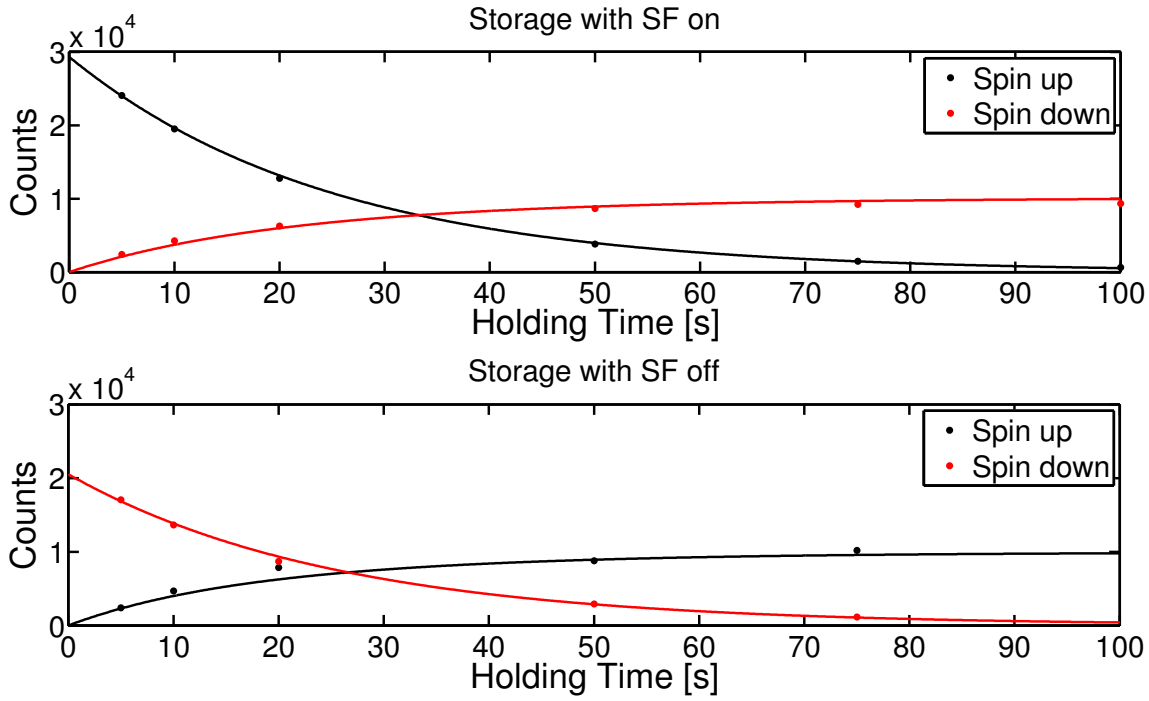

Figure 2.12.: Data as in Fig. 2.11 together with the prediction of the rough model.

A similar equation as above can be constructed for the amount of UCN counted during the storage with SF on and off. In those cases, we have

$$N_{det}(t) = \int_0^t \frac{1}{\tau_{foil}} N_0 e^{-t'\left(\frac{1}{\tau_{foil}}+\frac{1}{\tau_{chamber}}+\frac{1}{\tau_{s/g}}\right)} \mathrm{d}t' \tag{2.22}$$

where the characteristic time constant for UCN of the wrong spin state to pass through polariser foil τ_{foil} (e.g., due to spin flips) and the loss time constant of the system shutter and guide alone $\tau_{s/g}$ is introduced. Naturally, one has

$$\frac{1}{\tau_{s/g/f}} = \frac{1}{\tau_{s/g}} + \frac{1}{\tau_{foil}}. \tag{2.23}$$

With this set of equations in place, one can reproduce the measured data of Fig. 2.11 having the following free parameters: initial number of UCN for SF on N_{on}, the initial number for SF off N_{off}, the degree of polarisation ϵ for measurements with SF on (defined as $\epsilon = N_{up}/(N_{up}+N_{down})$ and the corresponding value for SF off determined by the measured T_2 time of ~170 s), and the values for the characteristic time constants $\tau_{s/g}$ for the two cases SF on and off. The matching of the model to the data is shown in Fig. 2.12. The value for ϵ_{on} was fixed to 0.95 and correspondingly ϵ_{off} to 0.86. The data are then described best with $N_{on} = 35000$, $N_{off} = 24500$, $\tau_{s/g,on} = 55 \pm 5$ s, and $\tau_{s/g,off} = 62 \pm 5$ s, where the errors on $\tau_{s/g}$ reflect the fixing of ϵ to a certain value.

Table 2.4 shows the summary of the measured and calculated time constants relevant for the spin analysis scheme of the nEDM apparatus. With these numbers, one can calculate the amount of UCN detected during the three detection phases of counting spin up for 8 s, spin down for 20 s and again spin up for 12 s. The results are given in

	Value	Comment
chamber losses $\tau_{chamber}$	83.2 ± 0.6 s	measured
spin storage τ	SF on: 25.0 ± 0.1 s SF off: 25.4 ± 0.2 s	measured
shutter/guide/foil losses $\tau_{s/g/f}$	SF on: 35.7 ± 0.3 s SF off: 36.6 ± 0.3 s	calculated from τ and $\tau_{chamber}$
counting time const. τ_{count}	11.4 ± 0.6 s	measured
detection time const. τ_{det}	13.2 ± 0.8 s	calc. from τ_{count} and $\tau_{chamber}$
shutter/guide losses $\tau_{s/g}$	SF on: 55 ± 5 s SF off: 62 ± 5 s	fitted according to rough model
foil transmission τ_{foil}	SF on: 102 ± 17 s SF off: 89 ± 11 s	calculated from $\tau_{s/g/f}$ and $\tau_{s/g}$

Table 2.4.: Summary of the measured and calculated time constants relevant for the spin analysis scheme of the nEDM apparatus.

	% of initial spin up UCN detected	% of initial spin down UCN detected
spin up counting, 8 s	44%	8%
spin down counting, 20 s	7%	52%
spin up counting, 12 s	13%	1%

Table 2.5.: Fractions of initial spin up or down UCN detected during the different phases of the sequential spin analysis.

Table 2.5. They show clearly that the amount of leakage of the wrong spin component into the measurement is rather large and that at the same time the losses of storing one of the spin states while counting the other are sizeable. In principle, one would expect that during the counting period of 20 s one would measure $\left(1-\exp\left(-20\,\mathrm{s}/\tau_{det}\right)\right) = 78\%$ of the total amount of UCN. The resulting values given in the table are substantially lower even when counting in the number of wrongly detected UCN. In the light of these values, a double arm system that measures the two spin components simultaneously (spin up UCN in one arm and spin down UCN in the other) is certainly worthwhile as in that case the storing of the spin components is reduced. The construction of such a system is currently being pursued at the LPC Caen, France, and at PSI.

3 nEDM Apparatus at PSI

3.1. Expected Statistical Sensitivity at PSI

According to Monte Carlo simulations of the source performance, the expected UCN densities achieved in the EDM storage chamber are about 50 times higher than at ILL or about 100 UCN/cm^3 [61]. Assuming conservatively increasing statistics by a factor 25, i.e. $N = 350000$, and values for the performance of the apparatus of $\alpha = 0.75$, $E = 12$ kV/cm, $T = 150$ s, the statistical sensitivity (see Eq. (2.12)) is given by $\sigma(d_n) = 4 \times 10^{-25}\, e$cm per cycle of about 400 s. Scaling this up leads to a sensitivity of $\sigma(d_n) = 3 \times 10^{-26}\, e$cm per day and under the assumption of performing good measurements during 200 nights per year of $\sigma(d_n) = 3 \times 10^{-27}\, e$cm per year. This will result in a limit on the neutron EDM - if $d_n = 0$ - of $|d_n| < 4 \times 10^{-27}\, e$cm (95% C.L., statistics only) after two years of measurements. Obviously, the systematic error will have to be controlled on the same level to reach the goal. This will be shown in the next sections.

3.2. Geometric Phase Effects in nEDM Measurements

3.2.1. Introduction

The problem of geometric phase effects for particles in traps was first put forward by Pendlebury et al. [57]. The theory was then expanded and generalised by several further publications [62, 63, 64]. However, the conceptually easier papers to understand are, in my opinion, [57, 63] and thus the following arguments are based on these publications.

The basic problem lies in the fact that gradients $\partial B_{0z}/\partial z$ of the holding field B_{0z} in the nEDM apparatus will produce fields in the xy-plane due to $\nabla \cdot \boldsymbol{B} = 0$:

$$\boldsymbol{B}_{0xy} = -\frac{\partial B_{0z}}{\partial z}\frac{\boldsymbol{r}}{2} \tag{3.1}$$

Additionally, the UCN will experience a tiny effect of special relativity in the presence of a motional magnetic field due to the applied electric field $\boldsymbol{E}$

$$\boldsymbol{B}_v = \frac{\boldsymbol{E} \times \boldsymbol{v}}{c^2}. \tag{3.2}$$

In total, the UCN will thus experience a field in the xy-plane of

$$\boldsymbol{B}_{xy} = \boldsymbol{B}_{0xy} + \boldsymbol{B}_v = -\frac{\partial B_{0z}}{\partial z}\frac{\boldsymbol{r}}{2} + \frac{\boldsymbol{E} \times \boldsymbol{v}}{c^2}. \tag{3.3}$$

The effect of these fields in the xy-plane is a shift in the observed Larmor precession frequency called the Ramsey-Bloch-Siegert shift [65, 66] (see Appendix A.3 for a derivation). This happens as the fields are seen to be oscillating by the neutron as it moves

around in the storage chamber with angular speed $\omega_r \approx v_{xy}/R$, where v_{xy} is the velocity in the xy-plane and R the radius of the chamber. The deviation of the measured Larmor precession frequency ω_L from the frequency $\omega_0 = -\gamma B_{0z}$ - the Ramsey-Bloch-Siegert shift - is given as

$$\begin{aligned} \Delta\omega &= \omega_L - \omega_0 \\ &= \sqrt{(\omega_0-\omega_r)^2+\omega_{xy}^2} - (\omega_0-\omega_r) \qquad (3.4) \\ &\approx \frac{\omega_{xy}^2}{2(\omega_0-\omega_r)} \qquad (3.5) \end{aligned}$$

where one has defined $\omega_{xy} = -\gamma B_{xy}$.[1] For the field $\boldsymbol{B}_{xy}$ as given above, the shift will thus be proportional to

$$\omega_{xy}^2 = \gamma^2 \boldsymbol{B}_{xy}^2 = \left(\frac{\partial B_{0z}}{\partial z}\frac{\boldsymbol{r}}{2}\right)^2 + \left(\frac{\boldsymbol{E}\times\boldsymbol{v}}{c^2}\right)^2 + 2\frac{\partial B_{0z}}{\partial z}\frac{\boldsymbol{r}}{2}\cdot\frac{\boldsymbol{E}\times\boldsymbol{v}}{c^2}. \qquad (3.6)$$

While the first term does not depend on the electric field (but generally describes the influence of the fields B_{0xy} on the resonance frequency - see also Sec. 3.4.5) and the second term is quadratic in the electric field (see Sec. 3.4.8), only the last term is linear in the electric field and will thus lead to a shift in the resonance frequency mimicking a true EDM.

The third term in Eq. (3.6) above leading to a false EDM signal depends linearly on the velocity of the trapped particle. Naively, one would expect that the velocity averages to zero during the trapping period and thus it will not contribute. The fact that this is not the case lies in the nature of geometric phases.

3.2.2. Classical Analogon for a Geometric Phase

A suitable classical analogon of the geometric phases in quantum mechanics is the parallel transport of vectors on a sphere [67]. Two such examples are shown in Fig. 3.1: During the parallel transport of the vector on a closed path, the vector is coherently building up a phase shift with respect to its initial position. The analogon goes so far that even the mathematical description of the acquired phase during the parallel transport can be exactly matched to the description of the quantum mechanical phase acquired by the moving particle [67].

Exactly the same as with the vectors on the sphere is occurring in the case of spins of particles moving around in the storage trap. During their passage throughout the chamber, they experience a constant and coherent build up of a phase shift, which depends on the combination of the fields $\boldsymbol{B}_v$ and $\boldsymbol{B}_{0xy}$. The exact description of the phase acquired by spins in a magnetic field can be found in [68].

[1] It should be noted that in dealing with particles in a storage chamber, one will always have to look at the average of the two contributions with $\pm\omega_r$.

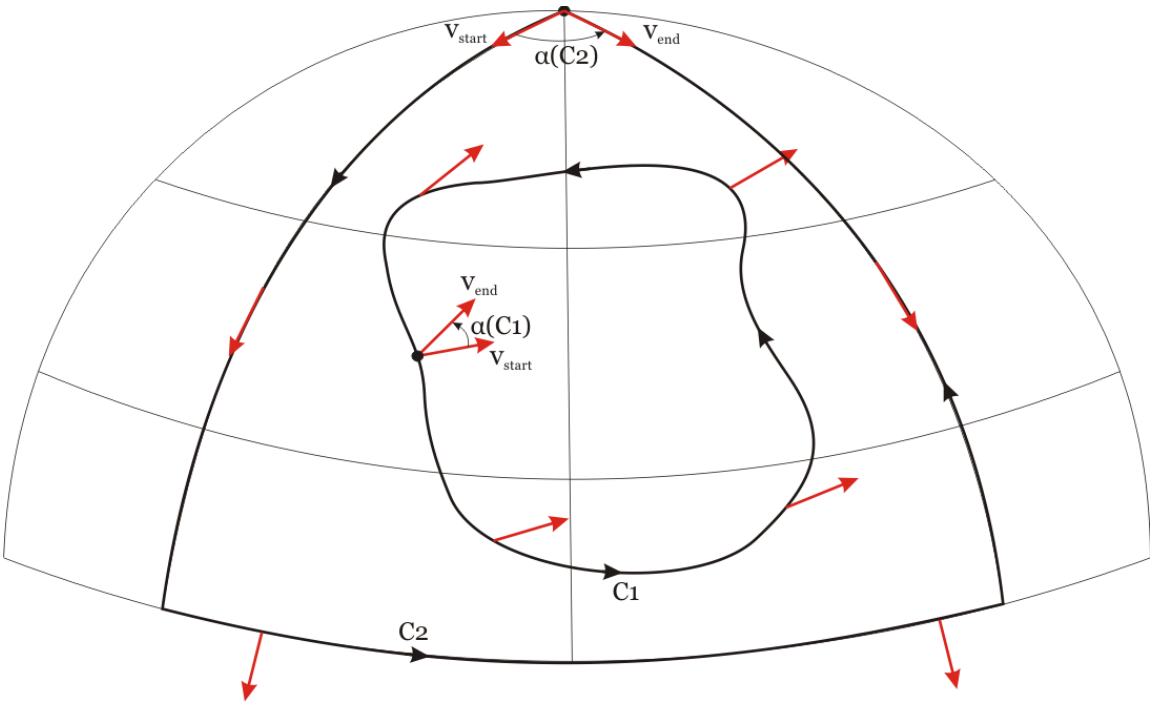

Figure 3.1.: This picture exemplifies the concept of geometric phases by the classical analogon of the parallel transport of vectors on a sphere. While transporting the vectors v parallel over the closed paths C_i indicated, they will still acquire a phase shift α that depends on the path covered.

3.2.3. MAIN RESULTS

ADIABATIC CASE $|\omega_r| < |\omega_0|$

This case holds for the movement of the UCN in the storage chamber. A properly weighted expression for ω_r is given in Eq. (28) of [57]:

$$\omega_r^{*2} = \frac{\pi^2}{6}\left(\frac{v_{xy}}{R}\right)^2 \tag{3.7}$$

It was then shown that the false EDM signal amounts in the adiabatic case to

$$d_{f,n} = -\frac{\hbar}{4}\left(\frac{\langle \partial B_{0z}/\partial z\rangle_V}{B_{0z}^2}\right)\frac{v_{xy}^2}{c^2}\left[1-\frac{\omega_r^{*2}}{\omega_0^2}\right]^{-1}. \tag{3.8}$$

$\langle \partial B_{0z}/\partial z\rangle_V$ denotes the volume averaged gradient and the equation thus holds for any shape of magnetic field inhomogeneity. The last term represents the breakdown of the adiabacity and the transition from the adiabatic to the nonadiabatic case.

NONADIABATIC CASE $|\omega_r| > |\omega_0|$

This is the case of the mercury atoms moving with a velocity of about 150 m/s. The properly weighted expression for ω_r is in that case (Eq. (38) of [57]) given by

$$\omega_r^{\dagger 2} = 0.65\left(\frac{v_{xy}}{R}\right)^2. \tag{3.9}$$

For that case the false EDM signal could only be calculated for a constant magnetic field gradient $\partial B_{0z}/\partial z$ and is given by

$$d_{f,Hg} = \frac{\hbar}{8}\left(\frac{\partial B_{0z}}{\partial z}\right)\frac{\gamma_{Hg}^2 R^2}{c^2}\left[1-\frac{\omega_0^2}{\omega_r^{\dagger 2}}\right]^{-1}. \tag{3.10}$$

Compared to the false EDM signal in the adiabatic case, the dependencies are completely different. While the $1/B_{0z}^2$ and v_{xy}^2 dependence is missing, it does depend on the square of the trap radius R^2. In [57], it was speculated whether one could also replace the gradient $\partial B_{0z}/\partial z$ by the volume average. [63] showed by a counterexample in the case of a dipole field, that one cannot.

Due to the normalisation of the neutron precession frequency with the mercury magnetometer, the geometric phase effect picked up by the mercury gets imparted onto the neutron measurement. The resulting false effect amounts to

$$d_{f,n,Hg} = \left|\frac{\gamma_n}{\gamma_{Hg}}\right| d_{f,Hg}\,. \tag{3.11}$$

Buffer Gas Collisions

It was shown [57, 62, 64], that a reduction of the mean free path length due to, e.g., buffer gas collisions will reduce the build up of the phase shift. While this is relevant for the EDM experiment operating at a pressure of about 10^{-4} mbar He to improve the HV performance and the mercury atoms (amounting to a suppression of about 3%), it is less relevant for the UCN as collisions with buffer gas tend to knock the UCN out of the trap anyhow.

3.3. falseEDM: Simulation to Study nEDM Related False Effects

3.3.1. Basic Principle

The basic principle of the simulation depends of the numerical integration of the Bloch-equations for the spin precession in a magnetic field $\boldsymbol{B}$ (see Appendix A.4 for the connection of the Bloch-equations to a quantum mechanical description of spin precession) given by

$$\frac{\mathrm{d}\boldsymbol{s}}{\mathrm{d}t} = \gamma(\boldsymbol{s}\times\boldsymbol{B})\,. \tag{3.12}$$

The simulation is written in Matlab [69] and uses their solver for ordinary differential equations `ode113`. This is a multistep Adams-Bashforth-Moulton solver and has been implemented into Matlab according to [70]. It uses several past steps in order to calculate the next step in the solution of the ordinary differential equation (in contrast to the Runge-Kutta methods). The solver determines the variable step size automatically according to the given tolerances. The typical tolerances set in my calculations are a relative tolerance of 10^{-7} and an absolute tolerance of 10^{-9}. This results in an accuracy for the calculation of an EDM of $\mathcal{O}(10^{-30}\,e\mathrm{cm})$.

The sequence of the calculation is as follows:

1. The simulation reads the stored reflection points of a given trajectory. These trajectories can either come from a GEANT4UCN simulation or from a simple dedicated Matlab simulation that analytically calculates the reflection points in the storage chamber.

2. The numerical solver of the ordinary differential equation is started. At each step in time the corresponding position in space and velocity is calculated according to a parabolic interpolation through the preceding and subsequent reflection point (or linear interpolation in the simulations without gravity). For the reflection points $(\boldsymbol{x_0}, t_0)$ and $(\boldsymbol{x_1}, t_1)$ with $t_1 > t_0$ the corresponding position in space and velocity at time $t_0 < t < t_1$ is given by

$$\boldsymbol{x}(t) = \boldsymbol{x_0} + \frac{t-t_0}{t_1-t_0}(\boldsymbol{x_1}-\boldsymbol{x_0}) + \frac{1}{2}g(t-t_0)\begin{pmatrix} 0 \\ 0 \\ t_1-t \end{pmatrix} \tag{3.13}$$

$$\boldsymbol{v}(t) = \frac{1}{t_1-t_0}(\boldsymbol{x_1}-\boldsymbol{x_0}) - \begin{pmatrix} 0 \\ 0 \\ g(t-t_0) \end{pmatrix} \tag{3.14}$$

   where g is the gravitational acceleration. Using these values, $\boldsymbol{B}(\boldsymbol{x})$ and $\boldsymbol{E}(\boldsymbol{x})$ are calculated either analytically or from lookup tables and additionally $\boldsymbol{B}_v = (\boldsymbol{E} \times \boldsymbol{v})/c^2$ is evaluated. In order to save computation time, the two cases of parallel and anti-parallel fields are calculated at the same time along the same trajectory. The solver thus solves at the same time the motion of $\boldsymbol{s}_{\uparrow\uparrow}$ and $\boldsymbol{s}_{\uparrow\downarrow}$. The spins are initially oriented in x-direction.

3. From the calculated spin motion, the angles $\phi_{\uparrow\uparrow}$ and $\phi_{\uparrow\downarrow}$ in the xy-plane are calculated as

$$\phi(t) = \arctan\left(\frac{s_y(t)}{s_x(t)}\right). \tag{3.15}$$

   The buildup of the corresponding EDM signal d is thus given as

$$d(t) = -\frac{\hbar}{4E}\frac{\left(\phi_{\uparrow\uparrow}(t) - \phi_{\uparrow\downarrow}(t)\right)}{t}. \tag{3.16}$$

4. Additionally, the series $\phi(t)$ can also be used to calculate the precession frequency. For that end, the number of maxima and minima in $\phi(t)$ are counted. Each passage from an extremum to another then corresponds to a swept angle of $\pi/2$ (see Fig. 3.2). In the end, the total amount of swept angle ϕ_{tot} over the time T can be summed up and the precession frequency is given as $\omega_L = \phi_{tot}/T$. With this method of evaluating the total amount of swept angle, the precession frequency can be extracted for spin precessions in arbitrary directions in 3 dimensions.

5. In the end, the calculated $\boldsymbol{s}_{\uparrow\uparrow}(t)$ and $\boldsymbol{s}_{\uparrow\downarrow}(t)$ are saved to file and the calculated EDM signals and some further information are saved into a summary file of the calculated trajectories.

6. The process is repeated for the next trajectory.

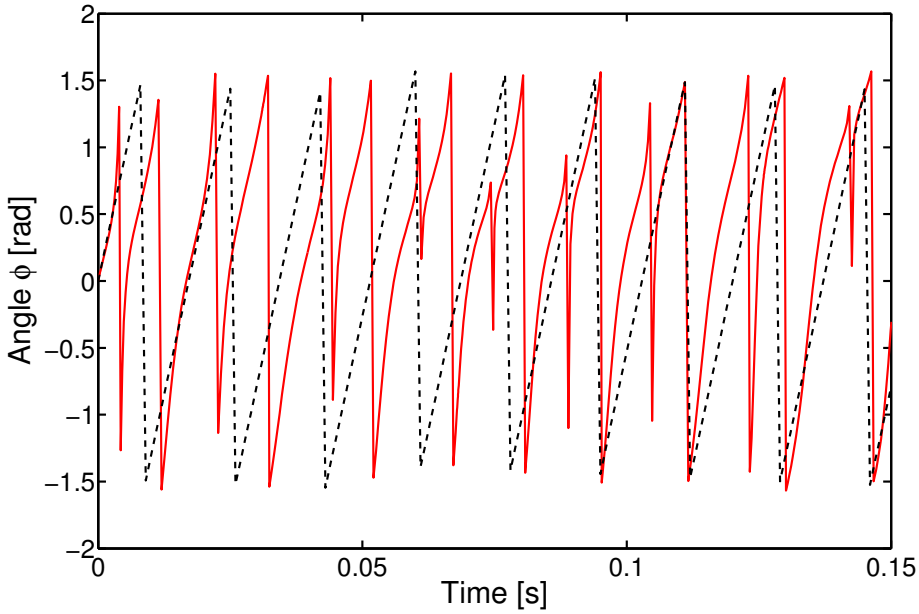

Figure 3.2.: Angle ϕ calculated according to Eq. (3.15) for the two cases of a constant 1 μT field in z-direction (dashed, black line) and the combination of a constant 1 μT field in z-direction and a large quadrupole like B_{xy} field of $\sim 1\,\mu$T (solid, red line; see Sec. 3.3.2).

3.3.2. Benchmarking

In order to check whether the simulation performs correctly, several benchmark tests were performed.

Ramsey Sequence

One of the first calculations was the spin precession during the Ramsey sequence. In this sequence, one has an applied linearly oscillating field at a certain frequency f with a duration of 2 s and a strength tuned to flip the spins from their initial orientation along z into the xy-plane on resonance [47]. This is followed by a certain time of free precession around the static field in z-direction. At the end, the oscillating field is again applied with the same parameters as above. The complete transition from the spin initially oriented into positive z-direction (spin up) to a spin oriented into negative z-direction (spin down) is only achieved if the applied frequency f matches the Larmor frequency during the free precession. For other frequencies, the characteristic Ramsey resonance pattern is formed due to the buildup of phase differences of the oscillating field and the spin during the free precession. The simulation of such a Ramsey sequence is shown in Fig. 3.3.

Geometrical Phases

In order to check the validity of the simulation in the calculation of false EDM signals, geometric phase effects as described above in Sec. 3.2 were simulated. An example can be found in Fig. 3.4. This shows the simulation for UCN under the influence of gravity in the storage chamber with an average holding field B_{0z} of 1 μT (the field B_{0z} changes with

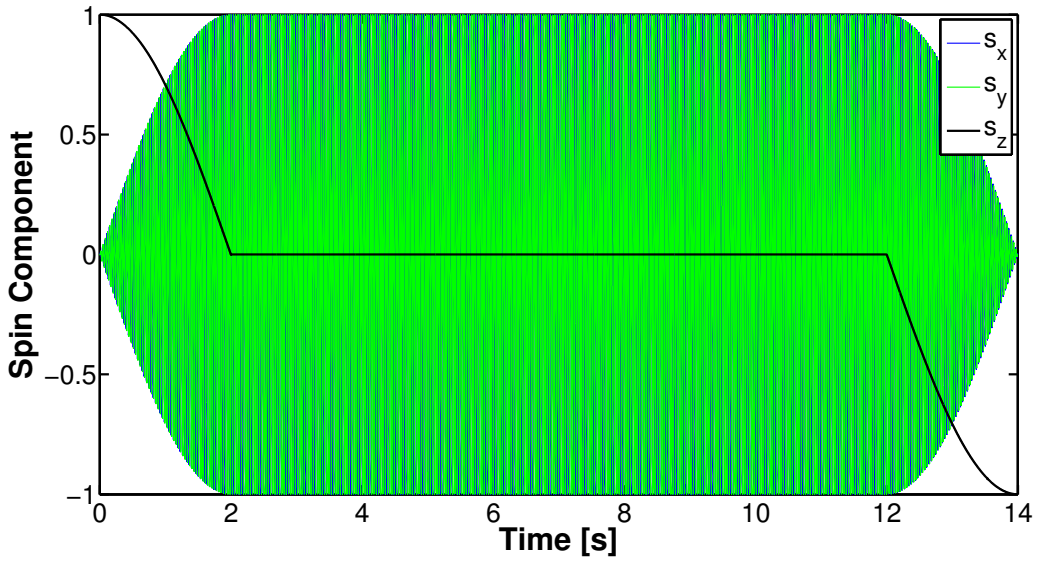

(i)

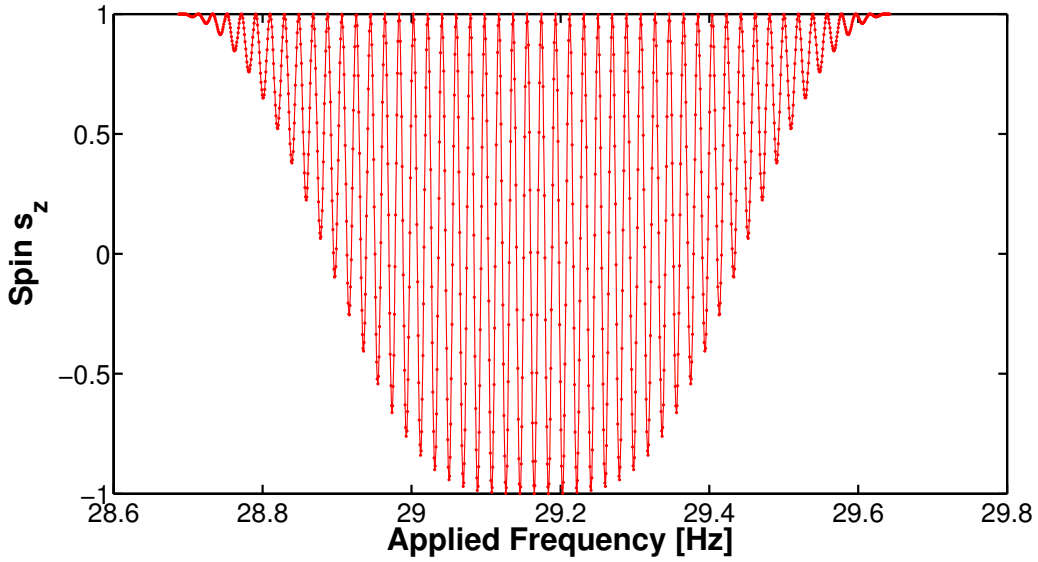

(ii)

Figure 3.3.: (i) Movement of the three spin components during the Ramsey sequence with a free precession time of 10 s and the frequency of the oscillating field matching the free precession frequency. (ii) Ramsey resonance pattern for a free precession time T of 50 s. The width of the central valley of the pattern is given approximaelty by $1/T$ [47].

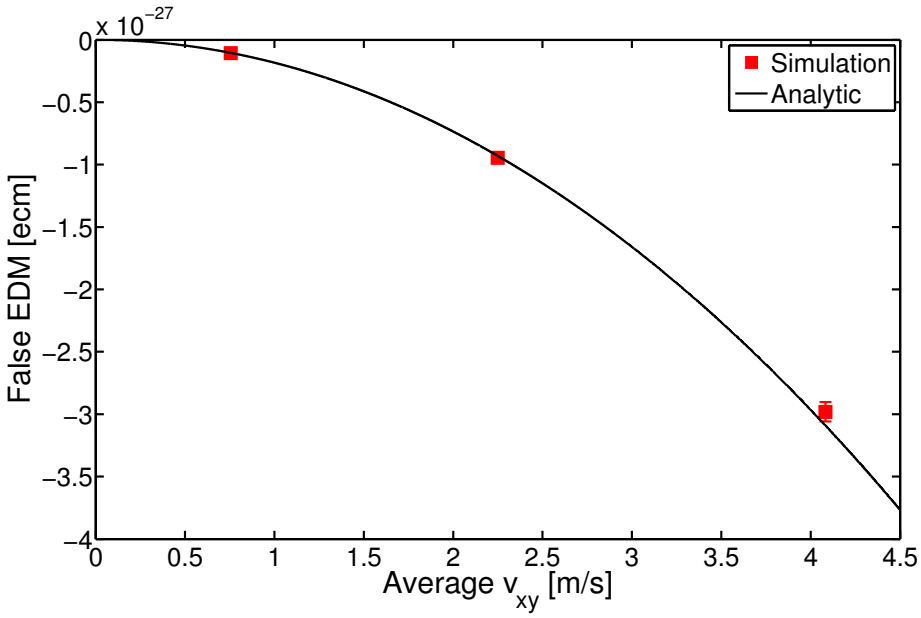

Figure 3.4.: Simulation of the false EDM signal for a gradient $\partial B_{0z}/\partial z$ of 1 nT/m. The analytic calculation is based on Eq. (3.8).

height due to the gradient) and a constant gradient $\partial B_{0z}/\partial z$ of 1 nT/m. The analytic calculation is the prediction of Eq. (3.8). The value for the average velocity in the xy-plane was calculated as $\langle v_{xy}^2 \rangle = \frac{2}{3}\langle v^2 \rangle$ where the value for $\langle v^2 \rangle$ was calculated according to the knowledge on the velocity distributions of UCN under the influence of gravity (see Appendix A.5). 3 sets of 100 trajectories were evaluated within the chamber of 12 cm height and 25 cm radius. Diffusivity at the walls was set to 100% following a $\cos\theta$ distribution. The velocities were set initially to 0.5, 2.75 and 5 m/s in the middle of the chamber. The errors on the simulated results were estimated from the standard deviation of the results of the different trajectories.

Additionally, the simulation was also checked for the case of fast moving particles such as the mercury atoms. The dependence of the false EDM is here completely different and Eq. (3.10) has to be used for comparison. The simulation is not completely optimal (and has also not been optimised) for the calculation of fast moving particles as here the number of reflection points is huge and correspondingly, one quickly runs into memory limitations. Consequently, only relatively short trajectories of approximately 10 s duration could be calculated. This situation could possibly be improved by a continuous calculation of the trajectory instead of reading in a pre-calculated trajectory. Additionally, due to the very quickly changing motional field $\boldsymbol{B}_v$ at every reflection point, the number of integration steps needed in the solution of the differential equation is large and thus the calculation much slower than in the UCN regime. Nevertheless, due to the excellent averaging over the storage volume of the fast moving particles, the results of the simulation from trajectory to trajectory scatter much less than in the UCN regime. For the calculations with typical parameters, the precision achieved in the calculation was with 10 trajectories and 10 s precession time more or less equal to the calculations for the UCN with 100 trajectories and 100 s precession time. In the simulation, the dependencies and non-dependencies of Eq. (3.10) could be confirmed (see Table 3.1).

v [m/s]	R [cm]	B_{0z} [μT]	$d_{f,Hg}$ (sim) [$e$cm]	$d_{f,Hg}$ (calc) [$e$cm]	$\lvert\omega_0\rvert$ [rad/s]	$\lvert\omega_r\rvert$ [rad/s]
150	25	1	$(1.20 \pm 0.17) \times 10^{-26}$	1.33×10^{-26}	47.7	322.5
150	25	0.1	$(1.31 \pm 0.04) \times 10^{-26}$	1.30×10^{-26}	4.8	322.5
250	25	1	$(1.22 \pm 0.09) \times 10^{-26}$	1.31×10^{-26}	47.7	537.5
50	25	1	$(1.32 \pm 0.99) \times 10^{-26}$	1.62×10^{-26}	47.7	107.5
150	12.5	1	$(3.31 \pm 0.13) \times 10^{-27}$	3.27×10^{-27}	47.7	645.0
150	50	1	$(4.1 \pm 1.2) \times 10^{-26}$	5.70×10^{-26}	47.7	161.2

Table 3.1.: Dependence of the false EDM on the parameters velocity v, radius of the trap R and magnetic field B_{0z} in the nonadiabatic regime. The gradient $\partial B_{0z}/\partial z$ used was 1 nT/m. The calculation of the false effect is the prediction of Eq. (3.10). In the cases of $|\omega_0| \approx |\omega_r|$, the available statistics in the simulation is not enough to resolve the resonance behaviour.

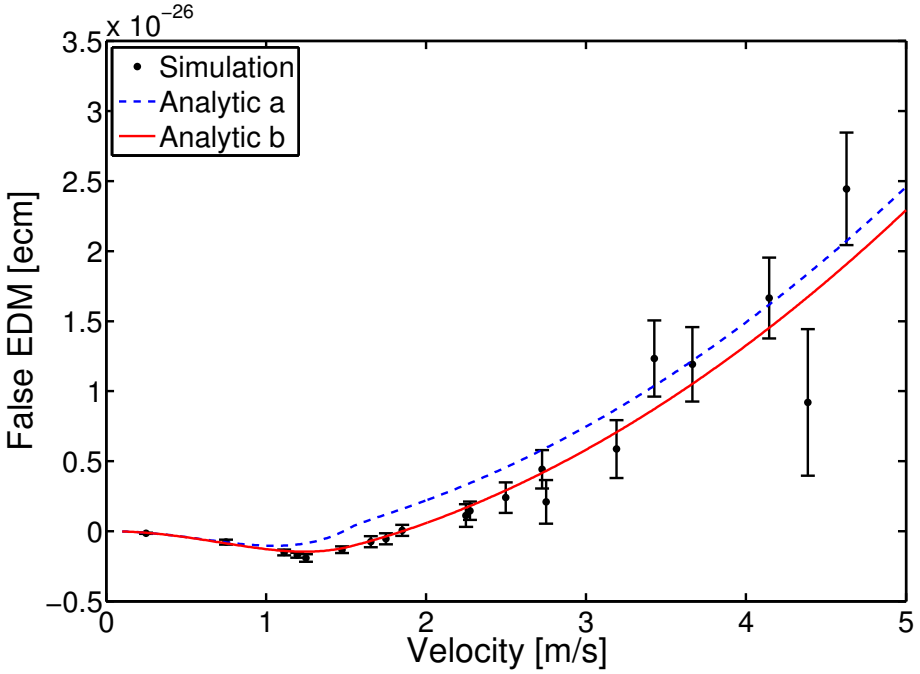

Figure 3.5.: Simulated false EDM signal for the non-constant gradient field given in Eq. (3.17). The analytic predictions are calculated according to Eq. (3.8) for the curve labelled “a” and according to Eq. (3.18) for the curve “b”. The second curve clearly fits the data much better.

As Eq. (3.8) claims to depend only on the volume averaged gradient and to be valid for any shape of magnetic field, a field B_z was used that is quadratic in z and came from a now obsolete simulation of the magnetic field generated by the coil of the nEDM apparatus [71]. The field could be simplified and expressed analytically to reasonable agreement by

$$\begin{aligned} B_x &= 7.5\times10^{-7}\,\frac{\mu\mathrm{T}}{\mathrm{mm}^2}\,xz \\ B_y &= -1.7\times10^{-7}\,\frac{\mu\mathrm{T}}{\mathrm{mm}^2}\,yz \\ B_z &= 1\,\mu\mathrm{T}+3.6\times10^{-7}\,\frac{\mu\mathrm{T}}{\mathrm{mm}^2}\,x^2-0.7\times10^{-7}\,\frac{\mu\mathrm{T}}{\mathrm{mm}^2}\,y^2-2.9\times10^{-7}\,\frac{\mu\mathrm{T}}{\mathrm{mm}^2}\,z^2 \end{aligned} \tag{3.17}$$

for z between -4.5 and 7.5 cm and x and y on a circle with radius 25 cm. Fig. 3.5 shows the simulated false EDM results as a function of the velocity of the UCN - under the influence of gravity - on the bottom of the storage chamber. The first analytic calculation (labelled a) corresponds to the prediction of Eq. (3.8). It is clear that this is not the correct description of the resulting false EDM values. It is not stated explicitly in [57], but Eq. (3.8) holds only when neglecting the influence of gravity. The description of the false EDM effect under the inclusion of gravity is given as

$$d_{f,n} = -\frac{\hbar}{4}\left\langle\left(\frac{\partial B_{0z}/\partial z}{B_{0z}^2}\right)\frac{v_{xy}^2}{c^2}\left[1-\frac{\omega_r^{*2}}{\omega_0^2}\right]^{-1}\right\rangle_V . \tag{3.18}$$

The averaging over the volume has to be performed using the appropriate height distribution of UCN in the storage chamber (see Appendix A.5). The gradient at the different heights thus gets weighted according to the velocity v_{xy} at that height. The prediction of Eq. (3.18) is also given in Fig. 3.5 (labelled b) and matches the simulated points very nicely.

Ramsey-Bloch-Siegert Shift

As the simulation also extracts precession frequencies, Ramsey-Bloch-Siegert shifts can be calculated as well. They were calculated for the case of a constant field B_{0z} of 1 μT, no gradient, no electric field, but a quadrupole like magnetic field in the xy-plane given by

$$B_{xy} = q\begin{pmatrix} y \\ x \end{pmatrix}. \tag{3.19}$$

The average over the radius of the storage chamber is then given by

$$\langle B_{xy}\rangle_R = q^2\frac{R^2}{2}. \tag{3.20}$$

The results of the simulated deviations away from the frequency $\omega_0 = -\gamma_n B_{0z}$ are shown in Fig. 3.6 and compared to the calculation using Eq. (3.4) and averaging over the two cases of $\pm\omega_r$. The simulation agrees very well with the calculation except for a presently not understood offset in the extraction of the precession frequency of $\sim 2\times10^{-7}$ rad/s, which is also present for the case of no other fields than B_{0z}. It has to be noted that in the case of the larger B_{xy} fields the plane of precession changes constantly while the

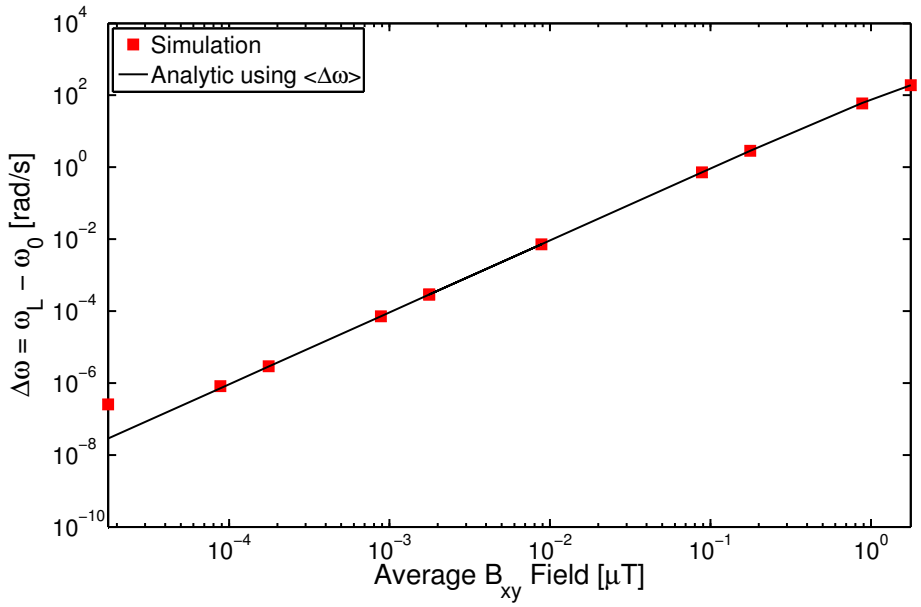

Figure 3.6.: Simulated and calculated Ramsey-Bloch-Siegert shift for quadrupole like B_{xy} fields. $\langle\Delta\omega\rangle$ denotes the averaging over the contributions with $\pm\omega_r$. For more details see text.

particle is moving around in the trap (see also Fig. 3.2). A very similar simulation has been performed looking at the Ramsey-Bloch-Siegert shift coming from the motional magnetic field $\boldsymbol{B}_v$ in the absence of a gradient. The simulation agreed also very well to the prediction of Eq. (3.4). In that case the plane of precession changed completely at each reflection point for very large electric fields while staying constant in between.

3.4. EXPECTED NEDM SYSTEMATICS DURING PHASE II

3.4.1. INTRODUCTION

Starting from the previous experiment [26] and its analysis of the systematic effects, one can discuss the points where improvements are necessary for the phase II measurement at PSI. Table 3.2 lists the systematic shifts and uncertainties of [26] and gives estimates and goals for the suppression of uncertainties to a level of $1-2\times10^{-27}$ $e$cm ($1\,\sigma$) which, combined with the aimed at statistics (see Sec. 3.1), would allow extracting at 95% C.L. a limit of 5×10^{-27} $e$cm after phase II. It would also permit to detect with $5\,\sigma$ significance a neutron EDM of 1.3×10^{-26} $e$cm.

Together with the experimental work of devising a system allowing for the velocity dependent detection of UCN (see Sec. 4), I also assessed the expected systematic uncertainties related to UCN velocity. In Table 3.2, these are the points 1, 2, 3, 4, 5, 6, and 9. In the following, I will give the arguments leading to the systematic uncertainties expected during the upcoming measurement period together with some more general remarks on the influence of certain magnetic fields on the measurements.

No.	Effect	Shift (Ref. [26]) [10^{-27} $e$cm]	σ (Ref. [26]) [10^{-27} $e$cm]	σ (Phase II) [10^{-27} $e$cm]
1.	Door cavity dipole	-5.60	2.00	**0.10**
2.	Other dipole fields	0.00	6.00	**0.40**
3.	Quadrupole difference	-1.30	2.00	**0.60**
4.	$\mathbf{v} \times \mathbf{E}$ translational	0.00	0.03	0.04
5.	$\mathbf{v} \times \mathbf{E}$ rotational	0.00	1.00	**0.10**
6.	Second-order $\mathbf{v} \times \mathbf{E}$	0.00	0.02	0.01
7.	ν_{Hg} light shift (geo phase)	3.50	0.80	**0.40**
8.	ν_{Hg} light shift (direct)	0.00	0.20	0.20
9.	Uncompensated B drift	0.00	2.40	**0.90**
10.	Hg atom EDM	-0.40	0.30	*0.06*
11.	Electric forces	0.00	0.40	0.40
12.	Leakage currents	0.00	0.10	0.10
13.	ac fields	0.00	0.01	0.01
	Total	-3.80	7.19	**1.31**

Table 3.2.: Systematic uncertainties in the nEDM measurements, adapted from [26]. Bold face is used for those entries for which improvements are crucial. The Hg atom EDM limit has been improved recently [59].

3.4.2. Main magnetic field B_{0z}

The main field serves as the holding field for the free spin precession of the neutrons and the ^{199}Hg atoms. The neutrons and mercury atoms precess at a rate given by their gyromagnetic ratios [10, 52]:

$$\omega_n = -\gamma_n B_0 = 2\pi \times 29.164702 \frac{\mathrm{Hz}}{\mu\mathrm{T}} \times B_0 \tag{3.21}$$

$$\omega_{Hg} = -\gamma_{Hg} B_0 = -2\pi \times 7.590313 \frac{\mathrm{Hz}}{\mu\mathrm{T}} \times B_0 \tag{3.22}$$

The way how the two species react to fields orthogonal to the main field $B_0 \approx B_{0z}$ lies at the heart of many of the systematic effects that will be described below. The reaction is given by the Ramsey-Bloch-Siegert shift (Eq. (3.5)). As ω_r for the neutrons is much smaller than ω_0, the neutrons will precess with a frequency corresponding to the averaged modulus of the magnetic field whereas the (thermal) mercury atoms will precess with a frequency corresponding to the averaged z-component of the magnetic field.

3.4.3. Magnetic field gradients $\frac{\partial B_{0z}}{\partial z}$

Magnetic field gradients will lead to a loss of polarisation and therefore a reduced transverse spin holding time T_2. Qualitatively, this can easily be understood as in the presence of gradients the spins will precess with different frequencies at different locations in the trap. As the particles move around in the trap, they will get more and more out of phase with respect to each other (see also Appendix A.2). For the fast moving atoms,

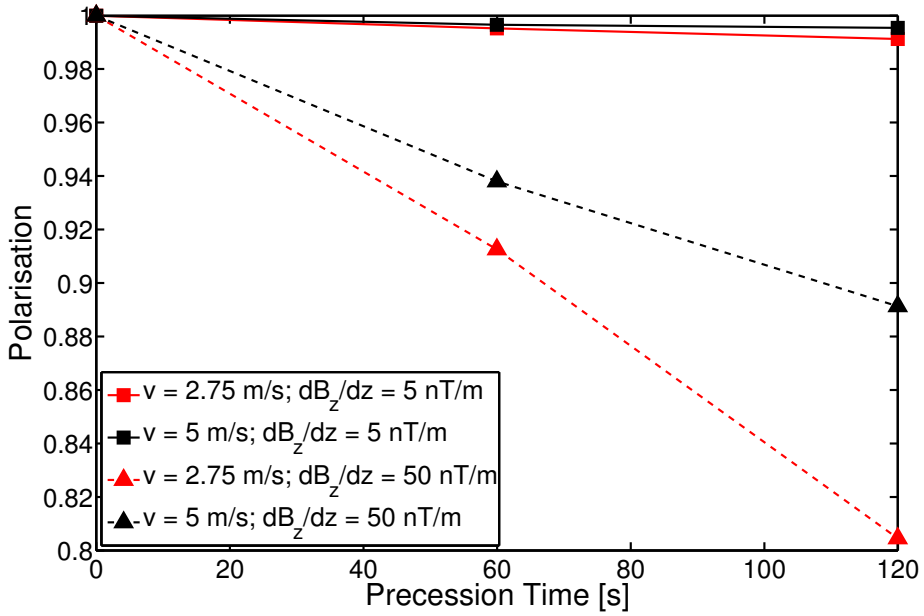

Figure 3.7.: Loss of polarisation along the trajectories due to a gradient in z-direction. For details see text.

this is less of a problem then for the slow moving ultracold neutrons. A rigorous calculation leads to the reduction of the T_2 time in a cylindrical trap with height h and radius R given by [72]:

$$\frac{1}{T_2} = \frac{1}{2T_1} + \frac{\gamma^2 h^4}{120D}\left(\frac{\partial B_{0z}}{\partial z}\right)^2 + \frac{7\gamma^2 r R^4}{96D}\left(\frac{\partial B_{0z}}{\partial r}\right)^2 \tag{3.23}$$

Here, T_1 is the polarisation holding time for the spin oriented along the main magnetic field ($T_1 \gg T_2$) and D is the diffusion coefficient ($L_D = \sqrt{4Dt}$ is the corresponding length covered after time t). From the prefactors given in front of the gradient dependence and inserting the typical values for the nEDM apparatus, it follows that the gradients $\frac{\partial B_{0z}}{\partial r}$ will play the dominant part in the loss of polarisation.

For an ensemble of spins, the polarisation is given as

$$|\boldsymbol{P}| = \left|\frac{1}{N}\sum_{i=1}^{N} \boldsymbol{s_i}\right|. \tag{3.24}$$

As this is accessible in the simulation that I described above in Sec. 3.3, I used this simulation to calculate the loss of polarisation during the storage of the UCN. The data set included different velocities - neglecting gravity, though - and different magnetic field gradients $\partial B_{0z}/\partial z$. A part of the data is shown in Fig. 3.7. The corresponding T_2 times were calculated by solving for T_2 in the expression $P = \exp(-T/T_2)$ at the point $T = 120$ s. The thus extracted T_2 times very nicely showed the dependence on $(\partial B_{0z}/\partial z)^2$ and a dependence on $1/v$ or equivalently $D \propto v$. By comparing the extracted T_2 values to the prediction of Eq. (3.23), the diffusion constant could be determined to be $D = 0.030\,\mathrm{m} \times v$. For the typical good gradient values of 1 nT/m, the T_2 time thus amounts to 1.4×10^6 s for the gradient in z-direction and to 1.1×10^4 s for the gradient in r-direction making this mechanism of depolarisation basically negligible.

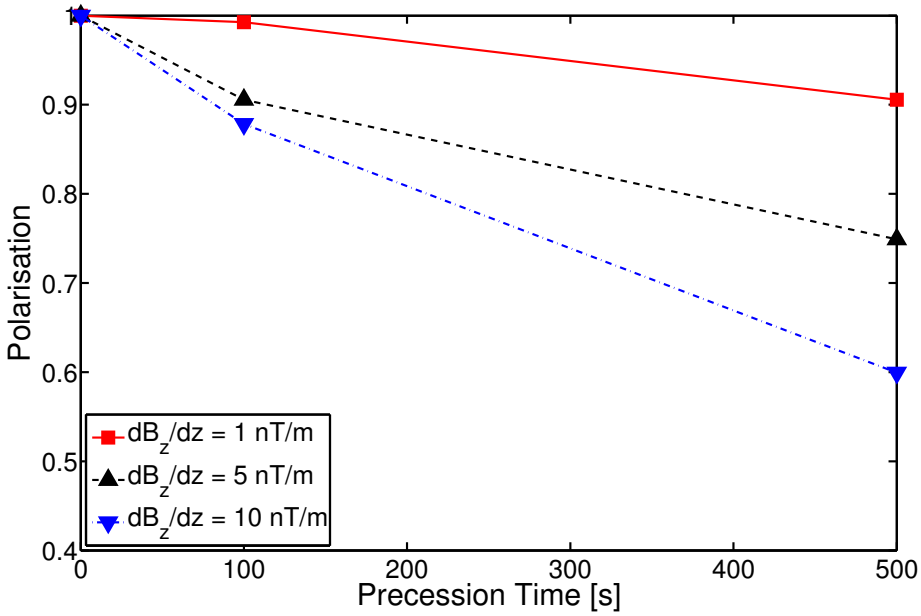

Figure 3.8.: Loss in polarisation due to the different centres of mass of UCN of different energies. For details see text.

The second, more severe effect of depolarisation is due to the fact that the UCN of different energies will have different centres of mass and thus will experience different average magnetic fields. One can imagine this in a simple picture as the UCN of different energies all sitting at different heights in the storage chamber, precessing at slightly different frequencies (corresponding to the magnetic field at that height) and thus getting more and more out of phase with respect to each other. In this simple picture, the phase difference acquired by two particles being separated in height by Δz after time T is given as

$$\Delta\phi = -\gamma \frac{\partial B_{0z}}{\partial z} \Delta z T \,. \tag{3.25}$$

This leads to a loss of polarisation of

$$\begin{aligned} P &= \frac{1}{2}\left|\begin{pmatrix} 1 \\ 0 \end{pmatrix} + \begin{pmatrix} \cos\Delta\phi \\ \sin\Delta\phi \end{pmatrix}\right| = \frac{1}{\sqrt{2}}\sqrt{1+\cos\Delta\phi} \approx 1 - \frac{\Delta\phi^2}{4} \\ &\approx 1 - \frac{1}{4}\left(\gamma \frac{\partial B_{0z}}{\partial z}\Delta z T\right)^2 \end{aligned} \tag{3.26}$$

and thus a loss in polarisation proportional to $(\partial B_{0z}/\partial z)^2$ as claimed in [26]. However, the shape of the loss in polarisation is different than in Eq. (3.23) where one has as the leading term a depolarisation going like $(\partial B_{0z}/\partial z)^2 T$. As this leading term linear in T is missing in Eq. (3.26), one cannot really assign a T_2 time to this depolarisation mechanism.

In order to calculate the effect of this depolarisation mechanism on the UCN, I set up a little simulation. It is based on a spectrum inside the nEDM storage chamber obtained in a Monte-Carlo simulation of the spectrometer [50]. For each energy in that spectrum, the simulation then calculates the corresponding centre of mass position $\langle z \rangle$ and the spin precession according to the field $B_{0z} + \partial B_{0z}/\partial z \langle z \rangle$. The corresponding phases are

then evaluated at different precession times and the resulting polarisation is plotted in Fig. 3.8 for three different constant gradients. Compared to Fig. 3.7, it is clear that this effect leads to much larger depolarisation. According to M. Pendlebury [73], the decrease in polarisation for gradients of 5 nT/m amounted due to this effect at 130 s to about 10% during their measurements [26]. This very nicely matches the observed drop in polarisation for the same parameters in Fig. 3.8.

Additionally, the gradient in z-direction will lead to false EDM signals due to the geometric phase effects described above. However, due to the clever analysis strategy devised in [26] and also explained in Sec. 2.2.5 the geometric phase effects coming from the constant magnetic field gradients are removed from the data.

3.4.4. DIPOLE FIELDS

DIRECT FALSE EFFECTS (NO. 9)

The "uncompensated B drift" refers to a magnetic field, e.g., caused by a magnetization of the Mu-metal in the region of the HV feedthrough generating a dipole-like field, which reverses sign when changing the electric field polarity. The induced false EDM is then given by

$$d_f = -\frac{\hbar}{4E}\gamma_n \Delta B \approx 3\times 10^{-12}\, e\text{cm}\,\frac{\Delta B}{1\text{ T}}. \tag{3.27}$$

In [26], when analyzing neutrons and ^{199}Hg independently, false EDM signals were obtained for both, $d_n \approx 17\times 10^{-26}\, e$cm and $d_{Hg} \approx -4\times 10^{-26}\, e$cm, consistent – as the effect scales as $\frac{\gamma_n}{\gamma_{Hg}}$ – with a common HV correlated magnetic field source of ±30 fT. In the analysis of the precession frequency ratio, this effect is compensated for a constant offset field and suppressed for a field gradient due to the close vicinity of the neutron and mercury centres of mass (as in Eq. (3.31) and (3.32)). The left over, uncompensated effect results from the vertical centre of mass separation $\Delta h = 2.8$ mm [26]. Assuming that the effect would be caused by a dipole at a distance of about $l = 0.55$ m (i.e. where the HV feedthrough penetrates the Mu-metal shield) then the difference in field seen by the neutron, which is further away by Δh, to the field B_{dip} seen by the Hg amounts to

$$\Delta B_{dip} = B_{dip} - B_{dip}\frac{l^3}{(l+\Delta h)^3} \approx B_{dip}\frac{3\Delta h}{l}. \tag{3.28}$$

The normalization of the neutron with the mercury frequency should suppress the effect thus by a factor of about $3\Delta h/l \approx 70$. The systematic uncertainty of $2.4\times 10^{-27}\, e$cm in Tab. 3.2 was then obtained by dividing d_n by 70. For phase II, one has to build and improve on this capability:

With the Cs magnetometers on top of and below the neutron precession chamber, one can measure for each neutron and Hg measurement (~100 s) field averages for the top and bottom magnetometers. The precision of these averages will not be limited by the sensitivity of the Cs sensors but by the actual magnetic field noise. Measurements so far suggest that one can expect it at a level of 1 pT (see Sec. 2.3) for individual channels and ~ 100 fT for the difference of the averages [74]. Assuming about 100 cycles with $+E$ and 100 with $-E$ per day will result in a sensitivity of 10 fT to HV correlated signals. A field change of ±10 fT corresponds to a false EDM signal of $d_n \approx 6\times 10^{-26}\, e$cm which gets suppressed by a factor 70 to $9\times 10^{-28}\, e$cm due to the normalisation with the mercury.

The programm of setting up the nEDM experiment thus has to foresee detailed measurements to investigate HV related field changes (charging currents, sparks, discharges, ...) with the before mentioned sensitivities. It is thus expected to limit and control these effects to such a precision.

Indirect False Effects (No. 1 & 2)

Magnetic fields stemming from a magnetic dipole of strength m will lead to inhomogeneous field distributions inside the storage chamber, which will result in false EDM signals. There are two mechanisms that lead to the false EDM signal. I will start with the first mechanism, which is due to geometric phase effects.

The field generate by a dipole $\boldsymbol{m}$ at the point $\boldsymbol{r}$ is given by

$$\boldsymbol{B}^{dip} = \frac{\mu_0}{4\pi r^3}\left(3\frac{(\boldsymbol{m}\cdot\boldsymbol{r})\boldsymbol{r}}{r^2} - \boldsymbol{m}\right). \tag{3.29}$$

From that expression, one can perform the somewhat tedious calculations for the volume averages relevant for the nEDM apparatus under the assumption of a dipole field oriented along z (partly also given in [63]). The volume averaged field of B_z^{dip} is shown in Fig. 3.9. The two volume evaluated are the large volume of the storage chamber and the adjacent small volume in the shutter mechanism (see Sec. 2.1). Additionally, one can also evaluate the corresponding gradient and again calculate the volume average (shown in Fig. 3.9 as well). The volume averages are performed according to the distribution (see Appendix A.5) for an energy that leads to a centre of mass offset $\Delta h = 2.8$ mm as given in [26].

Performing the calculations for the corresponding false effect due to the neutron geometric phase according to Eq. (3.18) leads to the values as shown in Fig. 3.10. While it is a sizable false effect in the small shutter volume, the UCN spends only a small amount of time in this volume and the actual effect can be estimated by weighting the calculated false effects by the volume fractions $V_i/(V_1+V_2)$, which amount to $\frac{V_1}{V_1+V_2} = 0.007$ and $\frac{V_2}{V_1+V_2} = 0.993$. The resulting effects are small and can be neglected compared to geometric phase effect picked up by the mercury (see next paragraph).

In the case of the mercury, the geometric phase effects are given by Eq. (3.10) and shown in Fig. 3.11. However, it was found in [63] that the false EDM signal is in the case of a dipole field enhanced by a factor $\left(1+\frac{R^2}{z_0^2}\right)$ (with z_0 the distance to the dipole) above the expectation stemming from the gradient alone. At the same time however, simulations showed that for small distances to the dipole ($z < 5$ cm) the actual enhancement factor is at least a factor 2 smaller. Fig. 3.12 shows the volume averaged enhancement factor $f(z_0) = \frac{1}{h}\int_0^h \left(1+\frac{R^2}{(z+z_0)^2}\right)\mathrm{d}z$ together with the results from the simulation. The enhanced false EDM (neglecting the simulated reduction of the enhancement factor) picked up by the mercury is thus given as

$$d_{f,Hg} = \frac{\hbar}{4}\left\langle\left(\frac{\partial B_z^{dip}(z)}{\partial z}\right)\left(1+\frac{R^2}{(z+z_0)^2}\right)\right\rangle_V \frac{\gamma_{Hg}^2 R^2}{c^2}\left[1-\frac{\omega_0^2}{\omega_r^{\dagger 2}}\right]^{-1}. \tag{3.30}$$

The prediction of this equation is also shown in Fig. 3.11.

Due to the normalisation procedure of the neutron frequency by the mercury measurements, the geometric phase picked up by the mercury gets imparted onto the neutron measurement (see Eq. (3.11)).

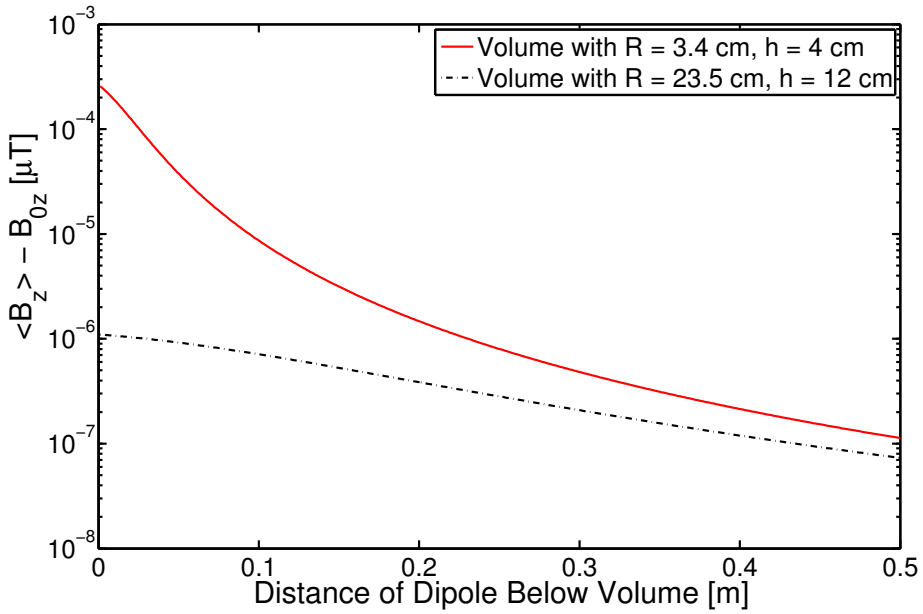

(i)

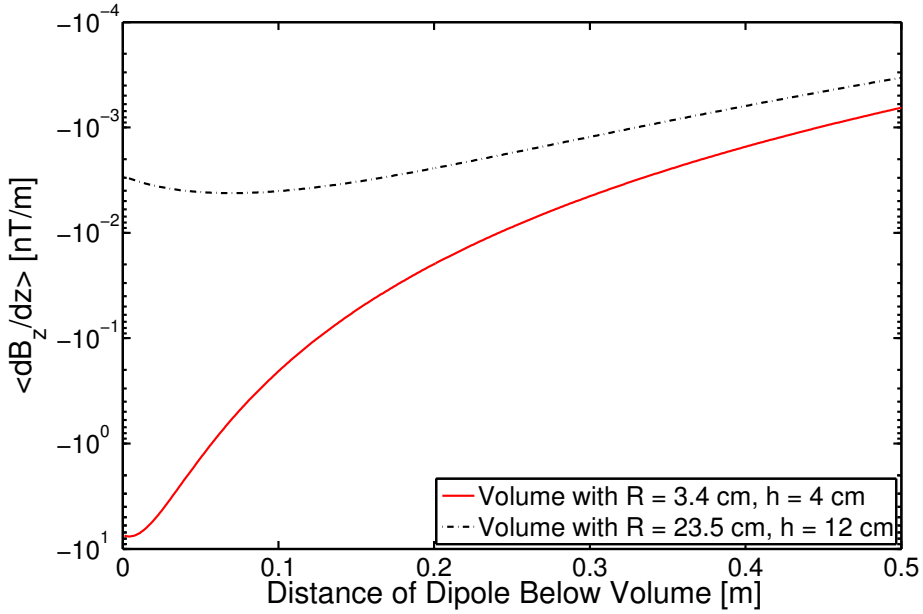

(ii)

Figure 3.9.: (i) Volume averaged field B_z^{dip} stemming from a dipole oriented in z-direction and located in the center at different distances below the two different volumes. The strength of the dipole amounts to $\mu_0 m = 10^{-13}$ T/m^3. (ii) Volume average gradient $\partial B_z^{dip}/\partial z$ for the same dipole. The volume averages are performed for an energy leading to the measured center of mass offset as given in [26].

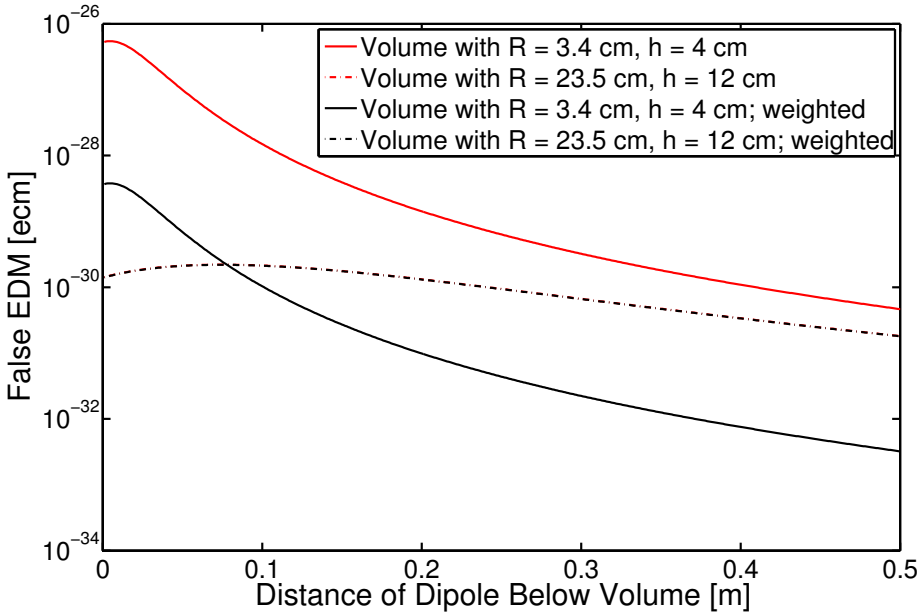

Figure 3.10.: False EDM signal picked up by the neutron due to the presence of a dipole below the volume. The strength of the dipole amounts to $\mu_0 m = 10^{-13}$ T/m^3. The weighting is performed according to the volume fractions $V_i/(V_1+V_2)$.

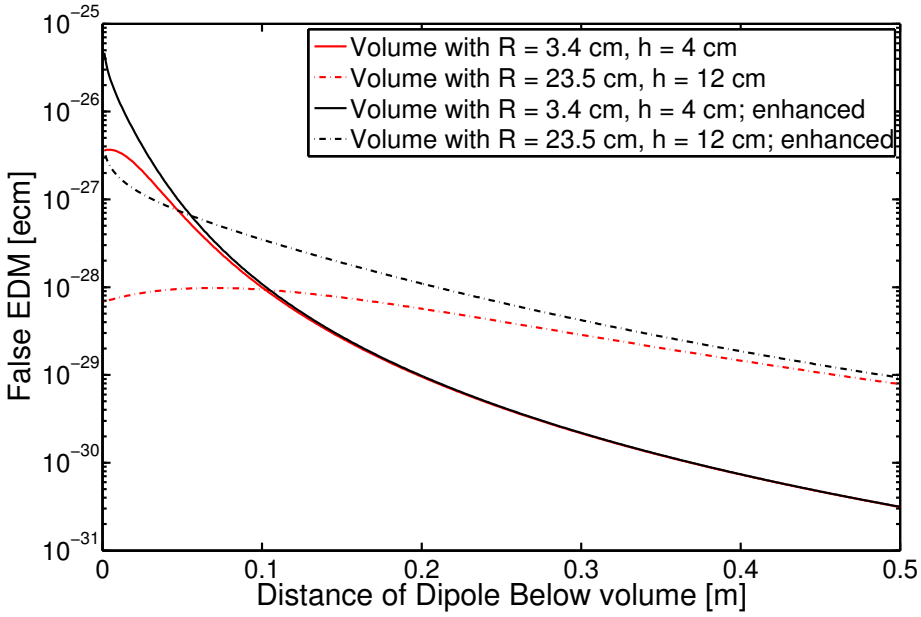

Figure 3.11.: False EDM signal picked up by the mercury atoms due to a dipole below the volume. The calculate predictions correspond to Eq. (3.30) with and without the enhancement factor $\left(1+\frac{R^2}{z^2}\right)$. The strength of the dipole amounts to $\mu_0 m = 10^{-13}$ T/m^3.

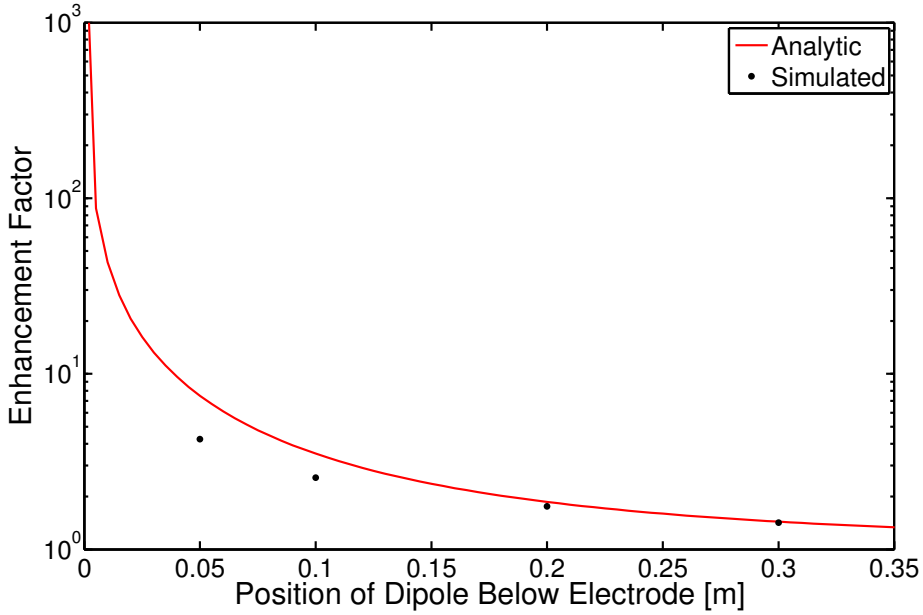

Figure 3.12.: Volume averaged enhancement factor as given by the analytic calculation and the simulation. For small distances to the dipole, the actual enhancement factor is at least a factor 2 smaller than given by the analytic calculation. Simulated data from [63]

A part of the false effect signal resulting in the neutron EDM measurement gets removed due to the procedure of extracting the EDM value at the crossing point of the two curves for B-field up and down (see [26] and Sec. 2.2.5). The removed part corresponds to the value of Eq. (3.30) without the enhancement factor $\left(1+\frac{R^2}{z^2}\right)$ as it then scales exactly in the same way as the effects from the constant gradient of the main field $\frac{\partial B_{0z}}{\partial z}$.

Figure 3.13 shows the resulting false EDM in the neutron measurement stemming from a dipole of strength $\mu_0 m = 10^{-13}\,\mathrm{Tm}^3$ (corresponding to a field of approximately 1…2 nT at 2 cm distance) averaged over the two volumes. The simulated reduction of the enhancement factor (Fig. 3.12) has not been taken into account.

The second mechanism to generate a false EDM signal is based on the change in precession frequency due to the B_z^{dip} component of the dipole field, which the neutron and the Hg average differently.[2] The Hg will precess with a frequency corresponding to

$$\omega_{Hg} = -\gamma_{Hg}\left(B_{0z} + \left\langle B_z^{dip}\right\rangle_{Hg}\right) \tag{3.31}$$

while the neutron will precess at a frequency given by

$$\omega_n = -\gamma_n\left(B_{0z} + \left\langle B_z^{dip}\right\rangle_{n}\right), \tag{3.32}$$

where the averaging is given by

$$\left\langle B_z^{dip}\right\rangle_n = \int_0^h B_z^{dip} f_n(z, E_n)\mathrm{d}z. \tag{3.33}$$

[2] Ramsey-Bloch-Siegert shifts due to the B_{xy}^{dip} components are more than 2 orders of magnitude smaller for the relevant dipole strengths.

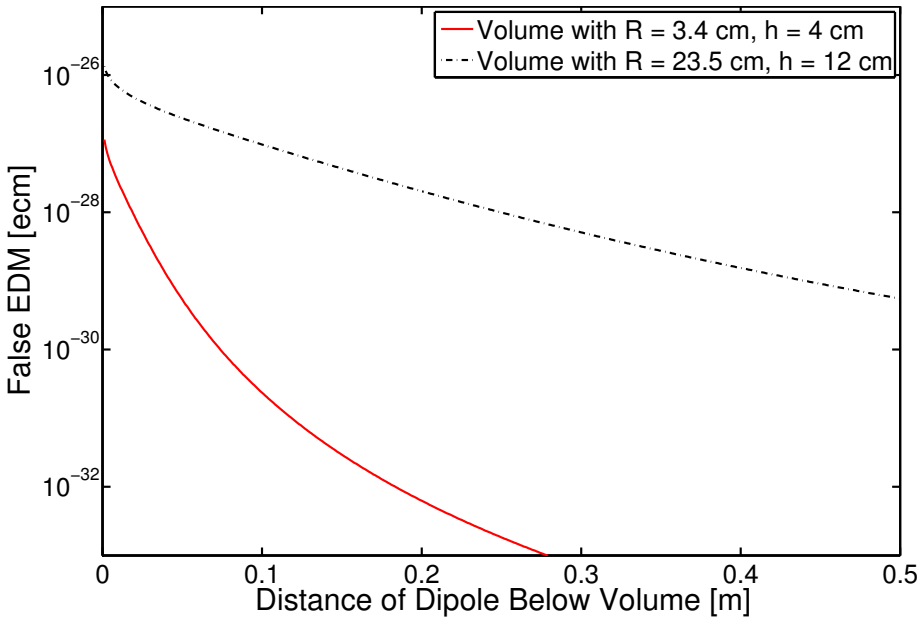

Figure 3.13.: Resulting false EDM in the neutron measurement due to a dipole field stemming from the geometric phase effect of the Hg. The values have been weighted by their volume fractions $\frac{V_i}{V_1+V_2}$. The strength of the dipole amounts to $\mu_0 m = 10^{-13}$ T/m^3. For more details see text.

$f_n(z, E_n)$ is the height distribution under the influence of gravity of a UCN of energy E_n inside the storage chamber (see Appendix A.5). As above, I will use for the averages the energy E_n such that the difference in the centres of mass for Hg and neutrons ($\langle z\rangle_{Hg} - \langle z\rangle_n$) amounts to 0.28 cm as in [26].

This difference in averaging will shift the ratio of precession frequencies $R_a = \left|\frac{\omega_n}{\omega_{Hg}}\frac{\gamma_{Hg}}{\gamma_n}\right|$ and additionally it will shift R_a in different directions for B-field up or down (see Fig. 3.14). If in the analysis one extracts the EDM at the crossing point (see Sec. 2.2.5), any such differential shift will show up as a false EDM contribution:

$$d_{meas} = d'_n + k\left(\frac{R^{\uparrow}_{a0} - R^{\downarrow}_{a0}}{2}\right) \tag{3.34}$$

Figure 3.15 shows the resulting false EDM of the differential shifts of R_a for a dipole of strength $\mu_0 m = 10^{-13}$ Tm^3 and a static field of 1 μT. The values for the averages over the two volumes have again been weighted by the corresponding volume fractions.

As a conclusion let us look at two possible scenarios:

(i) A dipole of strength $\mu_0 m = 10^{-13}$ Tm^3 located on or near the surface of the main volume. In that case, only the geometric phase effect of the main volume contributes and the maximal false effect amounts to (see Fig. 3.13):

$$d_f \approx \frac{1}{2} \times 1.3 \times 10^{-26}\, e\text{cm} \approx 7 \times 10^{-27}\, e\text{cm}, \tag{3.35}$$

where the factor $\frac{1}{2}$ is approximately the reduction of the enhancement factor at short distances as discussed above.

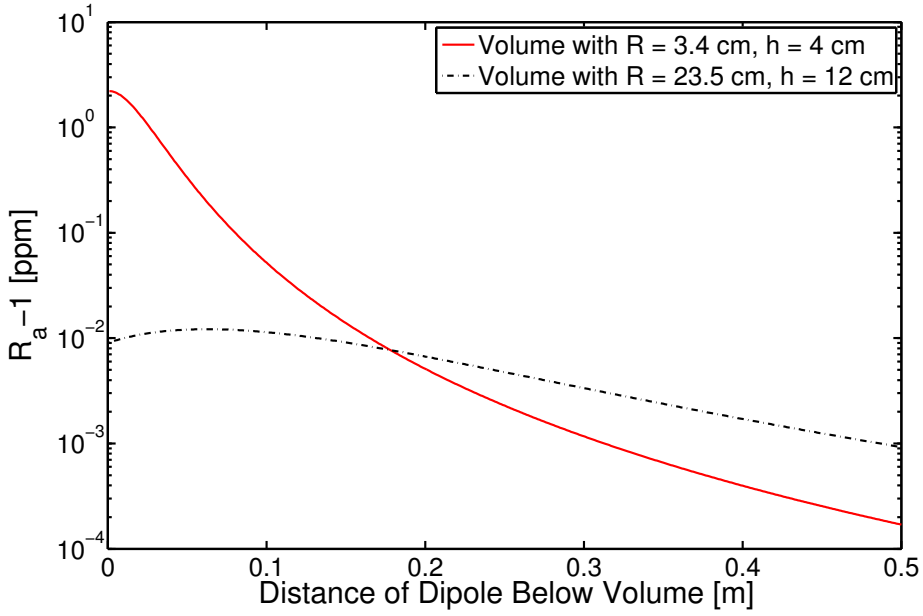

(i)

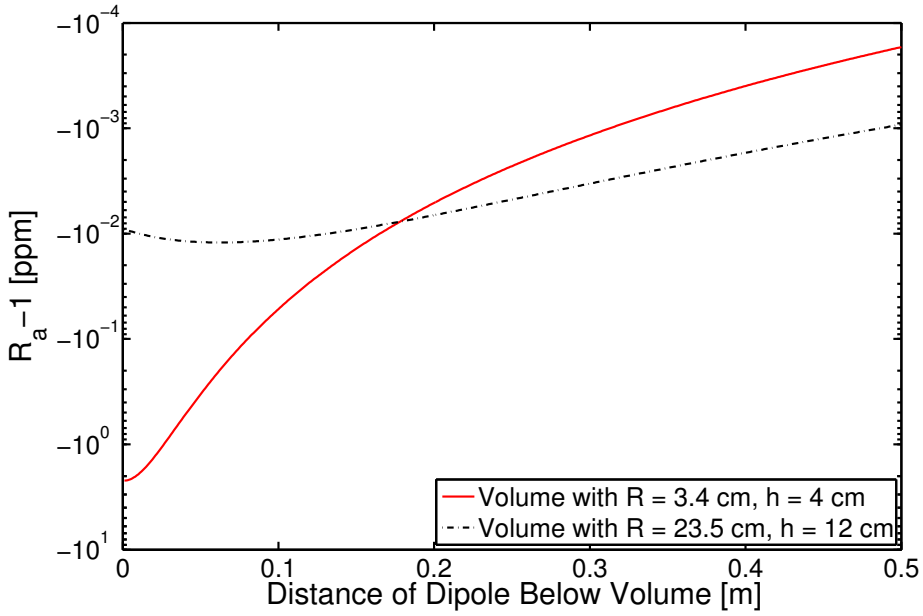

(ii)

Figure 3.14.: Shift of the value R_a due to a dipole below the storage volume for the two cases of (i) parallel dipole and main field direction and (ii) anti-parallel dipole and main field direction. The strength of the dipole amounts to $\mu_0 m = 10^{-13}$ T/m^3.

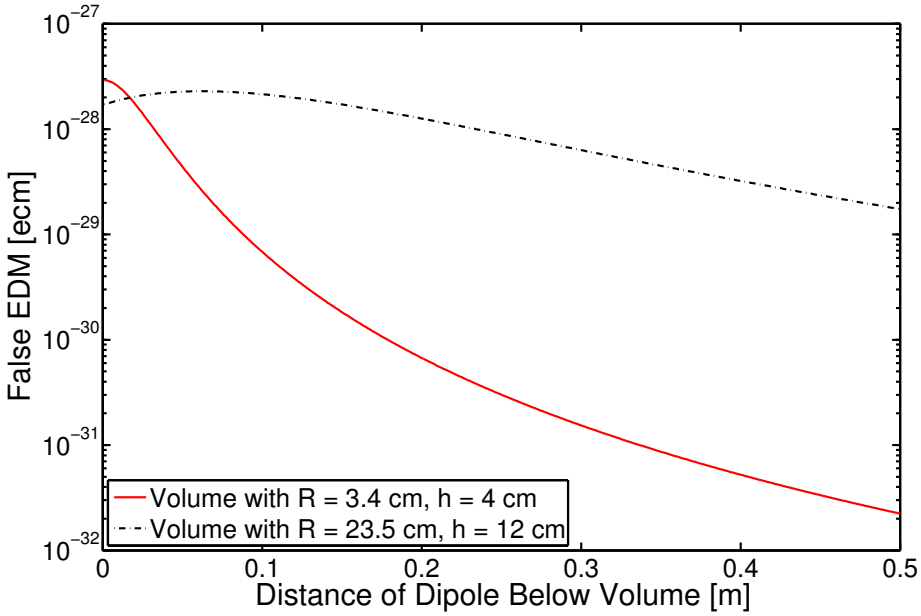

Figure 3.15.: Resulting false EDM due to a dipole field stemming from the differential shift in R_a for B-field up or down. The values have been weighted by their volume fractions $\frac{V_i}{V_1+V_2}$. The strength of the dipole amounts to $\mu_0 m = 10^{-13}$ T/m^3. For more details see text.

(ii) A dipole of strength $\mu_0 m = 10^{-13}\,\mathrm{Tm}^3$ located on or near the surface of the door cavity volume. One has the geometric phase contributions from the door cavity volume and the main volume amounting to approximately $5\times10^{-28}\,e$cm and $1\times10^{-27}\,e$cm (see Fig. 3.13) and the contributions from the differential R_a shift for the two volumes of $3\times10^{-28}\,e$cm and $2\times10^{-28}\,e$cm (see Fig. 3.15), respectively. In total this false effect amounts to:

$$d_f \approx (0.5+1+0.3+0.2)\times10^{-27}\,e\mathrm{cm} \approx 2\times10^{-27}\,e\mathrm{cm} \tag{3.36}$$

With the available equipment at PSI and at the Physikalische-Technische Bundesanstalt (PTB) Berlin, it is possible to scan all relevant parts with a sensitivity to dipoles of $0.5\times10^{-14}\,\mathrm{T\,m}^3/\mu_0$ (resolution of about 10 pT in 3-4 cm) before placing them into the apparatus. As the contributions scale linearly with the dipole strength, this will result in a maximal false EDM effect of $\pm0.1\times10^{-27}\,e$cm for a dipole in the door cavity (systematic effect no. 1) and of $\pm0.4\times10^{-27}\,e$cm for a dipole located on the surface of the main volume (systematic effect no. 2).

3.4.5. Quadrupole Fields (No. 3)

Figure 3.16 shows the comparison of a quadrupolar field as described by the full formula and a simplification as given by

$$B_{xy} = q\begin{pmatrix}-x\\ y\end{pmatrix}. \tag{3.37}$$

The average relative agreement is of the order 1% if the poles of the quadrupole are located 5 times further away than the area investigated. For the further elaborations, the simplified description of the quadrupolar field will thus be used.

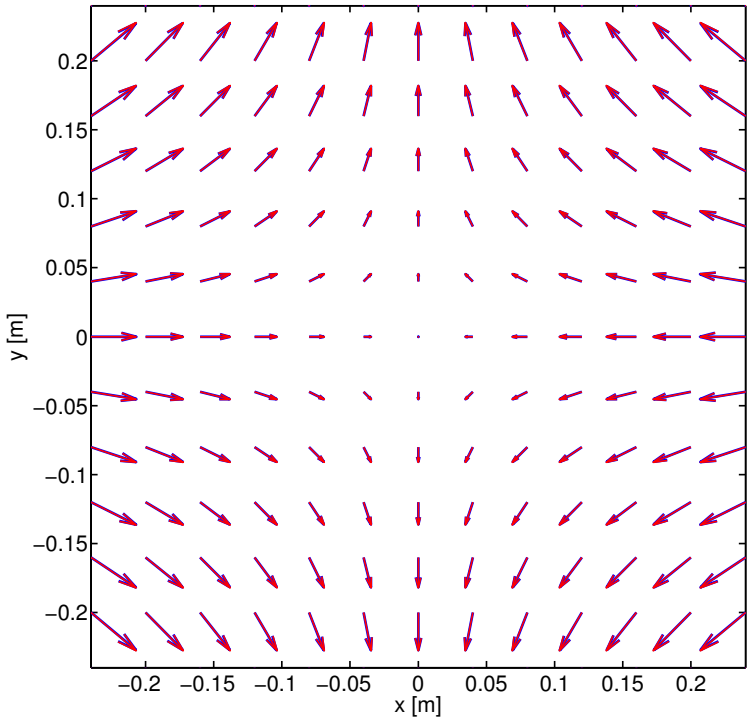

Figure 3.16.: Comparison of the mathematical description of a quadrupolar field. In blue is the full description of a quadrupolar field, whereas superimposed in red is the simplified description as given in Eq. (3.37). The blue arrows are drawn twice as thick as the red ones.

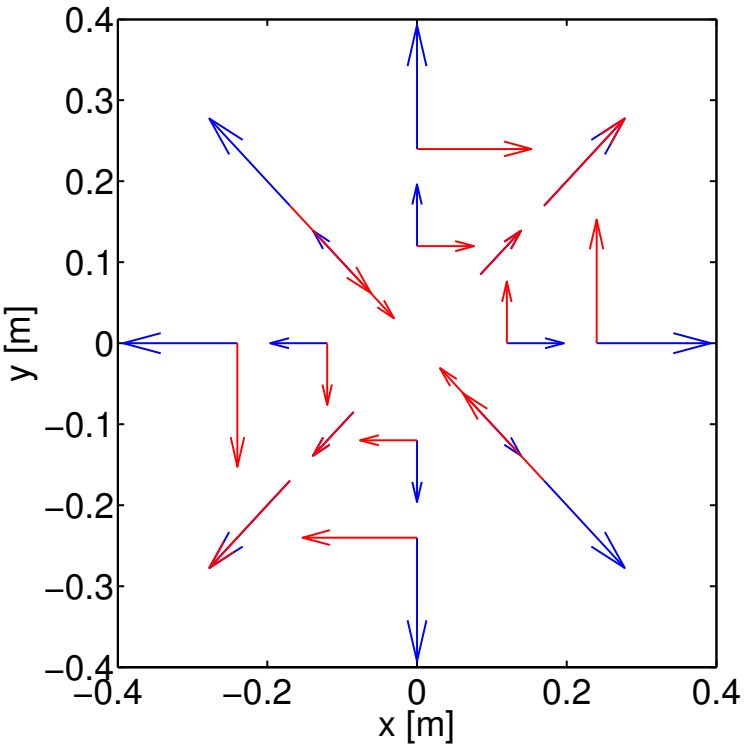

Figure 3.17.: B_{xy} field components for various positions on two radii from a gradient $\frac{\partial B_{0z}}{\partial z}$ (blue) and from a quadrupolar field (red). See also Eq. (3.40).

As the Hg will average out the B_{xy} components of the quadrupolar field due to their velocity whereas the neutrons will not, the ratio R_a of the two precession frequencies will be shifted (assuming a constant quadrupolar field over the storage volume) due to the Ramsey-Bloch-Siegert shift (see Appendix A.3 and Eq. (3.20)):

$$R_a = \left| \frac{\omega_n}{\omega_{Hg}} \frac{\gamma_{Hg}}{\gamma_n} \right| = 1 + \frac{q^2 R^2}{4 B_0^2} \tag{3.38}$$

R denotes the radius of the storage chamber and B_0 the main field. For values $qR = 1\,\mathrm{nT}$ and $B_0 = 1\,\mu\mathrm{T}$ the shift amounts to $\frac{1}{4}$ ppm independent of main field direction or quadrupole orientation (around the main field direction).

Due to the fact that the quadrupole does not introduce any gradient in the main field direction $\frac{\partial B_{0z}}{\partial z}$ (or equivalently the radial field components B_r are averaged to 0 over the volume), there will be no false effect stemming from geometric phases. However, a false effect can occur if one evaluates the neutron EDM at the crossing point in the presence of differential shifts in R_a (see Sec. 2.2.5). Thus changes in the quadrupole field strength q for B-field up and down will introduce a false effect.

The strategy to counter this effect lies in its direct measurement using the Cs magnetometers and possibly additional trim coils to cancel such quadrupolar fields.

Due to geometric imperfections and misalignment, the B_{xy} components measured by the Cs magnetometers will be given by:

$$B_{xy}^{meas} = B_{xy}^{true} \pm 10^{-3} B_0 \tag{3.39}$$

Thus the absolute sensitivity to transversal fields will be in the order of 1 nT, whereas the differential sensitivity to trace changes in the B_{xy} fields will be in the order of 100 pT (assessing conservatively the expected signal to noise of the Cs magnetometers) if the stability of B_0 is less than 10 nT [75].

The measured B_{xy} will have two major contributions. One from gradients in the main field $\frac{\partial B_{0z}}{\partial z}$ and the second from the quadrupolar fields[3]:

$$B_{xy}^{meas} = -\frac{1}{2}\frac{\partial B_{0z}}{\partial z}\begin{pmatrix} x \\ y \end{pmatrix} + q\begin{pmatrix} y \\ x \end{pmatrix} \tag{3.40}$$

Comparing the measured B_{xy} field at two positions on the same radius separated by 90 degree allows an assessment of the quadrupolar field strength. Taking the difference of the first B_{xy} vector with the second vector turned by 90 degree leaves only the quadrupole contribution (see Figure (3.17)):

$$B_{xy}^{meas,1} - \mathrm{Rot}\left(\frac{\pi}{2}\right) B_{xy}^{meas,2} = -\frac{1}{2}\frac{\partial B_{0z}}{\partial z}\begin{pmatrix} r \\ 0 \end{pmatrix} + q\begin{pmatrix} r \\ 0 \end{pmatrix} + \frac{1}{2}\frac{\partial B_{0z}}{\partial z}\begin{pmatrix} r \\ 0 \end{pmatrix} - q\begin{pmatrix} -r \\ 0 \end{pmatrix} = 2q\begin{pmatrix} r \\ 0 \end{pmatrix} \tag{3.41}$$

Using the available Cs magnetometers, a measurement of the absolute quadrupole field with a sensitivity of 1 nT and changes thereof with a sensitivity of 100 pT seems thus feasible. This allows to measure and correct changes in $R_a - 1$ due to quadrupolar fields with a sensitivity of 0.03 ppm. Using the measured value for the slope k in Eq. (3.34) of $1.9 \times 10^{-26}\,e\mathrm{cm/ppm}$ [26], this translates into a systematic uncertainty for false effects due to differences in quadrupolar field strength of $\pm 6 \times 10^{-28}\,e\mathrm{cm}$.

[3] The description of the quadrupolar field by $q\binom{-x}{y}$ or $q\binom{y}{x}$ is equivalent for the purpose of this analysis.

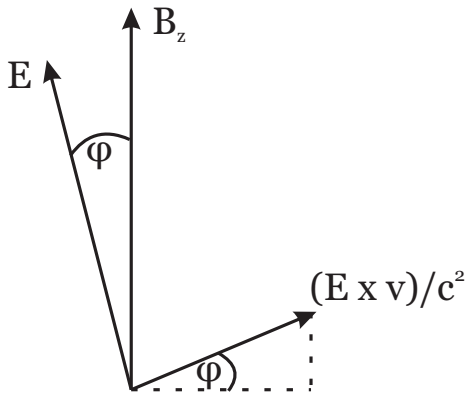

Figure 3.18.: Electric and magnetic fields tilted by an angle ϕ and the corresponding component of the motional field $B_v = \frac{\boldsymbol{E}\times\boldsymbol{v}}{c^2}$ in the direction of the main field direction.

3.4.6. $\boldsymbol{v}\times\boldsymbol{E}$ TRANSLATIONAL (NO. 4)

If the volume averaged directions of the electric and magnetic field are not exactly parallel but are tilted by an angle ϕ, any ordered, translational motion of the center of mass of the UCN ensemble will lead to magnetic fields in the main field direction B_z (see Fig. 3.18). In the case of parallel (antiparallel) E and B field, the resulting field strength is thus given by

$$B \approx B_z \pm \sin\phi \frac{\boldsymbol{E}\times\boldsymbol{v}}{c^2}. \tag{3.42}$$

This leads to a false EDM signal via

$$d_f = -\frac{\hbar}{4E}\Delta\omega = \frac{\hbar}{4E}\gamma_n(B_{\uparrow\uparrow} - B_{\uparrow\downarrow}) \tag{3.43}$$

Assuming a tilt angle ϕ as large as 5° and a translational upwards movement of the centre of mass as large as 1 mm due to low energy heating over the course of the measurement period (150 s), this results in a false EDM signal of $d_f \approx \pm 4\times10^{-29}\,e$cm.

3.4.7. $\boldsymbol{v}\times\boldsymbol{E}$ ROTATIONAL (NO. 5)

Any transversal electric field components E_t together with a net rotational flow of the UCN ensemble around the storage chamber with velocity v_r will create finite B_z fields that change sign upon HV reversal. The corresponding false effect on the neutron measurement will be given by

$$\begin{aligned} d_f &= -\frac{\hbar}{2E}\left(\omega^{\uparrow\uparrow} - \omega^{\uparrow\downarrow}\right) \\ &= -\frac{\hbar}{2E}\frac{v_r\gamma_n}{c^2}\left(E_t^{\uparrow\uparrow} - E_t^{\uparrow\downarrow}\right). \end{aligned} \tag{3.44}$$

Electric field simulations gave average transversal fields of strength $E_t \sim \frac{1}{30}E$ with E being the total electric field strength [50].

Any net rotational flow acquired during filling will be damped during storage due to diffuse scattering at the walls. Typical values for the diffuse scattering probability

are between 5 and 10% leading to typical decay times τ of such ordered motion of $\frac{1}{\tau} = 5\% f_c \sim 1\,\mathrm{s}$ with f_c being the wall collision frequency of roughly 20 Hz (see Table 5.2). Due to this damping any initial rotational velocity v_r^{ini} stemming from the filling process will be reduced significantly. After the closing of the UCN shutter, 2 s of filling Hg and 2 s of Hg $\frac{\pi}{2}$-flip follow. The reduction factor during that time amounts to: $e^{-4\,\mathrm{s}/\tau} \sim 0.02$. During the precession time T of 130 s any net flow is further average out, leading to a reduction of $\frac{\tau}{T} \sim 0.008$. The emptying and filling time of the apparatus amounts to approximately 10 s. Therefore during the last 2 seconds of the filling, which lasts for 40 s, approximately 20% of the UCN are exchanged and contribute directly with the above reduction factors while the other 80% have still further suppressed net motion. The final false effect is thus given by

$$d_f = 0.2 \times 0.02 \times 0.008 \times 4 \times 10^{-24} \frac{v_r^{ini}}{1\,\frac{\mathrm{m}}{\mathrm{s}}}\, e\mathrm{cm} \approx 1 \times 10^{-28} \frac{v_r^{ini}}{1\,\frac{\mathrm{m}}{\mathrm{s}}}\, e\mathrm{cm}\,. \tag{3.45}$$

Thus even for initial rotational ordered motion with velocities as high as $1\,\frac{\mathrm{m}}{\mathrm{s}}$, the corresponding false effect is $d_f = \pm 1 \times 10^{-28}\, e\mathrm{cm}$ and is thus well below the expected sensitivity.

Moreover, any additional delay of the first neutron $\frac{\pi}{2}$-pulse after the closing of the neutron shutter will reduce this effect even further.

3.4.8. Second Order $\boldsymbol{v} \times \boldsymbol{E}$ (No. 6)

The motional field $B_v = \frac{\boldsymbol{E} \times \boldsymbol{v}}{c^2}$ will lead to an increased field strength

$$B = \sqrt{B_z^2 + B_v^2} \approx B_z + \frac{B_v^2}{2B_z} \tag{3.46}$$

which depends on the square of the electric field strength and will thus not directly lead to a false EDM signal. However, if the electric field strengths for the two field directions are not exactly equal - let us assume a difference as large as $\Delta E = 0.1E$ - then this will lead to a shift in the precession frequency of

$$\Delta\omega = -\gamma(B_{\uparrow\uparrow} - B_{\uparrow\downarrow}) = \gamma \frac{v_{xy}^2}{2B_z c^4}(E_{\uparrow\uparrow}^2 - E_{\uparrow\downarrow}^2)\,. \tag{3.47}$$

Assuming an electric field strength of $E = 130\,\mathrm{kV}/12\,\mathrm{cm}$, a magnetic field $B_z = 1\,\mu\mathrm{T}$ and velocity $v_{xy}^2 = \frac{2}{3}v^2 = 6\,\mathrm{m}^2/s^2$, this leads to a false EDM signal of $d_f \approx \pm 1 \times 10^{-29}\, e\mathrm{cm}$.

4 VELOCITY DEPENDENT UCN DETECTION

4.1. INTRODUCTION

As described in Section 3.4, one of the limiting systematic effects in nEDM measurements today are the so called geometric phase effects. They arise through the combination of a field gradient of the static magnetic field with the motional magnetic field $\boldsymbol{B}_v = (\boldsymbol{E} \times \boldsymbol{v})/c^2$ experienced by the ultracold neutrons during their storage time [57, 62, 63, 64]. Their magnitude scales with the magnetic field gradient $\partial_z B_{0z}$, the magnetic field B_{0z} and the velocity v of the neutrons:

$$d_{fn} \propto \frac{\partial_z B_{0z}}{B_{0z}^2} v^2 \tag{4.1}$$

A way to directly observe this effect in a measured EDM is to measure the EDM as a function of velocity, i.e., by measuring the velocity of the UCN. Apart from the above geometrical phase effect, more systematic effects depending on the neutron velocity are known (described in Section 3.4) and even more might be discovered while experiments are pushing towards a sensitivity of 10^{-28} $e$cm.

As the detection of a UCN can only be accomplished by an absorption process with the release of sufficient energy (of the order MeV), any information on the kinetic energy of the UCN (of the order 100 neV) is lost. Typical reactions used for this purpose are:

$$^{10}\mathrm{B} + n \rightarrow {}^{7}\mathrm{Li} + \alpha + 2.3/2.8\,\mathrm{MeV} \tag{4.2}$$

$$^{6}\mathrm{Li} + n \rightarrow {}^{3}\mathrm{H} + \alpha + 4.8\,\mathrm{MeV} \tag{4.3}$$

$$^{3}\mathrm{He} + n \rightarrow {}^{3}\mathrm{H} + p + 0.8\,\mathrm{MeV} \tag{4.4}$$

$$\tag{4.5}$$

A measured pulse height spectrum of a detector using the boron reaction (Eq. (4.2)) is shown in Fig. 4.1. The two different α peaks stemming from the two different reaction energies (94% of the reactions end up in an excited state of lithium) are clearly visible.

Therefore, any information on the UCN energy has to be obtained beforehand by sorting out the UCN according to their velocity (with according losses). Commonly used techniques so far [9, 11] are shown in Fig. 4.2 and shortly described here: (i) Time-of-flight spectrometry using choppers, (ii) transmission through foils with different Fermi potentials as cut-offs, transmission through an absorbing gas at different pressures, or transmission through magnetic fields of different strengths, (iii) rotatable "inverted-U" shaped UCN guide going up and down against gravity, (iv) UCN absorbers at different heights and (v) measurement of the reach in the gravitational field for highly collimated beams. All of these rely on selecting only a small portion of the available UCN to extract the velocity. So far however, no efficient (which is a necessity in a EDM experiment) way of determining the velocity of UCN is known.

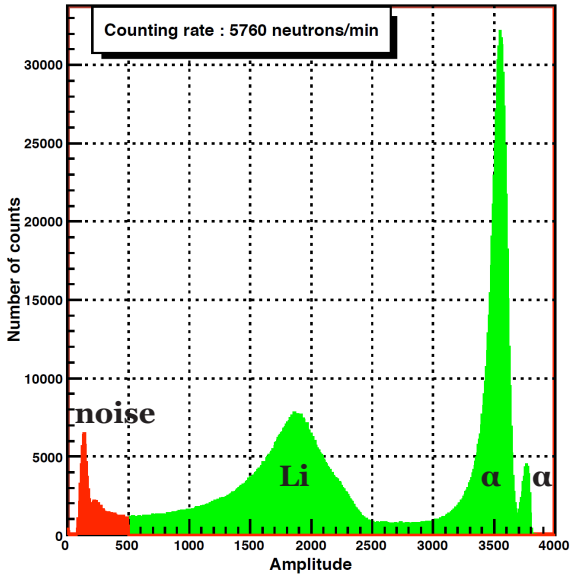

Figure 4.1.: Pulse height spectrum of a UCN detector using ^{10}B as an absorber. One can clearly see the two different α peaks at the right hand side of the the amplitude spectrum stemming from the two different reaction energies. Additionally, the electronic noise is seen on the left and the discrimination threshold is marked by the changing colour at an amplitude of ~500. As the amplitude distribution stemming from the Li is too broad, the two single peaks from the two different reactions become combined into a single broad peak.

4.2. CASCADE DETECTORS

The ^{3}He detectors widely used in UCN measurements are single channel devices and only capable of handling UCN rates up to a few kHz, which was sufficient in the usual experiments performed at ILL. With the expected increase in UCN density ρ to 1000/cm^3 at the new PSI UCN source and the large diameter UCN guides used (d = 18 cm), one can expect directly at the exits of the beamlines rates R of

$$R = \rho \frac{v}{4} \frac{\pi d^2}{4} \approx 40\,\text{MHz}. \tag{4.6}$$

The factor 1/4 is due to the random directions of the UCN in the guide [76] and thus reduces the velocity v of the UCN in forward direction. In order to cope with these high rates and large diameters, a new UCN detector has been purchased: the Cascade-U detector.

The Cascade-U detectors have been developed by [77]. They rely on the capture of neutrons in ^{10}B (see Eq. (4.2)). A layer of 200 nm of ^{10}B is deposited onto the backside of a 100 μm thick aluminium entrance window. Here, the UCN gets absorbed and the two charged decay products are emitted back to back. Thus, only one of the two charged particles will enter out of the boron layer and into the detection volume. The detection volume is constantly flushed with a gas mixture of argon and carbon dioxide (ranging in mixtures of 70/30 to 90/10). The charged particle will ionise the argon atoms while passing through the gas volume resulting in free electrons.

The electrons in the charge cloud are then accelerated through a so called GEM-foil

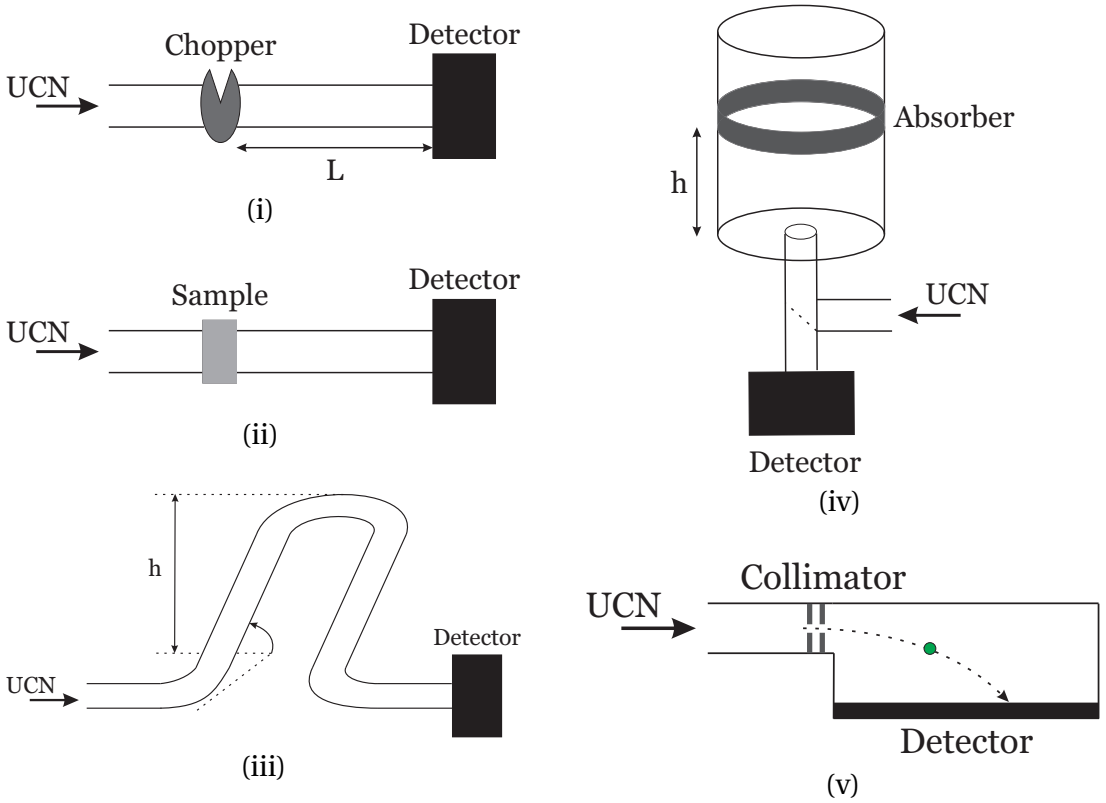

Figure 4.2.: Common techniques to measure UCN velocities. For a short description, see text.

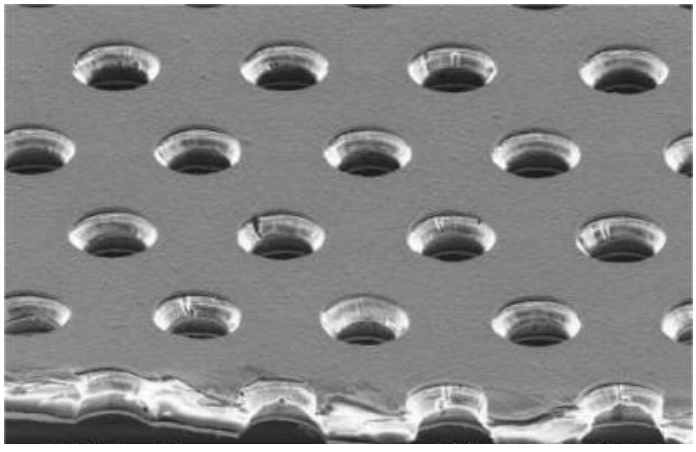

Figure 4.3.: AFM picture of a GEM foil. The diameter of the holes is 70 μm and the holes are separated by 140 μm. The amplification of the electrons is achieved due to the differential voltage applied to the top and bottom side of the foil producing large electric fields inside the holes where the electrons are drifted through. Picture from [78]

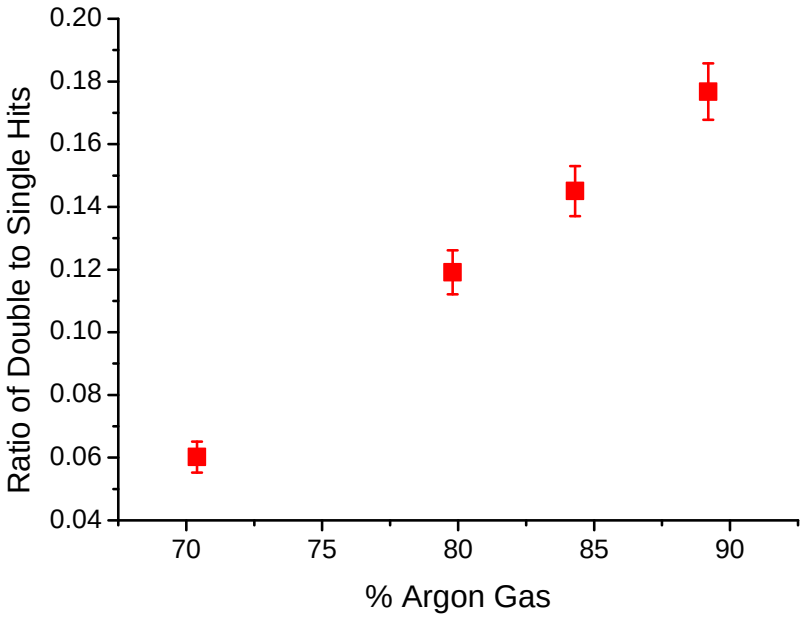

Figure 4.4.: Ratio of double to single pixel hits in the Cascade-U detector as a function of gas composition. Plot from [80].

(gas electrons multiplier) [79]. Fig. 4.3 shows the basic principle of a GEM foil: Applying a differential voltage onto the conducting top and bottom layers - insulated by an insulating material (kapton) - of the GEM foil leads to electric fields that guide the electrons through the holes and at the same time due to the very high electric field in the holes to an amplification of the electrons. In order to control the size of the resulting charge cloud CO_2 is added as a quenching gas. By changing the mixture ratio, the size of the charge cloud can be manipulated. After the GEM foil, the electrons are drifted further onto a pixelised read-out structure.

The charges collected on the different pixels are read out by the so called CIPix chip. It consists of 64 low noise, charge sensitive preamplifiers connected to a discriminator resulting in digital signals sent to the next stage. The data of maximally 4 CIPix are collected and processed by an FPGA mounted on the so called CDR board. The main processing of the incoming data stream is related to a filter algorithm that searches for clusters of firing pixels, which stem from charge clouds being collected by more than one pixel. Figure 4.4 shows the ratio of charge clouds hitting two pixels to charge clouds hitting only one pixel as a function of the amount of argon in the gas mixture. It is nicely visible that as the percentage of argon is increased, the charge clouds and consequently the double hits are increased as well. The CDR board is also responsible for the distribution of the low voltage, the communication with an external PC (via optical fibre link), the storage of the data in an on-board memory and the acceptance of external triggering signals (as, e.g, provided by a chopper in time-of-flight measurements).

The Cascade-U detectors have several advantages over the standard ^{3}He detectors widely used in UCN applications:

- Due to the fact that the detector has a solid converter layer, the counting gases can be flushed through the detector thereby reducing effects of aging and loss of detector efficiency.

- As the detector concept relies on fast electronics coming from high-energy physics, it is a very fast detector. The physical limitation for one CIPix amounts to 10 MHz due to the pulse lengths of the UCN counts. Currently, an upgrade of our detector is under way to being able to record a total of 40 MHz. This detector will be used to characterise the PSI UCN source once it is coming online.

- The Cascade-U detectors are available with GEM foils of dimension $100 \times 100\,\mathrm{mm}^2$ or $200 \times 200\,\mathrm{mm}^2$. They are thus ideally suited for the 180 mm diameter UCN guides at the PSI UCN source. So far, the standard ^{3}He detectors were usually adapted to ~70 mm diameter.

4.3. PRELIMINARY STUDIES

4.3.1. ZIGZAG DETECTOR

The basic idea behind the Zigzag-detector is shown in Fig. 4.5. UCN from the storage volume fall into a zigzgag-like structure of boxes where each of the boxes holds at its bottom side an entrance window of a certain Fermi potential into a UCN detector. As the UCN is falling down, it gains energy and at the point where its initial kinetic energy plus the gained potential energy are larger than the Fermi potential of the entrance window, it can penetrate into one of the detectors. The detector has been simulated using GEANT4UCN [81] and one of the results is shown in Fig. 4.5. The parameters in the simulation were 9 zigzag-boxes with Fermi potentials to the detectors of 220, 230, 240, 250, 200, 210, 220, 230, 50 neV and an overall diffusivity of 80%. In the following, I summarise the basic pros and cons of such a system:

- Pro: Good energy resolution achievable. This is reached by controlling the Fermi potentials of the entrance windows at a level of about 10 neV producing relatively sharp edges for the lower energy cutoffs of the three energy bins and by increasing the amount of zigzag-boxes and increasing the diffusivity sharpening the higher energy cutoff of the three energy bins. After all, there is only a small overlap of about 10% of the UCN in the different energy bins.

- Contra: With the increasing amount of zigzag-boxes and diffusivity, the average time for detection of the slowest UCN is also heavily increased. For the configuration shown in Fig. 4.5, the average time of detection in the lowest zigzag-box amounts to ~50 s. Also for other configurations simulated, the average time was always > 10 s.

- Contra: Again with the increase of the amount of zigzag-boxes and diffusivity, the losses are increased from ~10% up to ~20% for the system shown in Fig. 4.5 and not including slits.

- Contra: Controlling the Fermi potentials at the required level is challenging. If lucky there exists a material with the required potential or otherwise it has to be designed with an appropriate multilayer structure [82].

- Contra: Mechanical construction of the zigzag-boxes is difficult while at the same time minimising the amount of slits in the system.

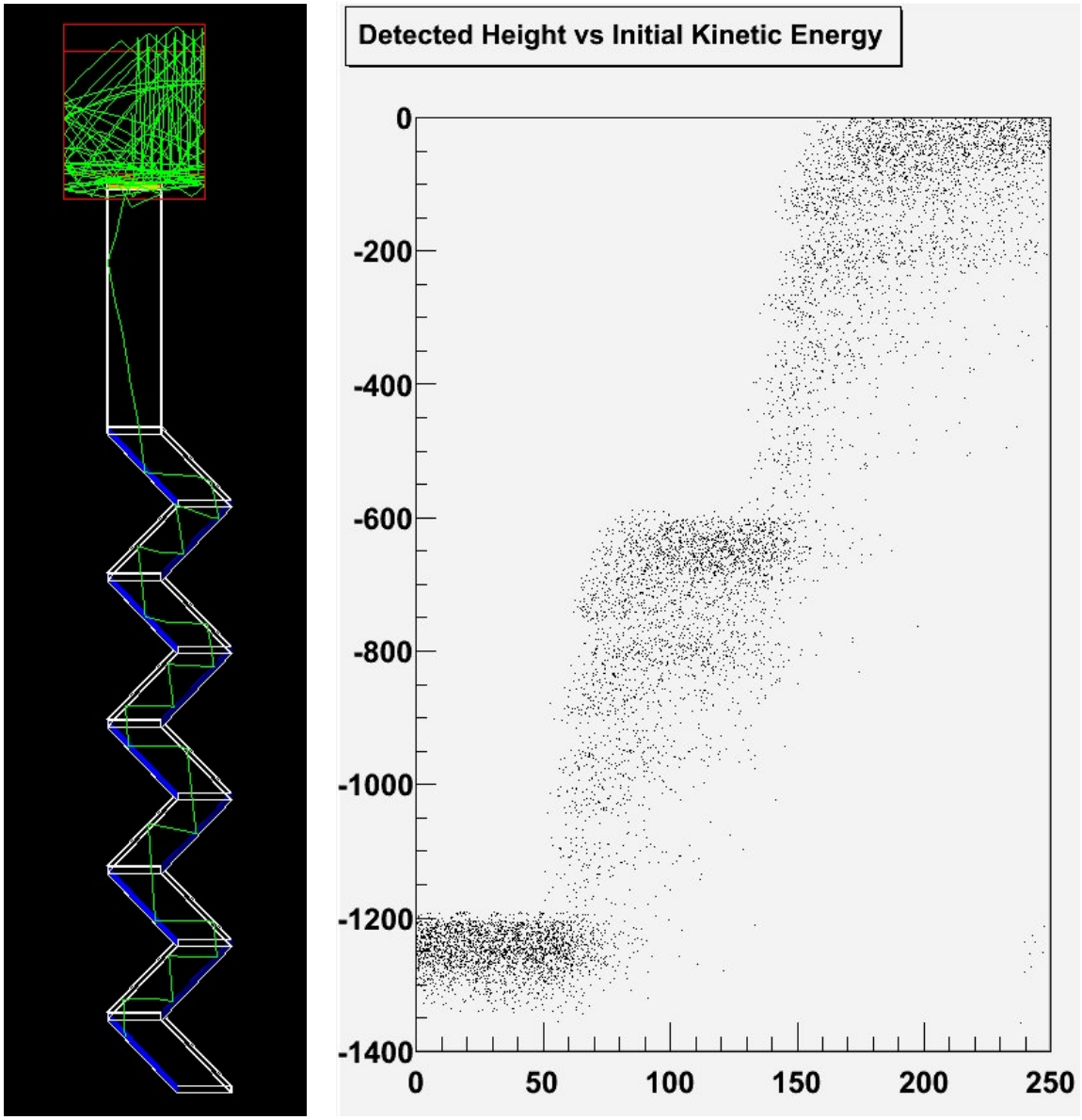

(i) (ii)

Figure 4.5.: (i) Picture showing the working principle of the Zigzag-detector. Below the storage volume, several zigzag-like boxes are placed each with an entrance window of a different Fermi potential leading into a UCN detector. The UCN zigzags down and is detected at the height where its kinetic plus potential energy is large enough to penetrate the window. (ii) Simulated point of detection versus initial kinetic energy for the Zigzag-detector. The detector consists of 9 zigzag-boxes with Fermi potentials 220, 230, 240, 250, 200, 210, 220, 230, 50 neV and an overall diffusivity of 80%.

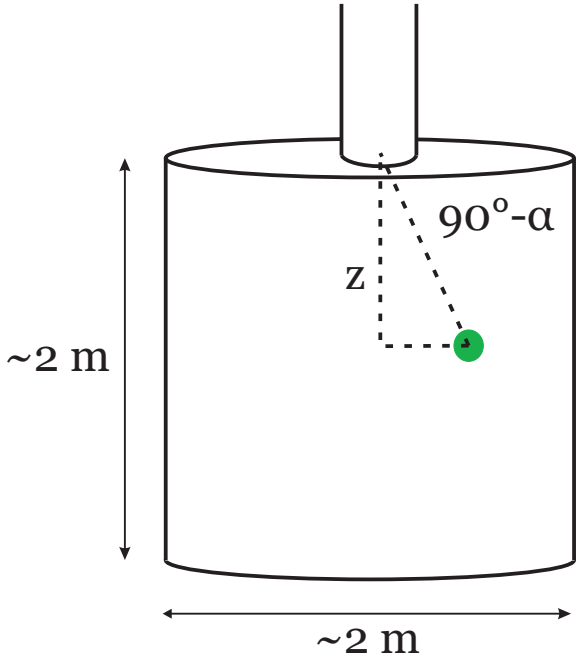

Figure 4.6.: Basic principle of the gas-reach detector. The place of absorption is detected in 3d in a large volume filled with low pressure ^{3}He. From the angular and depth distribution, the spectrum is extracted.

Due to the reasons given above, the study of a Zigzag-detector was not pursued.

4.3.2. GAS-REACH DETECTOR

The basic principle of the gas-reach detector is shown in Fig. 4.6. A large volume filled with a low pressure of ^{3}He of about 1 mbar is used to detect the point of absorption of the UCN. From the depth and the angular distribution of the detected UCN, the spectrum can be extracted.

The point of the absorption is determined by the mean free path length λ of the UCN inside the gas. The probability p of absorption along the path l is determined by [76]

$$\frac{\mathrm{d}p}{\mathrm{d}l} = -\frac{p(l)}{\lambda}. \tag{4.7}$$

The mean free path length is given by $\lambda = \frac{v}{\rho\sigma_{^3\mathrm{He}} v_{\mathrm{therm}}}$ with the UCN velocity v, the density of the ^{3}He atoms ρ, the absorption cross section $\sigma_{^3\mathrm{He}}$ of ^{3}He and the reference velocity v_{therm} of thermal neutrons. Due to the increasing velocity of UCN in the detector volume, λ is not constant but depends on the depth z inside the detector volume and the initial angle α with which the UCN entered the detector volume. While for a straight trajectory, the corresponding ordinary differential equation can still be solved analytically, the solution for a parabolic trajectory has to be calculated numerically. For this, a simulation using Matlab [69] was set up that tracked the trajectory of the UCN in small steps and calculated the point of absorption. The resulting depth distribution is shown in Fig. 4.7 together with the analytic calculation for a straight trajectory of the same initial angle.

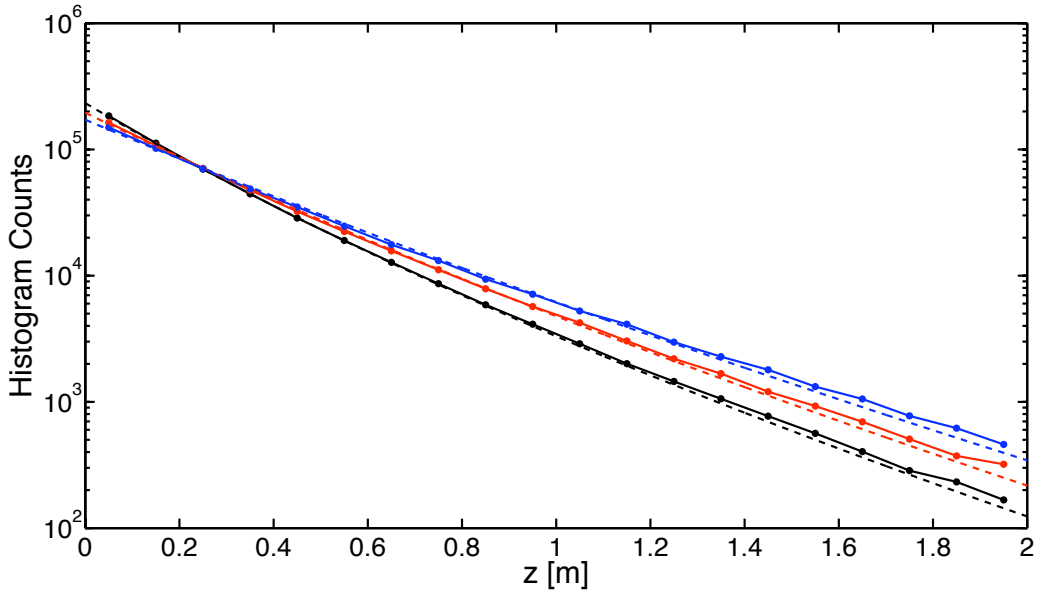

Figure 4.7.: Amount of UCN detected as a function of penetration depth in the gas-reach detector. In blue for an energy of 120 neV, in red for 200 neV and in black for 280 neV. The dashed lines are an analytic calculation for a straight trajectory. In the calculation, a pressure of 0.7 mbar of ^{3}He was used.

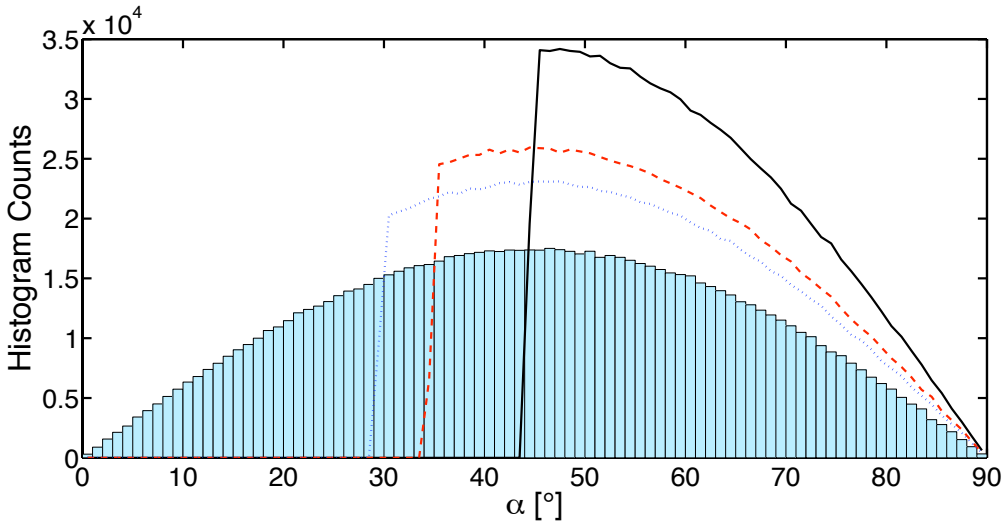

Figure 4.8.: Angular distribution of an initially $\cos\theta$ distributed UCN ensemble after falling a distance of 0.75 m. The initial distribution is shown as a histogram, while the transformed distributions are shown for 80 neV (black, solid line), for 160 neV (red, dashed line) and for 240 neV (blue, dotted line).

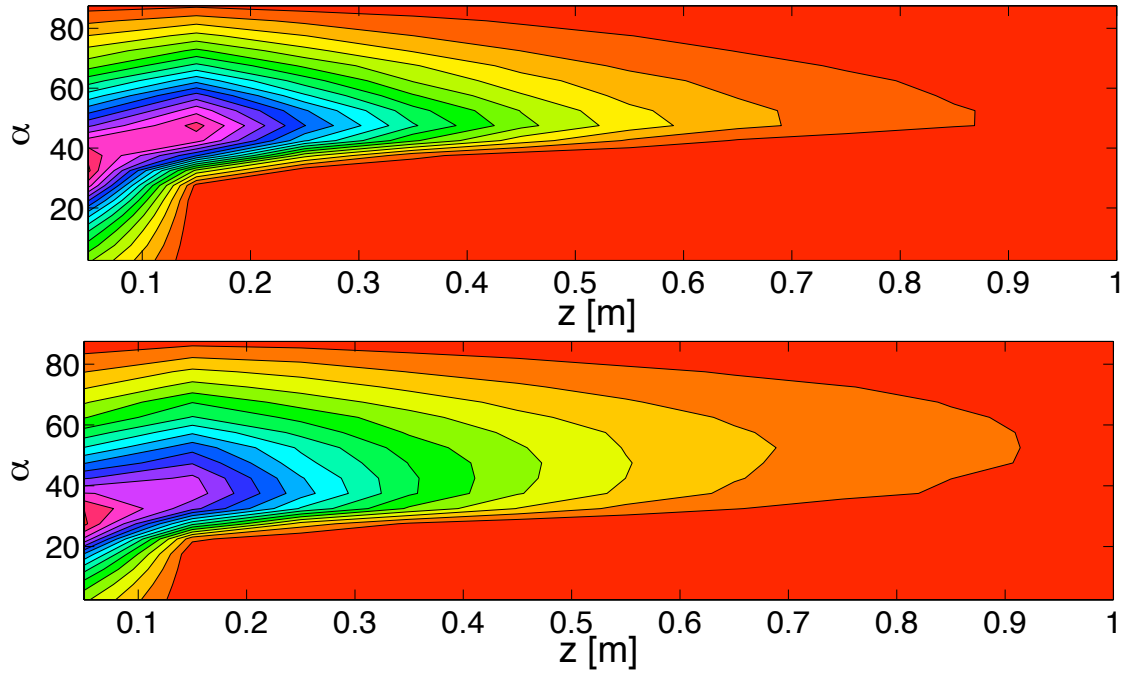

Figure 4.9.: 2d histograms of the positions of absorption given by the depth z and the angle α. The top picture is for an energy of 120 neV while the bottom picture is for 280 neV.

As the UCN are falling down from the storage volume, their angular distribution changes as

$$\sin\alpha = \sqrt{\frac{v_{0,z}+2gh}{v_0+2gh}}. \tag{4.8}$$

Here, α is the angle measured with respect to the normal onto the guide axis, v_0 and $v_{0,z}$ the velocity at the exit of the storage volume and the component in the direction of gravity (and the guide axis), h the falling distance and g the gravitational acceleration. As the angle depends on the initial velocity, the change in the angular distribution is different for different velocities. This is shown in Fig. 4.8. Slow UCN become much more peaked in forward direction than faster UCN.

In the end, the information on the depth and angle of the detected UCN is fed into a 2d histogram as shown in Fig. 4.9. The corresponding histogram can then be fitted using simulated 2d histograms of fixed energies thus obtaining an estimate of the incoming spectrum.

Let me conclude with the pros and cons of such a device:

- Pro: Fast detector and basically no additional loss of UCN compared to a standard UCN detector.
- Pro: Single volume and well understandable and controllable gas dynamics and properties.
- Contra: The amount of UCN needed for a reliable detection of UCN is large as the differences in the 2d histograms are small due to the smearing of the incoming

angles over the guide diameter. The typical amount needed is on the order of 10^6 for a reliable extraction of the spectrum.

- Contra: Challenging to detect the actual position of the absorption process. Apart from ^{3}He a counting gas is needed which should not absorb the UCN itself. For that reason only ^{4}He is suited as a counting gas. The detector has to be built then as a time projection chamber drifting the charge down onto a readout structure. For the timing, one would have to detect the He scintillation light in the extreme ultraviolet.

Due to these reasons, the study of a gas-reach detector was not pursued.

4.4. GRAVITATIONAL SPECTROMETER GRAVISPECTRO

4.4.1. BASIC IDEA AND DIMENSIONS

The basic principle of the gravitational spectrometer Gravispectro is best seen in Fig. 4.10. The UCN enter from the left into a large guide - the main spectrometer guide - which is inclined against gravity. At four different heights, vertical UCN guides attached to the main spectrometer guide lead into conventional UCN detectors. From the distribution of counts over the four detectors, the incoming UCN energy spectrum can then be estimated in up to four energy bins.

The dimensions of the spectrometer were optimised using Monte Carlo simulations with Geant4UCN [81] and adapted to mechanical constraints and possible designs. A detailed listing of the dimensions can be found in Fig. 4.11. In the following, position 1/detector 1 will always refer to the highest position, going down to position 4/detector 4 at the lowest position. Some general remarks:

- The positions of the four detectors have been chosen such as to collect in detector 4 all of the available UCN, in detector 3 UCN with energies higher than ~50 neV, in detector 2 UCN with energies higher than ~100 neV and in detector 1 UCN with energies higher than ~150 neV.

- The incoming UCN beamline is cut at an angle of 45 degree to improve the percentage of UCN reaching into the upper detectors.

- The main spectrometer has to be much larger than the incoming UCN beamline in order to reduce the amount of UCN diffusing back.

- Due to the large spectrometer guide, the vertical guides into the detectors have to be large as well in order to quickly detected all the UCN entering into the spectrometer volume.

- The lowest vertical guide has to be even larger to improve the speed of detecting the lowest energy UCN. This is not equally necessary for the higher vertical guides, because the UCN reaching into those are (i) faster, and (ii) are able to reach more than one detector.

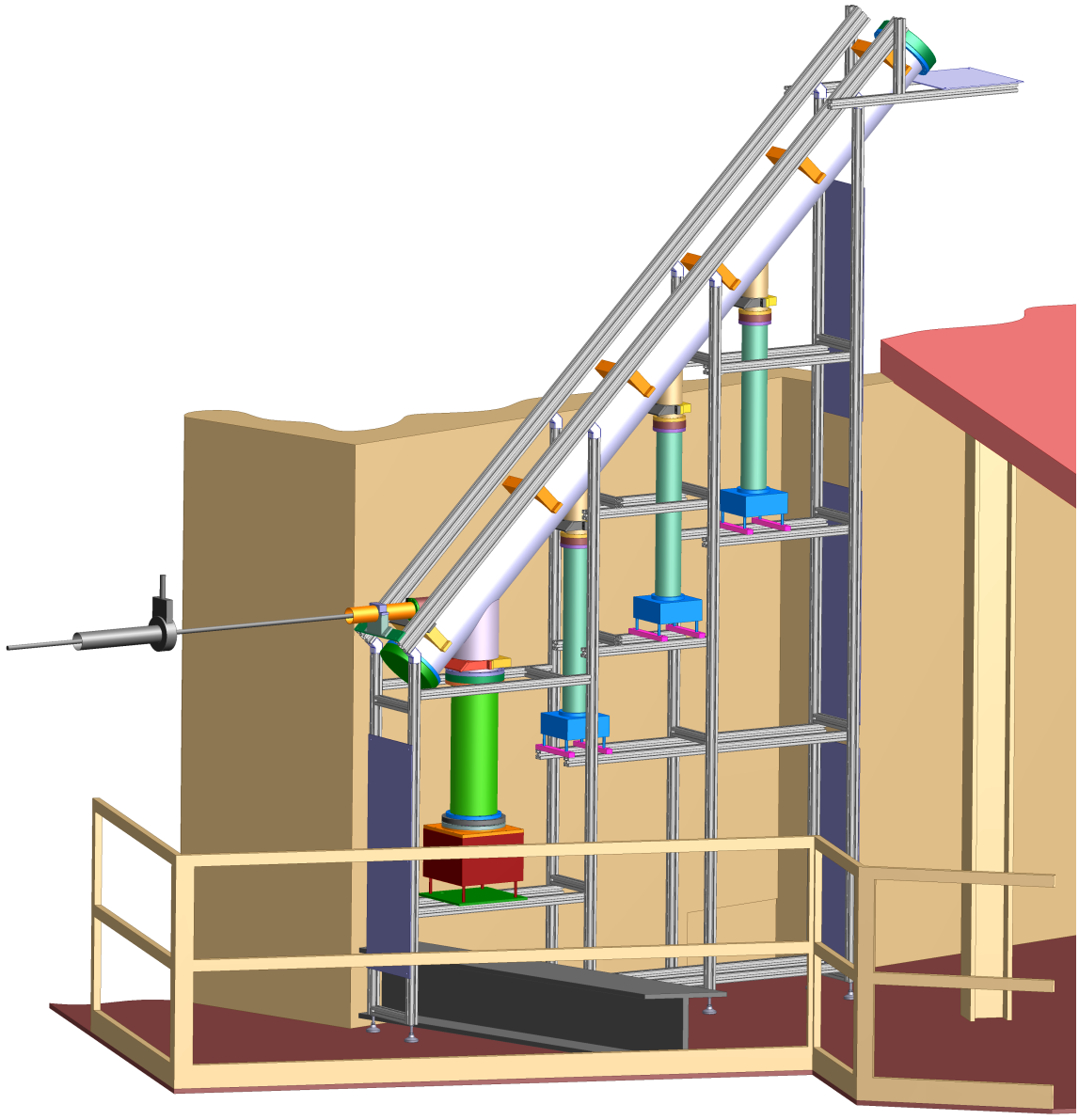

Figure 4.10.: CAD drawing of the gravitational spectrometer Gravispectro. UCN enter from the left into the main spectrometer guide which is inclined against gravity. At four different heights, vertical UCN guides lead to standard UCN detectors thus sampling the energy distribution of the incoming UCN beam.

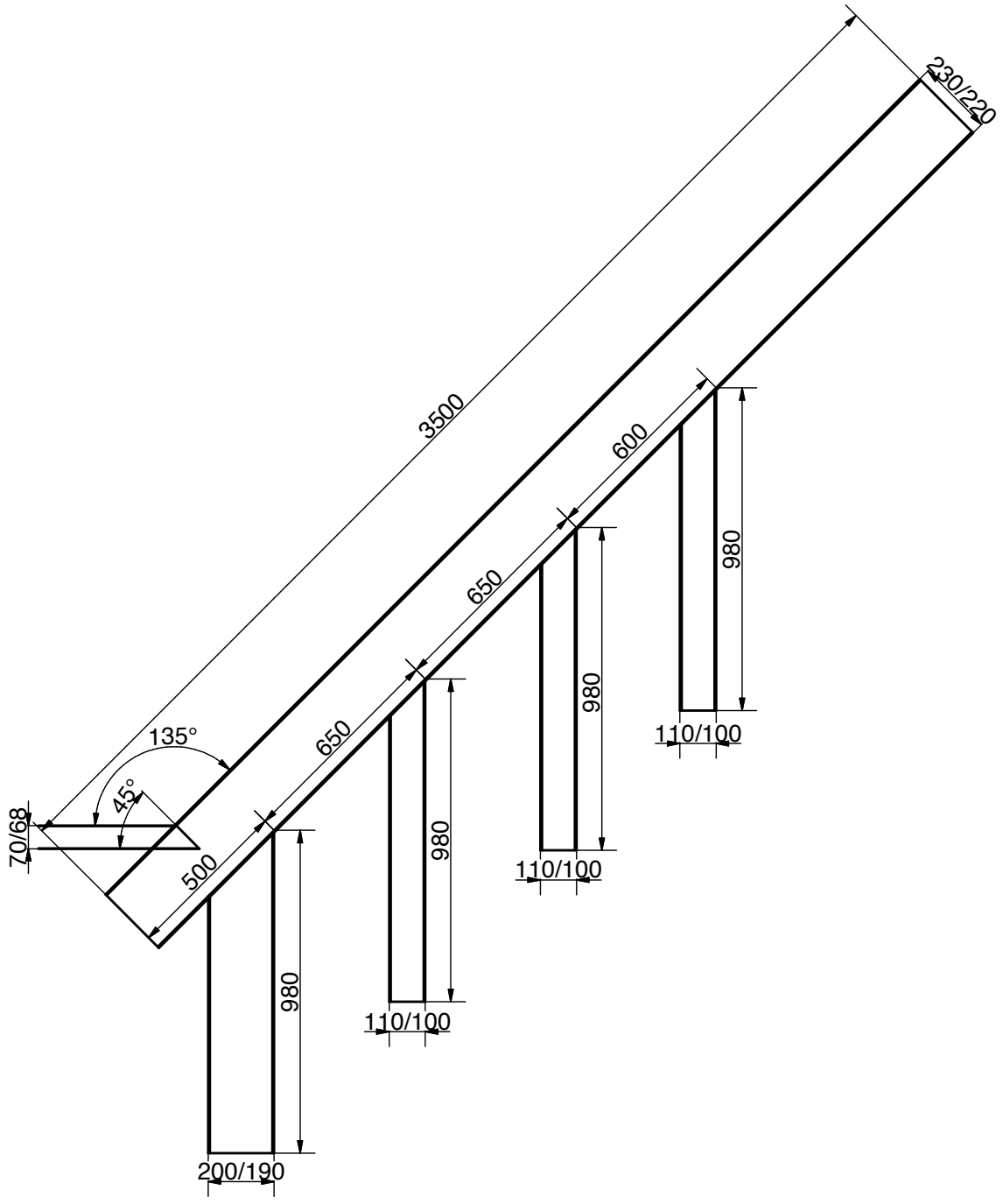

Figure 4.11.: Dimensions of Gravispectro in mm. The dimensions were optimised using Monte Carlo simulations.

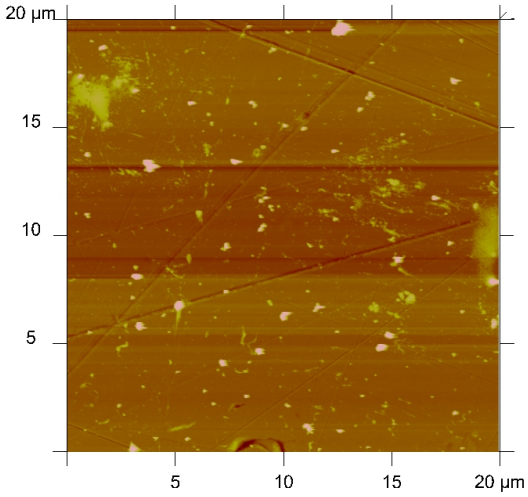

Figure 4.12.: AFM picture of the inside of a plexiglas tube. The lightest colour corresponds to peaks of up to 100 nm and most probably stem from dust particles located on the plexiglas. The typical measured roughness R_a over $10 \times 10\,\mu\text{m}^2$ amounts to 5 nm.

4.4.2. CONSTRUCTION

INCOMING UCN BEAMLINE

The incoming UCN beamline is a standard stainless steel guide from Nocado [83].[1] These are electropolished on the inside resulting in a typical average roughness R_a of about 10 nm measured over areas of $10 \times 10\,\mu\text{m}^2$ by atomic force microscopy (AFM) [84].

SPECTROMETER GUIDES

The guides of the spectrometer are made from Plexiglas® from Röhm [85]. The type of plexiglas used is the so called "Plexiglas® XT", which corresponds to tubes that have been extruded from the liquid plexiglas compound (instead of cast, which would be the other technique used). An AFM picture of the inside of one of these plexiglas tubes is shown in Fig. 4.12. The typical average roughness R_a amounts to 5 nm measured over $10 \times 10\,\mu\text{m}^2$. As such, plexiglas guides should exhibit smaller diffuse scattering than the electropolished stainless steel guides.

The appropriate holes in the large spectrometer guide and the exact shaping of the vertical guides have been crafted by Mecacryl [86]. The shapes of the pieces to be machined are shown in Fig. 4.13. In the machining process the form was first approximately cut out of the plexiglas by sawing and and then the exact form was achieved by slowly grinding the plexiglas to the specifications. After the machining, the plexiglas was put into an oven at around 40 degrees centigrade for several hours to release built up stress in the material.

Before sending the plexiglas tubes off for coating (see below), they were first cleaned using soap water and sponges operated by a drilling machine, then rinsed with normal

[1] These stainless steel tubes are usually used in the milk industry.

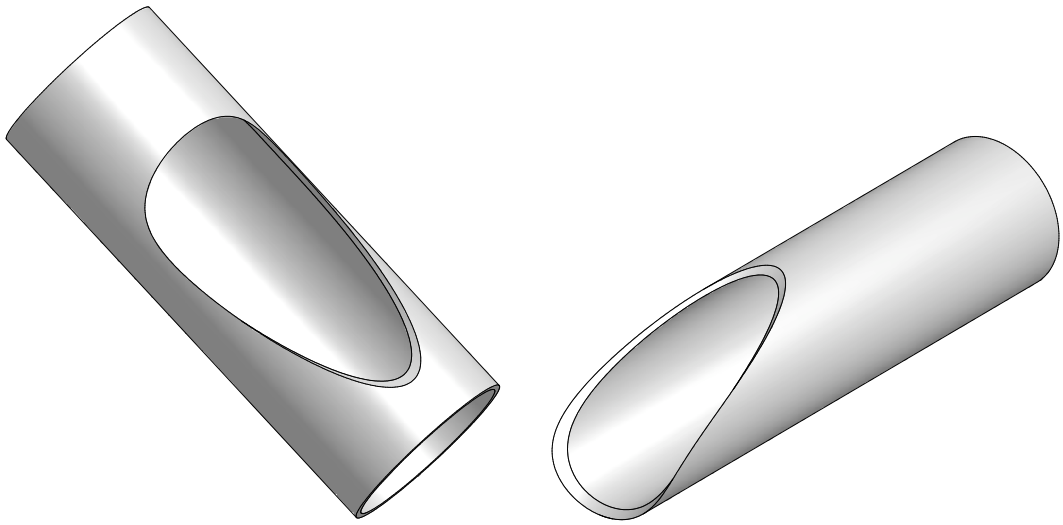

(i) (ii)

Figure 4.13.: CAD models of (i) the holes that had to be machined into the large spectrometer guide and (ii) the corresponding piece needed to adapt the vertical guides to the large spectrometer guide.

and demineralised water and lastly carefully wiped out in a cleanroom using high purity methanol and cleanroom tissues. The goal of this last procedure was to remove all of the dust particles still present on the inside, which would produce holes in the coating. Additionally, an "antistatic gun" was used repeatedly to reduce electrostatic charging of the plexiglas resulting in continuous attraction and sticking of dust particles. The machined holes in the plexiglas tube were then closed by taping Mylar foils over them. The front and end holes were also closed by Mylar foil attached by a special system which could later be opened inside the vacuum chamber of the coating facility once the pressure had dropped down low enough [87].

The plexiglas tubes were coated on the inside with 500 nm of nickel/molybdenum (85%/15% in weight) by S-DH [88] using sputtering. This coating is the standard coating used in the construction of the guides for the PSI UCN source. The mixture of nickel and molybdenum is used to obtain a non-magnetic material and thus an equal Fermi potential for both spin states. The maximal length which can be covered by the sputtering lance amounts to 2 m with a vacuum extension up to 4 m. The large spectrometer guide thus had to be turned in the middle of the coating process. The Fermi potential of the NiMo coating has been measured using cold neutron reflectometry and amounts to 232 ± 10 neV [84]. While the coating of the larger plexiglas tubes went without any problems, there was some damage to the smaller 110/100 mm plexiglas tubes at the inclined end pieces as shown in Fig. 4.14. The damage is most probably due to heating of the plexiglas during the coating process. As the three inclined end pieces showed different degrees of damage (the one shown in Fig. 4.14 being the medium degree of damage), it was decided to mount the one with the least damage at position 1 of the spectrometer, the medium affected one at position 2 and the most affected one at position 3.

The adhesion of the NiMo coating on the plexiglas is not perfect and does not withs-

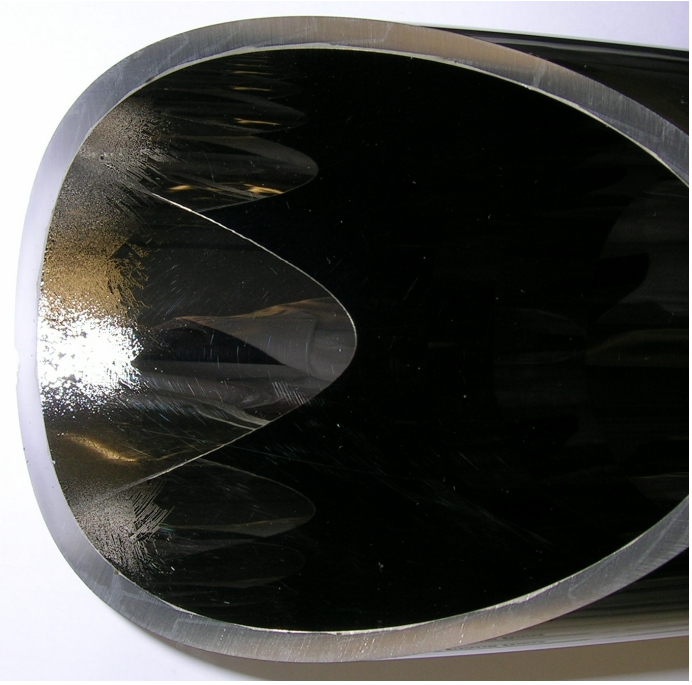

Figure 4.14.: Damage of the coating of the small plexiglas tubes at the inclined ends. The damage is probably due to heating of the plexiglas during the sputtering process.

tand too large mechanical contact[2]. However, spontaneous delamination was never observed and thus NiMo coated plexiglas tubes can be used well as UCN guides if handled with the appropriate care. They even serve as an excellent motif for photographes as shown in Fig. 4.15.

END FLANGES OF THE LARGE SPECTROMETER GUIDE

The end flanges of the large spectrometer guide are machined out of aluminium. The diameter of the opening of the flange corresponds to the outer diameter of the spectrometer guide and thus the larger spectrometer guide resides in the flange with an overlap of 30 mm. The top flange has an additional hole to mount vacuum equipment (ISO 160 standard). While the top flange was left untreated, the lower one was hand polished [90] and afterwards electropolished [91]. After this procedure, the flange was DLC coated by the Fraunhofer Institut Dortmund [92]. Unfortunately, the coating failed and delaminated at several points. The suspicion is that the electropolishing did not sufficiently remove all the remainder of the polishing paste and thus the adhesion of the DLC onto the aluminium was not sufficient. As a substitute, I then used an already existing stainless steel foil which had been first nickel and then DLC coated and placed it at the bottom of the flange (see Fig. 4.16).

[2] As an example, it does not withstand the tape test [89], i.e., it delaminates under the action of taking off an attached tape.

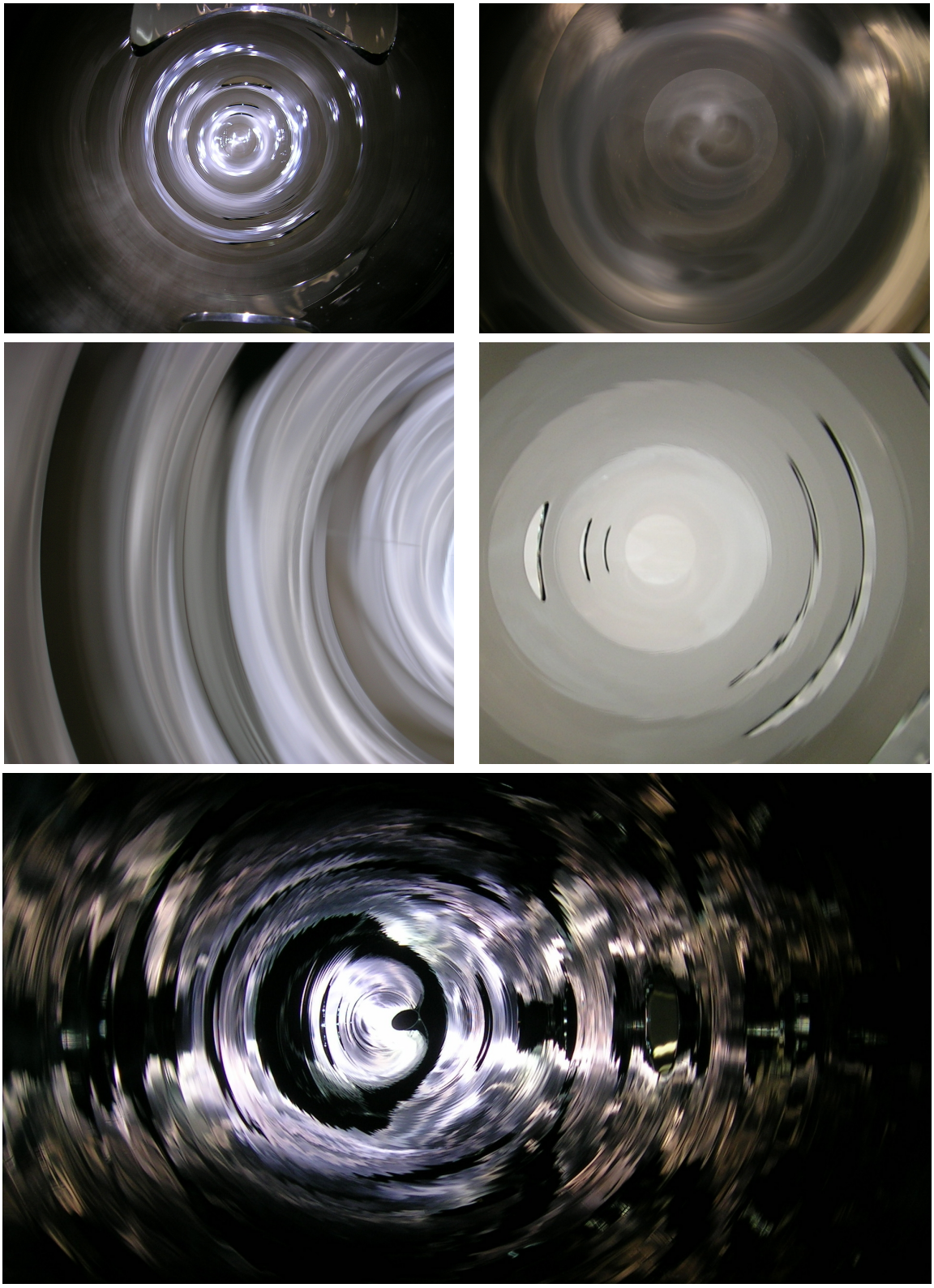

Figure 4.15.: Guide art.

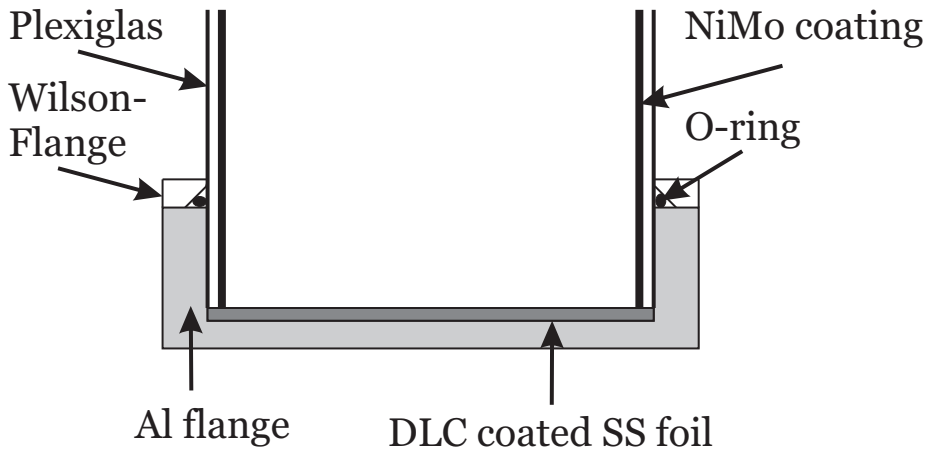

Figure 4.16.: Bottom flange of the large spectrometer guide showing the placement of the inserted DLC coated stainless steel foil and the functioning of a Wilson flange.

VACUUM EQUIPMENT

All of the sealings were done with O-rings. For the ones connected to UCN guides, so called "Wilson-flanges" were used. The principle of these sealings is shown in Fig. 4.16. For the connection of the turbo pump, the ISO standard was followed. Care has to be taken when tightening of the Wilson-flanges to not exert too much force onto the plexiglas tube as this damages the coating.

On the top flange, an adapter from ISO 160 to ISO 100 and an ISO 100 90° degree bend was installed in order to not have to mount the turbo pump upside down. The turbo pump was a standard ISO 100 model used at PSI connected to a roughing pump. Typical pressures achieved were below 10^{-4} mbar throughout the full volume and incoming beamline.

JOINING OF THE PLEXIGLAS GUIDES

After evaluating several different glues, the model Acrifix® 192 from [85] was chosen. It is a special one-component glue for plexiglas, which hardens under UV light. Typical hardening times are 30 min with standard room lightning and down to 10 min under illumination from a UV lamp. Gluing the NiMo coated plexiglas pieces, it was found that for these non-transparent materials the hardening time was greatly increased (a fact that the company [86] also observed for coloured plexiglas). Its vacuum compatibility was tested by the vacuum group at PSI [93]: the outgassing rate was approximately $10^{-7}\,\frac{\text{mbar}}{\text{s}}\,\frac{\text{l}}{\text{cm}^2}$ and thus compatible with UCN applications.

The edges of the plexiglas tubes, where the glue would have to join the large spectrometer guide and the vertical guides, have been covered with sticky tape to avoid the deposition of coating material at these places (see also Fig. 4.14). In order to avoid the leakage of glue into the spectrometer, a small amount of glue was deposited around the hole in the large spectrometer guide using a syringe. Afterwards, the pre-adjusted vertical guide was lowered in its holding frame onto the spectrometer guide and pressed onto the glue. In order to produce a vacuum tight sealing, the joint was then once more covered from the outside with a much larger amount of glue. Figure 4.17 shows

Figure 4.17.: The finished joining of the spectrometer guide and the vertical guides.

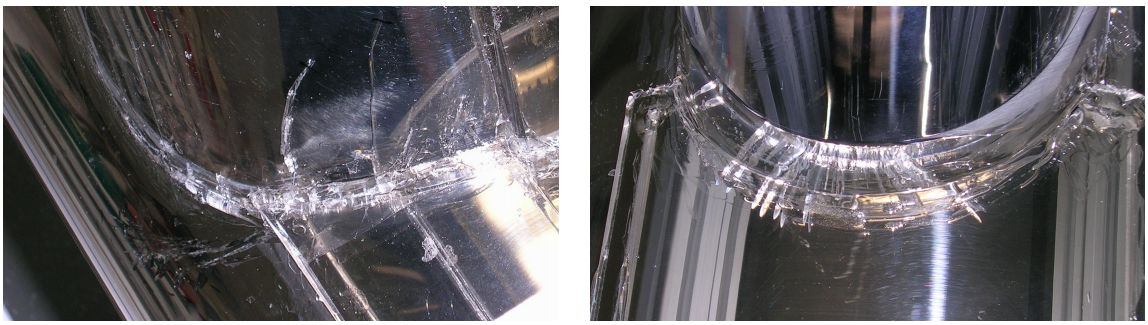

(i) (ii)

Figure 4.18.: Cracks in the plexiglas that formed during evacuation of the spectrometer guide: (i) in the spectrometer guide and vertical guide at the lowest position and (ii) at the position of the incoming UCN beamline.

the completed spectrometer. Also shown in Fig. 4.17 are the large support rings which were glued onto the spectrometer guide to improve its stability, and the small patches of plexiglas glued onto the inclined pieces of the vertical guides to improve the stability at the point where the stress onto the material is highest. For practical reasons, the vertical guides were built in two parts: (i) the first small part with the inclined end, and then (ii) the extension guide resulting in the total length of 980 mm as given in Fig. 4.11.

In order to learn the procedure of the joining of the pieces and the performance under vacuum, a test piece had been manufactured beforehand. The test piece consisted of a shortened version of the spectrometer guide and the attached lowest and largest vertical guide. Naturally, only uncoated plexiglas pieces were used. The test was successful concerning vacuum tightness and stability. It came as quite a surprise then, when growing cracks were discovered in the final large spectrometer guide after evacuation at the place of the attached lowest vertical guide and the incoming UCN beamline (see Fig. 4.18). Maybe, the fact that in the test piece the hole for the incoming UCN beamline had been missing did make the difference in stability. The spectrometer could be saved (thus the smile on my face in Fig. 4.17) by the company that already machined the pieces [86] by manufacturing a jacket around the part which had been affected, thereby essentially doubling and partly tripling the wall thickness to 10 or 15 mm. The pieces of the jacket were then glued onto the existing pieces. Parts of this jacket can also be seen in Fig. 4.18.

UCN DETECTORS

As UCN detector, the Cascade-U detectors acquired from [77] were used. The large Cascade-U 200 (having an active region of $200 \times 200\,\mathrm{mm}^2$) was mounted on the bottom, whereas three smaller Cascade-U 100 (active regions of $100 \times 100\,\mathrm{mm}^2$) where placed at the higher positions. The amount of pixels in the large detector had been reduced to 64 (feeding one pre-amplifier board CIPix). The three smaller detectors were also operated with 64 pixels. They were each equipped with their own CIPix mounted on the backside of them and an additional board changing the TTL-signals, which are sent out by the CIPix, to the LVDS standard (low-voltage differential signalling, better suited over large distances than TTL signalling). The LVDS signals were then fed via SCSI-cables into the electronics of the large detector (at the end of the cables they had to be changed back to

TTL) able to process 256 pixels. The SCSI-cables also provided the required low voltage to the small detectors and had separate lines to send the necessary commands to the CIPix boards. The filtering algorithm of the main electronics searching for clusters of activated pixels in space and time representing one UCN was not adapted. The amount of UCN lost due to that was estimated to be negligible at the expected UCN rates. The readout of the four detectors was started and stopped simultaneously via the main electronics.

For the high voltage, a two channel HV power supply was used. One channel fed the large Cascade detector, whereas the other channel supplied the three little detectors in parallel. The operating voltages were 1400 and 1080 V, respectively. A gas mixture of 80%/20% argon/carbondioxid was used regulated by a digital flowmeter. The detectors were fed by the gas in series.

The aluminium entrance windows of the detectors were reinforced by stainless steel support grids. While the support grid of the large detector has a thickness of 5 mm and an open area of ~89.9%, the support grid for the three smaller detectors has a thickness of 3 mm and an open area of ~93.4%.

Additionally, two standard ^{3}He detectors [94] had been mounted in the incoming UCN beamline. They were operated at a gas mixture of 18/12/1070 mbar of ^{3}He/CO_2/Ar and at high voltages of 1100 and 1000 V. The amplified signals were read using a gated ADC. The readout chain was set up as in [87].

All the detectors were shielded with sheets of pure cadmium (absorption cross section of ~2500 b) of thicknesses 0.5 - 2 mm including extension sleeves over the UCN guides.

4.4.3. MEASUREMENTS

The first test measurements with the spectrometer were conducted at ILL in Grenoble. The setup of the spectrometer at the PF2/TEST beamline is shown in Fig. 4.19. In order to calibrate the system, two additional features were added to the incoming beamline (see Fig. 4.20):

(i) A rotatable U-shaped guide was added in order to reduce the amount of UCN with energies above the Fermi potential of the guide due to its bends and more importantly to provide different lower energy cut-offs to the spectrum. This in order to change the spectrum and see its effects on the count distribution over the four detectors of the spectrometer and, by taking the difference in count rate of two U positions, measure the effect of UCN in the energy interval given by the difference in U heights. Due to the severe space constraints, the U had to be installed in quite a special way compared to the standard installation (see Fig. 4.2). Additionally, the U could not be rotated all the way down into a horizontal position. Fortunately, not only the long arms were available (2000 mm straight arm section, as seen in Fig. 4.20) but also smaller arms (750 mm straight arm section). These could be rotated (to the back in Fig. 4.20) almost all the way down into a horizontal position. With these two different U, heights between 170 and 2300 mm could be covered (with no overlap). The guides used for the 4 bends and straight sections were stainless steel guides from Nocado [83] with outer diameter 76 and inner diameter 73 mm. Adapters made from stainless steel were used to change to the otherwise used diameters of 70/68 mm. Two ^{3}He monitor detectors were installed in front of and after the U. The position of the U was measured by means of a plumb-

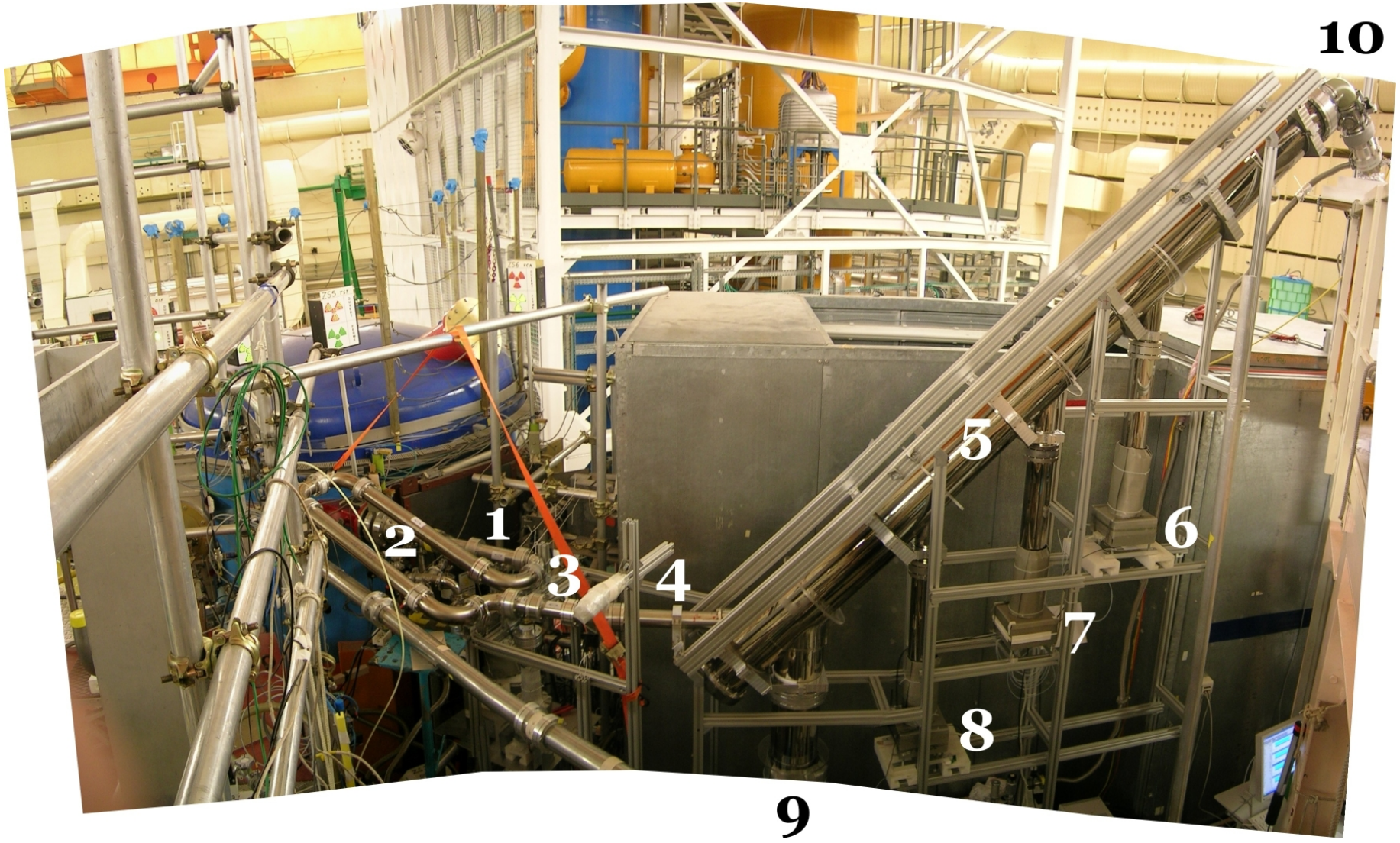

Figure 4.19.: Panorama of the gravitational spectrometer located at the PF2/TEST beamline at ILL, Grenoble. The labels denote: (1) PF2/TES beamline, (2) U-shaped guide used for calibration, (3) gas cell used for calibration, (4) input guide to the gravitational spectrometer, (5) main guide of the spectrometer, (6) - (9) detectors C1 - C4, (10) vacuum equipment.

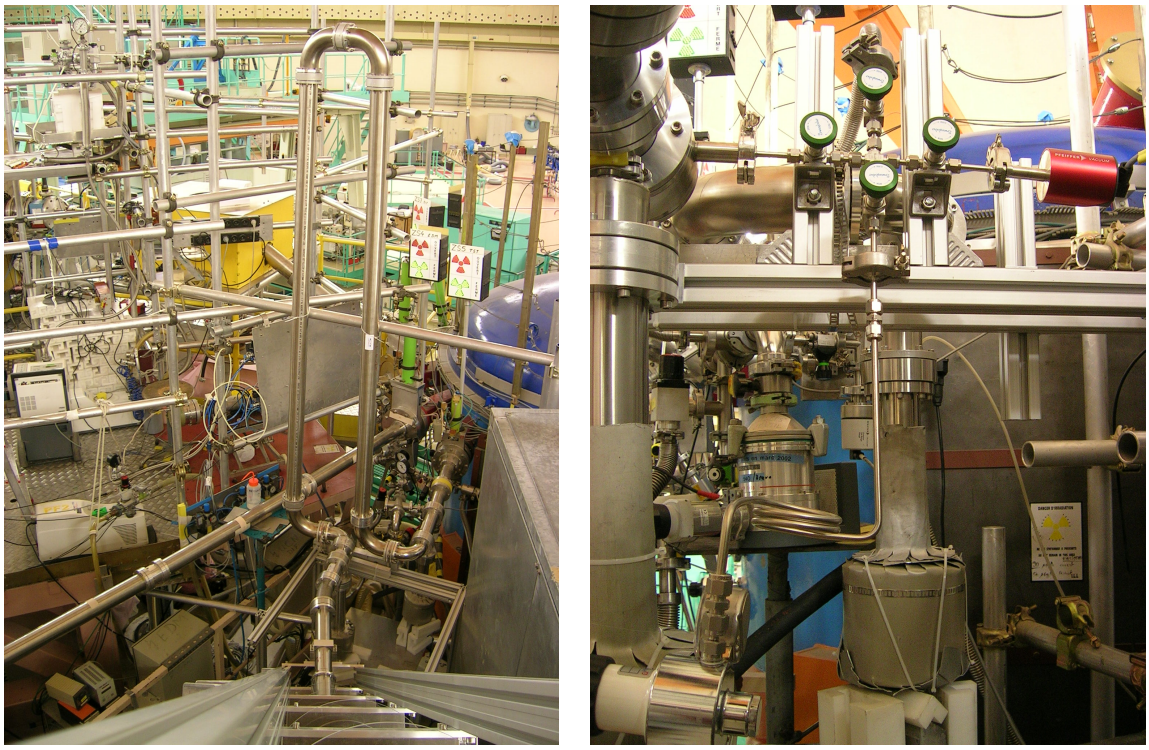

(i) (ii)

Figure 4.20.: Tools used for the calibration of the spectrometer: (i) a rotatable U-shaped guide and (ii) a gas cell through which the UCN have to pass before entering into the detector. The gas cell is located in the top left corner of the picture. Additionally, one can see the two ^{3}He monitor detectors installed in front of the turned down U and behind the gas cell. For more details see text.

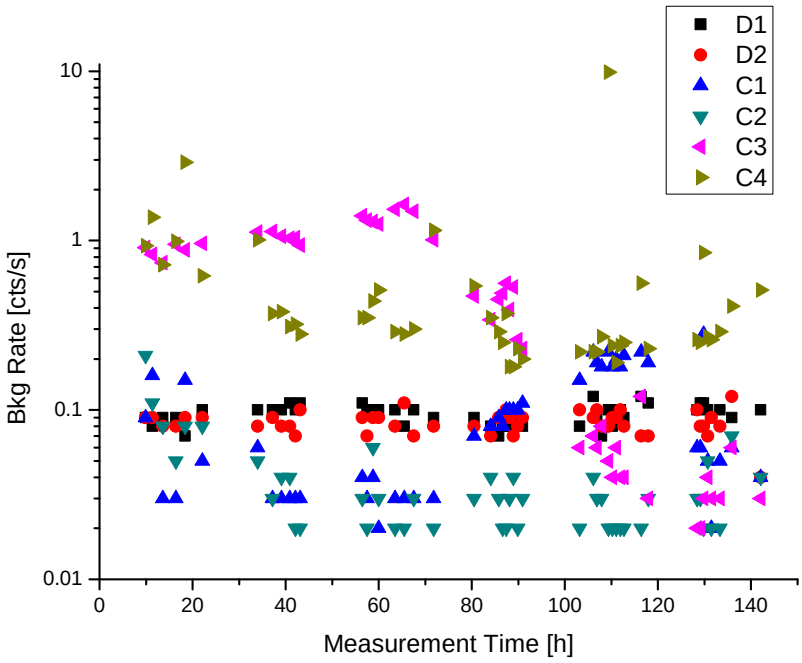

Figure 4.21.: Part of the measured background rates of the two ^{3}He monitor detectors (D1 and D2) and the four Cascade-U detectors (C1-C4). The large fluctuations in the background rates of the Cascade-U detectors are clearly visible compared to the background rates of the ^{3}He detectors.

line attached to the top and the calculated inclination then cross checked by means of a goniometer. The accuracy of the measured heights is approximately 10 mm.

(ii) For parts of the measurements, a gas cell was placed in the incoming UCN beamline and the installed small U turned all the way down. It was made of stainless steel closed in the front and back by 100 μm thick aluminium windows supported on the outside by grids. The support grids were installed to minimise deformation of the cell (and therefore an increase in path length) under pressure. Also visible in Fig. 4.20 is the gas handling system used to evacuate the cell, fill it with different gases at different pressures and the gauge measuring the absolute pressure in a range 0.1 - 1000 mbar (model CMR 361 from [95]). Its value was read out every minute and later combined to the average pressure for a given measurement.

Towards the end of the beamtime, the measurements with the spectrometer were complimented with time-of-flight measurements of the velocity distributions after the U, the gas cell and of the direct beam.

4.4.4. ANALYSIS & SIMULATION

For the following section, I would like to remind that I use the convention that position 1 in the spectrometer and correspondingly detector 1 is the highest one, going down to position 4 and detector 4 at the lowest position.

BACKGROUND

Fig. 4.21 shows a part of the measured rates during separate background runs. For these runs, the vacuum shutter at the incoming beamline had been closed, but otherwise data had been taken as under normal operation. While the two ^{3}He detectors show a constant background of approximately 0.1 Hz, the background rate of the Cascade-U detectors varies drastically. The large Cascade-U 200 detector (C4 in Fig. 4.21) shows variations between 0.2 Hz and up to several Hz. Two of the smaller Cascade-U 100 detectors (C1 and C3) show variations on a similar scale, whereas the fluctuations in the background rate for the third Cascade-U 100 detector is somewhat smaller. Several test lead to the suspicion that this varying noise has been picked up by the cables connecting the three smaller detectors to the electronics of the large one. Especially, the connector pieces combining two 2 m SCSI-cable to a 4 m long cable were very susceptible to noise.[3] During previous operations of the large detector in stand-alone mode, such large fluctuations in the noise level had never been observed.

For that reason, every measurement was preceded and followed by a separate background run lasting for about 10 min. The average count rate of these two measurements were then subtracted. An error of 50% was attributed to this average to allow for the largest observed differences in these two separate background measurements.

NON-STATISTICAL DEVIATIONS IN MEASURED COUNT RATES

Due to the noise problems (as described above) or due to sparks in the detector volume of the Cascade-U detectors, non-statistical fluctuations in the measured count rates occurred. For that reason, all the measurements were recorded as time series. In normal measurements, entries exceeding the average value by 4σ were then discarded. In TOF measurements (see below), entries exceeding the average over the 6 surrounding entries (i.e. 6 ms for the usual time binning of 1 ms) by 5σ were replaced by the average over those of the 6 entries not exceeding the 5σ limit.

MONITOR DETECTORS

The detected count rate in the monitor detectors was relatively modest compared to the ones with the Cascade-U detectors. They amounted to approximately 20 Hz for the detector in front of the U and maximally 40 Hz for the detector after the U (the areas of the holes in the beamline leading to the monitor detectors were different by about a factor 2). From their data, it could be seen that the reactor delivered a constant UCN flux with a variation not higher than 1% over several hours. As this stability is sufficient and as the measured count rates were too small, their data was not used to normalise the measured rates in the spectrometer.

U MEASUREMENTS

Figure 4.22 shows the measured UCN count rates after background subtraction as a function of the U height. Statistical errors are smaller than the shown symbols and amount to 0.1 - 1 Hz depending on detector. The large step at a height of 1100 mm

[3] By delaying the data of the large detector and having the three cables to the small detectors all of the same length, the data stream remained synchronised with respect to the clock cycle.

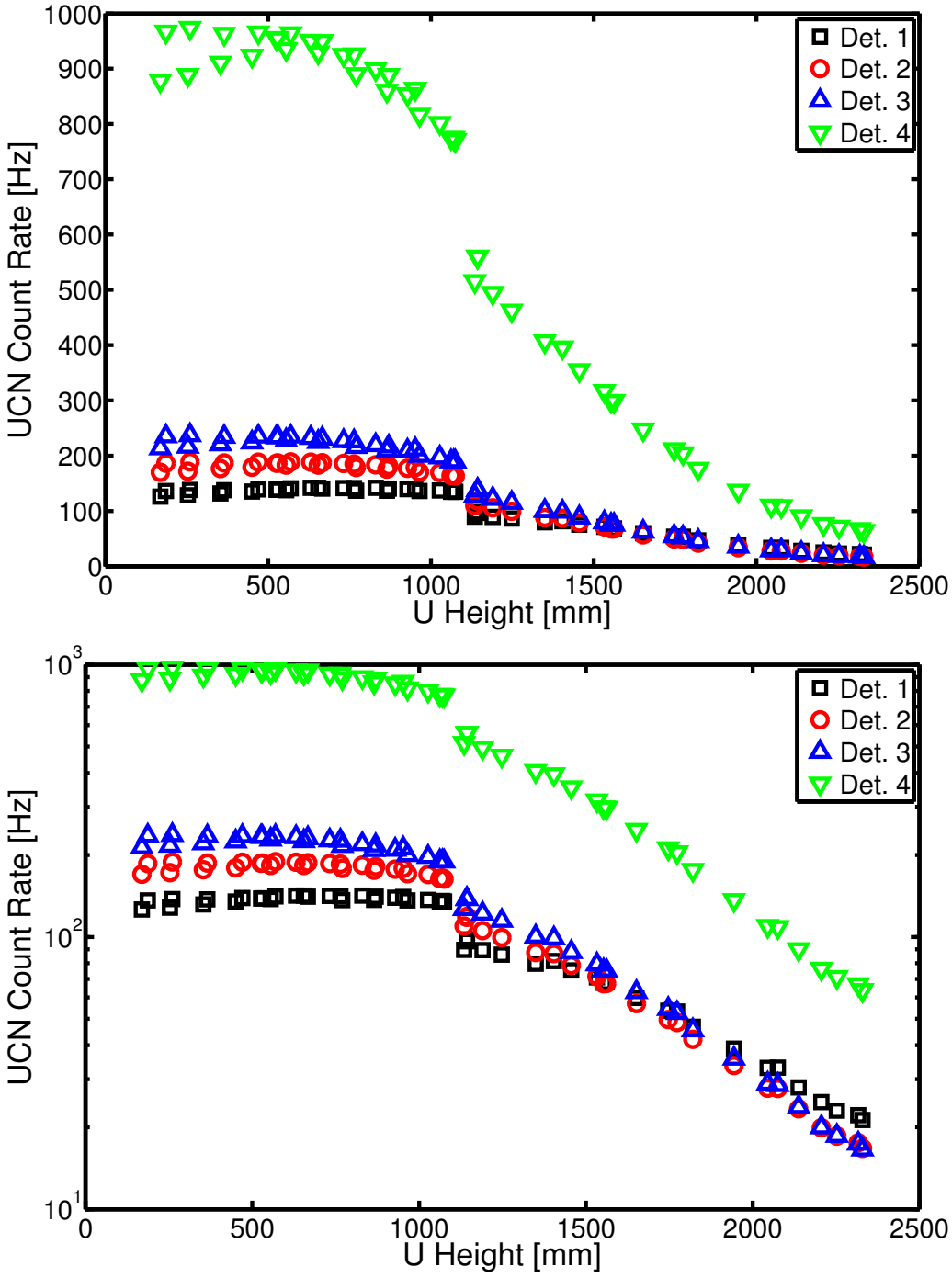

Figure 4.22.: Measured count rates as a function of U height on a linear and logarithmic scale. On the linear scale, the large fluctuations due to slits are clearly visible, whereas on the logarithmic scale the crossing of the count rates in detectors 1 to 3 is apparent. The step in count rate at a height of 1100 mm is due to the change from the small U to the large U.

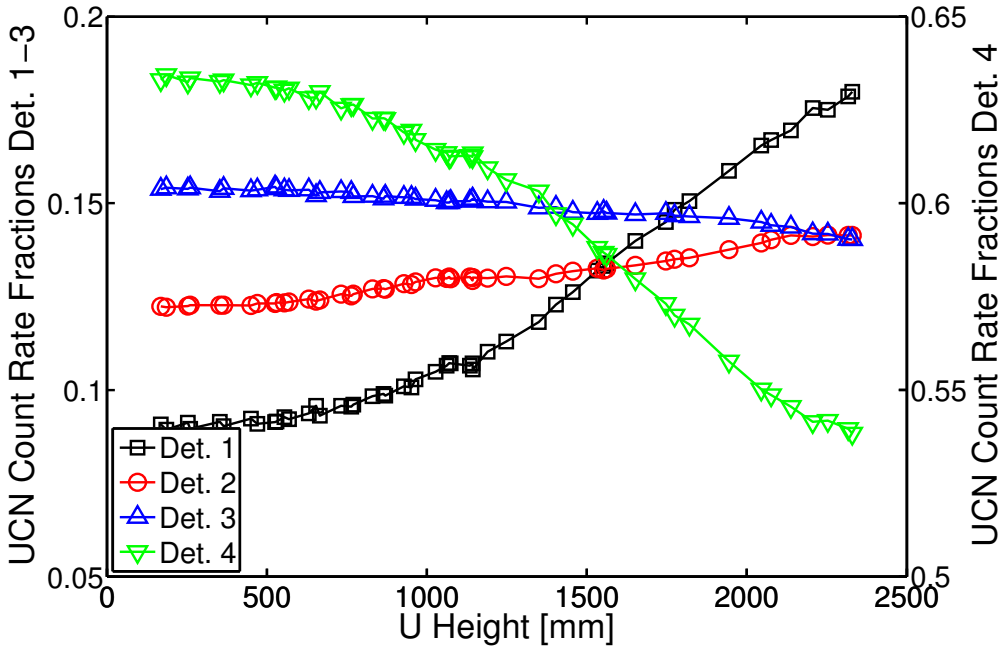

Figure 4.23.: Fraction of the total count rate as a function of U height measured by the different detectors. Note that the scale for detector 4 is on the right hand side.

is due to the change from the small U to the large U and the thus increased guide length of 2.5 m. Two features are apparent:

(i) There are large fluctuations in the UCN count rates visible for low U heights. These differences are due to slits opening and closing in the Wilson-flanges in which the U is rotating. Due to the space constraints mentioned above, the U had to be mounted in a very special way and resulting in a lot of tension on all the connections. Care had been taken to avoid such slits as well as possible but could not be completely eliminated. There were also frequent vacuum leaks appearing during the evacuation after the turning of the U. While the influence of the slits is easily discernible at low positions of the U, it is not equally clear for higher positions of the U where the change in count rate due to slits is mixed up with the change in count rate due to cutting off the low energy part of the spectrum. As such, the measured data with the U are very hard to analyse and especially the original plan of analysing differences between U positions became impossible.

(ii) For high U position, the measured count rate in detector 1 crosses the count rates in detectors 2 and 3 and the count rates in detector 2 and 3 become almost equal. This is a clear indication that the different detectors do indeed count different portions of the energy spectrum and as the spectrum gets harder and harder (higher U positions) the amount of detected UCN count rate in detector 1 relative to the other detectors becomes increased. This is more clearly seen in Fig. 4.23. In this figure, the fraction of the total count rate for a given U position as measured by the four detectors is shown. The ratio of counts greatly reduces the influence of fluctuations in counts common to all four detectors, i.e. independent of UCN energy. The dependence between the distribution of counts over the four detectors and the incoming UCN spectrum is clearly visible

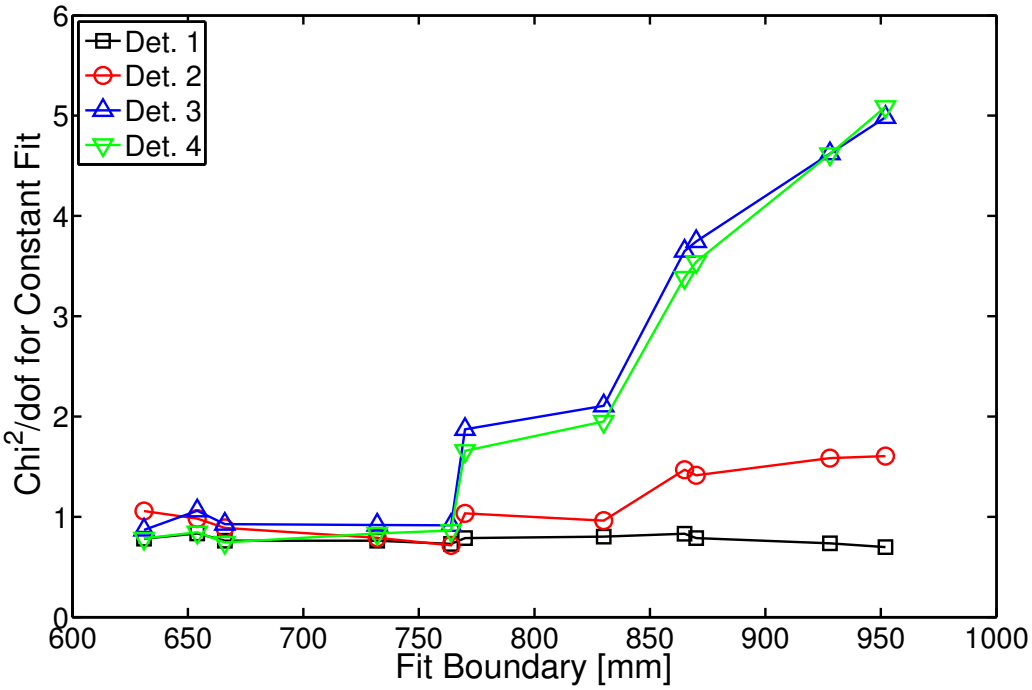

Figure 4.24.: Constant fit to the data in Fig. 4.22 between 450 mm and the value given in the plot as fit boundary. The departure from $\chi^2/\text{dof} \approx 1$ is an indication for a kink in the measured count rate correlated to the lower cut off in the energy spectrum due to the U.

and is proof that the spectrometer works as expected.

From the data taken with the small U, some more information can be extracted regarding the point where the initially constant rate starts to drop off due to the increased height of the U. In order to have a bit more reliable data, the measurements below 450 mm, where the fluctuations are largest, are discarded. For detector 1, which in principal should not be affected at these small U positions, the standard deviation between the measured data points up to 1100 mm was calculated and this relative error is assigned to the measured count rates of all four detectors. In order to see the kink in the measured data, the χ^2/dof was calculated for a constant fit between 450 mm up to a varying boundary. The results are shown in Fig. 4.24. It is clear that detector 1 shows a χ^2/dof of approximately 1 throughout the full varying of the upper fit boundary as the errors have been scaled to do so. However, it is nicely visible that detectors 3 and 4 deviate from a constant at the same point indicating that, as expected due to the aluminium window at the entrance of the beamline, there are no UCN in the energy range 0 - 50 neV. Detector 2 does not see the loss of these UCN, thus the UCN responsible for the deviation from a constant in detectors 3 and 4 have energies between 50 and 100 neV. For detector 2, the deviation from a χ^2/dof of 1 starts later (approximately above 850 mm) correlated to a decreased transmission probability over the U of UCN with energies above 100 neV.

MEASUREMENTS WITH THE GAS CELL

Measurements were conducted with different types of gases: nitrogen, argon, oxygen, and ^{3}He. While nitrogen, argon, and oxygen did not manage to stop all of the UCN over

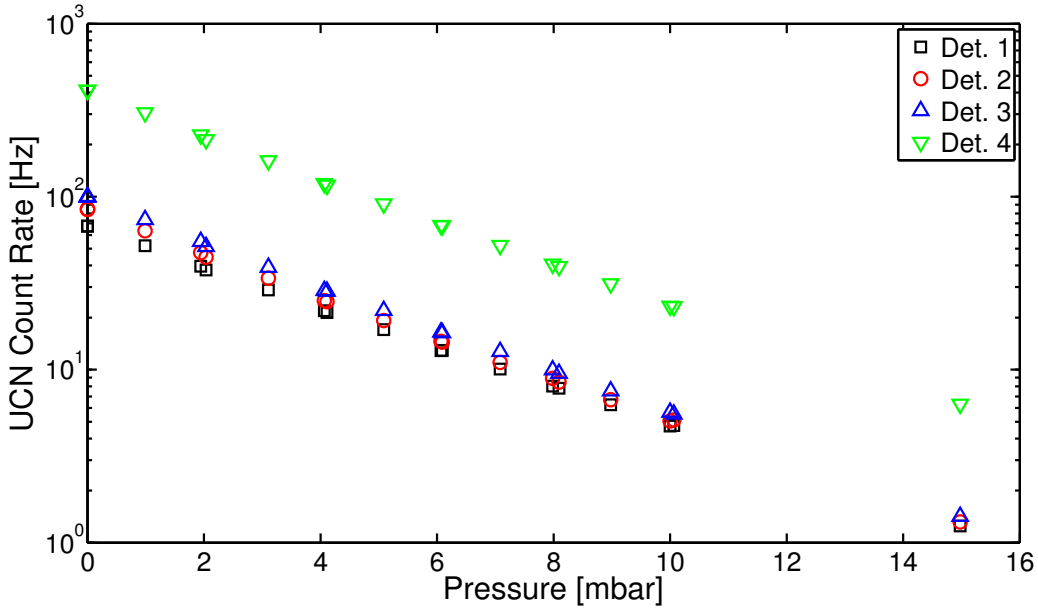

Figure 4.25.: Measured count rates as a function of ^{3}He pressure.

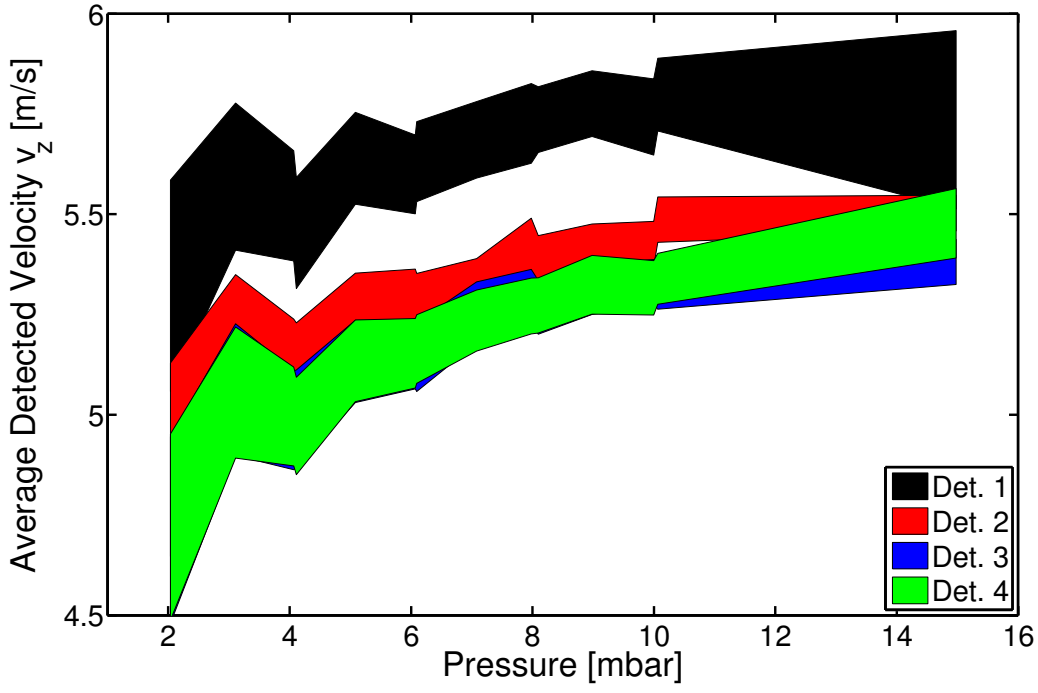

Figure 4.26.: Calculated average velocity from the data shown in Fig. 4.25. The bands show the $\pm 1\sigma$ interval of the total error on the extracted velocity.

the 53 mm distance in the gas cell even at pressures as high as 1 bar, 20 mbar of ^{3}He was enough to stop essentially all of the UCN.

Figure 4.25 shows the measured count rates as a function of ^{3}He pressure. The loss of UCN during the passage through the gas cell is given as:

$$N = N_0 \exp\left(-\rho\sigma_{^3\mathrm{He}} v_{\mathrm{therm}} \frac{d}{v_z}\right) \tag{4.9}$$

Here, N_0 and N are the amount of UCN before and after the passage, ρ the gas density, $\sigma_{^3\mathrm{He}} = 5333 \pm 10$ b [96] the absorption cross section for thermal neutrons with velocity $v_{\mathrm{therm}} = 2200$ m/s and $\frac{d}{v_z}$ the time the UCN with velocity v_z parallel to the guide needs to traverse the length $d = 5.3 \pm 0.1$ cm of the gas cell. The gas density is related to the pressure p (measured with an accuracy of 0.1 mbar in the given range of pressures) using the equation of state

$$\rho = \frac{n}{V} = \frac{N_A p}{RT}. \tag{4.10}$$

In this equation, one has the number of mole n, their volume V, the Avogadro constant N_A and molar gas constant R, and the temperature $T = 294.5 \pm 0.5$ K. Using the more refined van der Waals equation changes the resulting densities only marginally. Thus, one can calculate from the data in Fig. 4.25 the average velocity of the detected UCN in the four different detectors. This is done in Fig. 4.26. It shows the bands given by the $\pm 1\sigma$ intervals of the total error. While for small pressures, the systematic error from the 0.1 mbar accuracy on the measured pressure dominates, for large pressures the error coming from the background subtraction is the main source. It is clearly visible that the upper detectors detect higher energy UCN and that detector 3 and 4 sample the same UCN spectrum as there are no UCN with energies below ~50 neV present in the spectrum due to the aluminium windows.

TOF MEASUREMENTS

Our group has a long tradition of performing time-of flight measurements with UCN [87, 89, 97, 98, 99, 100]. Many details on how to perform TOF measurements can be found in those references. I will thus only sketch the basic principles.

The delay between the triggering signal of the chopper to the actual opening was calibrated by performing TOF measurements at the full beam using three chopper frequencies $f_{Chopper}$: 0.8, 1.0 and 1.25 Hz. The peaks of the resulting TOF-distributions were fitted using a Lorentz-function and the resulting peak positions were fitted with

$$t_{peak} = t_0 + \frac{\Delta t}{f_{Chopper}}. \tag{4.11}$$

t_0 is the true time-of-flight of the UCN in the peak and Δt is the frequency dependent offset between the triggering signal and the actual opening. Its value amounted to $\Delta t = 197 \pm 3$ ms Hz compatible with previous measurements [87, 100].

The normal measurements were performed at a chopper frequency of 1 Hz and a flight length of $l = 1025 \pm 3$ mm using the Cascade-U 200 detector. The measured TOF t (after subtraction of the offset $\Delta t / f_{Chopper}$ and the subtraction of the background rate

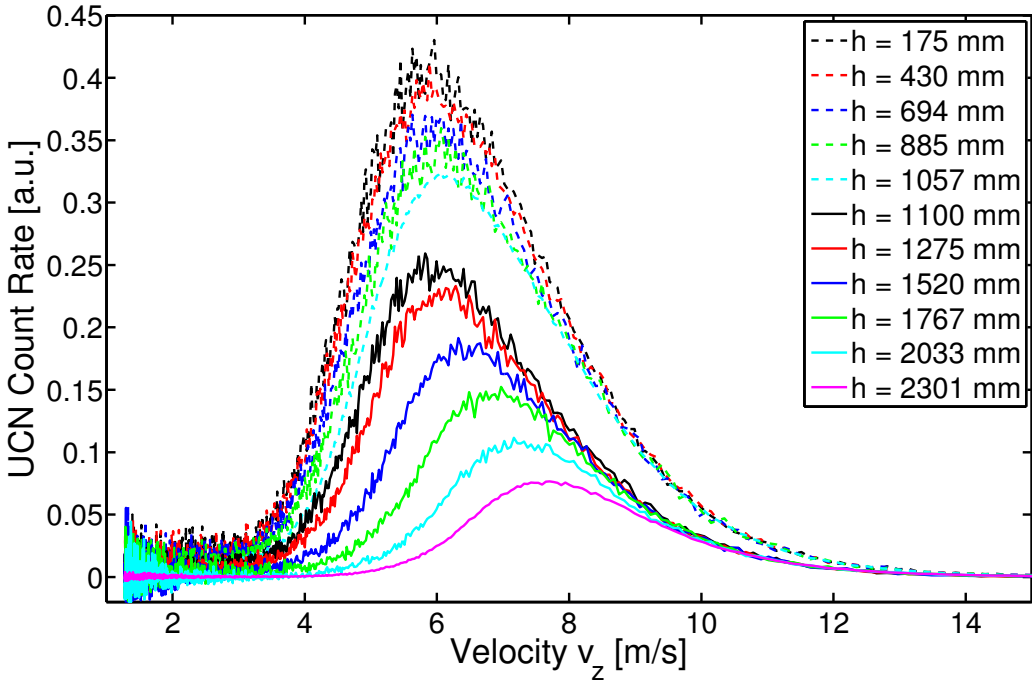

Figure 4.27.: Measured velocity distributions for different positions of the small (dashed lines) and the large (solid lines) U.

estimated by averaging the counts over the first period of time $\Delta t / f_{Chopper}$[4]) is then converted into the information on the velocity along the guide axis v_z using

$$v_z = \frac{l}{t} \tag{4.12}$$

and the measured rates $\frac{\mathrm{d}N}{\mathrm{d}t}$ are converted to

$$\frac{\mathrm{d}N}{\mathrm{d}v_z} = \frac{\mathrm{d}N}{\mathrm{d}t}\left|\frac{\mathrm{d}t}{\mathrm{d}v_z}\right| = \frac{\mathrm{d}N}{\mathrm{d}t}\frac{l}{v_z^2}. \tag{4.13}$$

Figure 4.27 shows the measured velocity distributions for different U positions for the small and the large U. In order to reduce the influence of count rate fluctuations and the small differences arising in the data processing, the data between 10 and 14 m/s were fitted using an exponential decay. The measurements for the small and the large U were then separately normalised to each other using these fit values. In addition, the ratios of total count rates at the heights 1057 mm (small U) and 1100 mm (large U) to the total rate as measured with the gravitational spectrometer at these positions were used as second normalisation factors. A few features are clearly visible: (i) There is still are very large amount of UCN in the spectrum with velocities higher than the critical velocity of the stainless steel guides of approximately 6 m/s in spite of the many bends in the beamline. (ii) The decrease of low velocity UCN with increasing U position, (iii) the slight softening of the spectrum by changing to the larger U either due to loss of high velocity UCN in slits or along the larger U arms (this softening of the spectrum at the

[4]This background rate consists of true background (external neutrons and electronic noise) and stored UCN.

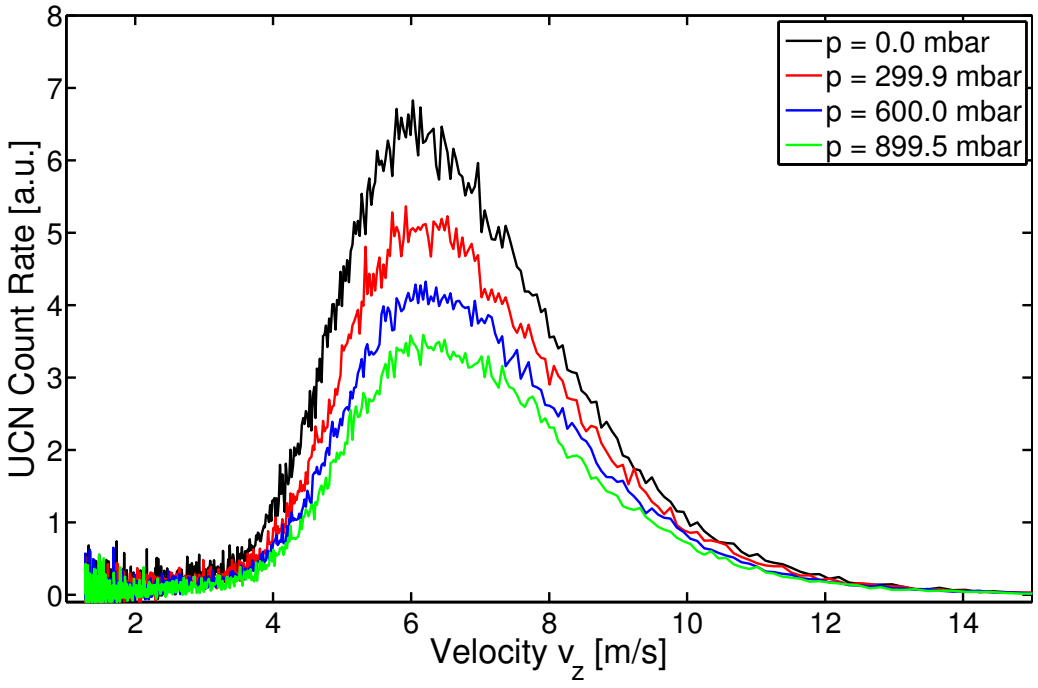

Figure 4.28.: Measured velocity distributions for different pressures of nitrogen in the gas cell.

change of Us can also be seen in Fig. 4.23), and (iv) the absence of UCN below 50 neV from the comparison of the spectra at heights 175 and 430 mm (as concluded from the spectrometer measurements above).

With the gas cell inserted, TOF flight measurements were performed for the empty cell and the cell filled with 300, 600 and 900 mbar of nitrogen and are shown in Fig. 4.28. The shift to higher velocities is the direct consequence of the $\frac{1}{v_z}$ dependence of the loss in the gas cell (see Eq. (4.9)). Forming the ratio of measured rate with respect to the empty cell allows to extract the effective loss cross section in nitrogen. As the ratios show despite the performed "spark cleaning" (see above) some non-statistical fluctuations between 4 and 6 m/s, the fit was performed for velocities between 6 and 10 m/s using Eq. (4.9) for the combined data set of different pressures. The resulting χ^2/dof of 230/212 is excellent and gives $\sigma = 15.1 \pm 0.1\,(\text{stat}) \pm 0.3\,(\text{syst})$ b per molecule. The systematic error is estimated from the systematic errors on ρ, d and v_z, which are 0.3%, 1.9% and 2.9%, respectively.

SIMULATION AND CALIBRATION

The simulation of the gravitational spectrometer was setup in GEANT4 using the package GEANT4UCN [81]. It includes the model and dimensions as found in Fig. 4.11. With the simulation, it is possible to calculate exactly for each energy the distribution of counts over the four detectors as a function of the material parameters of the spectrometer. Fig. 4.29 shows, as an example, the percentage of UCN for each energy being detected in one of the four detectors, diffusing back into the beamline or being lost. As can be seen, a higher diffusivity generally leads to less UCN being detected in the upper detectors. Additionally, the simulation can be used to calculate the time needed to

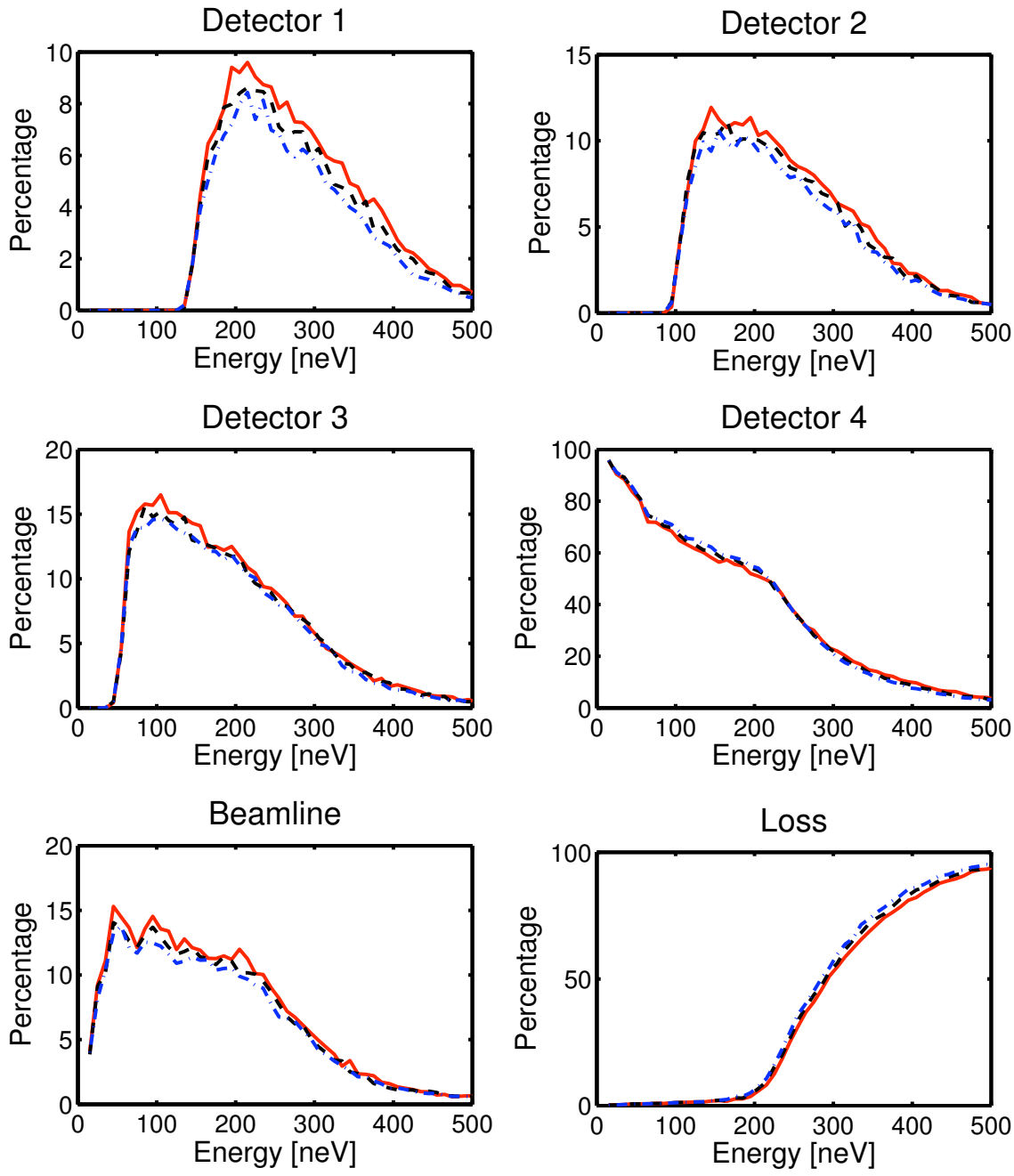

Figure 4.29.: Percentage of UCN being either detected in one of the four detectors, diffusing back into the beamline or being lost. Material parameters were set as $V_F = 232$ neV, $\eta = 4 \times 10^{-4}$ and diffusivity $d = 6\%$ (blue, dash-dot line), $d = 4\%$ (black, dashed line), and $d = 2\%$ (red, solid line), respectively.

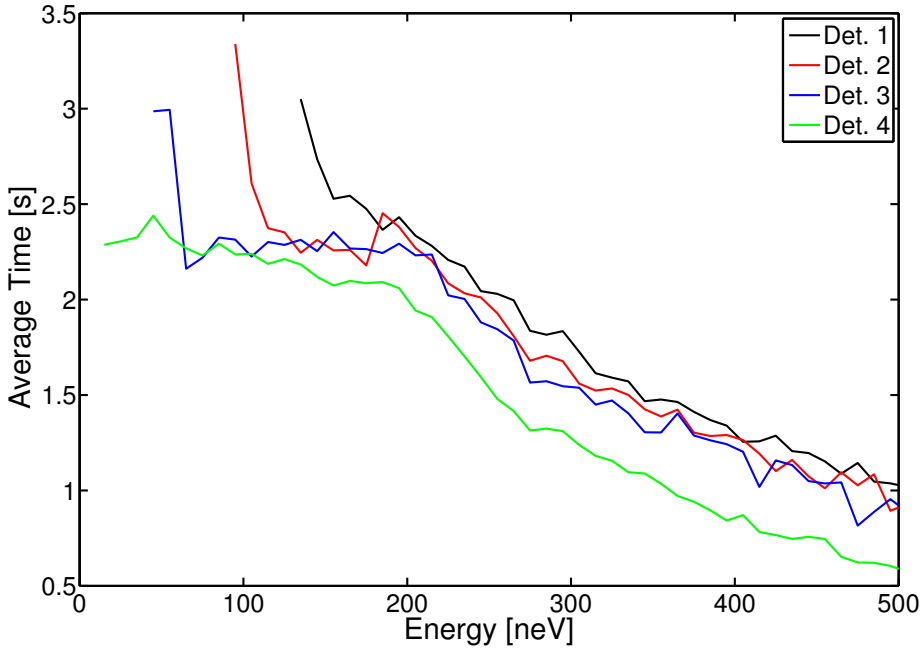

Figure 4.30.: Average time needed for the UCN to being detected. The simulation includes 1 m of incoming beamline. The median time is generally about 0.5 s lower corresponding to an asymmetric distribution with a tail to higher times.

detect the UCN as shown in Fig. 4.30. It shows that the detection process takes place reasonably fast - as intended in the optimisation of the geometry (see Sec. 4.4.1).

Due to the problems with the U measurements, in order to match the simulation to the data the actual spectrum entering into the detector is needed in the simulation. For this, the measured TOF spectra were used. However, firstly the TOF spectra needed conversion from spectra of the velocity along the guide axis to spectra of the absolute velocity. The biggest problem in this process is the knowledge of the actual angular distribution of the UCN during their transportation through UCN guides, which additionally depends on the velocity itself. A simple model of an angular distribution was used in which the general distribution is set to be $\cos\theta$ with respect to the guide axis and additionally it was required that the value of the velocity perpendicular to the beam axis $v_\perp$ was less than the critical velocity v_c of stainless steel of 6.03 m/s and the value of the velocity parallel to the beam axis $v_{||}$ more than the critical velocity v_c of aluminium of 3.24 m/s. There is even an additional complication: the TOF spectra were measured with the UCN detector on beamline level. In this configuration, the aluminium entrance window of the detector additionally suppresses the low energy UCN due to their increased loss in the passage through the foil with respect to the higher energy UCN and due to storage effects of the slow UCN between the aluminium windows. For a plot of the transmission function of UCN through 100 μm of aluminium see, e.g., Fig. 4 of [99]. In order to cope with this, the resulting spectrum was slightly modified by hand and later re-weighted by fitting to the data (see below).

With the above conditions in place, the matrix connecting v and $v_{||}$ was calculated in

the following way:

$$\begin{pmatrix} v_{||}^1 \\ \vdots \\ v_{||}^n \end{pmatrix} = \begin{pmatrix} R_{11} & \cdots & R_{1n} \\ \vdots & \ddots & \vdots \\ R_{n1} & \cdots & R_{nn} \end{pmatrix} \begin{pmatrix} v^1 \\ \vdots \\ v^n \end{pmatrix} \tag{4.14}$$

The matrix element R_{ij} is the amount of UCN with velocity v^j having velocity $v_{||}^j$. As UCN with velocity $v_{||}^n$ only stem from UCN with v^n, the matrix equation can easily be solved by backwards insertion and the corresponding v-spectrum be extracted from the measured $v_{||}$-spectrum. In order to produce a nice spectrum, it was then smoothed and the amount of low velocity UCN somewhat increased by hand. This spectrum was then used in the simulation to start UCN trajectories. Velocities v are chosen at random corresponding to the spectrum and the velocity components then calculated with the same conditions in place as given above.

First, I tried to match the simulation to the measured data with the ^{3}He filled gas cell. For this, the TOF spectrum taken with the empty gas cell was used. In a first step, the matrix connecting the amount of detected UCN in the four detectors (D_1 to D_4) to the amount of UCN in the four energy bins 0-50, 50-100, 100-150 and 150-1000 neV (denoted s_1 to s_4) was calculated. The spacing is somewhat unfortunate but is needed due to the large amount of UCN with energies above the Fermi potential of the stainless steel UCN guides. Again, a matrix equation can be used:

$$\begin{pmatrix} D_1 \\ D_2 \\ D_3 \\ D_4 \end{pmatrix} = \begin{pmatrix} T_{11} & \cdots & T_{14} \\ \vdots & \ddots & \vdots \\ T_{41} & \cdots & T_{44} \end{pmatrix} \begin{pmatrix} s_1\,\epsilon_1 \\ s_2\,\epsilon_2 \\ s_3\,\epsilon_3 \\ s_4\,\epsilon_4 \end{pmatrix} \tag{4.15}$$

T_{ij} is the amount of UCN from energy bin s_j being detected in detector D_i. The values ϵ_i are possible differences in the efficiencies of the detectors. As the three small detectors D_1 to D_3 are all identical and fed from the same HV, one can expect $\epsilon_1 = \epsilon_2 = \epsilon_3 \equiv \epsilon$ and set $\epsilon = 1$. The larger detector D_4 has a different support grid of the entrance window. From the covered area of the grid, one expects $\epsilon_4 < 0.96$ as the additional influence of the larger thickness of the grid of detector 4 is difficult to estimate. ϵ_4 is thus left as a free parameter. As seen above, there are no UCN with energies below 50 neV and thus we have $s_1 = 0$, which leaves 4 free parameters s_2, s_3, s_4 and ϵ_4 for the four measured rates with the empty gas cell.

The rates for a filled gas cell were then predicted from the simulation in the following way: The results of the simulation for the empty cell were binned with 10 neV binsize. In each of the bins, the amount of UCN was then decreased corresponding to the average absorption in the gas cell for this energy bin (see Eq. (4.9)) using the simulated v_z-distribution in this bin. With this reweighted values, the decrease in total count rate for the four detectors with respect to the empty cell results was calculated (factors A_1 to A_4) and a reweighted matrix $T^\star$ for use in Eq. (4.15) formed. In the case of a filled gas cell, Eq. (4.15) is thus given as:

$$\begin{pmatrix} D_1 \\ D_2 \\ D_3 \\ D_4 \end{pmatrix} = \begin{pmatrix} T_{11}^\star & \cdots & T_{14}^\star \\ \vdots & \ddots & \vdots \\ T_{41}^\star & \cdots & T_{44}^\star \end{pmatrix} \begin{pmatrix} s_1\,A_1 \\ s_2\,A_2 \\ s_3\,A_3 \\ s_4\,\epsilon_4\,A_4 \end{pmatrix} \tag{4.16}$$

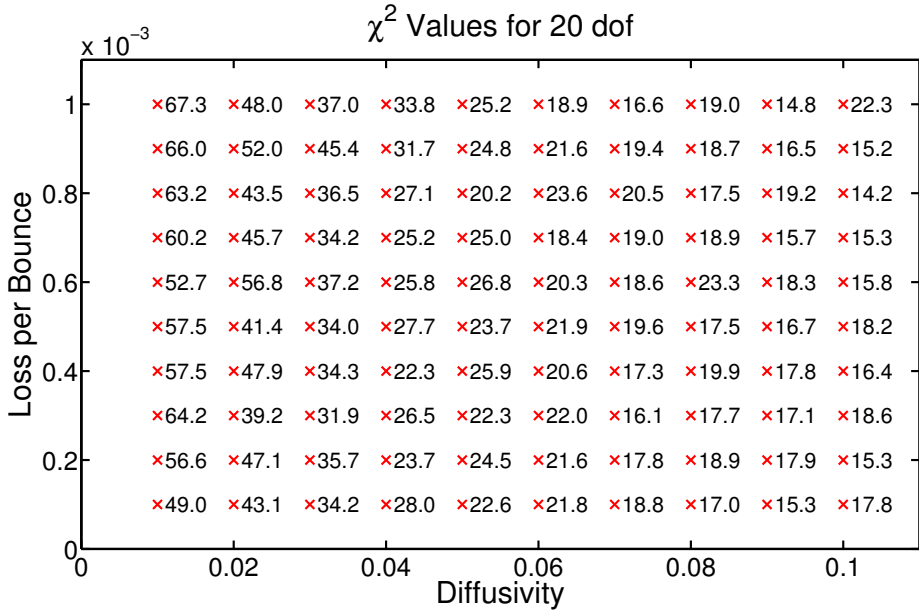

Figure 4.31.: χ^2-scan of the parameter space of diffusivity and loss parameter of the spectrometer for the data taken with the gas cell. For details see text.

In order to calibrate the detector, the parameter space of diffusivity d and loss parameter η was scanned with the simulation and at each point the measured data were compared to the simulated count rates for the gas cell filled with approximately 0, 2, 4, 6, 8, and 10 mbar of ^{3}He. The quality of the agreement was checked by calculating the χ^2, where in the error of the simulation not only the statistical error due to the number of simulated trajectories but also the systematic error (being dominant) in the calculation of the average absorption was included. The result of this scan is shown in Fig. 4.31. From the actual χ^2 values, diffusivity values of 9 - 10% seem to be favoured. However, in that region the fitting procedure results in unlikely low relative efficiency ϵ_4 of ~80% and spectrum contents s_2 and s_3 with $s_2 > s_3$, which also is very unlikely. Both is due to the fact that for large diffusivities less UCN reach into the upper detectors (see Fig. 4.29). Additionally, diffusivities larger than ~5% seem unlikely per se for a surface showing smaller roughness than stainless steel (see Sec. 4.4.2). From that point, a description of the spectrometer with a diffusivity of ~4% and a moderate loss per bounce of $\sim 4 \times 10^{-4}$ seems to be more likely. However, for a better calibration of the detector additional measurements are needed (see Sec. 4.4.7).

For completeness, the same procedure of matching simulation and data was also tried with the U data. To that end, the transmission of UCN over a U of the special shape as shown in Fig. 4.20 was simulated and is shown in Fig. 4.32. While the transmission of UCN over the U depends strongly on the diffusivity of the guide, its effect is greatly reduced in the comparison of the transmission with respect to a different height. Having simulated Us of heights 1100, 1248, 1652, 1821, 2045 and 2253 mm and calculated the ratios with respect to the height 1100 mm, the analysis was then in complete analogy as above with these ratios playing the role of the absorption. The basis of the analysis was the TOF measurement at a height of 1100 mm. From this, the corresponding velocity spectrum was calculated as above and used in the simulation. The binned results of the simulation were then reweighted with the above mentioned ratios and the matrix

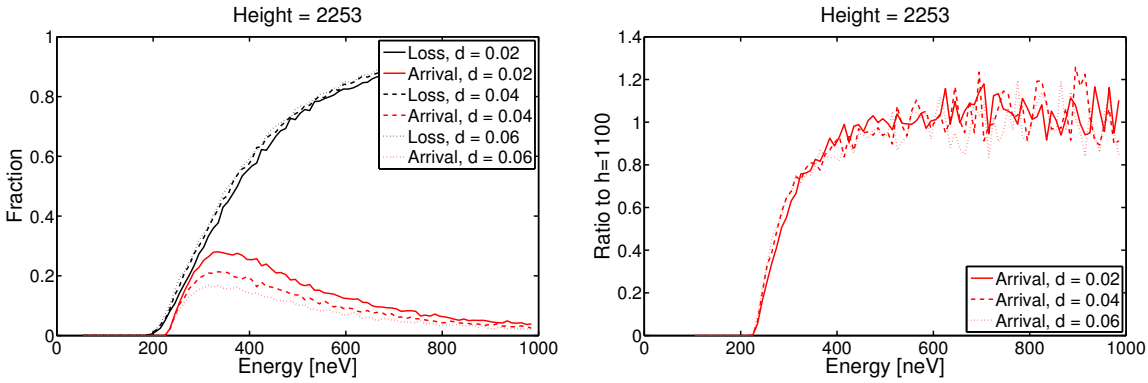

(i) (ii)

Figure 4.32.: (i) Simulated transmission and loss of UCN over a U for different diffusivities. (ii) Ratio of the simulated transmissions with respect to the transmission at a height of 1100 mm.

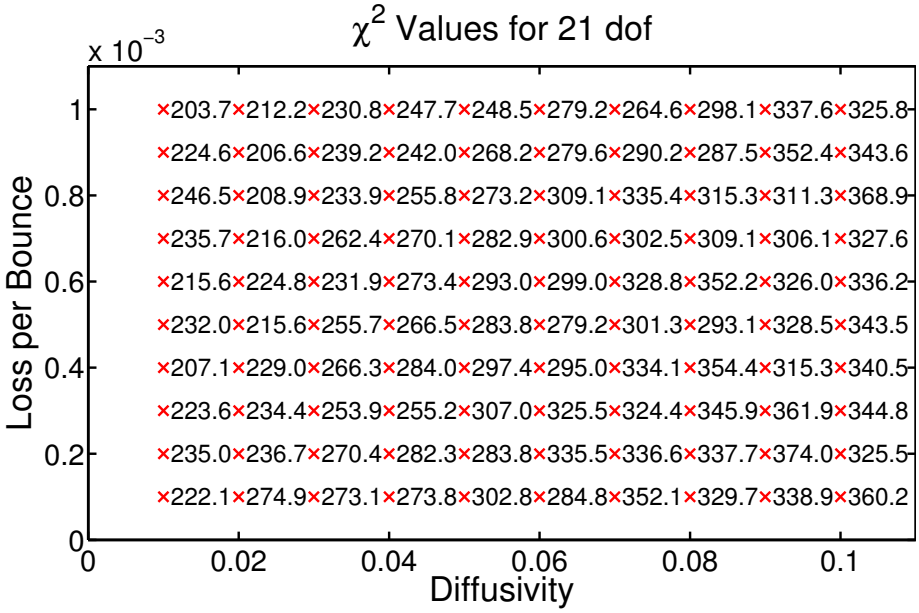

Figure 4.33.: χ^2-scan of the parameter space of diffusivity and loss parameter of the spectrometer for the data taken with the rotatable U. For details see text.

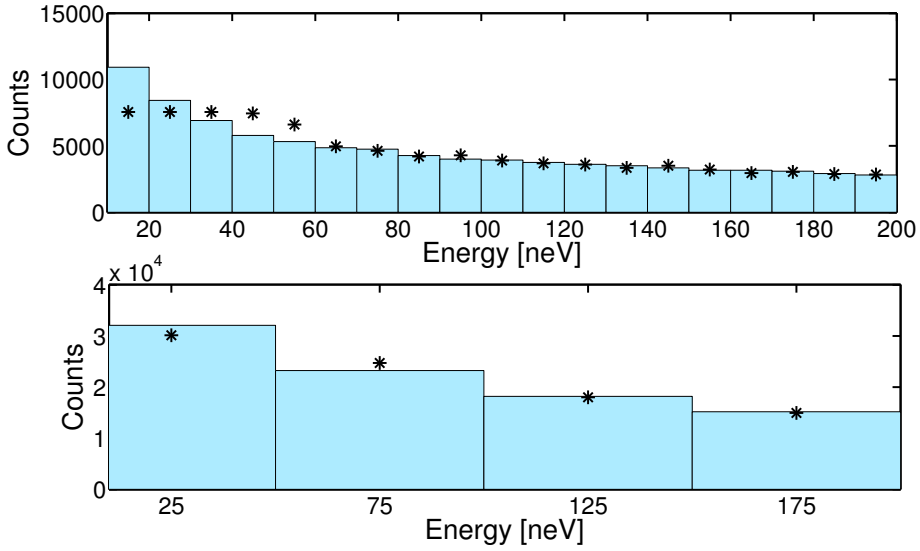

Figure 4.34.: Extraction of the detected spectrum using simulated data. Above: Spectrum as extracted by inverting Eq. (4.17). Bottom: Combination of the spectrum in the upper plot to four energy bins.

$T^\star$ and the reduction in the incoming spectrum calculated. After this procedure, the simulation was compared to the measured data at heights of 1248, 1652, 1821, 2045 and 2253 mm including as a systematic error the differences in the simulated transmissions over the U. With the initial U position at 1100 mm, in addition to $s_1 = 0$ one also has $s_2 = 0$. The result of the following χ^2 scan is shown in Fig. 4.33. It is immediately clear, that the description of the data with the simulation is exceptionally bad. There are two reasons possible: (i) during the dismounting of the spectrometer and the installation of the TOF-setup, the situation in the beamline changed producing a drastically different velocity spectrum or (ii) during the rotation of the U, spectrum is not only changed due to the different heights but also due to a systematic changing in the slits, which is not included in the simulation.

4.4.5. EXTRACTION OF SPECTRA

The basic method of extracting the spectrum from the measured count rates at the four detectors is given in Eq. (4.15). By inverting the matrix T, the incoming spectrum can be extracted. One can then calculate the detected spectrum by multiplying the incoming spectrum with the corresponding detection percentages $\sum_i T_{ij}$. However, as the four energy bins are fairly large (typically 0-50, 50-100, 100-150 and 150-200 neV) knowledge on the shape of the spectrum is already needed in the simulation of the values T_{ij}. Two ways are possible to overcome this problem:

(i) An iterative approach, where in the first iteration a flat spectrum is used in the calculation of T_{ij}. The extracted spectrum using these values is then fitted with an approximate shape and the fit fed back into a refined calculation of the values T_{ij} and so on until the values converge.

(ii) It is possible to write down Eq. (4.15) in the form

$$\begin{pmatrix} D_1 \\ D_2 \\ D_3 \\ D_4 \end{pmatrix} = \begin{pmatrix} T_{11} & \cdots & T_{1n} \\ \vdots & \ddots & \vdots \\ T_{41} & \cdots & T_{4n} \end{pmatrix} \begin{pmatrix} s_1 \\ \vdots \\ s_n \end{pmatrix} \tag{4.17}$$

with, e.g., energy bins of 10 neV (and thus $n > 4$) for which a flat spectrum is a good enough approximation. This forms an overdetermined set of linear equations. Thus the matrix T cannot be inverted directly anymore and the system has no solutions (except for degenerate cases). One way of solving this equation is by using a generalised inverse such as the Moore-Penrose-Inverse [101, 102]. This inverse solves the overdetermined set of linear equations in a least squares sense (see Appendix A.6 for its derivation and calculation). Denoting the generalised inverse with T^+, the spectrum is given as $s = T^+ D$. The resulting spectrum then approximates the true spectrum and the number of UCN can be combined to the amount of UCN in the four energy bins as given above. Figure 4.34 shows this extraction process for a simulated, detected spectrum using a matrix T simulated with the same parameters. Due to the fact, that all UCN with energies below 50 neV end up in detector 4, the extraction using the generalised inverse cannot adequately describe the shape of the spectrum in that region but assigns equal numbers of UCN for each energy bin. As for the lowest energy bin above 50 neV, it still holds that almost all of the UCN end up in detector 4, this then leads to the observed discrepancy after the combination to four energy bins.

The quality of the extraction process can be increased by the knowledge on the minimal and maximal energy in the spectrum and by consequently constraining the available energy bins in Eq. (4.17) to this energy range.

The observed difference between the extracted and actual spectrum is of systematical nature and will lead to a systematic shift of the assigned average energy of the different energy bins. The exact size of the systematic error will have to be studied thoroughly once the full calibration of the detector has been performed (see Sec. 4.4.7). However, being a systematic error it will not disturb the measurement of the neutron precession frequency during EDM measurements (see Sec. 4.4.6).

4.4.6. EDM MEASUREMENTS USING GRAVISPECTRO

It is clear that this gravitational spectrometer cannot be used in connection with the Sussex-RAL-ILL apparatus during phase II, but only later in connection with the new apparatus n2EDM during phase III where the storage chamber will be placed on beamline level (see Sec. 1.3).

A velocity dependent shift in the precession frequency will manifest itself in separate Ramsey resonance patterns (see 1.7) for the different energies. Having a velocity dependent effect will thus lead to slightly different distributions of counts over the four detectors at the four working points of the applied RF-field.

Thus, one of the major components still missing in order to use Gravispectro in EDM measurements is the spin analysis. Two ways of doing this are conceivable: (i) Separate spin analysis above each of the four detectors or (ii) spin analysis placed in front of the spectrometer. Both of the systems have pros and cons:

- Advantage (i): The corresponding spin up and down UCN are detected immediately after the analysis and the amount of falsely identified spin components is small.
- Disadvantage (i): The development of a large analyser (diameters 100 and 190 mm) based on, e.g., an iron coated aluminium foil is challenging. It will be difficult to saturate the iron layer over the full area.
- Advantage (ii): Only one spin analysis system is needed and can basically be a copy of the existing system.
- Disadvantage (ii): The amount of falsely detected spins is increased as the paths into the detectors are large. The timing of counting spin up or down compared to the timing of spin flipper on or off is difficult.

One has to note that detecting only one spin component is not an appropriate way as averaging of the resonance frequency extracted from the spin up and down components helps to greatly reduce the effects of beam fluctuations[5].

With an appropriate spin analysis system in place, three ways of using Gravispectro are conceivable:

1. The easiest mode of operation is by just simply looking at the distribution of counts over the four detectors at the four working points. If the distributions all match each other, then there is no velocity dependent shift present in the measured resonance frequencies.
2. In the second mode of operation, each of the detectors is treated separately and for each of the detectors the measured UCN counts are used separately to calculate the resonance frequency. For a typical spectrum reaching up to ~6 m/s and an average velocity of ~4 m/s, the four detectors will thus detect UCN with average velocities of ~6 m/s (detector 1), ~5.5 m/s (detector 2), ~5 m/s (detector 3), and ~4 m/s (detector 4). The amount of the total count rate will be distributed as 1%, 4%, 12% and 83%, respectively. Measuring a false EDM effect scaling with v^2 and amounting to 1 ± 0.05 in arbitrary units over the full velocity spectrum, its effect would be 1 measured with sensitivity 0.06 in detector 4, 1.6 with sensitivity 0.15 in detector 3, 1.9 with sensitivity 0.25 in detector 2, and 2.3 with a sensitivity 0.5 in detector 4. It is clear from these values, that this mode of analysis is only feasible with high statistical sensitivity.
3. In the third mode of operation, one extracts in every cycle the amount of UCN in the different energy bins as shown in Sec. 4.4.5. For each of the different energy bins, one then extracts the corresponding resonance frequency separately. Systematic errors in the extraction of the spectrum will not affect the extracted resonance frequency, as they will shift the amount of UCN in the same direction at all four working points. They will only affect the matching of the measured resonance frequency to an average energy of the detected UCN in that energy bin. The statistical sensitivity will then be limited to the amount of UCN available in the different energy bins.

[5] Beam fluctuations will shift the measured resonance frequencies in opposite directions for spin up and down as can easily be seen by looking at Fig. 1.7

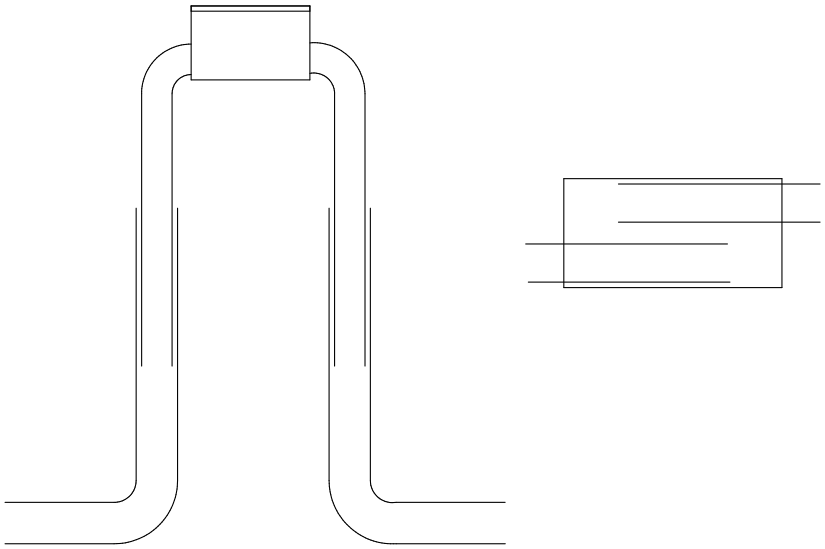

Figure 4.35.: Idea for a system producing a monoenergetic UCN beam. A box with two guides inserted into it as shown on the right and an absorbing roof is located on top of a telescope-like U. By moving the box up and down, distinct energy bins corresponding to the bottom and top height of the box can be selected.

4.4.7. IDEA FOR FUTURE CALIBRATION MEASUREMENTS

In order to achieve a reliable calibration of the detector which does not depend (or only marginally) on simulation, a monoenergetic UCN beam is needed. With such a beam the distribution of counts over the four detectors can be measured for each energy separately and directly. Fig. 4.35 shows a device which would be able to produce such a beam. The system relies on using a telescope-like U. With such a U, the problems associated with turning of the U (stress, slits, fixation, etc.) are greatly reduced. At the same time, it allows to mount a box on top which does not have to be levelled with every change in U position. The box will act as a so-called shaper [103] by having the guides reaching into the box and thus making sure that the UCN will undergo many reflections on the walls at many different angles of incidence. One can thus mount an absorbing plate onto the roof of the shaper, which will result in a higher energy cutoff for the UCN. The exact dimensioning of all the components will have to be done by trying to produce as sharp lower and upper energy cutoffs as possible while at the same time minimising the losses.

4.5. VELOCITY EXTRACTION WITH THE NEDM APPARATUS USING EMPTYING TIMES

During the work on the distributions and behaviour of the UCN in the storage chamber (see Appendix A.5), I realised that as the collision frequency of the UCN with the wall

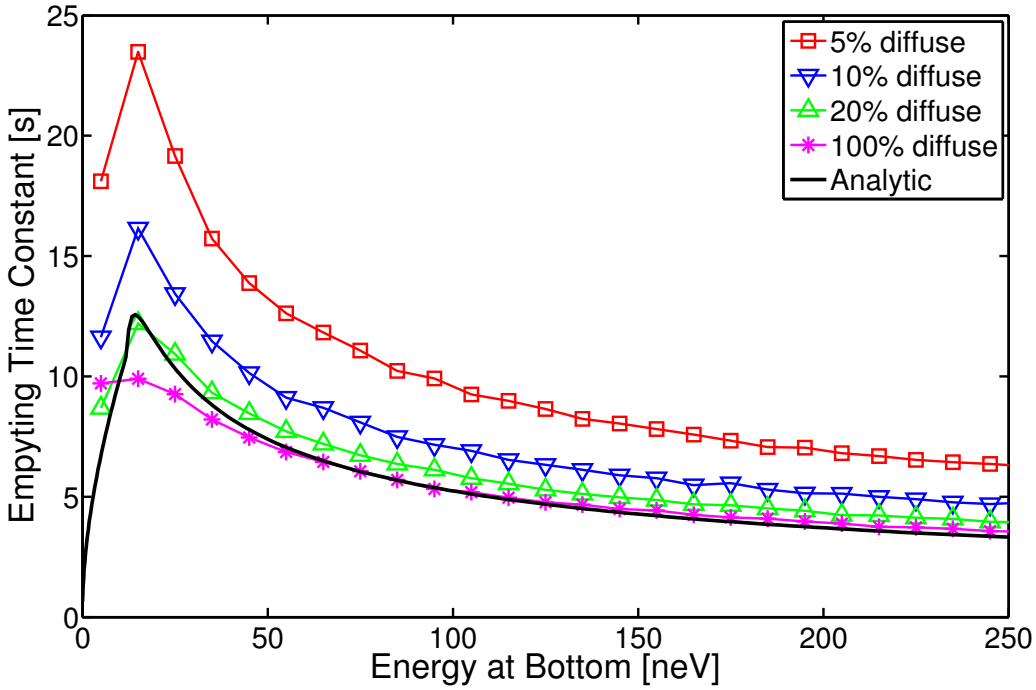

Figure 4.36.: Comparison of the emptying time constants obtained by an analytic calculation and in a simulation with different diffusivity values for the storage chamber as a function of the energy at the bottom of the chamber. For more details see text.

depends on energy, so should the time it takes for the UCN to leave the storage chamber depend on energy. In order to describe this process analytically, one hast to look at the area covered by the guide leading out of the storage chamber A_{exit} with respect to the total surface area A_{tot}. The probability of exiting the chamber on a wall collision (with frequency f_c) is then given as A_{exit}/A_{tot} and the characteristic time constant for leaving the trap thus amounts to

$$\tau = \left(\frac{A_{exit}}{A_{tot}} f_c\right)^{-1}. \tag{4.18}$$

For the UCN under the influence of gravity, the areas have to be properly weighted in order to reflect the correct distribution of the UCN in height (see Appendix A.5). The weighting function $f(h)$ is then given with Eq. (A.21) as

$$f(h) = \frac{n(E,h)}{n(E,h=0)} = \sqrt{1-\frac{h}{h_{max}}}. \tag{4.19}$$

For a UCN not reaching the top, the weighted total area in the storage chamber of radius r and height h thus amounts to

$$A_{tot} = f(0)\pi r^2 + \int_0^{h_{max}} f(h')2\pi r \mathrm{d}h' \tag{4.20}$$

while for a UCN reaching the top it is

$$A_{tot} = f(0)\pi r^2 + \int_0^{h} f(h')2\pi r \mathrm{d}h' + f(h)\pi r^2. \tag{4.21}$$

		τ [s]	χ^2/dof	p [%]
T = 30 s	spin up (1)	9.98 ± 0.10	1.79/8	98.7
	spin down	10.12 ± 0.03	34.51/32	34.9
	spin up (2)	10.56 ± 0.15	19.76/16	23.1
T = 130 s	spin up (1)	11.24 ± 0.15	7.50/8	48.4
	spin down	11.15 ± 0.04	26.94/32	72.1
	spin up (2)	11.12 ± 0.18	21.96/16	14.4
T = 230 s	spin up (1)	12.08 ± 0.31	8.39/8	39.6
	spin down	11.41 ± 0.08	22.91/32	88.1
	spin up (2)	12.09 ± 0.38	8.15/16	94.4

Table 4.1.: Results of the fits to the data shown in Fig. 4.37. The p-value is the probability of achieving the same or higher χ^2 for the given degrees of freedom. For more details see text.

In both cases, the weighted area leading out of the trap of radius r_{exit} amounts to

$$A_{exit} = f(0)\pi r_{exit}^2. \tag{4.22}$$

With these weighted areas in place the corresponding time constant can thus be calculate according to Eq. (4.18) and is shown in Fig. 4.36. As this reasoning of calculating the probability from the ratio of the areas assumes that the UCN are at all times distributed according to the weighting function given above, which is obviously not the case when one is emptying the storage chamber, a simulation has to be performed in addition to the analytic calculation. For this, I used the Matlab [69] simulation that was already in place for the simulation of trajectories used in Sec. 3.3. The implemented geometry included a storage chamber of radius 23.5 cm and height 12 cm and a guide leading to the detector of 2.28 m length and a radius of 3.4 cm (with 1% probability for diffiuse scattering). The slope of the simulated arrival times in the UCN detector were then fitted with $f(t) = N\exp(-t/\tau)$. The results are shown in Fig. 4.36 for different diffusivities in the storage chamber. One can clearly see that for low amounts of diffusivity, it takes much longer for the UCN to exit the chamber and that the high diffusivity cases better match the analytic calculation. This is due to the fact that for the high diffusivities the UCN tend to follow the appropriate distributions more quickly. The trend of approaching the analytic calculation by increasing the diffusivity can thus be understood. However, I currently do not have an explanation for the behaviour of the curve for 100% diffusivity at low energies where the simulated time constants are even below the predictions of the analytic calculation.

In order to see such kind of effects, several days of data could be taken in a parasitic mode with the EDM apparatus. For that end, the data acquisition system used already for the ^{3}He detectors during the measurements in Sec. 4.4.3 was mounted in parallel to the standard DAQ of the EDM apparatus. Equipped with an internal clock, it allows to record the arrival time of every single UCN. In addition to the UCN detector signal, the timing signal of the beginning and the end of the free precession period was also fed into the DAQ. With these signals, the measured arrival times could then be synchronised to the actual EDM measurement cycle. As it was seen in the simulation that the first three seconds of each counting period do not show a nice exponential behaviour as they are

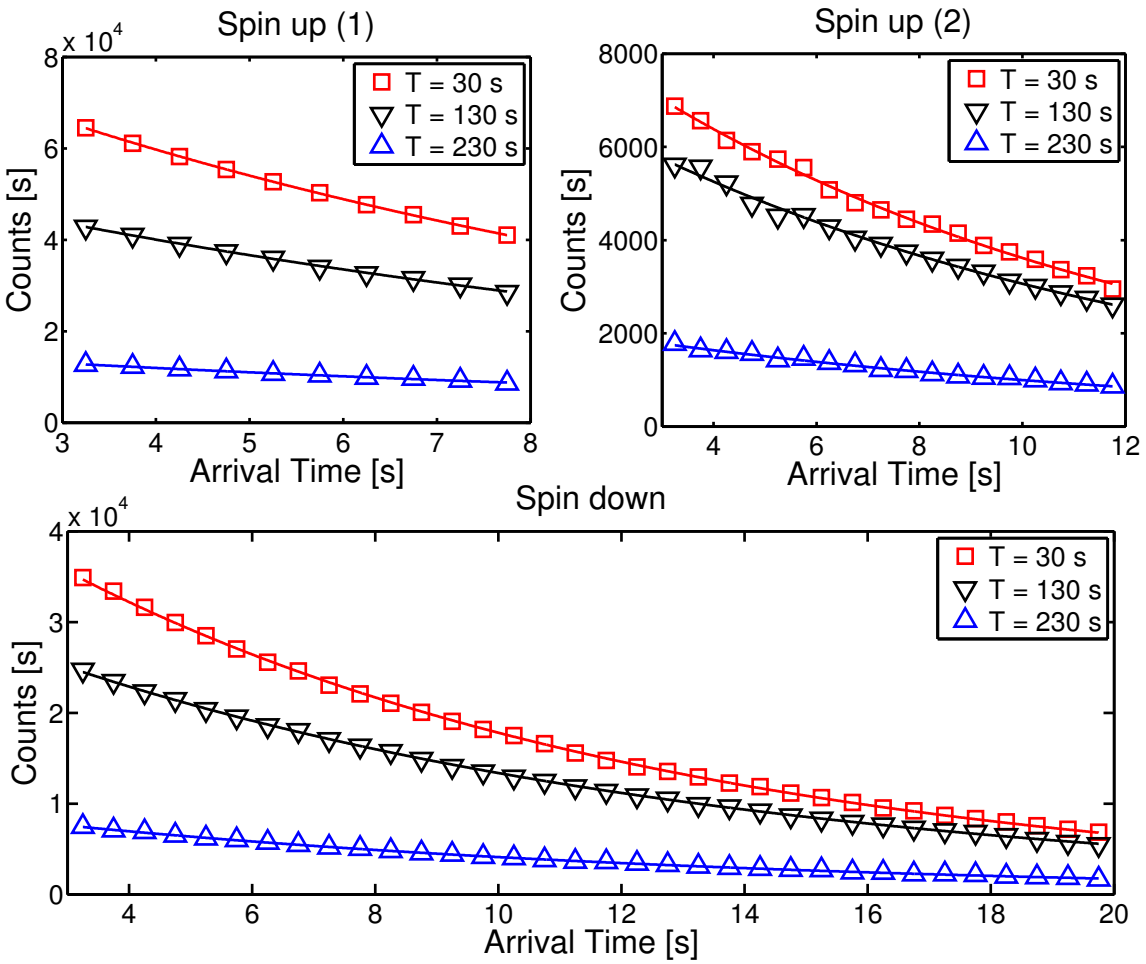

Figure 4.37.: Measured arrival times of the UCN in the detector during the three phases of counting spin up (8 s), spin down (20 s) and again spin up (12 s). The first three seconds of each measurement period have been discarded (see text). Data have been taken for the three different storage times where the shortest storage time corresponds to the hardest spectrum. The straight lines are exponential fits to the data. The results of the fits can be found in Table 4.1.

still affected by the opening of the shutter and much smaller emptying times for the UCN that just happen to be at the right place to leave the chamber, they were discarded. The measured data are shown in Fig. 4.37 for the three phases of measuring 8 s spin up, 20 s spin down and again 12 s spin up and for three different storage times. It is clearly visible that as the storage time is increased (corresponding to a softer spectrum) also the emptying times get larger. This is also confirmed in the fits to the data, the results of which are shown in Table 4.1. One obtains emptying time constants of about ~10 s for a storage time of 30 s, ~11 s for a storage time of 130 s and ~12 s for a storage time of 230 s. The fits have been performed with a single exponential and the obtained χ^2/dof confirm a good description of the data with this single exponential.

However, for the extraction of the spectrum a clear deviation from a single exponential behaviour would be necessary in order to see the influence of the different energy UCN all arriving at the detector with their corresponding characteristic time constants. I tried to extract a spectrum anyway and used two different methods: (i) Using a matrix relation in analogy to Eq. (4.17) and solving for the spectrum by matrix inversion and (ii) fitting the measured arrival times directly by a sum of exponentials corresponding to different energies, where the weighting factors in front of the different exponentials would yield an estimate of the spectrum. Both methods lead to results, which were clearly not the true spectrum as the values were oscillating between positive and negative contributions as a function of energy.

It remains to be seen whether the method of extracting the spectrum by using the emptying times becomes feasible in the measurements with the EDM apparatus at PSI. Possibly, the influence of the different time constants becomes more pronounced with the expected much higher UCN statistics. It will certainly also be worthwhile to perform dedicated measurements with the system proposed in Sec. 4.4.7 in order to calibrate the system with quasi monoenergetic UCN and being able to determine the emptying time constants for the different energies directly. This would then also reduce the uncertainty from the amount of diffuse scattering probability used in the simulation (see Fig. 4.36).

5 NEUTRON TO MIRROR-NEUTRON OSCILLATIONS

The results of the following searches for neutron to mirror-neutron oscillations have been published in [104, 105]. This chapter is based on these two publications while at the same time giving more details on the measurements and analyses and a more general introduction.

5.1. INTRODUCTION TO THE IDEA OF MIRROR MATTER

The idea of restoring global parity symmetry by introducing mirror particles dates back to Lee and Yang. In their famous paper [106], they write in one of the last paragraphs:

> *If such asymmetry is indeed found, the question could still be raised whether there could not exist corresponding elementary particles exhibiting opposite asymmetry such that in the broader sense there will still be over-all right-left symmetry.*

In [107], this idea has been significantly expanded and was later adapted to the framework of the Standard Model of particle physics [108]. An excellent review of the historical evolution of the idea of mirror particles is [109]. In the "Mirror World", there would exist a complete copy of our "ordinary" particle spectrum, the only difference being a weak interaction of the form $V+A$. In this way, parity would, in a global sense, be restored. This is shown in Fig. 5.1 where the up/down-asymmetry of the decay electrons for polarised ^{60}Co - the experimental discovery of parity violation [110] - is matched by the opposite asymmetry of the ^{60}Co$'$.

Being an exact copy of our ordinary particle spectrum, the masses of the mirror particles and the interaction in between mirror particles (mediated by mirror exchange bosons) are exactly the same as for ordinary particles. Interactions between ordinary and mirror particles are possible. As gravity is understood to be linked to the curvature of space and as both ordinary and mirror particles exist in the same space[1], they gravitationally attract each other. Apart from gravity, new interactions could lead to mixings between neutral particles — such as neutrinos, pions, kaons, photons, Higgses, or neutrons — and their mirror partners. In the past, a mirror matter explanation has been put forward to explain many so called anomalies. In the following, I will briefly describe them.

DARK MATTER, MIRROR STARS, MIRROR PLANETS

It has already been noted in [107, 111], that mirror matter could form macroscopic bodies that are invisible to us apart from their gravitational interaction. In [112], mirror

[1] "Mirror World" thus being a misleading term.

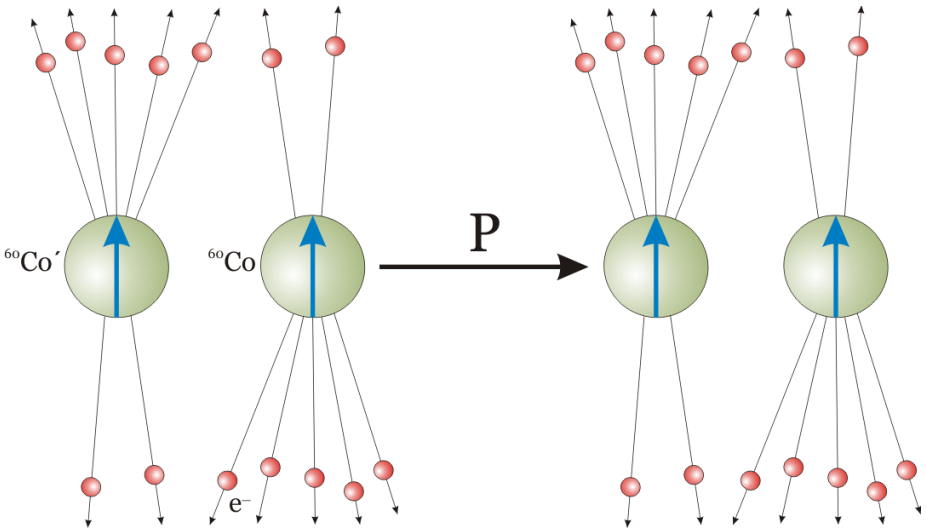

Figure 5.1.: Example of the restoration of parity by adding mirror particles: The observed up/down-asymmetry in the decay of polarised ^{60}Co is matched by the inverse asymmetry of ^{60}Co′

stars were put forward as an explanation for massive compact halo objects (MACHOs). Additionally, in [113] it was speculated that exoplanets detected using the doppler shift technique could actually be mirror planets. Of course, mirror matter is also a candidate for general Dark Matter. So far, several articles, e.g. [114, 115, 116, 117], showed the viability of mirror matter as a Dark Matter candidate and the implications for cosmology. According to [118], the mirror matter explanation for Dark Matter also naturally leads to a positive detection signal for the DAMA/LIBRA experiment [119] whilst being invisible to the other Dark Matter search experiments.

VIOLATION OF THE GREISEN-ZATSEPIN-KUZMIN CUTOFF

The Greisen-Zatsepin-Kuzmin (GZK) cutoff [120, 121] denotes an upper energy limit for ultra-high energy cosmic rays from distant sources impinging on earth. Above this limit, their energy is high enough to produce pions in scatterings with photons from the cosmic microwave background. Thus, they continuously loose energy until it falls below the cutoff. Measurements from the AGASA collaboration [122] showed a violation of the GZK cutoff. Many theories have been put forward to explain this violation among which were fast neutron to mirror-neutron oscillations [123, 124, 125]. According to this theory the ultra-high energy cosmic ray would cover parts of its path in its mirror state. Due to cosmological constraints, the temperature of the mirror cosmic background has to be lower [126] and thus the mirror photon density in the universe is smaller leading to less scatterings between mirror protons and mirror photons. In the meantime, newest data seem to confirm the existence of the GZK cutoff [127, 128].

ORTHOPOSITRONIUM LIFETIME ANOMALY

For quite some time, there was a discrepancy of several standard deviations between the measured and calculated lifetime of orthopositronium. In the meantime, this dis-

crepancy has been reconciled [129]. Invisible decays of orthopositronium were one of the possibilities to explain the difference. As such, the decay of orthopositronium into its mirror partner due to photon–mirror-photon mixing was one of the candidates [130]. So far, no invisible decay of orthopositronium has been found [131, 132]. However, the null results allowed to set limits on the strength of a possible photon–mirror-photon mixing.

NEUTRINO MIXING ANOMALIES

As oscillations between neutrinos and their mirror partners are possible in addition to the oscillations between ordinary neutrinos, the parameter space for mixing angles, etc., is enlarged. The additional degrees of freedom can be used to incorporate otherwise contradicting results as those of the LSND experiment [133, 134].

PIONEER ANOMALY

The two space crafts Pioneer 10 and Pioneer 11 are on trajectories leading out of the solar system. Calculating the accelerations acting on them due to gravity, there remains for both of them a residual, small acceleration directed towards the sun of $\sim 8 \times 10^{-10}\,\mathrm{m/s^2}$ [135]. Many explanations have been put forward. Among those is also an attempt to explain the acceleration as the result of the interaction (due to photon mirror-photon mixing) of the spacecraft with mirror matter [136].

ANOMALOUS IMPACTS

There happened several meteor-like impacts on earth for which it remained doubtful whether it really was a meteoroid that hit the earth (e.g., due to the lack of meteoritic debris). Among those is the famous event in Tunguska, Russia, in the year 1908. In [114, 116], it was speculated that such events could be due to a mirror meteoroid hitting the earth. There are even two techniques proposed to detect the mirror matter now lying on the surface: (i) cooling down of samples due to mirror-photon radiation [137] and (ii) the weight loss of samples after centrifuging [138].

5.2. FIRST DIRECT EXPERIMENTAL LIMIT ON nn' OSCILLATIONS

5.2.1. INTRODUCTION

As described above, fast neutron (n) to mirror-neutron (n') oscillations were put forward in [124] to explain ultra-high energy cosmic rays. As no limit on the oscillation time $\tau_{nn'}$ existed, a crude limit of $\tau_{nn'} \gtrsim 1\,\mathrm{s}$ [124] was derived from the measured neutron loss of 5% in the magnetically shielded flight tube of the experiment searching for neutron to antineutron oscillations [139].

The typical energy scale probed by nn' oscillations is on the order of 10 TeV (see Appendix A.8).

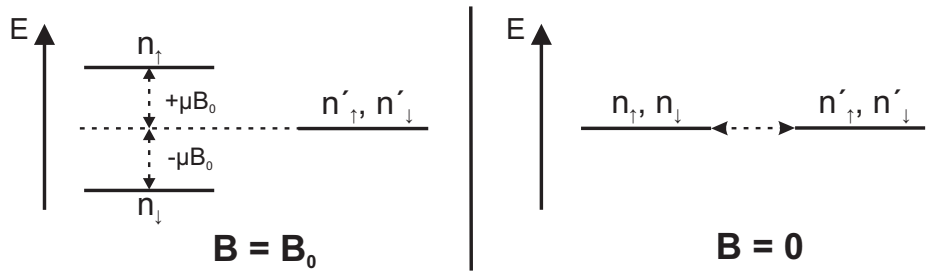

Figure 5.2.: Energies of spin up and down neutrons n and mirror neutrons n'. In the case of an applied magnetic field B, the energy splitting amounts to $\mu_n B$. For zero magnetic field, the two states are degenerate.

The fact that no direct limit on neutron to mirror-neutron oscillations existed, was one of the biggest motivations to conduct an experiment searching for those oscillations.

5.2.2. EXPERIMENTAL TECHNIQUE

Possible approaches to nn' oscillation experiments with sensitivities of several hundred seconds have been discussed in [140]. One approach is to search for nn' oscillations by comparing the storage of ultracold neutrons in vacuum in a trap in the presence and the absence, respectively, of a magnetic field. The essential idea is that the neutron and mirror neutron states would be degenerate in the absence of a magnetic field and nn' transitions could occur (see Fig. 5.2). Here, the absence of mirror magnetic fields at the location of the experiment has to be assumed. Neutron to mirror-neutron oscillations in the presence of a mirror magnetic field will be discussed in Section 5.3. The interaction of the neutron with a magnetic field lifts the degeneracy and suppresses the transition into a mirror neutron which, of course, does not interact with the ordinary magnetic field, nor with the trap via the ordinary strong interaction. Thus, the oscillation into mirror neutrons adds a loss channel for ultracold neutron storage. If nn' transitions occurred, the storage time constant for ultracold neutrons in a trap with magnetic field would be longer than without magnetic field. One should note that this disappearance method only measures neutron loss as a function of an applied magnetic field. A signal will not prove the oscillation into mirror neutrons, only that some magnetic field dependent loss channel exists[2]. In the absence of a signal, however, limits can be set on $\tau_{nn'}$. One can imagine other exotic disappearance channels for the neutron, among which only the antineutron channel is tightly constrained [139].

5.2.3. THEORY OF nn' OSCILLATIONS AND APPLICATION TO UCN STORAGE EXPERIMENTS

The formulation of the nn' oscillation is analogous to the evolution of other simple two state systems such as spin $\frac{1}{2}$, $K^0\bar{K}^0$, or $n\bar{n}$ mixing (see, e.g., [141, 142] and Appendix A.7).

[2] In order to prove the oscillation mechanism, one would have to observe, e.g., regenerating neutrons in an adjacent storage chamber.

The energy difference between neutron and mirror neutron states due to magnetic field interaction with the neutron magnetic moment μ is μB (see Fig. 5.2). For convenience, the notation of [11, 140] is adopted and a characteristic frequency $\omega \equiv \frac{\mu B}{2\hbar}$ defined, which corresponds to half the energy splitting. The probability $P_{nn'}$ for a UCN to be found as a mirror neutron after a time t can then be written as

$$P_{nn'}(t) = \frac{\sin^2(\sqrt{1+(\omega\tau_{nn'})^2} \times t/\tau_{nn'})}{1+(\omega\tau_{nn'})^2}. \tag{5.1}$$

The time t is limited by the free flight time t_f between two wall collisions. The wall collision frequency is determined by $\frac{1}{t_f}$. The effective transition rate of UCN into mirror neutrons is then given by

$$R = \frac{1}{t_f} P_{nn'}(t_f). \tag{5.2}$$

For a real system, the factors on the right hand side of Eq. (5.2) must be properly averaged over the distribution of flight times between collisions during the storage time t_s:

$$R_s = \frac{1}{\langle t_f \rangle_{t_s}} \langle P_{nn'}(t_f) \rangle_{t_s} \tag{5.3}$$

In experiments, one searches for a weak coupling, thus long $\tau_{nn'}$: so in practice $\omega\tau_{nn'} \gg 1$ in Eq. (5.1). Two limits are considered for Eq. (5.1): In the first case ("$\uparrow\downarrow$"), $\omega_{\uparrow\downarrow} t_f \gg 1$ (large B-field), many oscillations take place and the $\sin^2(..)$ term of Eq. (5.1) is averaged to $\frac{1}{2}$ because t_f varies along UCN trajectories:

$$R_{s,\uparrow\downarrow} = \frac{1}{\langle t_f \rangle_{t_s}} \frac{1}{2(\omega_{\uparrow\downarrow}\tau_{nn'})^2} \tag{5.4}$$

In the second case ("0"), $\omega_0 t_f \ll 1$ (small B-field), the n' component grows quadratically in time during the free flight:

$$R_{s,0} = \frac{1}{\langle t_f \rangle_{t_s}} \frac{\langle t_f^2 \rangle_{t_s}}{\tau_{nn'}^2} \tag{5.5}$$

Also regular losses of UCN must be considered, such as absorption and upscattering (during wall interactions or in collisions with rest gas), trap leakage and β decay. All these loss mechanisms contribute to the UCN storage time constant τ_{store} of the system; $\lambda_{\text{store}} = 1/\tau_{\text{store}}$ is the corresponding loss rate. Generally, the loss rate depends on UCN energy and for a spectrum of stored UCN the decay curve is a sum of exponentials. The total effect can be modelled by the relative populations c_i of different velocity classes, each with its own storage loss rate $\lambda^{(i)}$.

After storing an initial number $n(t{=}0)$ of UCN for some time t_s in a given magnetic field, one will detect the number of surviving UCN

$$n(t_s) = n(t{=}0) \times \sum_i c_i \exp[-(\lambda^{(i)}_{\text{store}} + R_s)\, t_s] \tag{5.6}$$

with the simple normalization condition $\sum_i c_i = 1$. For measurements in the limits $\uparrow\downarrow$ and 0 (only the magnetic field is changed), the ratio of detected UCN becomes independent of all the regular UCN loss mechanisms

$$N_{0/\uparrow\downarrow} \equiv \frac{n_0(t_s)}{n_{\uparrow\downarrow}(t_s)} = \exp[(R_{s,\uparrow\downarrow} - R_{s,0})\, t_s]. \tag{5.7}$$

In the absence of other effects, neutron to mirror-neutron oscillations lead to $N_{0/\uparrow\downarrow} < 1$.

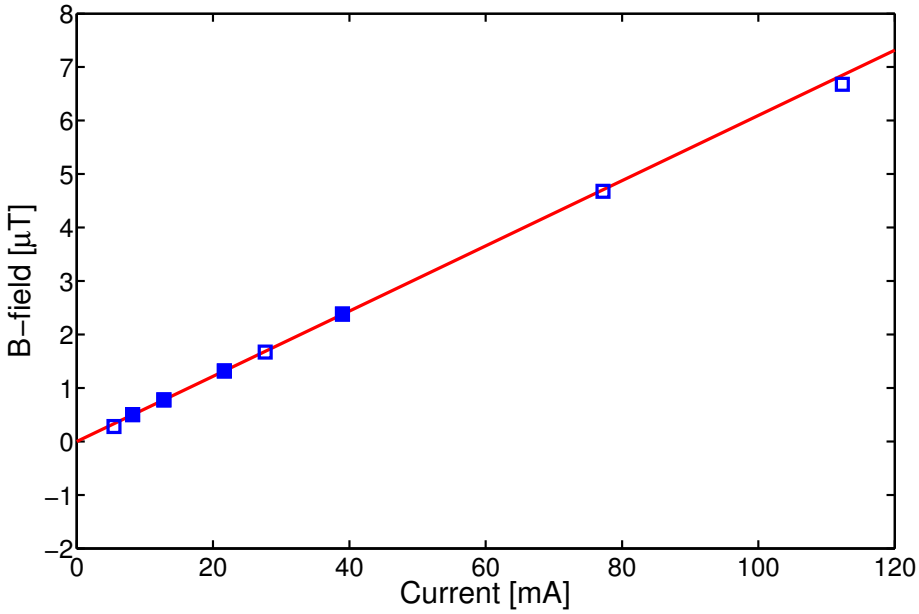

Figure 5.3.: The magnetic field measured by the cohabiting mercury magnetometer as a function of current in the main coil (blue squares). The red solid line shows a linear fit to the 4 data points marked with a filled symbol.

5.2.4. MEASUREMENTS

The UCN storage experiments were performed at the Institut Laue-Langevin using the experimental setup of the neutron EDM experiment [26, 58]. A typical measurement cycle consisted of (i) a filling time of 40 s with the beam switch connecting the storage chamber to the ILL PF2/EDM beam line [15] allowing *unpolarized* UCN to enter the storage volume, (ii) different storage times t_s when the UCN isolation shutter to the storage chamber was closed and (iii) 40 s counting time with the UCN shutter open and the beam switch connecting the storage chamber to the ^{3}He filled UCN detector [94]. The pressure inside the storage chamber was always better than 10^{-3} mbar in order to make sure that the nn' degeneracy is not lifted by the interaction of UCN with the rest gas.

The UCN storage chamber has a volume $V \sim 21$ l and a surface area of $A \sim 5400\,\mathrm{cm}^2$. The limit for stored UCN velocity is 4.1 m/s. From kinetic gas theory, the mean free path of UCN between wall collisions is $\frac{4V}{A} \approx 0.16$ m, the mean velocity is about 3 m/s [57] and, thus, $\langle t_f \rangle \approx 0.053$ s. One obtains $\omega \langle t_f \rangle \sim 1$ at a magnetic field of $B \sim 0.42\,\mu$T; the limiting cases are obtained for magnetic fields of more than a few μT ($\uparrow\downarrow$) and of less than a hundred nT (0), respectively.

Different magnetic field configurations were used: up ($B_\uparrow$), off ($B_0 = 0$) and down ($B_\downarrow$). The strength of the magnetic field was adjusted by the current through the main magnetic field coil. The relevant measurements were taken at $|B_{\uparrow\downarrow}| \approx 6\,\mu$T (100 mA). The magnetic field (B_z, along the main magnetic field direction) as a function of the applied current was measured using the Hg cohabiting magnetometer [51] for fields between 0.3 μT and 7 μT (see Fig. (5.3)). For lower fields the Hg magnetometer could not be used. A linear fit to 4 data points between 0.5 and 2.5 μT, for which the DAQ

could successfully extract the Larmor frequency, was performed resulting in an offset of $a = (-0.0023 \pm 0.0026)\,\mu$T and a slope of $b = (0.06097 \pm 0.00017)\,\mu$T/mA. The errors of a and b are dominated by the error on the current I in the coil. The error of I was scaled to produce a reduced χ^2 of 1 to compensate for only guessing the errors on the applied voltage and the measured resistance. In order to assess the errors on a and b, the endpoints of the $\Delta\chi^2 = 1$ error ellipsis were evaluated. The Hg data set shows a perfectly linear dependence of the field on applied current and results in $|B_{z,0}| = 2.3 \pm 2.6$ nT when extrapolated to zero current. This value for the magnetic field along the main field axis indicates a residual absolute B-field below 13 nT because of the absence of a preferred spatial direction[3]. The zero field B_0 for the actual measurements was set by switching off the coil current and demagnetizing the four-layer Mu-metal shield surrounding the storage chamber. Additionally, 3-axis fluxgate sensors were used directly above the storage chamber in order to verify that the residual B-field was sufficiently small for the purpose of our experiment. The B-field configurations of the experiment were very well reproducible, and in particular B_0 within less than 1 nT. The direct limit on $|B_0|$ obtained from the fluxgates is, however, somewhat weaker: it was found that the connectors of the commercial devices are slightly magnetic, leading to offset fields at the location of the sensor on the order of 25 nT. Although the residual field is probably on the level of a few nT, we give a conservative limit of $|B_0| < 50$ nT, which is sufficient for our purpose here, i.e., for the limiting case "0".

Most of the measurements were performed repeating the sequence (a) (B_0, $B_\uparrow$, $B_\downarrow$, B_0, B_0, $B_\downarrow$, B_0, $B_\uparrow$) with field changes typically every 1.5 h during day time. The demagnetization procedure before B_0 measurements took about half an hour. For a given B-field configuration 16 UCN cycles were measured: 4 for each storage time of $t_s = 100$ s, 50 s, 175 s, and again 100 s. Night runs were taken for longer periods at one B-field configuration with $t_s = 100$ s. They were used to check on the long term stability of the system. It was found that drifts of the count rates were slow and on a level below 0.3% over several hours. This agrees in magnitude with changes in the reactor power, but a direct correlation could not be established. The count rate drifts were sufficiently slow to be averaged out in the day runs with frequent changes of the B-field configuration. For $t_s = 50$ s, some data was taken using another sequence (b), ($B_\uparrow, B_\downarrow, B_0$) while checking on an unexpected count ratio $N_{0/\uparrow\downarrow}$ (see below).

The time constant for UCN to leave the storage chamber with the shutter open was measured to be $\tau_{op} = 11.4 \pm 0.6$ s. Mirror neutrons can leave the system also during filling and counting. The relevant average times t_s^* in our storage system are thus longer than the times between closing and opening the UCN shutter. One can replace t_s in Eq. (5.7) by t_s^* and, because R_s changes only rather weakly with t_s and τ_{op} is much smaller than t_s, one finds to very good approximation $t_s^* = t_s + 2\tau_{op}$. We assign a conservative systematic error of ± 3 s to t_s^*.

5.2.5. DATA ANALYSIS & DETERMINATION OF A LIMIT ON $\tau_{nn'}$

For data analysis, each B-field configuration was first treated separately. The distributions of single-cycle counts n were found to be consistent with Gaussians with standard deviations $\sigma \approx \sqrt{n}$ with no additional systematics. As an example, Fig. 5.4 shows the

[3] At 95% C.L., one has $B[nT] < \sqrt{3}(2.3 + 1.96 \times 2.6)^2$.

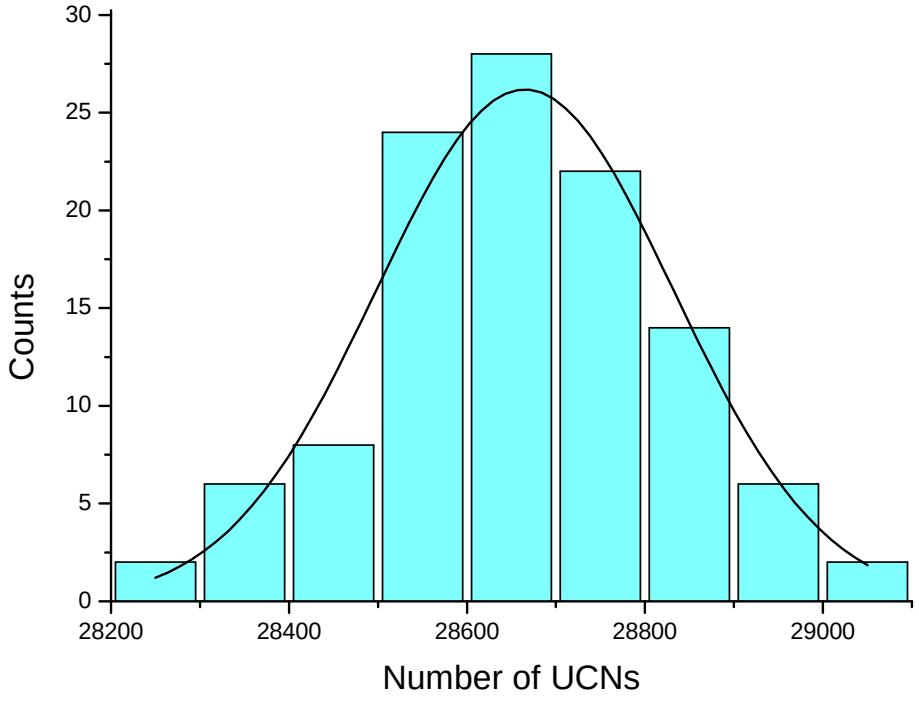

Figure 5.4.: Histogram of the measured UCN counts for the storage time of 100 s. The solid line is a gaussian fit to the data. The fitted width is in perfect agreement with a width expected from statistics.

t_s [s]	50 (a)	50 (b)	100 (a)	175 (a)
t_s^* [s]	73 ± 3 (a)	73 ± 3 (b)	123 ± 3 (a)	198 ± 3 (a)
$n(B_0)$	44317 ± 40	44363 ± 53	28635 ± 21	17015 ± 22
$n(B_\uparrow)$	44197 ± 53	44443 ± 53	28671 ± 30	17047 ± 31
$n(B_\downarrow)$	44128 ± 53	44316 ± 46	28596 ± 30	16974 ± 31
$n(B_{\uparrow\downarrow})$	44163 ± 38	44371 ± 35	28633 ± 22	17011 ± 22
$N_{0/\uparrow\downarrow}$	1.0035(13)	0.9998(15)	1.0001(11)	1.0002(18)
	1.0019(10)			

Table 5.1.: Measured total UCN counts n normalized per cycle for the day sequences ((a), (b), see text) at different storage times t_s^* (with systematic error) and magnetic field configurations. $n(B_{\uparrow\downarrow})$ is the weighted average of $n(B_\uparrow)$ and $n(B_\downarrow)$, and $N_{0/\uparrow\downarrow} = n(B_0)/n(B_{\uparrow\downarrow})$.

t_s [s]	50	100	175
$\langle t_f \rangle_{t_s}$ [s]	0.0498(5)	0.0515(5)	0.0543(5)
$\langle t_f^2 \rangle_{t_s}$ [s^2]	0.00420(8)	0.00450(9)	0.00505(10)

Table 5.2.: Results for $\langle t_f \rangle_{t_s}$ and $\langle t_f^2 \rangle_{t_s}$ using Monte Carlo distributions of flight times between wall collisions [50]. Variation of parameters in the simulation is used to assign systematic uncertainties.

histogram of the measured UCN counts for the storage time of 100 s together with a gaussian fit. The fitted average UCN counts are $\mu = 28665 \pm 18$ and the width of the distribution $\sigma = 167 \pm 16$ – perfectly consistent with $\sqrt{\mu} = 169$. The counts per cycle for each configuration were thus statistically averaged, see Table 5.1. Figure 5.5 shows, that the averaged n data show some tendency to a linear dependence on the magnetic field. The effect to be constrained depends on $|B|^2$ (via ω^2), so the direct average of the +6 and -6 μT measurement values cancels any linear systematic effect, leaving only the possible oscillation effect and possibly remaining quadratic systematic contributions. The averaged n data is then used to calculate the count ratios $N_{0/\uparrow\downarrow}$ according to Eq. (5.7). For 50 s storage time and sequence (a), the count ratio $N_{0/\uparrow\downarrow}$ is larger than 1 by 2.7 standard deviations, which led to a remeasurement at this storage time (using sequence (b)) corroborating that this deviation was a statistical fluctuation. Both ratios $N_{0/\uparrow\downarrow}(50\,\text{s})$ are given in the table along with the obtained average. The individual results for $N_{0/\uparrow\downarrow}$ show no signal within their respective sensitivities and, as they are independent, can be used in a combined analysis. Following Eq. (5.7), one writes $N_{0/\uparrow\downarrow} = \exp(a\,t_s)$ with a fit parameter a. The fit gives $a = (5.38 \pm 5.78) \times 10^{-6}\,\text{s}^{-1}$. The value at the limit of the experimentally measured range ($t_s^* = 198$ s) was used to set the constraint on the neutrons which may have been lost, yielding

$$N_{0/\uparrow\downarrow}(t_s^* = 198\,\text{s}) = 1.00106 \pm 0.00114\,. \tag{5.8}$$

Results with $N_{0/\uparrow\downarrow} > 1$ are unphysical for nn' oscillations. In order to derive a limit on $N_{0/\uparrow\downarrow}$, the Bayesian approach described by the Particle Data Group is adopted (page 324 of Ref. [10]; probability distribution set to zero for $N_{0/\uparrow\downarrow} > 1$; see Fig. 5.6 for the graphical illustration of the method) and one obtains

$$N_{0/\uparrow\downarrow}(t_s^* = 198\,\text{s}) > 0.99835 \text{ s (95\% C.L.)}. \tag{5.9}$$

In order to derive the limit on $\tau_{nn'}$, the flight time distribution averages $\langle t_f \rangle_{t_s}$ and $\langle t_f^2 \rangle_{t_s}$ are needed as additional input. A better determination than the one from the kinetic gas theory argument given above was obtained by Monte Carlo calculations using Geant4UCN [81]. The parameters of the simulation (mainly material properties, such as Fermi pseudo-potential, loss probability per wall reflection, and fraction of diffuse to specular reflection) have been tuned to reproduce measurements of the UCN beam energy spectrum and filling, storage, and emptying time curves of the apparatus. Excellent agreement with the observables is obtained, which justifies the extraction of the

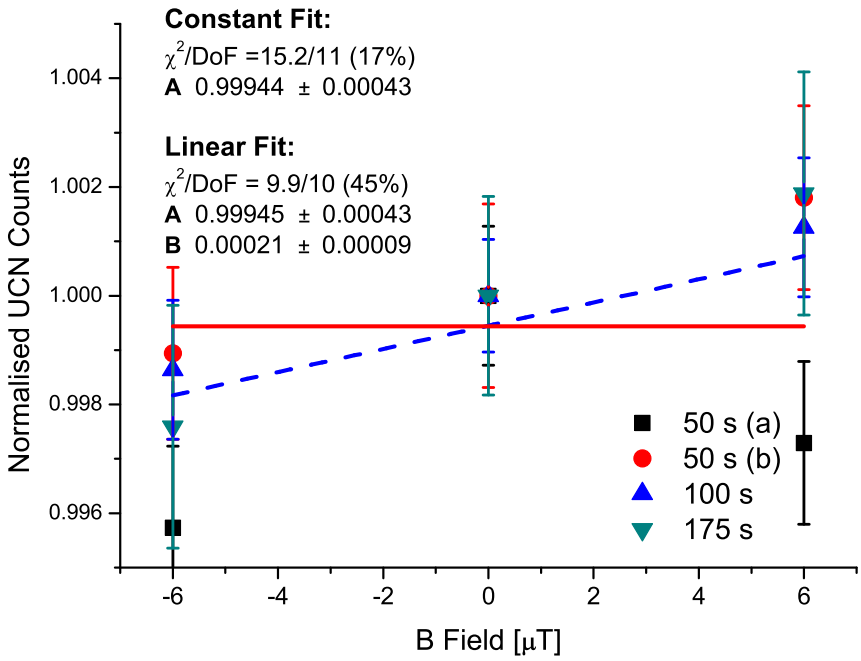

Figure 5.5.: Data from Table 5.1 plotted as a function of applied magnetic field B and normalised to 1 at zero magnetic field. Positive (negative) B corresponds to field direction up (down). Additionally, a constant and a linear fit to the data is given. The percentages correspond to the probability of obtaining an equal or higher χ^2 for the given degrees of freedom. The data favour a linear fit with the constant fit not being excluded.

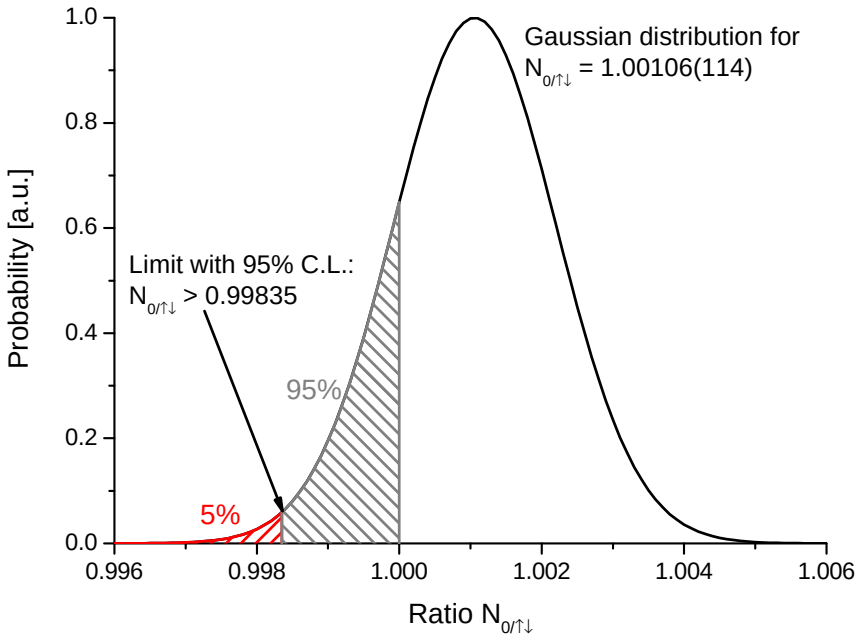

Figure 5.6.: Derivation of a limit for a given confidence level (C.L.) near a physical boundary ($N_{0/\uparrow\downarrow} > 1$) using the Bayesian approach as described in [10].

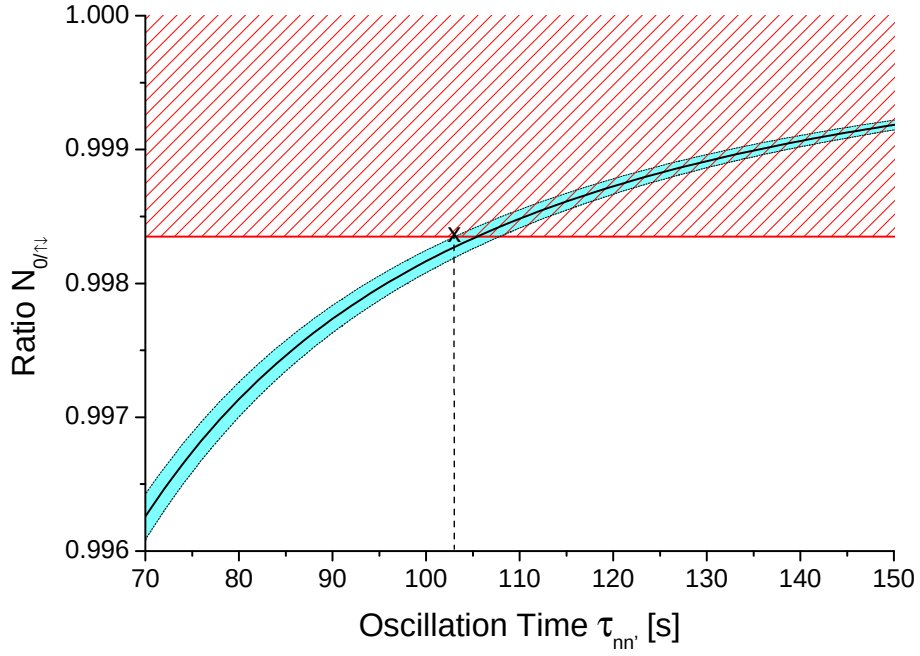

Figure 5.7.: The count ratio $N_{0/\uparrow\downarrow}$ as a function of the oscillation time (see Eq. (5.7)). The dashed region indicates the allowed region of Eq. (5.9). The error band of the curve displays the systematic uncertainties, see text. The x indicates the point at which the limit on $\tau_{nn'}$ is evaluated.

required flight time distributions. The averages are given in Table 5.2. The assigned systematic uncertainties were derived by varying the material parameters of the simulation, the largest influence coming from the loss probabilities per wall collision.

The limit on the oscillation time is obtained using the limit on lost neutrons, Eq. (5.9), the average free flight time values (at $t_s = 175$ s, from Table 5.2) in Eq. (5.7) and solving for $\tau_{nn'}$. The systematic uncertainties are taken into account for the limit on $\tau_{nn'}$ by adding (or subtracting) them simultaneously in order for them to weaken the limit, i.e., $\langle t_f \rangle_{t_s} = 0.0548$ s, $\langle t_f^2 \rangle_{t_s} = 0.00515\,\text{s}^2$ and $t_s^* = 195$ s. With a reminder of the assumptions (negligible mirror magnetic field, no conventional strong or electro–magnetic interactions of the mirror neutron n', and degeneracy of n and n' in the gravitational field), the final limit on the oscillation time $\tau_{nn'}$ is given as

$$\tau_{nn'} > 103\,\text{s (95\% C.L.)}\,. \tag{5.10}$$

Figure 5.7 displays the dependence of $N_{0/\uparrow\downarrow}$ on $\tau_{nn'}$ (see Eq. (5.7)) with the band indicating the influence of the systematic uncertainties. The 95% confidence limit of Eq. (5.9) is shown and the cross marks the point which determines the limit on the oscillation time.

5.2.6. DISCUSSION

The result impacts the role nn' oscillations can play in the transport of ultra-high energy cosmic rays over large distances [124, 125] but it may not completely rule out the nn'

explanation for events above the GZK cutoff. This would only be the case for limits on $\tau_{nn'}$ much larger than the neutron lifetime τ_n. However, the newest data on ultra-high energy cosmic ray seem to indicate no violation of the GZK cutoff (see Section 5.1), thereby diminishing this motivation for nn' searches. Nevertheless, the search for nn' oscillations is an excellent tool to constrain the theory of mirror matter or new theories yet to be developed. This was also acknowledged by the Particle Data Group with the inclusion of the above limit (Eq. (5.10)) into the the "Review of Particle Physics" (page 1071 of [10]). Only a few weeks after the publication of the result, a new limit of $\tau_{nn'} > 414$ s (90% C.L.) was reported [143] and in the meantime further improved to $\tau_{nn'} > 448$ s (90% C.L.) [144] using the same measurement technique and analysis method. They benefitted from a ten times larger storage volume, thus increasing the free flight time by a factor two and the stored UCN by roughly a factor 10 [143].

Rewriting Eq. (5.7) in a simplified form, one obtains

$$N_{0/\uparrow\downarrow} = 1 - \frac{t_f t_s}{\tau_{nn'}^2} = 1 - \frac{t_f^2}{\tau_{nn'}^2}\frac{t_s}{t_f}. \tag{5.11}$$

This corresponds to $\frac{t_s}{t_f}$ measurements with a single neutron where every free flight time contributes a factor $\frac{t_f^2}{\tau_{nn'}^2}$ to the suppression of the ratio $N_{0/\uparrow\downarrow}$[4]. From Eq. (5.11) it is straightforward to calculate the limit that one is able to set given a null-result:

$$\tau_{nn'} > \sqrt{\frac{t_f t_s}{1 - N_{0/\uparrow\downarrow} + \mathscr{C}\Delta N_{0/\uparrow\downarrow}}} \tag{5.12}$$

$\mathscr{C}$ is a constant and depends on the level of confidence for which the limit should hold and $\Delta N_{0/\uparrow\downarrow}$ denotes the error of the ratio $N_{0/\uparrow\downarrow}$. The limit on $\tau_{nn'}$ can thus mainly be improved by increasing the free flight time t_f (scaling like $\sqrt{t_f}$) and improving the statistics N (scaling like $\sqrt[4]{N}$). Measuring with longer storage times (scaling like $\sqrt{t_s}$) reduces at the same time the available statistics due to the ordinary losses during storage (characterised by the time constant τ_s). It is straightforward to calculate, that for a single measurement the storage time with the highest sensitivity to $\tau_{nn'}$ is given by $t_s = 2\tau_s$.

With a storage chamber occupying the whole inner space of the new shielding for the n2EDM experiment (cylinder with height 3 m and radius 1.5 m and thus $t_f \sim 0.3$ s), filling during each cycle all of the UCN produced in the PSI UCN source ($\sim 10^9$ UCN) and running for one year, it would be possible to set a lower limit on the oscillation time of $\mathscr{O}(10\,000$ s). An intermediate step with a larger storage chamber built into the existing shielding (reaching $t_f \sim 0.15$ s) and limited running time would reach sensitivities of the order $\mathscr{O}(1000$ s).

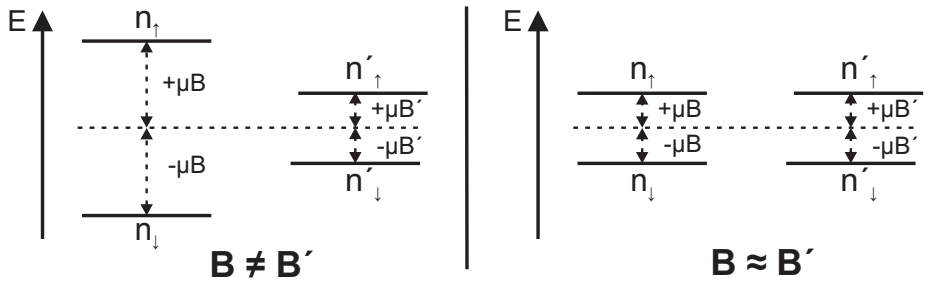

Figure 5.8.: In analogy to Fig. 5.2, this figure shows the energies of spin up and down neutrons n and mirror neutrons n' in the presence of B and B'. In the case $B \approx B'$, nn' oscillations can occur.

5.3. nn' OSCILLATIONS IN THE PRESENCE OF MIRROR MAGNETIC FIELDS

5.3.1. INTRODUCTION

In the previous section, the final result of the averaged UCN counts showed a slight asymmetry between magnetic field up and down in three of the four data sets (see Fig. 5.5). For negligible B', this asymmetry does not influence the final limit on $\tau_{nn'}$ as the oscillation probability depends only on the magnitude of B. However, in the presence of non-negligible B' such asymmetries could naturally arise [145]. So far, the limits on the oscillation time $\tau_{nn'}$ were obtained assuming a negligible mirror magnetic field B' (apart from an attempt in [144] for mirror magnetic fields in the range 0 to 1.2 μT). However, the limits on B' from, e.g., a limit on the amount of mirror matter inside the earth [146] are very weak. Photon–mirror-photon mixings, e.g., could provide an efficient mechanism to capture mirror matter in the earth allowing for B' of several μT [145]. Mirror magnetic fields not bound to the earth are also conceivable and would additionally lead to daily modulations in the UCN counts – an unmistakable signature of a possible origin of B'. In this section, the first systematic search for nn' oscillations in the presence of B' will be described. The basic measurement principle remains unchanged with the exception of scanning B in order to find a resonance of maximal UCN losses at $B \approx B'$ instead of at $B \approx 0$. In analogy to Fig. 5.2, Fig. 5.8 shows the energy levels of neutron and mirror-neutron in the presence of B and B' (neglecting the orientation of B and B').

5.3.2. THEORY OF nn' OSCILLATIONS IN THE PRESENCE OF A MIRROR MAGNETIC FIELD

For the calculation of the nn' oscillation probability with finite B', the arguments of [145] are followed. Defining $2\hbar\boldsymbol{\omega} \equiv \mu_n \boldsymbol{B}$ and $2\hbar\boldsymbol{\omega'} \equiv \mu_n \boldsymbol{B'}$ and introducing the oscillation time $\tau_{nn'}$ and the Pauli matrices $\boldsymbol{\sigma}$, the transition from the ordinary to the mirror state (and

[4] Thus, in beam experiments one has to compensate the factor $\frac{t_s}{t_f}$ by increased statistics while at the same time controlling the systematic beam fluctuations.

vice versa) is described by the interaction Hamiltonian

$$\mathscr{H} = \hbar \begin{pmatrix} 2\boldsymbol{\omega}\cdot\boldsymbol{\sigma} & \tau_{nn'}^{-1} \\ \tau_{nn'}^{-1} & 2\boldsymbol{\omega'}\cdot\boldsymbol{\sigma} \end{pmatrix}. \tag{5.13}$$

Defining a coordinate system with $\boldsymbol{b} = (0,0,b)$, $b = |\boldsymbol{\omega} + \boldsymbol{\omega'}|$, and $\boldsymbol{a} = (a_x, 0, a_z)$, $a_x = 2|\boldsymbol{\omega} \times \boldsymbol{\omega'}|/|\boldsymbol{\omega} + \boldsymbol{\omega'}|$, $a_z = (\boldsymbol{\omega}^2 - \boldsymbol{\omega'}^2)/|\boldsymbol{\omega} + \boldsymbol{\omega'}|$, leads to the 4×4 matrix

$$\mathscr{H} = \hbar \begin{pmatrix} b - a_z & -a_x & \tau_{nn'}^{-1} & 0 \\ -a_x & -b + a_z & 0 & \tau_{nn'}^{-1} \\ \tau_{nn'}^{-1} & 0 & b + a_z & a_x \\ 0 & \tau_{nn'}^{-1} & a_x & -b - a_z \end{pmatrix}. \tag{5.14}$$

$\mathscr{H}$ can be diagonalised using a transformation matrix with mixing angles fulfilling $\tan 2\theta = 1/(a_z \tau_{nn'})$, $\tan 2\phi = a_x/(b - \tilde{a}_z)$, and $\tan 2\phi' = a_x/(b + \tilde{a}_z)$ with $\tilde{a}_z = a_z\sqrt{1 + 1/(a_z\tau_{nn'})^2}$ [145]. The eigenvalues of $\mathscr{H}$ are $\pm 2\tilde{\omega}$ and $\pm 2\tilde{\omega}'$ given by $2\tilde{\omega} = a_x \sin 2\phi + (b - \tilde{a}_z)\cos 2\phi$ and $2\tilde{\omega}' = a_x \sin 2\phi' + (b + \tilde{a}_z)\cos 2\phi'$. The time dependent probability for the transition from n to n' is then given by

$$P_{nn'}(t) = \sin^2(2\theta)\left[\cos^2(\phi - \phi')\sin^2(t/\tau_-) + \sin^2(\phi - \phi')\sin^2(t/\tau_+)\right], \tag{5.15}$$

where $\tau_\pm = |\tilde{\omega} \pm \tilde{\omega}'|^{-1}$ are the effective oscillation times. The oscillation probability depends on the magnitude of B and B', the direction of B' given by the angle β relative to the up-direction of B (see below), the oscillation time $\tau_{nn'}$, and the time t.

5.3.3. APPLICATION OF THE OSCILLATION PROBABILITY TO UCN STORAGE EXPERIMENTS

During the storage of UCN inside a chamber, the relevant time t is the free flight time t_f between wall collisions in which the wave function is projected onto its pure n or n' state. The loss rate of UCN due to nn' oscillations is thus given as (see Eq. 5.3)

$$R_{t_s} = f_c P_{nn'} = \frac{1}{\langle t_f \rangle_{t_s}} \langle P_{nn'}(t_f) \rangle_{t_s}, \tag{5.16}$$

where f_c denotes the collision frequency and $\langle \ldots \rangle_{t_s}$ the averaging over the distribution of free flight times t_f during the storage time t_s.

There are two distinct regions for the evaluation of the nn' oscillation probability. The first is the off–resonance region. From evaluations of Eq. (5.15), this holds for $|B - B'| > 0.4\,\mu$T. In this region, the time dependent terms in Eq. (5.15) oscillate quickly and average to 1/2 over the t_f distribution. The loss rate is then expressed explicitly as

$$R_{t_s}^{\text{off}} = \frac{1}{\langle t_f \rangle_{t_s}} \frac{B'^2 + B^2 + 2B'B\cos\beta}{(B'^2 - B^2)^2} \frac{2\hbar^2}{\mu_n^2 \tau_{nn'}^2}. \tag{5.17}$$

On–resonance, $|B - B'| < 0.4\,\mu$T, the first term in Eq. (5.15) dominates for most of the parameter space. For that part of the parameter space, one has $\phi \approx \phi'$ and, since t/τ_- is small, $\sin^2(t/\tau_-) \approx (t/\tau_-)^2$. Therefore, one can replace t in Eq. (5.15) by $\sqrt{\langle t_f^2 \rangle_{t_s}}$ and write the loss rate as

$$R_{t_s}^{\text{on}} \approx \frac{1}{\langle t_f \rangle_{t_s}} P_{nn'}\left(\sqrt{\langle t_f^2 \rangle_{t_s}}\right). \tag{5.18}$$

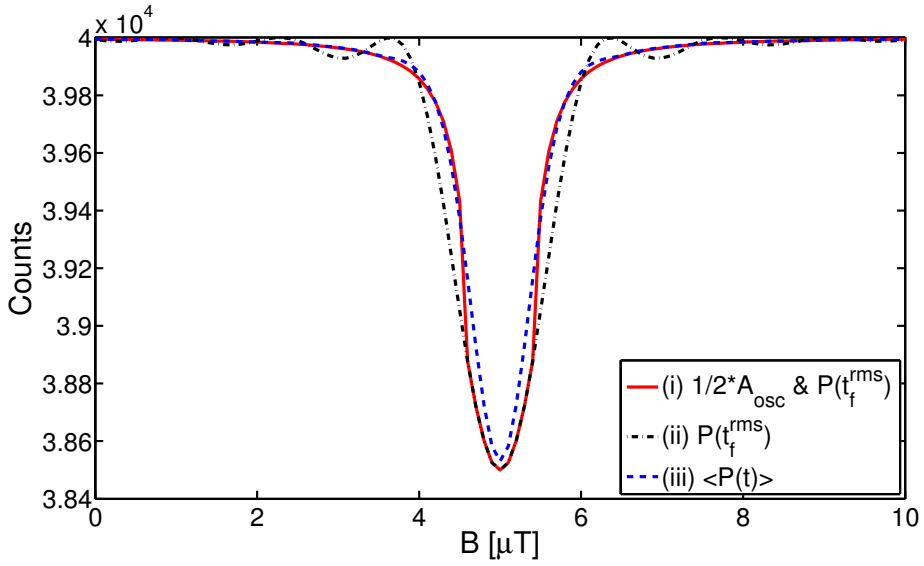

Figure 5.9.: The figure shows the counted UCN for an initial number of 40000 UCN and parameters $B' = 5\,\mu$T, $\tau_{nn'} = 10\,$s and $\beta = 0°$. The three curves correspond to evaluations of (i) the on/off-resonance combination of Eq. (5.17) and (5.18), (ii) the evaluation of Eq. (5.18) over the full B range and (iii) the full averaging over a realistic t_f distribution using Eq. (5.15). Deviations between (i) and (iii) are less than 1%.

The validity of Eq. (5.18) was checked by comparing to a full averaging over a realistic t_f distribution (see Fig. 5.9). Deviations were less than 1%. Anyhow, our final limit is based on calculations using Eq. (5.17).

In order to obtain the values for $\langle t_f \rangle_{t_s}$ and $\sqrt{\langle t_f^2 \rangle_{t_s}}$, as in Sec. 5.2 a detailed Monte Carlo simulation of the experiment was performed using GEANT4UCN [81] with parameters tuned to reproduce experimental data (such as characteristic time constants for filling, emptying, or storage). The t_f distributions were obtained from the time of the reflections of individual trajectories inside the storage chamber. Results are shown in Fig. 5.10 and given in Table 5.3 for the two storage times t_s used in the measurements. The parameters of the simulation were varied in ranges still reproducing the experimental data to assess the systematic uncertainties.

t_s [s]	75	150
$\langle t_f \rangle_{t_s}$ [s]	0.0403(4) → 0.0407	0.0442(4) → 0.0446
$\sqrt{\langle t_f^2 \rangle_{t_s}}$ [s]	0.0532(5) → 0.0527	0.0586(6) → 0.0580
t_s^* [s]	98(3) → 95	173(3) → 170

Table 5.3.: Results for $\langle t_f \rangle_{t_s}$ and $\sqrt{\langle t_f^2 \rangle_{t_s}}$ using Monte Carlo calculations of flight times between wall collisions and the effective storage times t_s^*. The values at the right side of the arrow denote the values used in the analysis in order obtain a conservative result.

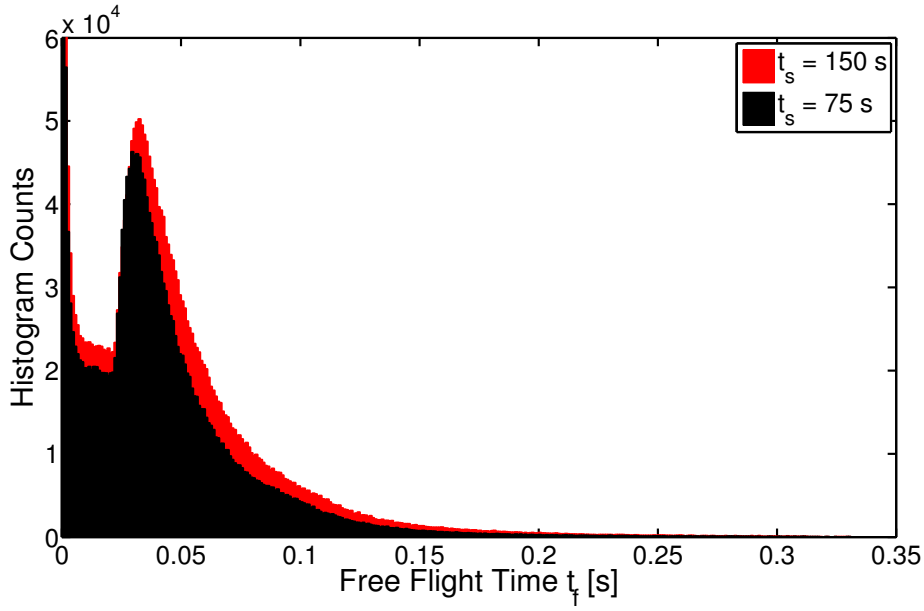

Figure 5.10.: Distribution of free flight times t_f inside the DPS storage chamber [44] of the nEDM apparatus for the two storage times $t_s = 75\,\mathrm{s}$ and $t_s = 150\,\mathrm{s}$. The distributions were obtained using a detailed GEANT4UCN [81] Monte Carlo simulation. The simulation here is an adapted version of the one used to calculate the values in Table 5.2 [50].

The number of surviving UCN after storage is

$$N(t_s^*) = N'_{0,t_s} \exp\left(-R_{t_s} t_s^*\right) \tag{5.19}$$

where N'_{0,t_s} is the initial number of UCN reduced by the usual losses during storage, and t_s^* is the effective storage time for the UCN, including not only the time when the neutrons are fully confined, t_s, but also the effects of storage chamber filling and emptying. The values for t_s^* are given in Table 5.3.

In the case of a mirror magnetic field not bound to the earth, the observed neutron counts could be modulated with a period corresponding to a sidereal day ($d_{sid} = 23.934\,\mathrm{h}$) as the angle β would be modulated. For the off–resonance case, the observed counts are then given by $N(t) = \mathscr{C} + \mathscr{A} \frac{t_s^*}{\langle t_f \rangle_{t_s}} \cos\left(2\pi(t - t_0)/d_{sid}\right)$ with

$$\begin{aligned} \mathscr{C} &\approx N'_0 \left(1 - \frac{t_s^*}{\langle t_f \rangle_{t_s}} \frac{B'^2 + B^2}{(B'^2 - B^2)^2} \frac{2\hbar^2}{\mu_n^2 \tau_{nn'}^2} \mp \frac{t_s^*}{\langle t_f \rangle_{t_s}} \frac{BB'_{||}}{(B'^2 - B^2)^2} \frac{4\hbar^2}{\mu_n^2 \tau_{nn'}^2} \sin\lambda\right), \\ \mathscr{A} &\approx \mp N'_0 \frac{BB'_{\perp}}{(B'^2 - B^2)^2} \frac{4\hbar^2}{\mu_n^2 \tau_{nn'}^2} \cos\lambda\,. \end{aligned} \tag{5.20}$$

$B'_{||}$ and $B'_{\perp}$ are the components of B' parallel and perpendicular to the earth's rotation axis, λ the latitude at the experimental site, t_0 the phase, and the $-(+)$ sign stands for magnetic field up (down).

5.3.4. MEASUREMENTS

The UCN storage experiments were conducted at the PF2/EDM beamline [15] at the Institut Laue-Langevin (ILL) using the apparatus for the search of the neutron electric dipole moment [26]. The main features of the apparatus are: (i) The possibility to efficiently store UCN in vacuum in a chamber made from deuterated polystyrene [44] and diamond-like carbon and (ii) the surrounding 4-layer Mu-metal shield together with an internal magnetic field coil that allowed to set and maintain magnetic fields with a precision of $\sim 0.1\,\mu$T. A typical measurement cycle consisted of filling unpolarised UCN for 40 s into the storage chamber of 21 litres, confining the UCN for 75 s (150 s) and subsequently counting $\sim 38\,000$ ($\sim 24\,000$) UCN over 40 s in a ^{3}He detector [94]. For a given magnetic field value, always 8 cycles were performed with a storage time of 75 s and 8 cycles with a storage time of 150 s. After these 16 cycles, the magnetic field direction was reversed from up to down and measurements continued for again 16 cycles. The averages of the different B field settings, applied randomly, were 0, 2.5 μT, 5 μT, 7.5 μT, 10 μT, 12.5 μT. Before doing a zero field measurement, the 4-layer magnetic shield was demagnetised resulting in $B < 50$ nT. In total, data taken continuously over approximately 110 hours were used for the analysis.

5.3.5. NORMALISATION OF THE UCN DATA

The data showed a trend to higher UCN counts over the course of the measurement period. The increase amounted to ~2.5% for 75 s storage time and ~5% for 150 s storage. This increase is attributed to slowly improving vacuum conditions inside the chamber. A combined fit to the two data sets was performed with the function

$$f(t) = N_{t_s} \exp\left(-C_p t_s e^{-\frac{t}{\tau_p}} - C_R t_s^2 e^{-\frac{t}{\tau_R}}\right) \tag{5.21}$$

with two normalisation constants N_{75} and N_{150} and two constants proportional to a decreasing overall pressure C_p (with a characteristic time τ_p) and a decreasing outgassing rate C_R (characteristic time τ_R and leading to an average pressure proportional to $C_R t_s$ during storage) of the storage chamber, which is sealed off from the pumps during storage, respectively. The measured UCN counts for $t_s = 75$ s together with the fit are shown in Fig. 5.11. The fitted parameters amount to: $N_{75} = 37\,970 \pm 23$, $N_{150} = 23\,845 \pm 29$, $C_p = (22.4 \pm 0.9) \times 10^{-5}\,\mathrm{s}^{-1}$, $\tau_p = (40.3 \pm 5.1)$ h, $C_R = (12.8 \pm 1.3) \times 10^{-5}\,\mathrm{s}^{-1}$, and $\tau_R = (2.7 \pm 0.5)$ h. The χ^2 per degree of freedom of 1385.7/1204 is satisfactory. Assuming a UCN loss cross section per molecule of $\mathcal{O}(10$ b), the fitted constants C_p and C_R translate into an initial pressure of $\mathcal{O}(10^{-3}$ mbar) and an initial outgassing rate of $\mathcal{O}(10^{-7}\frac{\mathrm{mbar}}{\mathrm{s}}\frac{\mathrm{l}}{\mathrm{cm}^2})$ which seem realistic [44]. The UCN counts for a given cycle were normalised by the prediction of Eq. (5.21) and the statistical error was slightly increased by adding the fit error in quadrature. Figure 5.12 shows the remaining drifts after normalisation. The residual drifts are less than 0.5% over several hours. Calculating the Pearson product-moment correlation coefficient $r = \frac{1}{n-1}\sum_{i=1}^{n}\frac{x_i-\langle x\rangle}{\sigma_x}\frac{y_i-\langle y\rangle}{\sigma_y}$ (see, e.g., [147]) between the UCN data sets and the reactor power (as shown in Fig. 5.12) results in values $0.1 \leq r \leq 0.3$ depending on the averaging of the reactor power. Such values of r are regarded as a small correlation. The effect of the residual drifts on the final result is negligible and no additional normalisation was thus performed.

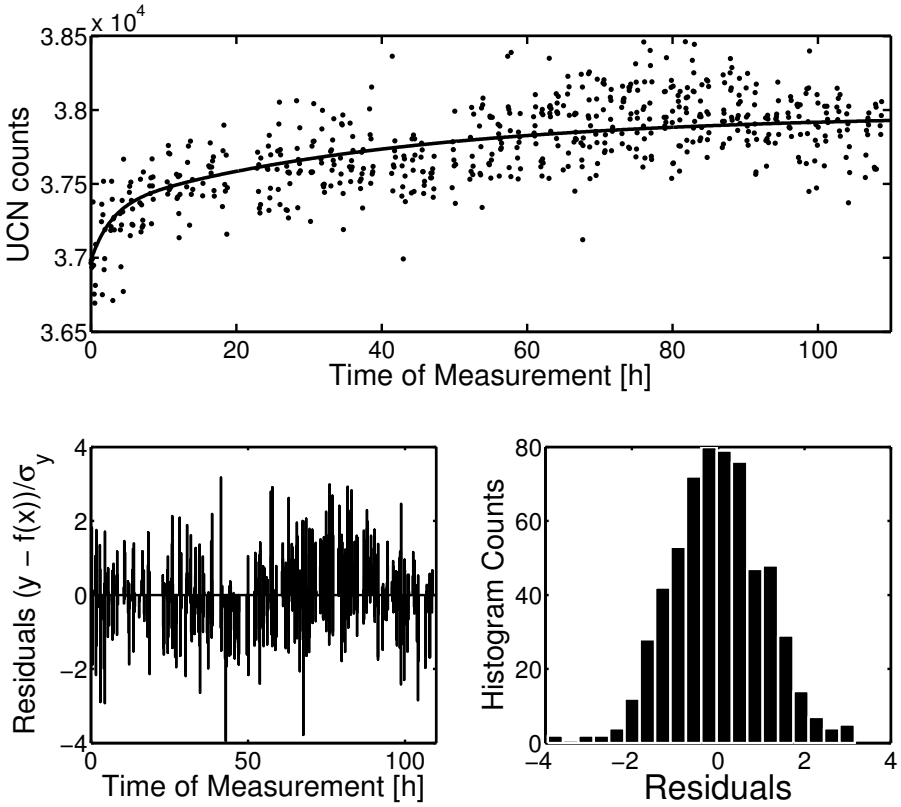

Figure 5.11.: Plot of the measured UCN counts for $t_s = 75\,\mathrm{s}$ storage time as function of time together with the fit using Eq. (5.21). Shown are also the residuals of the fit values $\left(\frac{y-f(x)}{\sigma_y}\right)$ and a histogram of those residuals.

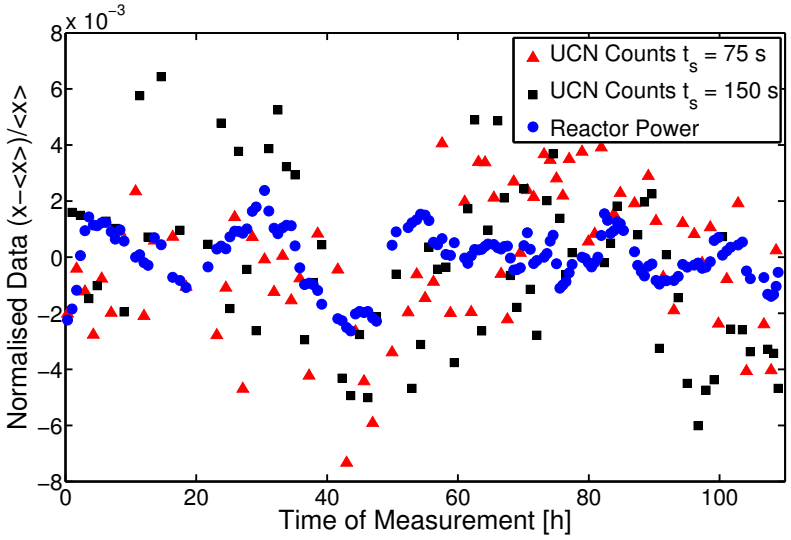

Figure 5.12.: Fluctuations in the measured UCN counts (after normalisation) and the one hour averages of the ILL reactor power. The UCN counts exhibit a small correlation to the reactor power.

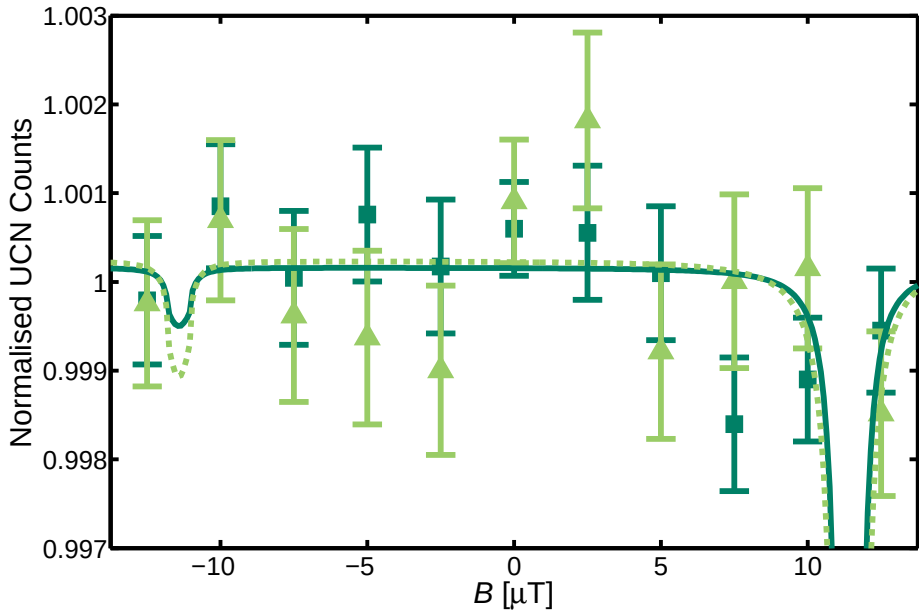

Figure 5.13.: Combined fit to the normalised UCN counts as a function of applied magnetic field B for 75 s (dark green squares and solid line) and 150 s (light green triangles and dashed line). Positive (negative) B values correspond to B field up (down).

5.3.6. ANALYSIS

Two different types of analyses were conducted: (i) The search for a modulation in the UCN counts and (ii) the search for a resonance in the UCN counts as a function of B. It is clear from Eqs. (5.20) and (5.17) that the resonance analysis will always be sensitive to nn' oscillations regardless of the origin of the mirror magnetic field and possible modulation periods whereas the modulation analysis is not. In Eq. (5.17), $\cos\beta$ will either be a fixed value or the average over a modulated $\cos\beta$. Additionally, the amplitude of the modulation tends to zero for small B' and the constant term $\mathscr{C}$ of the oscillation probability is for all parameters larger or equal to the modulated part $\mathscr{A}$ ($B'^2 + B^2 \geq 2B'B\cos\beta$). Given the same statistics and no systematic errors from averaging over longer periods, the resonance analysis will always yield tighter constraints on $\tau_{nn'}$ than the modulation analysis. As a means of cross-checking and discovering the possible origin of B', both types of analyses have been performed.

SEARCH FOR A RESONANCE

In order to search for a resonance in the loss rate at the point $B \approx B'$, all normalised UCN counts for individual B field settings were averaged (thereby averaging out any remaining long term drifts) and the results plotted as a function of B (see Fig. 5.13). A combined fit to the two data sets was performed using Eq. (5.19) with the following free parameters: two normalisation constants N'_{75} and N'_{150}, the magnitude of B', the angle β, and the oscillation time $\tau_{nn'}$. The value for B' was constrained to lie in the region $0\ldots12.5\,\mu$T as only in that region one would have unambiguous evidence for a possible resonance. The relevant, fitted parameters are $B' = 11.4\,\mu$T, $\beta = 25.3°$, and $\tau_{nn'} = 21.9\,$s.

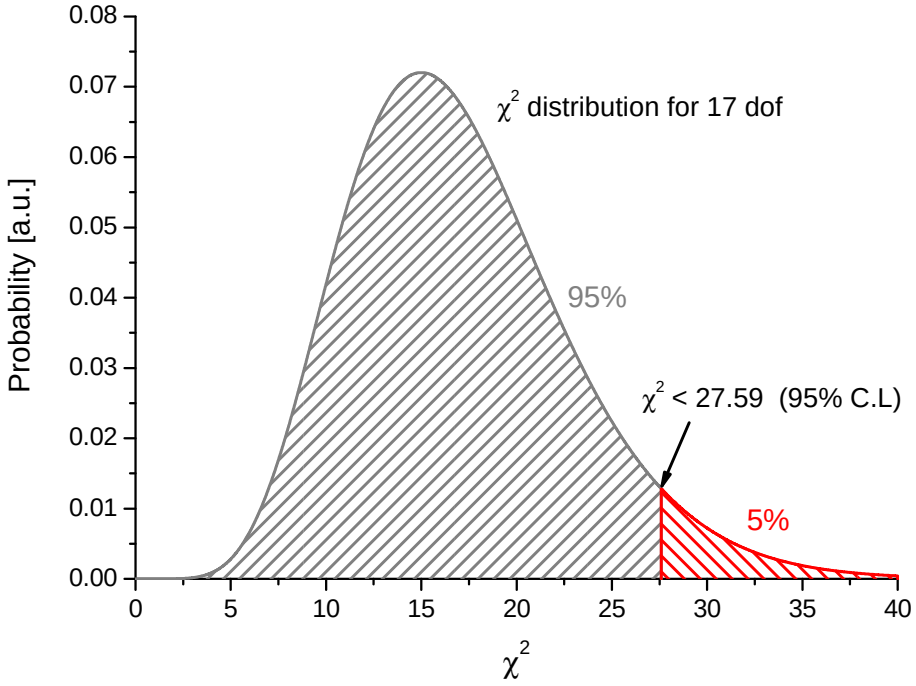

Figure 5.14.: χ^2-distribution for 17 degrees of freedom. At the value $\chi^2 = 27.59$ lies the 95% C.L. limit to obtain a smaller χ^2.

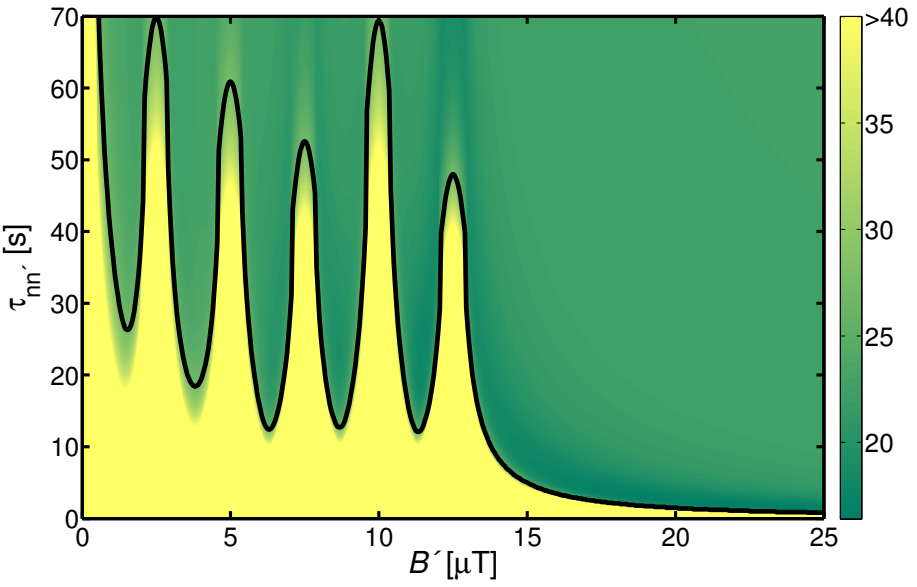

Figure 5.15.: Contour plot of the minimal χ^2 at the points $(B', \tau_{nn'})$. The solid line denotes the 95% C.L. contour line for an exclusion of $\tau_{nn'}$. The lower limit on $\tau_{nn'}$ was evaluated at the minimum of this contour for B' between 0 and 12.5 μT.

The χ^2 per degree of freedom (χ^2/dof = 17.86/17) is comparable to the one obtained with a constant fit (χ^2/dof = 22.72/21) and, additionally, the fitted resonance lies in between measured data points. There is therefore no evidence for nn' oscillations and the data were used to set a limit on $\tau_{nn'}$ for mirror magnetic fields between 0 and 12.5 μT. To do so, the minimal χ^2 at the points (B', $\tau_{nn'}$) was calculated by fitting the remaining free parameters N'_{75}, N'_{150}, and β, see Fig. 5.15. The 95% C.L. contour corresponds to $\chi^2 = 27.59$, the 95% C.L. for a χ^2 distribution with 17 degrees of freedom (see Fig. 5.14). Figure 5.15 also shows the loss of sensitivity to nn' oscillations for B' fields outside the range of applied magnetic fields. A lower limit on the oscillation time was evaluated as the minimal $\tau_{nn'}$ on this contour for B' between 0 and 12.5 μT:

$$\tau_{nn'} > 12.0\,\text{s (95\% C.L.)} \tag{5.22}$$

The 0.1 μT precision on individual non-zero B field values in the experiment leads in principle to a systematically improved limit. The improvement could not be quantified exactly, but an extreme case can be estimated from Table 5.5. An offset of 0.1 μT of all the measurements at one field configuration, would lead to a decrease of about 1% on the obtained limit at the maximum and lead to an increase of about 10% on the limit at the minimum of the exclusion contour. This effect is not included in the obtained result.

Additionally, the limit from Section 5.2 for negligible B' is improved by evaluating the exclusion contour line in Fig. 5.15 at the intercept with $B' = 0$: $\tau_{nn'} > 141\,\text{s}$ (95% C.L.).

ALTERNATIVE METHOD FOR THE LIMIT EXTRACTION

In order to gain more confidence in the chosen method to extract the limits on $\tau_{nn'}$, a frequentist confidence level analysis was performed for each value of B' (see Appendix A.9.2 for a description of the method). The results are shown in Fig. 5.16 together with the limits as obtained from the $\chi^2 = 27.59$ contour. The method failed to give a finite limit on $\tau_{nn'}$ for small B'. This is due to the fact that both of the normalised UCN counts for the two different storage times at $B = 0$ lie more than one standard deviation above 1. The probability for such an occurrence, expecting a value of 1, is 16% × 16% = 2.6%. In the frequentist analysis for a 95% C.L., searching for a dip in the UCN counts around $B = 0$ for small B', no limit is found as the Q-value lies in the 2.6% tail of the simulated distributions. For the remainder of the B' values, the extracted limits are quite comparable, with the χ^2-contour method being more conservative. Due to these two arguments, the χ^2-contour method was chosen to evaluate the final lower limit on the oscillation time.

ALTERNATIVE ANALYSIS FOR B'=0

For $B' = 0$, an analysis as given in Sec. 5.2 was performed. For that, the obtained normalised UCN counts for magnetic field up and down were averaged together and the value at 2.5 μT was discarded as it does not very well meet the necessary condition $\omega t_f \gg 1$ ($\omega t_f \sim 4.6$ for 2.5 μT) for averaging the $\sin^2(\ldots)$ term to $\frac{1}{2}$. The loss in statistics is negligible, as the limiting factor is the available statistics at $B = 0$ (see below). From those values, the ratio $N_{0/\uparrow\downarrow} \equiv \frac{n_0}{n_{\uparrow\downarrow}}$ as given in Eq. (5.7) was calculated. Fig. 5.17 shows the results of those ratios. As both of the values for the two storage times at $B = 0$ lie more

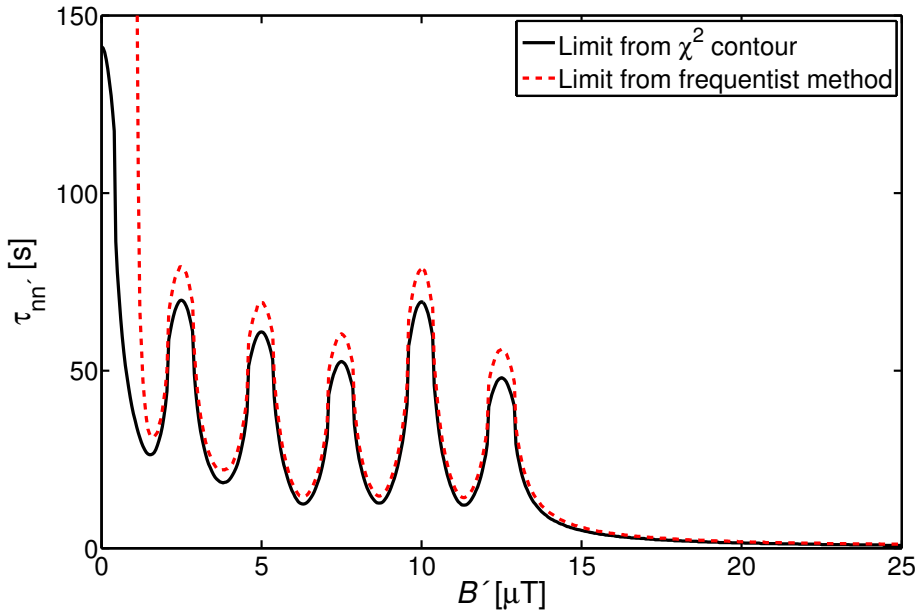

Figure 5.16.: Comparison of the lower limit on $\tau_{nn'}$ as calculated from (i) the $\chi^2 = 27.59$ contour and (ii) a frequentist confidence level analysis. The former, not failing for small B' and being more conservative, was chosen to evaluate the final limit.

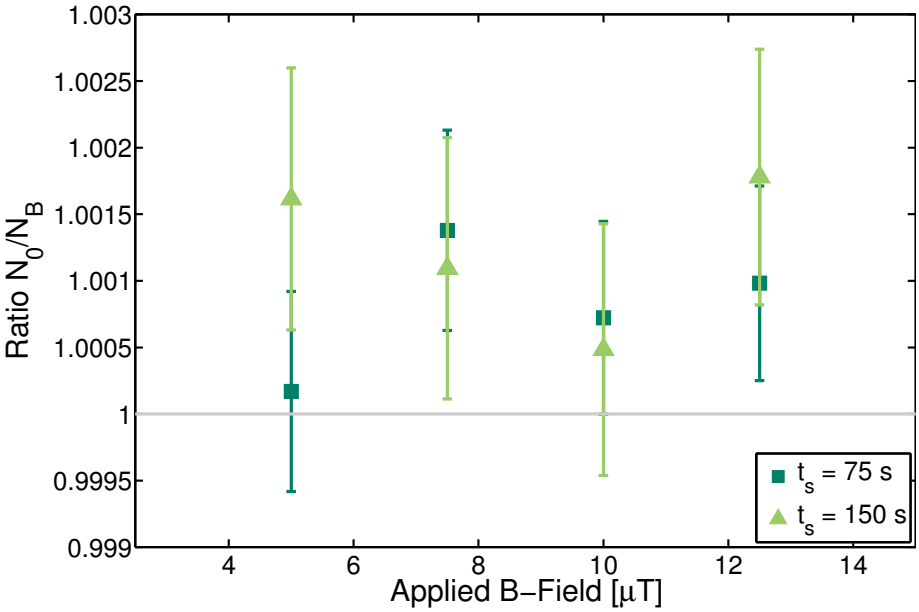

Figure 5.17.: Ratios of the normalised UCN count for zero and an applied magnetic field and the two storage times t_s used.

than $\sim 1\sigma$ above 1, also most of the ratios in Fig. 5.17 are $\sim 1\sigma$ above 1. In Section 5.2, the ratios were combined by fitting the data. Here, the procedure as used in [143] is chosen. Equation (5.7) can be inverted to give

$$\frac{1}{\tau^2_{nn'}} = \frac{\log N_{0/\uparrow\downarrow}}{\frac{t_s^*}{\langle t_f \rangle_{t_s}} \left(\frac{1}{2\omega^2} - \langle t_f^2 \rangle_{t_s} \right)} . \tag{5.23}$$

Care has to be taken in the averaging of the different values for $1/\tau^2_{nn'}$. The error imparted onto the calculation of $1/\tau^2_{nn'}$ stemming from the error of n_0 is common to all the measurements at the same storage time and has to be treated as a common systematic error. Thus, in averaging those values one has to follow the procedure as given in Appendix A.10 with the correlation factor ρ_i set to 1. The resulting averages for the two storage times amount to

$$\begin{aligned} \frac{1}{\tau^2_{nn'}}(t_s = 75\,\mathrm{s}) &= (-12.6 \pm 4.0 \pm 8.2) \times 10^{-5}\,\mathrm{s}^{-2} \\ \frac{1}{\tau^2_{nn'}}(t_s = 150\,\mathrm{s}) &= (-9.5 \pm 2.6 \pm 5.4) \times 10^{-5}\,\mathrm{s}^{-2} \end{aligned} \tag{5.24}$$

with statistical and systematical errors (in that order). The systematical error, i.e., the statistical sensitivity of the measurements for $B = 0$, dominates. As the systematic error for these two averages is uncorrelated, one can calculate the weighted average in the usual way (or by setting $\rho_i = 0$ in the formulas of Appendix A.10). The combined value is given as

$$\frac{1}{\tau^2_{nn'}} = (-10.5 \pm 5.0) \times 10^{-5}\,\mathrm{s}^{-2} . \tag{5.25}$$

The deviation from zero by 2σ still originates from the 1σ deviations for both normalised UCN counts for the two storage times at $B = 0$. As negative values for $1/\tau^2_{nn'}$ are unphysical, it is best to again adopt the Bayesian approach in the calculation of the limit as in Sec. 5.2. With a confidence level of 95%, one obtains $\frac{1}{\tau^2_{nn'}} < 5.1 \times 10^{-5}\,\mathrm{s}^{-2}$ and consequently

$$\tau_{nn'} > 139\,\mathrm{s}\ (95\%\ \mathrm{C.L.}) \tag{5.26}$$

in excellent agreement with the value of 141 s as extracted from the χ^2-contour above.

SEARCH FOR A DAILY MODULATION

A fast Fourier transformation was applied to the normalised fluctuations of the 1 min reactor power averages (see Fig. 5.18). A clear peak was found at a period of 24.3 h and also confirmed in a modulation fit with period d_{sid} resulting in a modulation amplitude of $(8.25 \pm 0.29) \times 10^{-4}$ in the normalised fluctuations. Although the correlation between UCN counts and reactor power is small (see Fig. 5.12), there might still be a small modulation imparted onto the UCN counts from the modulated reactor power. Therefore and in order to search for a modulation without being affected by the slow residual drifts present in the normalised UCN data, the up/down-asymmetries in the

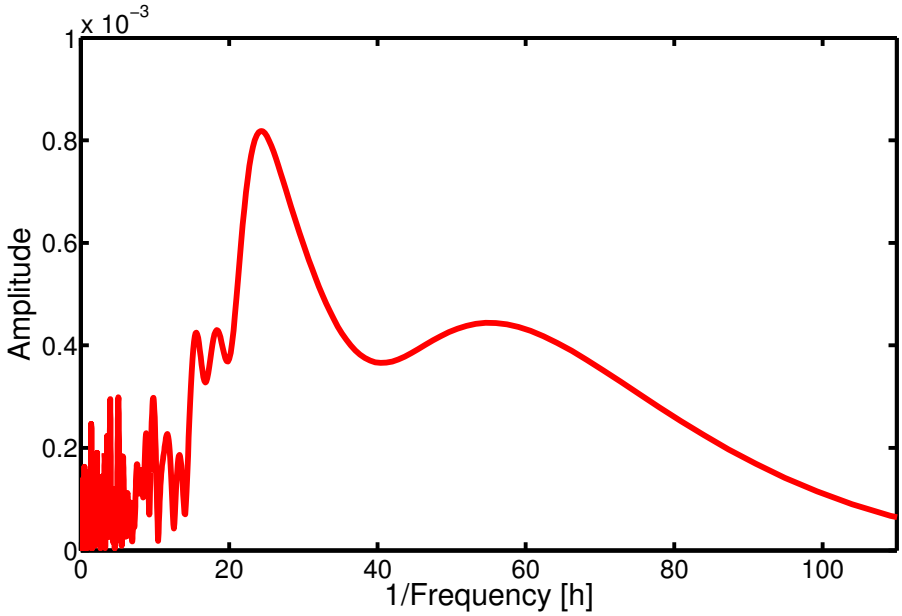

Figure 5.18.: Fast Fourier transformation of the normalised fluctuations of the reactor power. A clear peak is visible at a period of 24.3 h.

B [μT]	$\mathscr{A} \times 10^7$	t_0 [h]	χ^2/dof	$\mathscr{A}_{\text{lim}} \times 10^7$
2.5	1.3 ± 1.8	11.7 ± 9.4	6.53/10	6.6
5	2.4 ± 2.3	14.6 ± 3.0	5.92/10	6.4
7.5	3.5 ± 2.4	0.3 ± 2.0	5.52/10	7.6
10	0.6 ± 1.9	11.6 ± 12.6	18.05/12	5.0
12.5	1.0 ± 1.7	17.1 ± 9.8	10.13/12	5.0

Table 5.4.: Results of the fits using Eq. (5.27) to the up/down asymmetries for the five different magnetic field values and the upper limits on the amplitude of a daily modulation at 95% C.L. for any value of the phase t_0.

UCN counts $A = \frac{N_\uparrow - N_\downarrow}{N_\uparrow + N_\downarrow}$ were calculated from the two subsequent (within ~1 h) measurements at B field up and down. The two asymmetry data sets for 75 s and 150 s were separately normalised to have weighted means of zero. A modulation in the UCN counts would show up in the asymmetry with the same amplitude $\mathscr{A}$ as given in Eq. (5.20):

$$A(t) = \mathscr{A} \frac{t_s^*}{\langle t_f \rangle_{t_s}} \cos\left(\frac{2\pi}{d_{sid}}(t - t_0)\right) \tag{5.27}$$

A modulation was searched for in the 5 data sets of different B (2.5 μT, 5 μT, 7.5 μT, 10 μT, and 12.5 μT) by fitting Eq. (5.27) to the data. As an example, Fig. 5.19 shows the data and fit for an applied magnetic field of 7.5 μT. None of the fits showed a significant modulation. Limits on the amplitude were calculated performing a frequentist confidence level analysis along the lines of [56] and given in Appendix A.9.1. The results of the fits and the corresponding limits are listed in Table 5.4.

Additionally, limits on the oscillation time were obtained in the modulation analysis

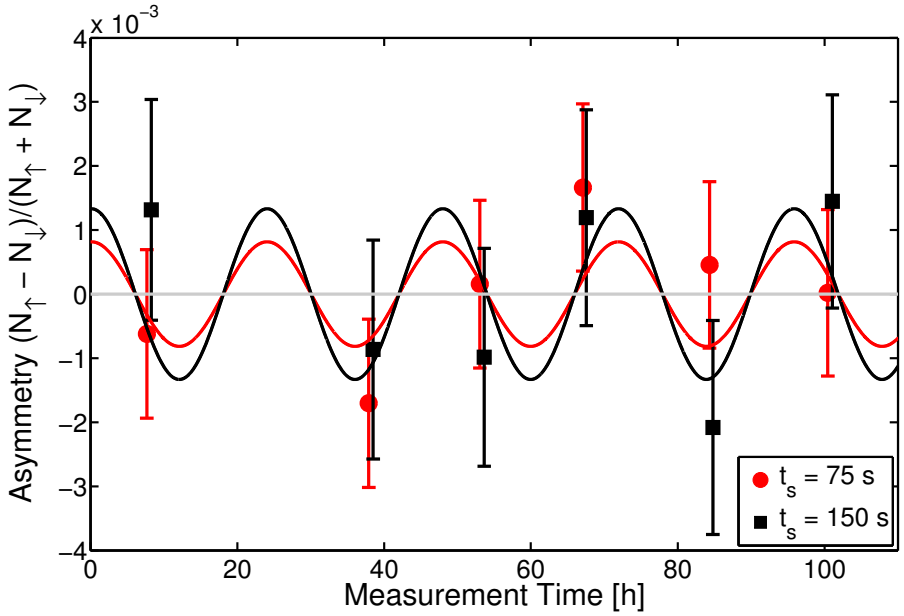

Figure 5.19.: Combined fit to the UCN counts asymmetry using Eq. (5.27) for 75 s (red circles and red line) and 150 s (black squares and black line). The data shown are for an applied magnetic field of 7.5 μT.

as well. It is clear by examining Eq. (5.20) that it is not possible to place at the same time constraints on $B'_\perp$ and $\tau_{nn'}$.[5] For the extraction of a lower limit on $\tau_{nn'}$, it was thus assumed that $B'_\perp$ is maximal (which leads to a lower limit on $\tau_{nn'}$), i.e., $B'_\perp = B'$. Under this assumption, the modulated angle β is fixed

$$\beta(t) = 90^\circ + (90^\circ - \lambda)\cos\left(\frac{2\pi}{d_{sid}}(t - t_0)\right) \tag{5.28}$$

and the expected asymmetry $A = \frac{N_\uparrow - N_\downarrow}{N_\uparrow + N_\downarrow}$ can directly be calculated. Free parameters are B', $\tau_{nn'}$, and t_0. The minimal χ^2 ($\chi^2/\text{dof} = 48.4/61$) is reached for $B' = 7.6\,\mu$T, $\tau_{nn'} = 47.5$ s, and $t_0 = 23.8$ h. The fit with a constant gives almost the same χ^2 ($\chi^2/\text{dof} = 50.5/63$). In analogy to the resonance analysis, limits were placed on the oscillation time by calculating at the points (B', $\tau_{nn'}$) the minimal χ^2 as a function of t_0. The exclusion contour for 61 dof is given with 95% C.L. at $\chi^2 = 80.23$. The resulting limit on $\tau_{nn'}$ as a function of B' can be seen in Fig. 5.20. In comparison with Fig. 5.15, one directly sees that the limits are, as expected, less tight and the limit goes to 0 for small B'.

5.3.7. DISCUSSION

These measurements were the first to systematically constrain nn' oscillations for any mirror magnetic field in the range 0 to 12.5 μT: $\tau_{nn'} > 12.0$ s (95% C.L.). For specific values of $B' \leq 12.5\,\mu$T, the limit is even better as can be seen in Fig. 5.15 reaching all the way up to the limit of $\tau_{nn'} > 141$ s (95% C.L.) for $B' = 0$. This improved the previously

[5] For this, an analysis also taking into account the averaged asymmetries and thus being sensitive to $B'_{||}$ would have to be performed.

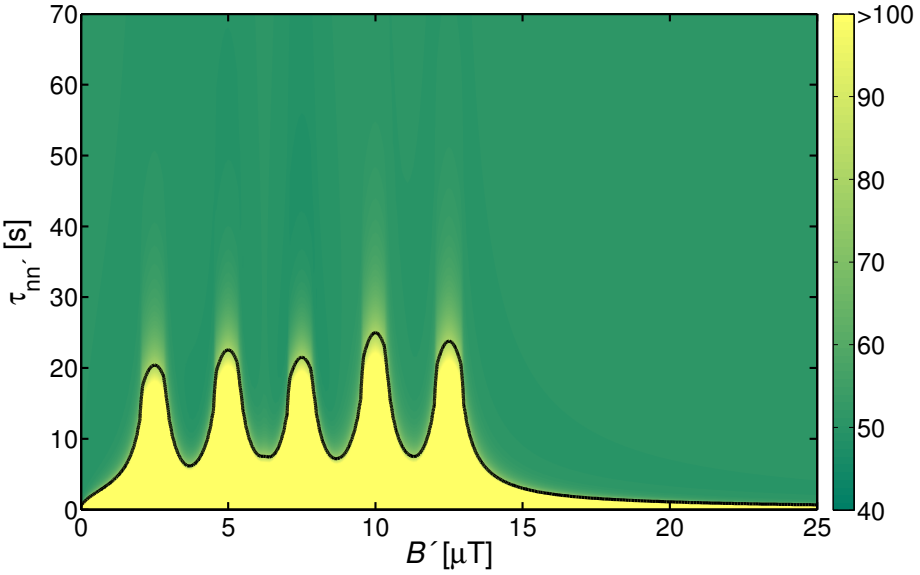

Figure 5.20.: Contour plot of the minimal χ^2 at the points $(B', \tau_{nn'})$ for the modulation analysis. The solid line denotes the 95% C.L. contour line for an exclusion of $\tau_{nn'}$.

obtained limit (see Section 5.2) but did not reach the current best limit on the oscillation time of $\tau_{nn'} > 448\,\text{s}$ (95% C.L.) [144].

However, the current best limit for $B' = 0$ is still about a factor 2 smaller than the neutron lifetime τ_n meaning that under suitable circumstances neutron escapes into the "Mirror World" could still compete with beta decay. A new experiment with a sensitivity to $\tau_{nn'} \gg 1000$ s is thus certainly worthwhile to pursue.

In order to transfer the envisaged sensitivities as discussed in Section 5.2.6 also to the searches in the presence of a mirror magnetic field, the spacings of the applied magnetic fields obviously have to be decreased. Evaluating Eq. (5.15) for $B = B'$ as a function of β, it was found that the nn' oscillation probability can be expressed as

$$P_{nn'}(t, B = B') \approx \sin^2\left(\frac{t}{\tau_{nn'}}\right)\frac{1}{2}(1+\cos\beta)\,. \tag{5.29}$$

ΔB [μT]	$P_{nn'}$ [%]	$\sqrt{P_{nn'}}$ [%]	ΔB [μT]	$P_{nn'}$ [%]	$\sqrt{P_{nn'}}$ [%]
0	100	100	0.7	19	44
0.1	98	99	0.8	15	39
0.2	93	96	0.9	12	35
0.3	85	92	1.0	10	32
0.4	75	87	1.1	8	28
0.5	38	62	1.2	7	26
0.6	26	51	1.3	6	24

Table 5.5.: Typical reductions of the oscillation probability $P_{nn'}$ at values $\Delta B = |B' - B|$ and the corresponding loss in sensitivity to $\tau_{nn'}$: $\sqrt{P_{nn'}}$.

The typical decrease in sensitivity when allowing for $B' \neq 0$ and measuring with an applied magnetic field pointing up and down thus amounts to

$$\frac{1}{2}\left(\sqrt{\frac{1}{2}\left(1+\cos\beta\right)}+\sqrt{\frac{1}{2}\left(1+\cos(180^\circ-\beta)\right)}\right)=0.5\ldots0.7\,. \tag{5.30}$$

Taking into account the factor 1.4 higher errors for the measurements at $B \neq 0$ in Fig. 5.15, the drop in sensitivity from 141 s to values between 50 s and 70 s is thus in accordance with the above considerations. The sensitivity in between the applied magnetic fields B, at values $\Delta B = |B' - B|$, is additionally suppressed due to the reduced oscillation probability. Typical values can be found in Table 5.5. For future measurements, an appropriate measurement spacing would be 0.6 μT, i.e. $\Delta B = 0.3\,\mu$T, leading to a loss in sensitivity of only ~10% in between the applied magnetic fields.

6 CONCLUSIONS

The work for this thesis was conducted within the nEDM project. As such, it offered the possibility to contribute to all three phases of the project. In the following, I will give short summaries and conclusions of the work found in the different chapters. Altogether, my thesis offered me the exciting opportunity to get to know one of the current major experiments in low energy particle physics [148] inside out.

6.1. CHAPTER 2: nEDM APPARATUS AT ILL

Most of the work done during this thesis on the nEDM apparatus was in the form of regular shifts while the apparatus was operational at the UCN source at the Institut Laue-Langevin in Grenoble, France. As such, I performed the first real EDM measurements where - for the first time - all the subsystems were running and operational. In total three days of continuous data had been taken and were analysed.

Together with these first EDM measurements, the influence of magnetic field fluctuations on the different magnetometers (neutron, mercury and cesium) was studied. While the neutron and the mercury signal showed an almost perfect agreement, the signals from the three Cs magnetometers located below the storage chamber differed. The stability of the magnetic field was found to be on the order of 10^{-6} during magnetically quiet periods and reached up to a few times 10^{-5} during magnetically more noisy periods.

In order to study the losses associated with the sequential spin analysis scheme, where during the counting of one of the spin components one has to store the other, dedicated measurements have been performed. In the analysis, the characteristic time constants connected to these losses have been extracted.

6.2. CHAPTER 3: nEDM APPARATUS AT PSI

Beginning of 2009, the nEDM apparatus was moved to PSI and EDM measurements are expected to start beginning of 2010 when the new UCN source at PSI starts its operation. From the increase in the available statistics, it is expected to achieve an improved sensitivity of a factor 5. To that end, also the systematics have to be controlled on the corresponding level. In this chapter, the expected systematic errors have been estimated and possible countermeasures suggested. They rely on an improved magnetometric control of the magnetic field inhomogeneities using the Cs magnetometers and improved scanning capabilities at PSI and PTB to detect magnetic impurities on the equipment.

From the available statistics and systematics, a measurement setting a limit of 5×10^{-27} $e$cm at 95% C.L. or detecting an EDM of 1.3×10^{-26} $e$cm with $5\,\sigma$ significance after

two years of data taking is expected.

6.3. CHAPTER 4: VELOCITY DEPENDENT UCN DETECTION

There exist several systematic false effects that depend on the velocity of the UCN. As such, one would greatly benefit from a measurement of the EDM as a function of the neutron velocity to check on such effects. While several techniques that allow to extract the UCN velocity are known, none of them is efficient enough to be compatible with EDM measurements. During this thesis, three detector concepts capable of efficient velocity dependent UCN detection have been studied. The favoured concept, a gravitational spectrometer, has been constructed and was successfully tested during measurements at ILL. Ideas for further measurements to achieve a reliable calibration of the detector are given.

6.4. CHAPTER 5: NEUTRON TO MIRROR-NEUTRON OSCILLATIONS

A proposed extension of the Standard Model of particle physics, that globally reconciles parity violation and provides a viable Dark Matter candidate in the form of mirror matter, can also allow for neutron to mirror-neutron oscillations. As they would manifest themselves in a magnetic field dependent loss rate in the EDM spectrometer, measurements have been performed searching for such a loss mechanism. While in the case of a negligible mirror magnetic field B' present at the experimental site, the neutron and mirror-neutron states are degenerate for $B \approx 0$ and oscillations would occur for this field setting, in the case of a non-zero B' losses would be maximal for $B \approx B'$. No indication for such oscillations have been found and a limit on the oscillation time $\tau_{nn'}$ has been set at $\tau_{nn'} > 141\,\mathrm{s}$ (95% C.L.) for $B' \approx 0$ and $\tau_{nn'} > 12.0\,\mathrm{s}$ (95% C.L.) for any B' between 0 and 12.5 μT.

A APPENDIX

A.1. CP VIOLATION AND THE CKM-MATRIX

It can be shown that a unitary 3×3 matrix can be reduced to possessing only one imaginary phase [149]. The CKM-matrix (named CKM after its discoverers Cabibbo, Kobayashi and Maskawa [23, 24]) mixing the flavour and weak interaction eigenstates of the quark is such a unitary matrix:

$$\begin{pmatrix} d' \\ s' \\ b' \end{pmatrix} = V_{CKM} \begin{pmatrix} d \\ s \\ b \end{pmatrix}, \tag{A.1}$$

where $'$ denote the weak interaction eigenstates.

The necessity to have a complex entry in the CKM-Matrix in order to violate CP can be illustrated in the Kaon decays [150]. It was discovered in 1964 that the CP odd state K_2 can decay into 2 Pions which are CP even. This transition has to occur via the CP even state K_1 by a Lagrangian having the form

$$\mathscr{L} = g_{eff} K_1 K_2^* + g_{eff}^* K_2 K_1^* \,. \tag{A.2}$$

g_{eff} is the coupling constant including the appropriate CKM-Matrix element. As K_1 is hermitian, K_2 anti-hermitian and the Lagrangian has to be hermitian, the coupling constant has to be imaginary.

It can also be seen directly from the term in the Standard Model lagrangian describing the coupling of the charged W-Boson to the quarks:

$$\mathscr{L} = g W_\mu^+ \bar{u} V_{CKM} d + g W_\mu^- \bar{d} V_{CKM}^\dagger u \tag{A.3}$$

Under a CP transformation the overall Lagrangian remains invariant except for the above part [151] resulting in

$$\mathscr{L} = g W_\mu^- \bar{d} V_{CKM}^T u + g W_\mu^+ \bar{u} V_{CKM}^* d \,. \tag{A.4}$$

As the CKM-Matrix has imaginary components, $V_{CKM} \neq V_{CKM}^*$ and $V_{CKM}^\dagger \neq V_{CKM}^T$ and CP invariance is violated.

A.2. DEPOLARISATION DUE TO INHOMOGENEOUS MAGNETIC FIELDS

Following the reasoning as given in [27], one can divide the precession volume into two parts with slightly different magnetic field values - expressed as a difference ΔB. As

the polarised atom or neutron moves between these two volumes with a diffusion time constant t_f, it will acquire each time a phase change $\pm\gamma\Delta B t_f$. During the precession time T, it will therefore acquire this phase change $\frac{T}{t_f}$ times resulting in a total rms phase change of

$$\phi = \gamma\Delta B t_f \sqrt{\frac{T}{t_f}} = \gamma\Delta B\sqrt{T t_f} \tag{A.5}$$

Assuming that the typical depolarisation time constant τ corresponds to $\phi = \pi/2$, one gets

$$\tau = \frac{\pi^2}{4(\gamma\Delta B)^2 t_f}. \tag{A.6}$$

For UCN, a typical t_f is approximately 0.05 s ($t_f = \frac{\lambda}{\langle v\rangle}$, $\lambda = \frac{4V}{A} = 0.16\,\mathrm{m}$, $\langle v\rangle = 3\,\frac{\mathrm{m}}{\mathrm{s}}$) and therefore to achieve a depolarisation time > 500 s, one needs $\Delta B < 2$ nT or gradients $< \mathcal{O}(10)$ nT/m.

A.3. DERIVATION OF THE RAMSEY-BLOCH-SIEGERT SHIFT

In [152] the use of rotating coordinates for magnetic resonance problems is described. The equation of motion for the magnetic moment is

$$\frac{\mathrm{d}\mathbf{J}}{\mathrm{d}t} = \gamma\left[\mathbf{J}\times\mathbf{B}\right]. \tag{A.7}$$

Using the rotation operator one derives

$$\frac{\mathrm{d}\mathbf{J}}{\mathrm{d}t} = \frac{\partial\mathbf{J}}{\partial t} + \omega\times\mathbf{J} \tag{A.8}$$

where $\frac{\partial}{\partial t}$ stands for differentiation in a coordinate system rotating with ω. Rearranging Eq. (A.7) yields

$$\frac{\partial\mathbf{J}}{\partial t} = \gamma\left[\mathbf{J}\times\left(\mathbf{B}+\frac{\boldsymbol{\omega}}{\gamma}\right)\right] = \gamma\left[\mathbf{J}\times\mathbf{B}_{eff}\right] \tag{A.9}$$

with the effective field $\mathbf{B}_{eff} = \mathbf{B} + \frac{\boldsymbol{\omega}}{\gamma}$.

In [66], the effect on the Larmor frequency is calculated. One has a large field in z-direction $\mathbf{B}_{0z}$ and a field $\mathbf{B}_{xy}$ in the xy-plane rotating at ω_r. The strength of the effective field in the rotating frame is therefore given by (see Fig. A.1)

$$|\mathbf{B}_{eff}| = \sqrt{\left(B_{0z}+\frac{\omega_r}{\gamma}\right)^2 + B_{xy}^2}. \tag{A.10}$$

With $\omega_0 = -\gamma B_{0z}$ and $\omega_{xy} = -\gamma B_{xy}$ the resulting precession frequency ω^* in the rotating frame is

$$\omega^* = \sqrt{(\omega_0-\omega_r)^2+\omega_{xy}^2}. \tag{A.11}$$

The observed frequency in the laboratory frame ω is then given by

$$\omega = \omega^* + \omega_r \tag{A.12}$$

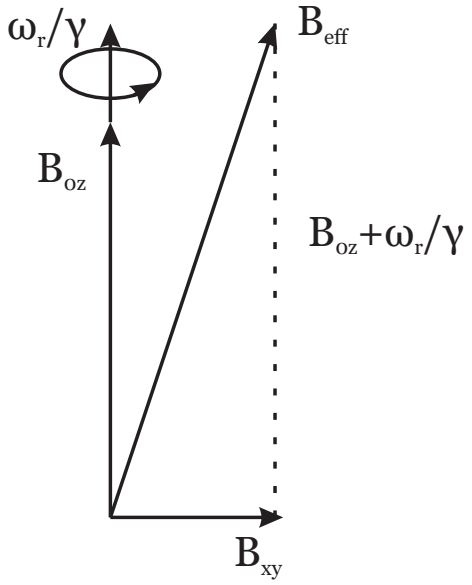

Figure A.1.: Magnetic fields in a rotating coordinate system as in [152].

resulting in

$$\begin{aligned} \Delta\omega = \omega - \omega_0 &= \sqrt{(\omega_0-\omega_r)^2+\omega_{xy}^2} - (\omega_0-\omega_r) && \text{(A.13)} \\ &\approx (\omega_0-\omega_r)\left[1+\frac{1}{2}\frac{\omega_{xy}^2}{(\omega_0-\omega_r)^2}\right] - (\omega_0-\omega_r) \\ &= \frac{\omega_{xy}^2}{2(\omega_0-\omega_r)}\,. && \text{(A.14)} \end{aligned}$$

Equations (A.13) and (A.14) are called the Ramsey-Bloch-Siegert shift - the later being applicable for the case $(\omega_0-\omega_r) \gg \omega_{xy}$.

A.4. QUANTUM MECHANICAL DESCRIPTION OF SPIN PRECESSION AND THE BLOCH-EQUATION

For a spin-1/2 particle, one can write the Hamiltonian as

$$\mathscr{H} = -\gamma \boldsymbol{s}\cdot\boldsymbol{B} \tag{A.15}$$

where $\boldsymbol{s}$ is the spin operator following $[s_i, s_j] = i\hbar\epsilon_{ijk}s_k$ and $\boldsymbol{B}$ the magnetic field vector. In the Heisenberg-picture, the time evolution of the spin is then given as

$$\begin{aligned} \frac{\mathrm{d}}{\mathrm{d}t}\boldsymbol{s} &= \frac{i}{\hbar}[\mathscr{H},\boldsymbol{s}] = -\gamma\frac{i}{\hbar}\left((\boldsymbol{s}\cdot\boldsymbol{B})\boldsymbol{s}-\boldsymbol{s}(\boldsymbol{s}\cdot\boldsymbol{B})\right) \\ &= -\gamma\frac{i}{\hbar}\begin{pmatrix} B_y(s_ys_x-s_xs_y)+B_z(s_zs_x-s_xs_z) \\ B_x(s_xs_y-s_ys_x)+B_z(s_zs_y-s_ys_z) \\ B_x(s_xs_z-s_zs_x)+B_y(s_ys_z-s_zs_y) \end{pmatrix} \\ &= \gamma(\boldsymbol{s}\times B) && \text{(A.16)} \end{aligned}$$

where the last transformation leads to the classical Bloch-equation for the spin precession. The same transformations also hold for the expectation value $\langle \boldsymbol{s} \rangle$.

Equally, one can derive the Bloch-equation also in the Schrödinger-picture. Here, one has the evolution of the wave function given as

$$|\Psi(t)\rangle = e^{-i\mathscr{H}t/\hbar}|\Psi\rangle\,. \tag{A.17}$$

The evolution of the expectation value for the spin precession is thus

$$\begin{aligned}
\frac{\mathrm{d}}{\mathrm{d}t}\langle \boldsymbol{s} \rangle &= \frac{\mathrm{d}}{\mathrm{d}t}\langle \Psi(t)|\boldsymbol{s}|\Psi(t)\rangle \\
&= \langle \Psi|e^{-i\boldsymbol{s}\cdot\boldsymbol{B}t/\hbar}\left(\frac{-i\boldsymbol{s}\cdot\boldsymbol{B}t}{\hbar}\boldsymbol{s} + \boldsymbol{s}\frac{i\boldsymbol{s}\cdot\boldsymbol{B}t}{\hbar}\right)e^{i\boldsymbol{s}\cdot\boldsymbol{B}t/\hbar}|\Psi\rangle \\
&= \langle \Psi(t)|\frac{-i\gamma}{\hbar}[\boldsymbol{s}\cdot\boldsymbol{B},\boldsymbol{s}]|\Psi(t)\rangle = \langle \Psi(t)|\gamma\boldsymbol{s}\times\boldsymbol{B}|\Psi(t)\rangle \\
&= \gamma\langle \boldsymbol{s}\rangle \times \boldsymbol{B}\,.
\end{aligned} \tag{A.18}$$

A.5. DISTRIBUTION OF UCN IN A STORAGE CHAMBER

The distribution of UCN in a storage chamber under the influence of gravity has been studied by Pendlebury and Richardson [153]. It can be derived by looking at the occupied volume in momentum space, which is equal to

$$4\pi p^2 \mathrm{d}p = \mathscr{C}\sqrt{E - m_n g h}\mathrm{d}E\,. \tag{A.19}$$

Here, E is the energy at height $h = 0$ and g the gravitational acceleration. The phase space density is independent of the position leading to

$$\frac{n(E,h)}{\mathscr{C}\sqrt{E - m_n g h}\mathrm{d}E} = \frac{n(E,h=0)}{\mathscr{C}\sqrt{E}\mathrm{d}E} \tag{A.20}$$

and thus one has the density of UCN as a function of height given as

$$n(E,h) = n(E,0)\sqrt{1 - \frac{mgh}{E}} = \mathscr{C}\sqrt{1 - \frac{h}{h_{max}}}\,. \tag{A.21}$$

$h_{max} = E/(m_n g)$ is the maximal attainable height for a UCN with energy E and the normalisation parameter $\mathscr{C}$ is introduced. With $n(E,h)\mathrm{d}h = n(E,v)\mathrm{d}v$, it follows that the distribution of velocities is given by

$$n(E,v) = \mathscr{C}v^2\,. \tag{A.22}$$

In order to being able to check also the components of the velocity, some more distributions are needed. In two dimensions, one has $v_x^2 + v_y^2 = v^2$ and as the components are independent $n(v_i) \propto \sqrt{1 - v_i^2/v^2}$. In three dimensions with $v_x^2 + v_y^2 + v_z^2 < v_{max}^2$, one has $n(v_z)\mathrm{d}v_z = n(v_x,v_y)\mathrm{d}v_x\mathrm{d}v_y = n(v_x)n(v_y)\mathrm{d}v_x\mathrm{d}v_y$ and thus using the distribution for two dimensions and as the components are independent

$$n(v_i) \propto \left(1 - \frac{v_i^2}{v_{max}^2}\right). \tag{A.23}$$

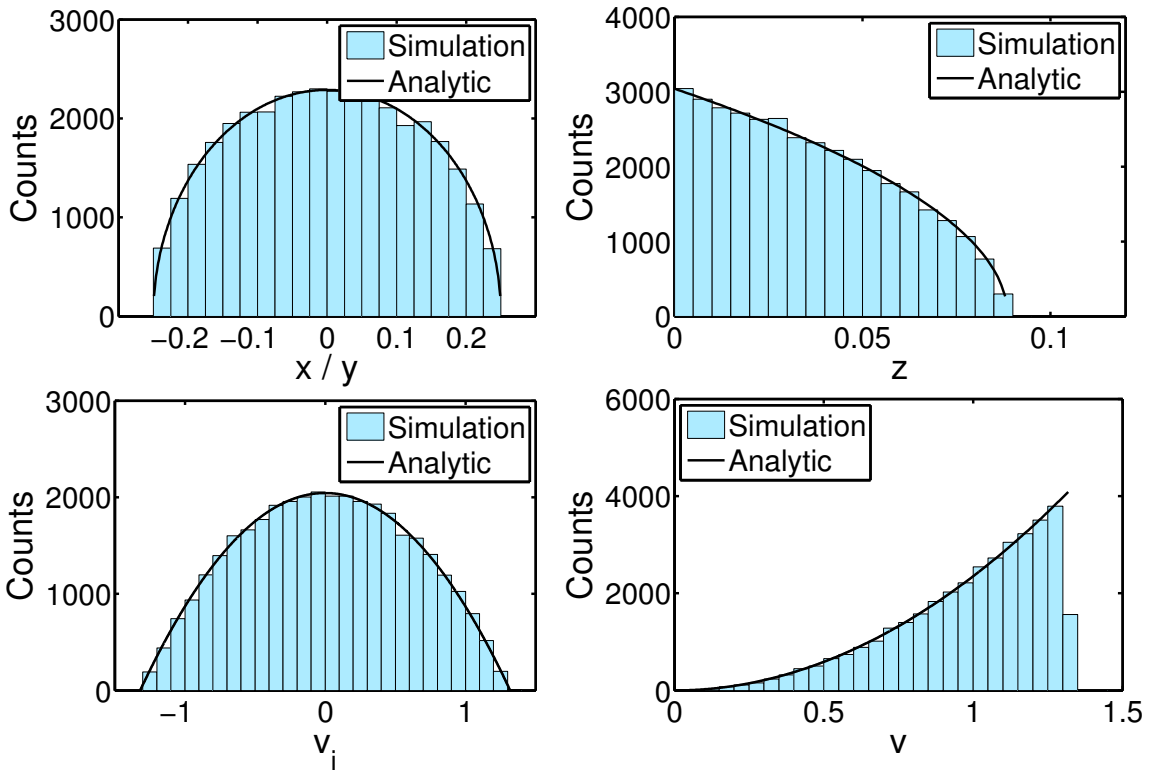

Figure A.2.: Distributions for the positions x, y and z and velocity v with components v_i for a UCN with $v_{max} = 1.3$ m/s in a cylindrical trap of height 12 cm and radius 25 cm under the influence of gravity.

For the cases, where the minimal velocity is not equal to zero, the corresponding missing part has to be subtracted after proper weighting from the distribution. In three dimensions and $v_{min} > 0$, one thus has

$$n(v_i) = \mathscr{C} \begin{cases} \left(1 - \frac{v_i^2}{v_{max}^2}\right), & |v_i| > v_{min} \\ \left(1 - \frac{v_i^2}{v_{max}^2}\right) - \left(\frac{v_{min}^2}{v_{max}^2}\right)^2 \left(1 - \frac{v_i^2}{v_{min}^2}\right), & |v_i| < v_{min} \end{cases} \tag{A.24}$$

While the distribution along z in the storage chamber is given by Eq. (A.21), the distribution on the circular area with radius r in x and y is uniform and given by

$$n(x) = \frac{1}{\pi} \frac{1}{\sqrt{r^2 - x^2}} \tag{A.25}$$

and the same for $n(y)$.

An example for the above distributions is shown in Fig. A.2. In the picture, the analytic calculations are compared to the simulation of the trajectories of UCN with $v_{max} = 1.3$ m/s in a cylindrical trap of height 12 cm and radius 25 cm under the influence of gravity.

It is also interesting to look at the mean free path lengths that the UCN samples while bouncing around in the storage chamber under the influence of gravity. In the case of no gravity, the mean free path length in the bounded space of volume V and surface

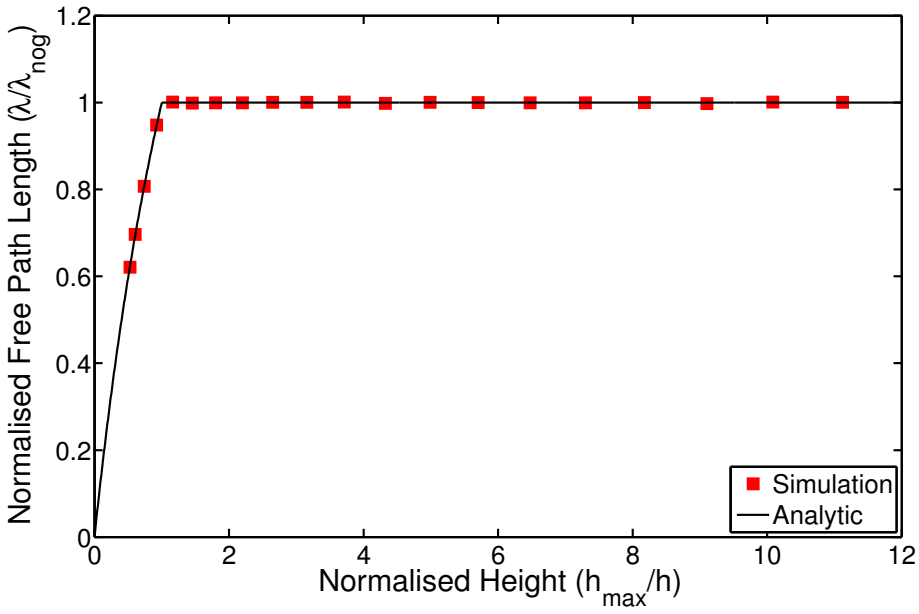

Figure A.3.: Mean free path lengths as a function of UCN energy h_{max} in a cylindrical trap of height h. The mean free path length in the case of no gravity is given by $\lambda_{nog} = \frac{4V}{A}$.

area A is simply given by

$$\lambda_{nog} = \frac{4V}{A} = \frac{2rh}{r+h} \tag{A.26}$$

where the expression is given for a cylindrical volume of radius r and height h. The case of the mean free path lengths under the influence of gravity has also been studied in [153]. In the case of UCN with energies $h_{max} = E/(m_n g)$ high enough to reach the top of the storage volume, one has $\lambda = \lambda_{nog}$. For the case of $h_{max} < h$ and cylindrical geometry, one has

$$\lambda = \frac{2rh_{max}}{r+h_{max}}. \tag{A.27}$$

This is shown in Fig. A.3 and compared to the mean free path lengths obtained in a corresponding simulation. In the simulation, one has to calculate the path length l by integrating over the parabolic trajectory

$$\boldsymbol{x}(t) = \boldsymbol{x}_0 + (t-t_0)\boldsymbol{v} - \frac{1}{2}g(t-t_0)^2 \begin{pmatrix} 0 \\ 0 \\ 1 \end{pmatrix} \tag{A.28}$$

in between two reflection points

$$l = \int_0^1 \mathrm{d}l = \int_{t_0}^{t_1} |\boldsymbol{x}(t+\mathrm{d}t) - \boldsymbol{x}(t)| = \int_{t_0}^{t_1} \sqrt{v^2 - 2g(t-t_0)v_z + g^2(t-t_0)^2}\,\mathrm{d}t. \tag{A.29}$$

It is interesting to note that the nice matching of simulated results and analytic calculations in Fig. A.2 and A.3 is only achieved, when the trajectories in the storage chamber are simulated using a non-zero fraction of diffuse reflections and the diffuse reflection is described by a $\cos\theta$ distribution. Also, only in that case the mechanical equilibrium condition $\langle v_x^2 \rangle + \langle v_y^2 \rangle + \langle v_z^2 \rangle = \langle v^2 \rangle$ holds for the calculated trajectories.

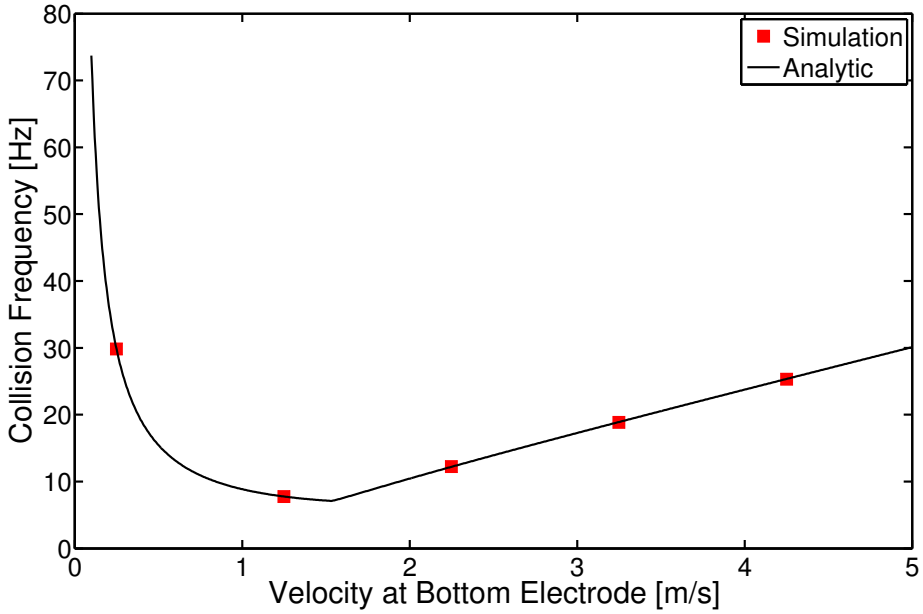

Figure A.4.: Simulated and calculated wall collision frequencies for UCN in a storage chamber of radius 25 cm and height 12 cm. The kink in the analytic description corresponds to the point at which UCN start to reach the top of the storage chamber.

With the knowledge on the mean free path lengths and the velocity spectrum in the storage chamber, one can calculate the collision frequency f_c of the UCN on the walls. For a given energy, the collision frequency is then given as

$$f_c = \frac{\langle v \rangle}{\lambda}. \tag{A.30}$$

λ is the calculated mean free path length as given in Eq. (A.26) and (A.27) and, using Eq. (A.22),

$$\langle v \rangle = \frac{3}{4\left(v_{max}^3 - v_{min}^3\right)}\left(v_{max}^4 - v_{min}^4\right). \tag{A.31}$$

The prediction of Eq. (A.30) is shown in Fig. A.4 together with the results of a simulation for a cylindrical storage chamber of radius 25 cm and height 12 cm. The data show a perfect agreement. It was also checked whether instead of Eq. (A.30) $f_c = \frac{\sqrt{\langle v^2 \rangle}}{\lambda}$ has to be used: The difference between $\langle v \rangle$ and $\sqrt{\langle v^2 \rangle}$ is constant for small velocities and amounts to ~3% for the given geometry and decreases to zero from the point where the UCN start to reach the top of the storage chamber. The simulation clearly matched the prediction of Eq. (A.30) much better.

A.6. GENERALISED MOORE-PENROSE-INVERSE

In the derivation, I follow the arguments given in [154].

A linear set of equations can be written as

$$\mathbf{y} = M\mathbf{x} \tag{A.32}$$

with the $n \times m$ matrix M, the known $n-$vector $\mathbf{y}$ and the unknown $m-$vector $\mathbf{x}$. For a overdetermined set of equations, we have $n > m$. One wants to find a solution that solves the system in a least squares sense, i.e. that minimises $\|\mathbf{y} - M\mathbf{x}\|$. One can rewrite that equation as

$$\begin{aligned} \|\mathbf{y} - M\mathbf{x}\| &= (\mathbf{y} - M\mathbf{x})^T(\mathbf{y} - M\mathbf{x}) \\ &= \mathbf{y}^T\mathbf{y} - \mathbf{y}^T M\mathbf{x} - \mathbf{x}^T M^T\mathbf{y} + \mathbf{x}^T M^T M\mathbf{x}. \end{aligned} \tag{A.33}$$

Differentiating the above equation with respect to $\mathbf{x}$ and setting the result equal to zero gives

$$-(\mathbf{y}^T M)^T - (M^T\mathbf{y}) + 2M^T M\mathbf{x} = 0 \tag{A.34}$$

and thus Eq. (A.32) is solved in the least squares sense by

$$\mathbf{x} = (M^T M)^{-1} M^T\mathbf{y}. \tag{A.35}$$

The $m \times n$ matrix $(M^T M)^{-1} M^T$ is then the generalised Moore-Penrose-inverse. In Matlab [69], Eq. (A.32) can be solved by calling `x = pinv(M)*y`.

A.7. CALCULATION OF THE TRANSITION PROBABILITY FOR A TWO STATE SYSTEM

I sketch the derivation as given in [141]. The relevant hamiltonian for the two-level system (neutron mirror-neutron mixing) is given by

$$H = H_0 + W = \begin{pmatrix} E_1 & W \\ W & E_2 \end{pmatrix}, \tag{A.36}$$

where $\Delta E = E_1 - E_2 = 2\hbar\omega = \mu B$ and the mixing energy W defines the oscillation time (also called mixing time):

$$\tau = \frac{\hbar}{W} \tag{A.37}$$

Solving the Schrödinger equation

$$i\hbar\frac{\mathrm{d}}{\mathrm{d}t}|\Psi(t)\rangle = H|\Psi(t)\rangle \tag{A.38}$$

results in the temporal evolution of the system given as

$$|\Psi(t)\rangle = \cos\frac{\theta}{2}e^{-i\frac{E_+ t}{\hbar}}|\Psi_+\rangle - \sin\frac{\theta}{2}e^{-i\frac{E_- t}{\hbar}}|\Psi_-\rangle \tag{A.39}$$

using $|\Psi(0)\rangle = |n\rangle$ as initial condition. $|n\rangle$ and $|n'\rangle$ are the eigenvectors of H_0 with eigenvalues $E_{1,2}$. $|\Psi_\pm\rangle$ and $E_\pm$ are the eigenvectors and eigenvalues of H:

$$\begin{aligned} E_\pm &= \frac{1}{2}(E_1 + E_2) \pm \frac{1}{2}\sqrt{(E_1 - E_2)^2 + 4W^2} \\ |\Psi_-\rangle &= \cos\frac{\theta}{2}|n\rangle + \sin\frac{\theta}{2}|n'\rangle \\ |\Psi_+\rangle &= -\sin\frac{\theta}{2}|n\rangle + \cos\frac{\theta}{2}|n'\rangle \\ \tan\theta &= \frac{2W}{E_1 - E_2} \end{aligned} \tag{A.40}$$

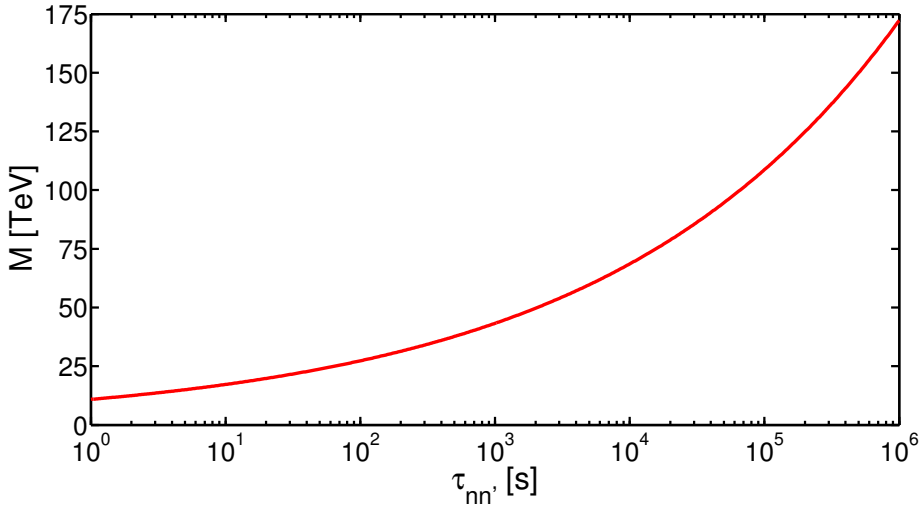

Figure A.5.: The figure shows the effective mass scale $\mathscr{M}$ corresponding to a given limit on the oscillation time $\tau_{nn'}$ as given in Eq. (A.48).

The probability to find the system in the state $|n'\rangle$ can then be calculated by evaluating

$$\begin{aligned} P_{n\to n'}(t) &= |\langle n'|\Psi(t)\rangle|^2 \\ &= \sin^2\theta \sin^2\left(\frac{E_+ - E_-}{2\hbar}t\right) \\ &= \frac{4W^2}{4W^2+(E_1-E_2)^2}\sin^2\left(\sqrt{4W^2+(E_1-E_2)^2}\,\frac{t}{2\hbar}\right) \\ &= \frac{1}{1+(\omega\tau)^2}\sin^2\left(\sqrt{1+(\omega\tau)^2}\,\frac{t}{\tau}\right). \end{aligned} \tag{A.41}$$

In the limit of no field ($\omega = 0$), Eq. (A.41) simplifies to

$$P_{n\to n'}(t) = \sin^2\left(\frac{t}{\tau}\right). \tag{A.42}$$

The oscillation time τ (basically only a redefinition of the mixing energy W in Eq. (A.36)) then has a direct connection to the transition time T from n to n':

$$T = \frac{\pi}{2}\tau \tag{A.43}$$

A.8. CONNECTION OF THE OSCILLATION TIME $\tau_{nn'}$ WITH A MASS SCALE

I follow here the arguments in [124] and [125]. In an effective theory, the operator necessary for nn' transitions would be a six fermion contact operator of the form

$$\mathscr{O}^{\rm mix} \sim \frac{1}{\mathscr{M}^5}(uud)(u'd'd'). \tag{A.44}$$

$\mathscr{M}$ is the typical mass scale with the dimension of 5 given by the fact that the dimension of $\mathscr{O}^{\rm mix}$ needs to be 4 (in order to obtain the dimensionless action $\mathscr{S} = \int \mathscr{L}\,{\rm d}^4x$

with the dimension of the wavefunctions being $\frac{3}{2}$). Typical expectation values for the wavefunctions will be of the order $\Lambda_{QCD} = 217\,\text{MeV}$ and thus

$$\langle \mathcal{O}^{\text{mix}} \rangle \sim \frac{\Lambda_{QCD}^6}{\mathcal{M}^5}. \tag{A.45}$$

This corresponds directly to the expected mixing energy for nn' transitions

$$W \sim \frac{\Lambda_{QCD}^6}{\mathcal{M}^5} \sim \left(\frac{10\,\text{TeV}}{\mathcal{M}}\right)^5 \times 10^{-15}\,\text{eV}. \tag{A.46}$$

The oscillation time $\tau_{nn'}$ is thus given by

$$\tau_{nn'} = \frac{\hbar}{W} \sim 0.66 \left(\frac{\mathcal{M}}{10\,\text{TeV}}\right)^5 \tag{A.47}$$

or inversely

$$\mathcal{M} \sim \sqrt[5]{\frac{\tau_{nn'}}{0.66\,\text{s}}}\,10\,\text{TeV}. \tag{A.48}$$

Figure A.5 shows the effective mass scale $\mathcal{M}$ corresponding to a given limit on the oscillation time $\tau_{nn'}$ as calculated by Eq. (A.48). Due to the fifth root of $\tau_{nn'}$, $\mathcal{M}$ scales only very weakly with $\tau_{nn'}$. Typical mass scales probed are therefore on the order of 10 to 100 TeV. It is possible to construct models where the mass of the exchange boson is much lower than the effective mass scale [123, 124].

A.9. FREQUENTIST CONFIDENCE LEVEL ANALYSIS

I use the notation and arguments as given in [56].

A.9.1. DAILY MODULATION

Searching for a daily modulated signal with an amplitude A , a phase t_0 and period d_{sid} (a sidereal day) given by the functional dependence $y(t) = A\sin\left(\frac{2\pi}{d_{sid}}(t_i - t_0)\right)$, one defines a quantity Q discriminating between a possible modulation signal and a constant:

$$\begin{aligned} Q_{\text{data}}(A, t_0) &= \chi^2_{\text{const}} - \chi^2_{\text{signal}} \\ &= \frac{1}{N}\sum_i^N \left(\frac{y_i}{\Delta y_i}\right)^2 - \frac{1}{N}\sum_i^N \left(\frac{y_i - A\sin\left(\frac{2\pi}{d_{sid}}(t_i - t_0)\right)}{\Delta y_i}\right)^2 \end{aligned} \tag{A.49}$$

N is the number of measurements $y_i \pm \Delta y_i$ at time t_i. In order to obtain the confidence level for Q_{data} in case of a signal, one generates a certain number of suites (denoted by index j) of random signal Monte-Carlo events at times t_i smeared out with standard widths Δy_i

$$y^j_{i,\text{MC}} = A\sin\left(\frac{2\pi}{d_{sid}}(t_i - t_0)\right) + r^j_{i,\text{norm}}\Delta y_i \tag{A.50}$$

with r_{norm} being a random number sampled from the normal distribution with $\mu = 0$ and $\sigma = 1$ and calculates Q^j_{MC}:

$$Q^j_{\text{MC}}(A, t_0) = \frac{1}{N}\sum_i^N \left(\frac{y^j_{i,\text{MC}}}{\Delta y_i}\right)^2 - \frac{1}{N}\sum_i^N \left(\frac{y^j_{i,\text{MC}} - A\sin\left(\frac{2\pi}{d_{sid}}(t_i - t_0)\right)}{\Delta y_i}\right)^2 \tag{A.51}$$

The confidence level for the measured data is then given by

$$CL(A, t_0) = \frac{\text{number of MC events with } Q_{\text{MC}} < Q_{\text{data}}}{\text{number of MC events}} \tag{A.52}$$

One can then place an upper limit on A at, e.g., 95% confidence level at the largest amplitude with $CL(A, t_0) < 5\%$ for all t_0. In the analysis in Section 5.3.6, t_0 was varied in steps of 0.2 h. For each combination of A and t_0, 10 000 Monte-Carlo Q^j_{MC} were calculated.

A.9.2. RESONANCE DUE TO nn' OSCILLATIONS

In using a frequentist confidence level analysis for the search of a resonance, some small changes in the above arguments are necessary. In principle $\tau_{nn'}$ takes over the role of the amplitude A, β the role of t_0 and the magnetic field B_i the role of the measurement time t_i. The data $y_i \pm \Delta y_i$ are the combined normalised UCN counts for 75 and 150 s storage time with a weighted average of 1. The first step consists in the calculation of the counts expected from the theory of nn' oscillations

$$y_{nn',i}(\tau_{nn'}, \beta) = \exp\left(-P_{nn'}(B_i, B', \tau_{nn'}, \beta, t_f)\frac{t_s}{t_f}\right) \tag{A.53}$$

taking into account the dependencies of the various parameters on the storage time. The values $y_{nn',i}$ are normalised to have a mean of 1. One can then calculate the Q-value for the data as:

$$\begin{aligned} Q_{\text{data}}(\tau_{nn'}, \beta) &= \chi^2_{\text{const}} - \chi^2_{\text{signal}} \\ &= \frac{1}{N}\sum_i^N \left(\frac{y_i - 1}{\Delta y_i}\right)^2 - \frac{1}{N}\sum_i^N \left(\frac{y_i - y_{nn',i}(\tau_{nn'}, \beta)}{\Delta y_i}\right)^2 \end{aligned} \tag{A.54}$$

Equally as above, one can generate the Monte-Carlo events as

$$y^j_{i,\text{MC}} = y_{nn',i}(\tau_{nn'}, \beta) + r^j_{i,\text{norm}}\Delta y_i\,. \tag{A.55}$$

The Monte-Carlo events are also normalised to a weighted average of 1 and used to calculate the Q-value for the Monte-Carlo data: Q^j_{MC}. The confidence level is then

$$CL(\tau_{nn'}, \beta) = \frac{\text{number of MC events with } Q_{\text{MC}} < Q_{\text{data}}}{\text{number of MC events}}\,. \tag{A.56}$$

The biggest difference to above is now that in calculating a 95% C.L. *lower* limit on $\tau_{nn'}$, this is given as the smallest $\tau_{nn'}$ for which one has $CL(\tau_{nn'}, \beta) > 5\%$ for *any* β. In the analysis in Section 5.3.6, β was varied in steps of 10°. For each combination of $\tau_{nn'}$ and β, 10 000 Monte-Carlo Q^j_{MC} were calculated.

A.10. AVERAGING OF VALUES WITH CORRELATED SYSTEMATIC ERRORS

In this section, I summarise the arguments as found in, e.g., [147]. The notation was adopted from [155]. Assume, one has two measurements a and b with systematic errors $Y^{a,b} = \sqrt{\sum_i (y_i^{a,b})^2}$ and statistical errors $T^{a,b}$. The total error is then given as $S^{a,b} = \sqrt{(Y^{a,b})^2 + (T^{a,b})^2}$. One defines a total correlation parameter as

$$\rho = \frac{\sum_i \rho_i y_i^a y_i^b}{S^a S^b} \tag{A.57}$$

with ρ_i being the correlation parameters of individual classes of systematic errors. ρ_i is typically either 0 (uncorrelated error between experiment a and b) or 1 (fully correlated or common error). With these definitions the weighted average value of the values Q^a and Q^b is then given as

$$\langle Q \rangle = \frac{Q^a S^b (S^b - \rho S^a) + Q^b S^a (S^a - \rho S^b)}{(S^a)^2 + (S^b)^2 - 2\rho S^a S^b} \tag{A.58}$$

with total error

$$S_{\langle Q \rangle} = \sqrt{\frac{(S^a S^b)^2 (1 - \rho^2)}{(S^a)^2 + (S^b)^2 - 2\rho S^a S^b}} \tag{A.59}$$

statistical error

$$T_{\langle Q \rangle} = \sqrt{(w^a T^a)^2 + (w^b T^b)^2}, \tag{A.60}$$

defining

$$w^{a,b} \equiv \sqrt{\frac{S^{b,a}(S^{b,a} - \rho S^{a,b})}{(S^a)^2 + (S^b)^2 - 2\rho S^a S^b}}, \tag{A.61}$$

and systematic error

$$Y_{\langle Q \rangle} = \sqrt{S^2_{\langle Q \rangle} - T^2_{\langle Q \rangle}}. \tag{A.62}$$

For the case in Section 5.3.6, where the values for $1/\tau^2_{nn'}$ of different magnetic field values but for the same storage time are averaged together, the above formulas yield the same result as a naive approach. In this the weighted average of $\frac{1}{\tau^2_{nn'}}$ is given by

$$\left\langle \frac{1}{\tau^2_{nn'}} \right\rangle = \frac{\sum_i \left(\frac{1}{\tau^2_{nn'}} \right)_i \frac{1}{(\sigma_i^{\text{tot}})^2}}{\sum_i \frac{1}{(\sigma_i^{\text{tot}})^2}} \tag{A.63}$$

and the error on the average

$$\sigma_{\left\langle \frac{1}{\tau^2_{nn'}} \right\rangle} = \frac{1}{\sum_i \frac{1}{(\sigma_i)^2}} + \sigma_c^2 \tag{A.64}$$

where the errors σ_i on $\frac{1}{\tau^2_{nn'}}$ stem from the statistical errors of the UCN counts at $B \neq 0$ and σ_c stems from the statistical uncertainty of the UCN counts at $B = 0$.

BIBLIOGRAPHY

[1] E. FERMI, Ricerca Scientifica **7**, 13 (1936).

[2] E. FERMI AND W. H. ZINN, *Reflection of Neutrons on Mirrors,* Phys. Rev. **70**, 103 (1946).

[3] E. FERMI AND L. MARSHALL, *Interference Phenomena of Slow Neutrons*, Phys. Rev. **71**, no. 10, 666 (1947).

[4] Y. B. ZEL'DOVICH, *Storage of Cold Neutrons*, Sov. Phys. JETP **9**, 1389 (1959).

[5] V. I. LUSHIKOV ET AL., *Observation of Ultracold Neutrons,* JETP Letters **9**, 23 (1969).

[6] A. STEYERL, *Measurements of total cross sections for very slow neutrons with velocities from 100 m/sec to 5 m/sec*, Phys. Lett. B **29**, 33 (1969).

[7] S. ARZUMANOV ET AL., *Neutron life time value measured by storing ultracold neutrons with detection of inelastically scattered neutrons*, Phys. Lett. B **483**, 15 (2000).

[8] A. SEREBROV ET AL., *Measurement of the neutron lifetime using a gravitational trap and a low-temperature Fomblin coating*, Phys. Lett. B **605**, 72 (2005).

[9] R. GOLUB, D. RICHARDSON AND S. K. LAMOREAUX, *Ultra-cold Neutrons*, Adam Hilger, Bristol, Philadelphia and New York (1991).

[10] C. AMSLER ET AL., *The Review of Particle Physics*, Phys. Lett. B **667**, 1 (2008).

[11] V. K. IGNATOVICH, *The Physics of Ultracold Neutrons*, Clarendon Press, Oxford (1990).

[12] F. ATCHISON ET AL., *Cold neutron energy dependent production of ultracold neutrons in solid deuterium*, Phys. Rev. Lett. **99**, no. 26, 262502 (2007).

[13] J. L. YARNELL ET AL., *Excitations in Liquid Helium: Neutron Scattering Measurements*, Phys. Rev. **113**, no. 6, 1379 (1959).

[14] A. STEYERL, *A "neutron turbine" as an efficient source of ultracold neutrons,* Nucl. Instr. Meth. **125**, 461 (1975).

[15] A. STEYERL ET AL., *A new source of cold and ultracold neutrons,* Phys. Lett. A **116**, 347 (1986).

[16] R. GOLUB AND J. M. PENDLEBURY, *Super-thermal sources of ultra-cold neutrons*, Phys. Lett. A **53**, 133 (1975).

[17] H. YOSHIKI ET AL., *Observation of ultracold-neutron production by 9-Å cold neutrons in superfluid helium*, Phys. Rev. Lett. **68**, no. 9, 1323 (1992).

[18] A. SAUNDERS ET AL., *Demonstration of a solid deuterium source of ultra-cold neutrons*, Phys. Lett. B **593**, 55 (2004).

[19] G. LÜDERS, *Proof of the TCP theorem*, Ann. of Phys. **2**, no. 1, 1 (1957).

[20] D. N. SPERGEL ET AL., *Three-Year Wilkinson Microwave Anisotropy Probe (WMAP) Observations: Implications For Cosmology*, Astrophys. J. Supp. **170**, no. 2, 377 (2007).

[21] A. D. SAKHAROV, *Violation of CP invariance, C asymmetry, and baryon asymmetry of the universe*, JETP Lett. **5**, 24 (1967).

[22] A. RIOTTO AND M. TRODDEN, *Recent Progress in Baryogenesis*, Ann. Rev. Nucl. Part. Sc. **49**, 35 (1999).

[23] N. CABIBBO, *Unitary Symmetry and Leptonic Decays*, Phys. Rev. Lett. **10**, no. 12, 531 (1963).

[24] M. KOBAYASHI AND T. MASKAWA, *CP-Violation in the Renormalizable Theory of Weak Interaction*, Prog. Theor. Phys. **49**, no. 2, 652 (1973).

[25] S. DAR, *The Neutron EDM in the SM: A Review*, arXiv:hep-ph/0008248v2 (2000).

[26] C. A. BAKER ET AL., *Improved Experimental Limit on the Electric Dipole Moment of the Neutron*, Phys. Rev. Lett. **97**, no. 13, 131801 (2006).

[27] I. B. KRHIPLOVICH AND S. K. LAMOREAUX, *CP Violation Without Strangeness*, Springer, Berlin (1997).

[28] R. D. PECCEI AND H. R. QUINN, *CP Conservation in the Presence of Pseudoparticles*, Phys. Rev. Lett. **38**, no. 25, 1440 (1977).

[29] S. A. ABEL AND O. LEBEDEV, *Neutron-electron EDM correlations in supersymmetry and prospects for EDM searches*, JHEP **1**, 133 (2006).

[30] M. POSPELOV AND A. RITZ, *Electric dipole moments as probes of new physics*, Annals of Physics **318**, 119 (2005).

[31] P. G. HARRIS, *The Neutron EDM Experiment*, arXiv:0709.3100v2 (2007).

[32] N. F. RAMSEY, *A Molecular Beam Resonance Method with Separated Oscillating Fields*, Phys. Rev. **78**, no. 6, 695 (1950).

[33] N. F. RAMSEY, *Electric-Dipole Moments of Particles,* Ann. Rev. Nucl. Part. Sci. **32**, 211 (1982).

[34] J. H. SMITH, E. M. PURCELL AND N. F. RAMSEY, *Experimental Limit to the Electric Dipole Moment of the Neutron*, Phys. Rev. **108**, no. 1, 120 (1957).

[35] C. G. SHULL AND R. NATHANS, *Search for a Neutron Electric Dipole Moment by a Scattering Experiment*, Phys. Rev. Lett. **16**, no. 7, 384 (1967).

[36] V. V. FEDOROV ET AL., *The Laue diffraction method to search for a neutron EDM. Experimental test of the sensitivity*, Nucl. Instrum. Methods Phys. Res., Sect. B **227**, 11 (2005).

[37] V. W. COHEN ET AL., *Electric Dipole Moment of the Neutron*, Phys. Rev. **177**, no. 5, 1942 (1969).

[38] S. APOSTOLESCU ET AL., *Upper Limit of the Electric Dipole Moment of the Neutron*, Rev. Roum. Phys **15**, 343 (1970).

[39] I. S. ALTAREV ET AL., *A Search for the Electric Dipole Moment of the Neutron Using Ultracold Neutrons*, Nucl. Phys. A **341**, 269 (1980).

[40] I. S. ALTAREV ET AL., *Search for the Neutron Electric Dipole Moment*, Phys. Atom. Nucl. **59**, 1152 (1996).

[41] J. M. PENDLEBURY ET AL., *Search for a Neutron Electric Dipole Moment*, Phys. Lett. B **136**, 327 (1984).

[42] http://nedm.web.psi.ch.

[43] http://www.neutronedm.org.

[44] K. BODEK ET AL., *Storage of ultracold neutrons in high resistivity, non-magnetic materials with high Fermi potential*, Nucl. Instr. Meth. A **597**, 222 (2008).

[45] S. GROEGER ET AL., *A high-sensitivity laser-pumped M_x magnetometer*, Eur. Phys. J. D **38**, 239 (2006).

[46] http://ucn.web.psi.ch.

[47] D. J. R. MAY, *A High Precision Comparison Of The Gyromagnetic Ratios of the ^{199}Hg Atom and The Neutron*, Ph.d. dissertation, University of Sussex (1998).

[48] A. I. EGOROV ET AL., *Production, Storage, and Polarization of Ultracold Neutrons*, Sov. J. Nucl. Phys. **19**, 147 (1947).

[49] P. GELTENBORT ET AL., *A compact, large-diameter adiabatic spinflipper for ultracold neutrons*, Nucl. Instrum. Methods Phys. Res., Sect. A **608**, 132 (2009).

[50] M. KUŹNIAK, *The Neutron Electric Dipole Moment Experiment: Research and Development for the New Spectrometer*, Ph.d. dissertation, Jagiellonian University (2008), available at: http://ucn.web.psi.ch/.

[51] K. GREEN ET AL., *Performance of an atomic mercury magnetometer in the neutron EDM epxeriment*, Nucl. Instrum. Methods Phys. Res., Sect. A **404**, 381 (1998).

[52] B. CAGNAC, *Orientation Nucléaire par Pompage Optique des Isotopes Impairs du Mercure*, Annales de Physique p. 467 (1961).

[53] Spellman High Voltage Electronics Co., http://spellmanhv.com/.

[54] D. D. DOYLE, *Systematic Effects in the Neutron EDM Experiment and its Constraints on Physics Beyond the Standard Model*, Ph.d. dissertation, University of Sussex (2004).

[55] S. ROCCIA, *Le co-magnétomètre mercure pour la mesure du moment électrique dipolaire du neutron: Optimisation et application au test de l'invariance de Lorentz*, Ph.d. dissertation, Université Joseph Fourier, Grenoble I (2009).

[56] I. ALTAREV ET AL., *Test of Lorentz Invariance with Spin Precession of Ultracold Neutrons*, Phys. Rev. Lett. **103**, no. 8, 081602 (2009).

[57] J. M. PENDLEBURY ET AL., *Geometric-phase-induced false electric dipole moment signals for particles in traps*, Phys. Rev. A **70**, 032102 (2004).

[58] P. G. HARRIS ET AL., *New Experimental Limit on the Electric Dipole Moment of the Neutron*, Phys. Rev. Lett. **82**, no. 5, 904 (1999).

[59] W. C. GRIFFITH ET AL., *Improved Limit on the Permanent Electric Dipole Moment of* ^{199}*Hg*, Phys. Rev. Lett. **102**, no. 10, 101601 (2009).

[60] J. D. RICHARDSON, *Ratio of g-Factors for the Neutron and* ^{199}*Hg, and nEDM Measurement Systematic Errors when Using a* ^{199}*Hg Co-Magnetometer*, Ph.d. dissertation, University of Sussex (2006).

[61] G. ZSIGMOND (2009), private communication.

[62] S. K. LAMOREAUX AND R. GOLUB, *Detailed discussion of a linear electric field frequency shift induced in confined gases by a magnetic field gradient: Implications for neutron electic-dipole-moment experiments*, Phys. Rev. A **71**, 032104 (2005).

[63] P. G. HARRIS AND J. M. PENDLEBURY, *Dipole-field contributions to geometric-phase-induced false electric-dipole-moment signals for particles in traps*, Phys. Rev. A **73**, 014101 (2006).

[64] A. L. BARABANOV, R. GOLUB AND S. K. LAMOREAUX, *Electric dipole moment searches: Effect of linear electric field frequency shifts induced in confined gases*, Phys. Rev. A **74**, 052115 (2006).

[65] F. BLOCH AND A. SIEGERT, *Magnetic Resonance for Nonrotating Fields*, Phys. Rev. **57**, no. 6, 522 (1940).

[66] N. F. RAMSEY, *Resonance Transitions Induced by Perturbations at Two or More Different Frequencies*, Phys. Rev. **100**, no. 4, 1191 (1955).

[67] A. SHAPERE AND F. WILCZEK, *Geometric Phases in Physics*, vol. 5 of *Advanced Series in Mathematical Physics*, chap. 1.1, p. 7, World Scientific, Singapore, New Jersey, London, Hong Kong (1989).

[68] M. V. BERRY, *Quantal phase factors accompanying adiabatic changes*, Proc. R. Soc. Lond. A **392**, 45 (1984).

[69] The MathWorks™, http://www.mathworks.com/.

[70] L. F. SHAMPINE AND M. K. GORDON, *Computer Solution of Ordinary Differential Equations: the Initial Value Problem*, W. H. Freeman, San Francisco (1975).

[71] G. QUÉMÉNER (2007), private communication.

[72] D. D. MCGREGOR, *Transverse relaxation of spin-polarized ^{3}He gas due to a magnetic field gradient*, Phys. Rev. A **41**, 2631 (1990).

[73] M. PENDLEBURY (2009), private communication.

[74] T. BRYS ET AL., *Magnetic field stabilization for magnetically shielded volumes by external field coils*, Nucl. Instrum. Methods Phys. Res., Sect. A **554**, 527 (2005).

[75] P. KNOWLES (2008), private communication.

[76] J. M. PENDLEBURY, *Kinetic Theory*, Student Monographs in Physics, Adam Hilger Ltd, Bristol and Boston (1985).

[77] CDT GmbH, http://www.n-cdt.com/.

[78] Gas Detectors Development Group, CERN, http://gdd.web.cern.ch/GDD/.

[79] F. SAULI, *GEM: A new concept for electron amplification in gas detectors*, Nucl. Instrum. Methods Phys. Res., Sect. A **386**, 531 (1997).

[80] P. NEF, *Calibration of the CASCADE-U UCN Detector*, Internship, ETH Zürich (2008).

[81] F. ATCHISON ET AL., *The simulation of ultracold neutron experiments using GEANT4*, Nucl. Instr. Meth. A **552**, 513 (2005).

[82] P. MAIER-KOMOR ET AL., *Design and advanced preparation of multilayer converters for ultracold-neutron detectors*, Nucl. Instrum. Methods Phys. Res., Sect. A **561**, 45 (2006).

[83] Nocado GmbH, http://www.nocado.de/.

[84] B. LAUSS, *UCN Guides for the Ultracold Neutron Source at PSI*, Proceedings of the workshop on Neutron Delivery Systems, ILL, Grenoble, France. (2009), available at: http://www.ill.eu/news-events/events/past-events/nds/program/.

[85] Evonik Röhm GmbH, http://www.plexiglas.de/.

[86] Mecacryl GmbH, http://www.mecacryl.ch/.

[87] L. GÖLTL-SIMMENAUER, *Measurements and Procedures for the Construction and Characterization of Ultra-Cold Neutron Guides*, Master thesis, University of Heidelberg & University of Mainz (2008), available at: http://ucn.web.psi.ch/.

[88] S-DH GmbH Heidelberg, http://www.s-dh.de/.

[89] S. HEULE, *Production, Characterization and Reflectivity Measurements of Diamond-like Carbon and other Ultracold Neutron Guide Materials*, Ph.d. dissertation, University of Zürich (2008), available at: http://ucn.web.psi.ch/.

[90] Reto Müller Schleiferei GmbH, http://www.muellerschleiferei.ch/.

[91] STALDER AG, http://www.stalderag.ch/.

[92] Fraunhofer Institut Werkstoff- und Strahltechnik, Dortmund, http://www.iws.fhg.de/.

[93] P. RÜTTIMANN (2008), private communication.

[94] STRELKOV ET AL., Joint Institute for Nuclear Research, Dubna, Russia.

[95] Pfeiffer Vacuum Inc., http://www.pfeiffer-vacuum.com/.

[96] V. F. SEARS, *Neutron scattering lengths and cross sections*, Neutron News **3**, no. 3, 26 (1992).

[97] P. FIERLINGER, A. PICHLMAIER AND H. RAUCH, *A time-of-flight chopper for ultracold neutrons*, Nucl. Instrum. Methods Phys. Res., Sect. A **557**, 572 (2006).

[98] F. ATCHISON ET AL., *Diamondlike carbon can replace beryllium in physics with ultracold neutrons*, Phys. Lett. B **642**, 24 (2006).

[99] F. ATCHISON ET AL., *Measurement of the Fermi potential of diamond-like carbon and other materials*, Nucl. Instrum. Methods Phys. Res., Sect. B **260**, 647 (2007).

[100] I. ALTAREV ET AL., *Neutron velocity distribution from a superthermal solid $^2H_2$ ultracold neutron source*, Eur. Phys. J. A **37**, 9 (2008).

[101] E. H. MOORE, *On the reciprocal of the general algebraic matrix*, Bull. Am. Math. Soc. **26**, 394 (1920).

[102] R. PENROSE, *A generalized inverse for matrices*, Proc. Cambridge Philos. Soc. **51**, 406 (1955).

[103] I. ALTAREV, E. GUTSMIEDL AND R. STÖPLER, *UCN shaper* (2008), private communication.

[104] G. BAN ET AL., *Direct Experimental Limit on Neutron–Mirror-Neutron Oscillations*, Phys. Rev. Lett. **99**, 161603 (2007).

[105] I. ALTAREV ET AL., *Neutron to mirror-neutron oscillations in the presence of mirror magnetic fields*, Phys. Rev. D **80**, no. 3, 032003 (2009).

[106] T. D. LEE AND C. N. YANG, *Question of Parity Conservation in Weak Interactions*, Phys. Rev. **104**, no. 1, 254 (1956).

[107] I. Y. KOBZAREV, L. B. OKUN AND I. Y. POMERANCHUK, *On the Possibility of Experimental Observation of Mirror Particles*, Sov. J. Nucl. Phys **3**, 837 (1966).

[108] R. FOOT, H. LEW AND R. R. VOLKAS, *A model with fundamental improper space-time symmetries*, Phys. Lett. B **272**, 67 (1991).

[109] L. B. OKUN, *Mirror particles and mirror matter: 50 years of speculation and search*, Physics-Uspekhi **50**, no. 4, 380 (2007), [arXiv:hep-ph/0606202v2].

[110] C. S. WU ET AL., *Experimental Test of Parity Conservation in Beta Decay*, Phys. Rev. **105**, no. 4, 1413 (1957).

[111] S. I. BLINNIKOV AND M. KHLOPOV, *Possible manifestations of "mirror" particles*, Sov. J. Nucl. Phys **36**, 472 (1982).

[112] R. FOOT, *Have mirror stars been observed?*, Phys. Lett. B **452**, 83 (1999).

[113] R. FOOT, *Have mirror planets been observed?*, Phys. Lett. B **471**, 191 (1999).

[114] R. FOOT, *Mirror matter-type dark matter*, Int. J. Mod. Phys. D **13**, 2161 (2004).

[115] Z. BEREZHIANI ET AL., *Structure Formation with Mirror Dark Matter: CMB and LSS*, Int. J. Mod. Phys. D **14**, 107 (2005).

[116] R. FOOT, *Experimental Implications of Mirror Matter-Type Dark Matter*, Int. J. Mod. Phys. A **19**, 3807 (2004).

[117] R. FOOT, *Generalized mirror matter models*, Phys. Lett. B **632**, 467 (2006).

[118] R. FOOT, *Mirror dark matter and the new DAMA/LIBRA results: A simple explanation for a beautiful experiment*, Phys. Rev. D **78**, 043529 (2008).

[119] R. BERNABEI ET AL., *First results from DAMA/LIBRA and the combined results with DAMA/NaI*, Eur. Phys. J. C **56**, 333 (2008).

[120] K. GREISEN, *End to the Cosmic-Ray Spectrum?*, Phys. Rev. **16**, no. 17, 748 (1966).

[121] G. T. ZATSEPIN AND V. A. KUZMIN, *Upper Limit of the Spectrum of Cosmic Rays*, JETP Lett. **4**, 78 (1966).

[122] M. TAKEDA ET AL., *Extension of the Cosmic-Ray Energy Spectrum beyond the Predicted Greisen-Zatsepin-Kuz'min Cutoff*, Phys. Rev. Lett. **81**, no. 6, 1163 (1998).

[123] R. N. MOHAPATRA, S. NASRI AND S. NUSSINOVA, *Some implications of neutron mirror neutron oscillation*, Phys. Lett. B **627**, 124 (2005).

[124] Z. BEREZHIANI AND L. BENTO, *Neutron–Mirror-Neutron Oscillations: How Fast Might They Be?*, Phys. Rev. Lett. **96**, 081801 (2006).

[125] Z. BEREZHIANI AND L. BENTO, *Fast neutron-mirror neutron oscillation and ultra high energy cosmic rays*, Phys. Lett. B **635**, 253 (2006).

[126] Z. BEREZHIANI, *Mirror World and its Cosmological Consequences*, Int. J. Mod. Phys. A **19**, no. 23, 3775 (2004).

[127] R. U. ABBASI ET AL., *First Observation of the Greisen-Zatsepin-Kuzmin Suppression*, Phys Rev Lett. **100**, no. 10, 101101 (2008).

[128] J. ABRAHAM ET AL., *Observation of the Suppression of the Flux of Cosmic Rays above* 4×10^{19} *eV*, Phys. Rev. Lett. **101**, no. 6, 061101 (2008).

[129] S. ASAI, O. JINNOUCHI AND T. KOBAYASHI, *Solution of the Orthopositronium Lifetime Puzzle*, Int. J. Mod. Phys. A **19**, 3927 (2004).

[130] R. FOOT AND S. N. GNINENKO, *Can the mirror world explain the orthopositronium lifetime puzzle?*, Phys. Lett. B **480**, 171 (2000).

[131] T. MITSUI ET AL., *Search for Invisible Decay of Orthopositronium*, Phys. Rev. Lett. **70**, no. 15, 2265 (1993).

[132] A. BADERTSCHER ET AL., *Improved limit on invisible decays of positronium*, Phys. Rev. D **75**, 032004 (2007).

[133] Z. BEREZHIANI AND R. N. MOHAPATRA, *Reconciling present neutrino puzzles: Sterile neutrinos as mirror neutrinos*, Phys. Rev. D **52**, no. 11, 6607 (1995).

[134] R. FOOT AND R. R. VOLKAS, *Implications of mirror neutrinos for early universe cosmology*, Phys. Rev. D **61**, 043507 (2000).

[135] S. G. TURYSHEV ET AL., *The Study of the Pioneer Anomaly: New Data and Objectives for New Investigation*, Int. J. Mod. Phys. D **15**, 1 (2006).

[136] R. FOOT AND R. R. VOLKAS, *A mirror world explanation for the Pioneer spacecraft anomalies?*, Phys. Lett. B **517**, 13 (2001).

[137] R. FOOT AND S. MITRA, *Detecting mirror matter on Earth via its thermal imprint on ordinary matter*, Phys. Lett. A **315**, 178 (2003).

[138] S. MITRA AND R. FOOT, *Detecting dark matter using centrifuging techniques*, Phys. Lett. B **558**, 9 (2003).

[139] M. BALDO-CEOLIN ET AL., *A new experimental limit on neutron-antineutron oscillations*, Z. Phys. C **63**, 409 (1994).

[140] Y. N. POKOTILOVSKI, *On the experimental search for neutron → mirror neutron oscillations*, Phys. Lett. B **639**, 214 (2006).

[141] C. COHEN-TANNOUDJI, B. DIU AND F. LALOË, *Quantum Mechanics, Volume One*, chap. IV, New York: Wiley (1977).

[142] R. N. MOHAPATRA AND R. E. MARSHAK, *Phenomenology of Neutron Oscillations*, Phys. Lett. B **94**, no. 2, 183 (1980).

[143] A. P. SEREBROV ET AL., *Experimental search for neutron – mirror neutron oscillations using storage of ultracold neutrons*, Phys. Lett. B **663**, 181 (2008).

[144] A. P. SEREBROV ET AL., *Search for neutron - mirror neutron oscillations in a laboratory experiment with ultracold neutrons*, arXiv:0809.4902v2 [nucl-ex] (2008).

[145] Z. BEREZHIANI, *More about neutron – mirror neutron oscillation*, arXiv:hep-ph/0804.2088v1 (2008).

[146] A. Y. IGNATIEV AND R. R. VOLKAS, *Geophysical constraints on mirror matter within the Earth*, Phys. Rev. D **62**, 023508 (2000).

[147] G. COWAN, *Statistical Data Analysis*, Clarendon Press, Oxford (1998).

[148] M. RAIDAL ET AL., *Flavor physics of leptons and dipole moments*, Eur. Phys. J. C **57**, no. 1, 13 (2008).

[149] L. WOLFENSTEIN, *Parametrization of the Kobayashi-Maskawa Matrix*, Phys. Rev. Lett. **31**, no. 21, 1945 (1983).

[150] C. JARLSKOG AND E. SHABALIN, *On Searches for CP, T, CPT and C Violation in Flavour-Changing and Flavour-Conserving Interactions*, Physica Scripta **T99**, 23 (2002).

[151] R. BARBIERI, *The Flavour Sector*, Lecture at the CHIPP Phd School in Näfels (2008).

[152] I. I. RABI, N. F. RAMSEY AND J. SCHWINGER, *Use of Rotating Coordinates in Magnetic Resonance Problems*, Rev. Mod. Phys. **26**, no. 2, 167 (1954).

[153] J. M. PENDLEBURY AND D. J. RICHARDSON, *Effects of Gravity on the Storage of Ultracold Neutrons*, Nucl. Instrum. Methods Phys. Res., Sect. A **337**, 504 (1994).

[154] B. K. P. HORN, *Solving over-and under-determined sets of equations* (2009), available at: http://people.csail.mit.edu/bkph/articles/Pseudo_Inverse.pdf.

[155] L. DEMORTIER ET AL., *Combining the Top QuarkMass Results for Run 1 from CDF and D0*, Tech. Rep. FERMILAB-TM-2084, Fermi National Accelerator Laboratory (1999).

ACKNOWLEDGMENTS

I would like to thank my PhD supervisor **Ulrich Straumann** for the continued support over the course of my thesis and the possibility of doing my PhD at the University of Zürich. Especially, I would like to thank for the freedom that I enjoyed to follow my own ideas and the willingness to help them come to a good end.

Huge thanks go to **Klaus Kirch**, my supervisor at PSI. For all the discussions, the help and support, the inspiration, the gentle guiding, and for the excellent company through all these years. I have learned a lot from you on how a physicist should work!

I want to thank former and current members of the PSI UCN Physics group: **Manfred Daum** (for hiring me in the first place), **Reinhold Henneck** (for the excellent company during several shifts at ILL), **Michael Meier** (for all the help concerning the mechanical design and construction of the gravitational spectrometer and the many other things where you were always willing to help), **Axel Pichlmaier** (for the supervision in the early stage of my thesis aiming at a neutron lifetime experiment), **Bernhard Lauss** (for the help in getting the plexiglas tubes clean and coated), **Géza Zsigmond** (for the help with simulations), **Stefan Heule** (for warning me time and time again that I should start writing - I partly followed your advice, but you were right), **Marcin Kuźniak** (for the introduction to GEANT4), **Marlon Horras** (for helping with the Gravispectro tests during the full three weeks of beamtime at ILL), **Lenny Göltl** (you're the senior PhD now..!), **Francis Atchison**, **Michael Wohlmuther**, **Fritz Burri**, **Aliko Mtchedlishvili**, **Małgorzata Kasprzak**, **Gerd Petzoldt**, **Edgard Pierre**, **Philipp Schmidt-Wellenburg**, **Johannes Zenner**, **Zema Chowdhuri** and **Marco Büchler**. You all made working at PSI a real pleasure!

The thesis would not have been possible without the help of the different workshops and support groups at PSI.

For all the support during the many beamtimes at ILL, I am grateful to the local crew: **Peter Geltenbort**, **Christian Plonka-Spehr** and **Thomas Brenner**.

I would like to thank also all the members of the nEDM collaboration for their interest in my work and several pleasant collaboration meetings throughout Europe.

Endless thanks go to **Caroline** - especially for your patience when my head was full of physics...

For all the support, I would like to thank my parents and family. Especially for your continuous effort of trying to understand what it is that I am doing.

Last but not least, I want to thank my friends and colleagues for all the enjoyable time

spent outside of physics. Special thanks go to my flatmates in Schlieren and Zürich: **Andrea**, **Andreas**, **Evelyn** and **Judith**.